

A Thesis Submitted for the Degree of PhD at the University of Warwick

Permanent WRAP URL:

<http://wrap.warwick.ac.uk/152458>

Copyright and reuse:

This thesis is made available online and is protected by original copyright.

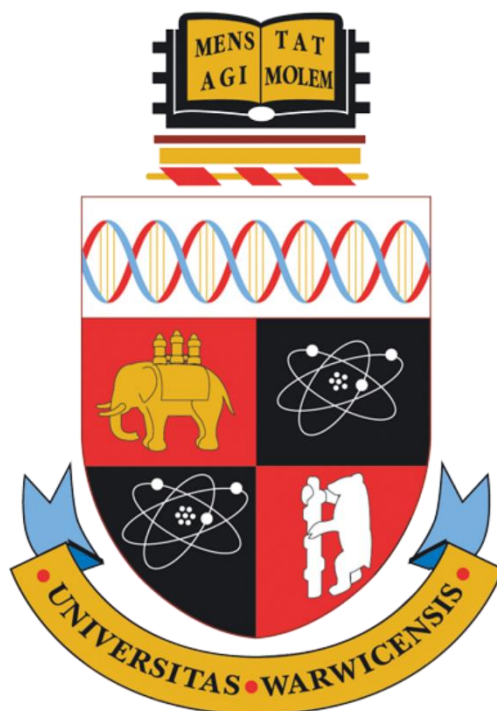
Please scroll down to view the document itself.

Please refer to the repository record for this item for information to help you to cite it.

Our policy information is available from the repository home page.

For more information, please contact the WRAP Team at: wrap@warwick.ac.uk

Zeolite and Metal-Organic Framework Catalysts for the Production of Value Added Platform Molecules from Biomass Derived Carbohydrates



by

Ryan Oozeerally

A thesis submitted in partial fulfilment of the
requirements for the degree of Doctor of Philosophy
in Engineering

University of Warwick, School of Engineering

December 2019

Table of Contents

Table of Contents

Acknowledgements	iv
Declarations.....	v
Publications	vii
Abstract.....	ix
List of Figures	x
List of Tables.....	xvii
General Introduction.....	1
Literature Review.....	3
Summary.....	3
2.1 Glucose Isomerisation in Industry	4
2.2 Base catalysed Glucose Isomerisation	5
2.3 Acid catalysed Glucose Isomerisation	6
2.4 Tin containing heterogeneous catalysts for Glucose Isomerisation.....	10
2.5 Tin Active Sites Within Beta Zeolite	12
2.6 Lewis Acid Tin Beta Active Sites and Isomerisation Mechanisms	14
2.7 Synthesis methods towards active Tin Beta.....	16
2.7 Glucose derived 5-hydroxymethylfurfural	19
2.8 Ionic Liquid Systems for HMF Production	21
Conclusion	30
Experimental	31
Summary.....	31
3.1 Zeolite Synthesis	31
<i>Synthesis Of Metal-Containing Beta Zeolites</i>	31
<i>Dealumination Of Commercial Zeolite Y</i>	33
<i>Post-Synthesis Addition Of Metals To Zeolite Y</i>	33
3.2 MOF Synthesis	34
<i>Zirconium MOFs</i>	34
<i>MIL-88B</i>	37
<i>Ytterbium MOF Yb₂(BDC)₃(DMF)₂(H₂O)₂</i>	37
<i>Ytterbium MOF Yb₆(BDC)₇(OH)₄(H₂O)₄</i>	38
<i>ZIF-8 Room Temperature Synthesis</i>	38
<i>ZIF-8 Hydrothermal Synthesis</i>	38
3.3 Material Characterization Techniques	39
3.4 Stability Testing.....	39
3.5 Batch Reactions	40
<i>Batch Reactions</i>	40
<i>Recycle Reactions</i>	40
3.6 Flow Reactor	41
3.7 Reactions Analysis	43
<i>High Performance Liquid Chromatography</i>	43
3.8 Extended X-ray Absorption Fine Structure (EXAFS) and X-ray Absorption Near Edge Structure (XANES) analysis	44

<i>Analysis Of Solid Materials During Reduction</i>	44
<i>In-situ Analysis Of Catalysts</i>	46
A Three-Day Crystallization of Metal-Containing Beta Zeolites and their Performances as Biomass Valorisation Catalysts.	48
Summary	48
4.1 Introduction	49
4.2 Results and Discussion	50
<i>Catalyst Characterization</i>	50
<i>Glucose Isomerisation and Dehydration towards HMF</i>	65
<i>Fructose Dehydration towards HMF</i>	71
<i>Flow Reactor</i>	73
4.3 Conclusions	77
Gallium and Tin Containing Zeolite Y for Glucose Isomerisation and 5-Hydroxymethylfurfural Production	79
Summary	79
5.1 Introduction	80
5.2 Results and Discussion	81
<i>Structure and Morphology</i>	81
<i>Glucose Isomerisation and Dehydration towards HMF</i>	91
<i>Fructose Dehydration to HMF</i>	95
<i>Catalyst Stability & Recycling</i>	96
<i>Reactant to Catalyst ratio</i>	101
<i>XANES analysis</i>	103
5.3 Conclusions	106
Exploring Metal-Organic Frameworks for the Isomerisation of Glucose and Production of 5-Hydroxymethylfurfural.	108
Summary	108
Iron and Scandium MIL-88B as a non-toxic alternative to Chromium Containing MIL-101 for glucose isomerisation and HMF production.	110
Summary	110
6.1 Introduction	111
6.2 Results and Discussion	112
<i>Structure and Morphology</i>	112
<i>Glucose dehydration to HMF</i>	119
<i>Reactant to Catalyst ratio</i>	121
<i>Stability and recyclability</i>	123
6.3 Conclusion	125
A ytterbium MOF catalyst for the isomerisation of glucose and production of HMF.	126
Summary	126
6.4 Introduction	127
6.5 Results and Discussion	128
<i>Structure and Morphology</i>	128
<i>Glucose dehydration to HMF</i>	130
<i>Stability and Recycling</i>	134
6.6 Conclusions	137

A room temperature and hydrothermal synthesis of ZIF-8 catalysts for glucose isomerisation in water.	138
Summary	138
6.7 Introduction	139
6.8 Results and Discussion	140
<i>Structure and Morphology</i>	140
<i>Glucose dehydration to HMF</i>	144
<i>Catalyst Stability & Recycling</i>	149
6.9 Conclusions	150
Exceptionally Efficient and Recyclable Heterogeneous UiO-66 Catalysts for Glucose Isomerization in Water.	151
Summary	151
6.10 Introduction	152
6.11 Results and Discussion	153
<i>Structure and Morphology</i>	153
<i>Glucose dehydration to HMF</i>	159
<i>Catalyst Stability & Recycling</i>	160
6.12 Conclusions	165
Fine-Tuning Zirconium Organic Frameworks Towards the Isomerisation of Glucose and Production of 5-Hydroxymethylfurfural	166
Summary	166
7.1 Introduction	167
7.2. Results and Discussion	168
<i>Structure and Morphology</i>	168
<i>Glucose dehydration to HMF: UiO-66 Catalysts</i>	176
<i>Glucose dehydration to HMF: UiO-67 Catalysts</i>	184
Stability and Recyclability	185
<i>Flow Reactor Study</i>	189
<i>Glucose to Catalyst Ratio</i>	192
<i>Reactions in DMSO</i>	194
<i>Fructose Dehydration Reactions</i>	196
7.3 Conclusion	198
Conclusions	200
Future Work	206
Metal-Containing Beta Zeolites	206
Metal-Containing Zeolite Y	207
MOF Catalysts	208
References	209
Appendix A	224
Appendix B	227
Appendix C	228
Appendix D	229

Acknowledgements

I would like to thank my supervisor Dr Volkan Degirmenci. Your continued support and encouragement throughout my PhD has been tremendous. I have learnt an incredible amount from you and I would like to thank you for providing me with the opportunity to pursue a PhD under your mentorship. Thank you!

I would also like to thank the collaborators that I worked with throughout my PhD. Firstly; I would like to thank Professor Richard Walton and his team who worked with me to develop metal-organic framework catalysts for glucose isomerisation and HMF production. In particular, I would like to thank Dr David Burnett for synthesising and helping to characterise a number of materials (UiO-66, UiO-67, MIL-88B, and Yb MOFs). I would also like to thank the Master students that I worked with during my PhD. Specifically; I would like to thank Ms Ralentri Pertiwi who originally worked with me to develop MIL-101, MIL-88, and ytterbium catalysts. Also, Mr Thomas Chamberlain who originally worked with me to develop UiO-66 catalysts. It was my initial work with these Master students that lead to my extended collaboration with Professor Walton and Dr Burnett. I would also like to thank Mr Chamberlain for continuing to make the ytterbium materials for me once Dr Burnett had completed his postdoc. Furthermore, I would also like to thank my collaborator, Mr Shivendra Ramkhelawan, who worked with me to develop ZIF-8 catalysts.

Within the School of Engineering, I would like to thank Mr John Pillier for his help and friendship throughout my PhD. Mr Pillier helped design and build a number of key pieces of equipment used in my studies. Thank you John! I would also like to thank Dr Nikolay Cherkasov for helping with my ammonia TPD studies and Professor Andre van Veen for his continued support and encouragement throughout my PhD. Furthermore, I would like to thank the friends that I have made whilst in the School of Engineering; Dr Erme Kiliç, Dr Guannan Hu, Dr John Humphreys, Mr Tosin Sorunke, and Mr Shigang Chen.

Finally, I would like to thank my family for their continued love and support throughout my studies. You have always encouraged me to pursue my dreams and try my best; Mum, Dad, and Islah, thank you!

Declarations

This thesis is submitted to the University of Warwick in support of my application for the degree of Doctor of Philosophy. It has been composed by myself and has not been submitted for any previous degree. The work presented in this thesis is my own except where it contains work based on collaborative research. Contributions are listed below.

Chapter 3

Contains synthesis, characterisation, and catalytic testing techniques. Specific details of contributions are given below.

Chapter 4

Beta zeolite materials were synthesised and characterised by the author. Ammonia TPD studies were performed by the author and Dr Nikolay Cherkasov. The author carried out all catalyst testing.

Chapter 5

Zeolite Y materials were synthesised and characterised by the author. Ammonia TPD studies were performed by the author and Dr Nikolay Cherkasov. Dr Volkan Degirmenci, Dr Erme Kiliç, Mr John Pillier, and Mr Paul Thompson, assisted the author in the collection of XANES and EXAFS data. The author carried out all catalyst testing.

Chapter 6

MIL-88B samples were synthesised by Dr David Burnett. Dr Burnett conducted XRD analysis, GSAS fittings, EDX mapping, and TGA. Dr Marc Walker conducted XPS measurements. Ammonia TPD studies were performed by the author and Dr Nikolay Cherkasov. The author and Mr Thomas Chamberlain collected FTIR data. The author carried out all catalyst testing. Post-recycle reaction XRD measurements were conducted by the author. (The author originally worked with Ms Ralentri Pertiwi on this project).

$\text{Yb}_6(\text{BDC})_7(\text{OH})_4(\text{H}_2\text{O})_4$ was synthesised by Dr David Burnett and Mr Thomas Chamberlain. The Walton Group collected XRD data at Diamond. Dr Burnett conducted GSAS fittings and TGA. Ammonia TPD studies were performed by the

author and Dr Nikolay Cherkasov. The author performed SEM imaging. The author carried out all catalyst testing. Post-recycle reaction XRD measurements were collected by the author. (The author originally worked with Ms Ralenti Pertiwi on this project).

ZIF-8 materials were synthesised by Mr Shivendra Ramkhelawan. Dr Volkan Degirmenci conducted FTIR measurements. The author performed all other material characterisation presented herein. The author carried out all catalyst testing.

UiO-66 materials were synthesised by Dr David Burnett. Dr Burnett conducted XRD analysis, GSAS fittings, SEM imaging, EDX mapping, FTIR analysis, and TGA. The author conducted surface area measurements. The author carried out all catalyst testing. (The author originally worked with Mr Thomas Chamberlain on this project).

Chapter 7

UiO-66 and UiO-67 materials were synthesised by Dr David Burnett. Dr Burnett conducted XRD analysis, FTIR analysis, and TGA. Dr Daniel Lester also collected some TGA measurements. The author conducted surface area measurements. The author carried out all catalyst testing.

Publications

The work contained within this thesis has also been presented in the following publications. Potential future publications have not been included in this list.

ZIF-8 Metal Organic Framework for the Conversion of Glucose to Fructose and 5-Hydroxymethyl Furfural. *Catalysts* 2019, 9, 812.

A hydrothermally stable ytterbium metal–organic framework as a bifunctional solid-acid catalyst for glucose conversion. *Chem. Commun.*, 2019,55, 11446-11449

Replacement of Chromium by Non-Toxic Metals in Lewis-Acid MOFs: Assessment of Stability as Glucose Conversion Catalysts. *Catalysts* 2019, 9(5), 437

Exceptionally Efficient and Recyclable Heterogeneous Metal–Organic Framework Catalyst for Glucose Isomerization in Water. *ChemCatChem*, 10(4), 706 - 709

Other works by the author

New Method Based on the UNIFAC–VISCO Model for the Estimation of Ionic Liquids Viscosity Using the Experimental Data Recommended by Mathematical Gnostics. *J. Chem. Eng. Data* 2016, 61, 11, 3908-3921

New Method for the Estimation of Viscosity of Pure and Mixtures of Ionic Liquids Based on the UNIFAC–VISCO Model. *J. Chem. Eng. Data* 2016, 61, 6, 2160-2169

To
Angela, Iqbal & Islah

Abstract

This thesis explores the development of zeolite and metal-organic framework (MOF) catalysts for the production of value-added monomers. In particular, work focuses on the production of a platform molecule, 5-hydroxymethylfurfural (HMF), from sugars obtained from widely available and renewable biomass resources. The production of HMF from glucose, the cheapest and most abundant hexose contained within lignocellulosic biomass, may proceed via an initial isomerisation reaction towards fructose. As such, the catalysts in this thesis target glucose isomerisation as well as HMF production.

Work begins with the production of metal-containing beta zeolites using a rapid synthesis technique. This method effectively reduces the synthesis times of metal-containing beta zeolites from 40 days to 3 days. A number of different metals were successfully introduced into the beta zeolite framework. The materials were tested as glucose isomerisation and dehydration catalysts in various reaction solvents. Following this, a post-synthesis technique was used to produce metal-containing zeolite Y catalysts. Again, materials were tested as glucose isomerisation and dehydration catalysts in various solvents.

With regards to MOFs, a series of initial studies explore the catalytic activities of several known frameworks; MIL-88B, $\text{Yb}_6(\text{BDC})_7(\text{OH})_4(\text{H}_2\text{O})_4$, ZIF-8, and UiO-66. Of these, a functionalised zirconium UiO-66 material was found to be of considerable interest as a glucose isomerisation catalyst in water. As such, the catalytic abilities of functionalised zirconium MOFs, UiO-66 and UiO-67, were studied further in a final experimental chapter. This final study highlights the potential to “fine-tune” MOF catalysts towards the production of fructose and HMF.

The catalytic tests within this thesis are generally preformed within batch reactors. However, a number of highly promising catalysts were also tested within a purpose built continuous flow reactor. The stability and reusability of numerous catalysts are explored. Preference is given to water mediated reactions, although alternative reaction solvents are also considered.

List of Figures

Figure 1.1. HMF as a platform molecule.

Figure 1.2. Reaction pathway from glucose to HMF via fructose.

Figure 2.1. Simplified schematic of a typical reactor system used to produce HFCS in industry.

Figure 2.2. Fischer projections illustrating the base catalysed isomerisation of glucose to fructose via the Lobry de Bruyn–Alberda van Ekenstein reaction mechanism.

Figure 2.3. Beta zeolite framework.

Figure 2.4. Reactions pathways towards fructose and mannose via framework Sn active sites as described by the Davis group.

Figure 2.5. Glucose isomerisation pathways via a base catalyst and Lewis acidic Sn-Beta.

Figure 2.6. Combined biphasic reactor and product extraction system proposed by Román-Leshkov, *et al.* for the production of fructose derived HMF.

Figure 2.7. Cr ion / Ionic Liquid reaction mechanism proposed by Pidko, *et al.* based on EXAFS experiments and DFT calculations.

Figure 3.1. Functionalised linker salts substituted during UiO-66 synthesis and (*) UiO-67 linker

Figure 3.2. Flow reactor unit specifically designed, built, and utilized for the purpose of this project.

Figure 3.3. Solid sample holder used for analysis at the ESRF.

Figure 3.4. Liquid sample holder used in experiments at the ESRF.

Figure 4.1: XRD patterns of synthesised metal-containing beta zeolites, commercial beta zeolite (CP814C), and simulated pattern.

Figure 4.2. Nitrogen adsorption hysteresis loops of synthesised beta zeolites containing 2 % metal **(a)** Commercial Beta **(b)** (2)Sn-Beta **(c)** (2)Zr-Beta **(d)** (2)Ga-Beta **(e)** (2)Zn-Beta **(f)** (2)Yb-Beta **(g)** (2)Sr-Beta.

Figure 4.3. SEM images of synthesised metal-containing zeolites (a) Commercial Beta (b) (2)Sn-Beta (c) (1)Sn-Beta (d) (0.5)Sn-Beta (e) (1)Sn(1)Zr-Beta (f) (1)Zr-Beta (g) (2)Zr-Beta (h) (2)Zn-Beta (i) (2)Yb-Beta (j) (2)Ga-Beta (k) (2)Sr-Beta.

Figure 4.4. UV-Vis DRF analysis of metal-containing beta zeolites synthesised in this study along side chosen metal oxides for comparison.

Figure 4.5. NH₃-TPD analysis of commercial and synthesised beta zeolites.

Figure 4.6. Reaction pathways towards fructose and mannose.

Figure 4.7. Reversible glucose isomerisation reaction.

Figure 4.8. Activity of (2)Sn-Beta in a purpose built continuous flow reactor. 40 mg catalyst, 10 wt.% aqueous glucose feedstock, 140 °C, WHSV of 21 h⁻¹.

Figure 4.9. XRD patterns of (a) simulated pattern (b) “fresh” (2)Sn-Beta and (c) “spent” (2)Sn-Beta* following use in the flow reactor and calcination.

Figure 4.10. Catalytic activity of ‘fresh’ (2)Sn-Beta and ‘spent’ (2)Sn-Beta*. Reaction conditions: 10 mg of catalyst, 3 mL of 10 wt.% glucose in water, 3 h, and 140 °C.

Figure 5.1. X-ray Powder Diffraction (XRD) patterns of (a) simulated pattern (b) H-Y (c) DeAl-H-Y (d) Sn-DeAl-H-Y (e) Ga-DeAl-H-Y.

Figure 5.2. BET isotherms of (a) H-Y (b) DeAl-H-Y (c) Sn-DeAl-H-Y (d) Ga-DeAl-H-Y.

Figure 5.3. BJH Desorption of (a) H-Y (b) DeAl-H-Y (c) Sn-DeAl-H-Y (d) Ga-DeAl-H-Y.

Figure 5.4. UV-vis diffuse reflective spectra of catalysts (a) H-Y (b) DeAl-H-Y (c) Sn-DeAl-H-Y (d) SnO₂ (e) Ga-DeAl-H-Y.

Figure 5.5. SEM imaging of catalysts (a) H-Y (b) DeAl-H-Y (c) Sn-DeAl-H-Y (d) Ga-DeAl-H-Y.

Figure 5.6. NH₃-TPD profile of (a) H-Y (b) DeAl-H-Y (c) Sn-DeAl-H-Y (d) Ga-DeAl-H-Y.

Figure 5.7. Glucose conversion in water on 40 mg zeolite Y catalysts. Reaction conditions: 140 °C, 3 h, stock solution of 10 wt. % glucose in deionized water.

Figure 5.8. Glucose conversion in acidic medium (pH = 1.0) on 40 mg of zeolite Y catalyst. Reaction conditions: 140 °C, 3 h, stock solution of 10 wt. % glucose.

Figure 5.9. Glucose conversion in DMSO on 40 mg of zeolite Y catalyst. Reaction conditions: 140 °C, 3 h, stock solution of 10 wt. % glucose in DMSO.

Figure 5.10. Fructose conversion in deionized water on 40 mg of zeolite Y catalyst. Reaction conditions: 140 °C, 3 h, stock solution of 10 wt. % fructose.

Figure 5.11. a) Glucose recycle reactions in water with Sn-DeAl-H-Y. Reaction conditions: 140 °C, 3 h, stock solution of 10 wt. % glucose in deionised water. **b)** SEM image of Sn-DeAl-H-Y post calcination. **c)** XRD of (a) simulated pattern and XRD of spent Sn-DeAl-H-Y (b) before calcination (c) post calcination.

Figure 5.12. a) Glucose recycle reactions in DMSO with Sn-DeAl-H-Y. Reaction conditions: 140 °C, 3 h, stock solution of 10 wt. % glucose in DMSO. **b)** SEM image of Sn-DeAl-H-Y post calcination. **c)** XRD of (a) simulated pattern and XRD of spent Sn-DeAl-H-Y (b) before calcination (c) post calcination.

Figure 5.13. a) Glucose recycle reactions in DMSO with Ga-DeAl-H-Y. Reaction conditions: 140 °C, 3 h, stock solution of 10 wt. % glucose in DMSO. **b)** SEM image of Ga-DeAl-H-Y post calcination. **c)** XRD of (a) simulated pattern and XRD of spent Ga-DeAl-H-Y (b) before calcination (c) post calcination.

Figure 5.14. In-situ liquid cell results of Sn-DeAl-H-Y in water.

Figure 5.15. XANES spectra of Sn-DeAl-H-Y in water with glucose.

Figure 6.1. Fitted diffraction patterns of synthesised MIL-88B materials.

Figure 6.2. EDX mapping of (FeSc)MIL-88B.

Figure 6.3. X-ray photoelectron spectroscopy (XPS) analysis of (FeSc)MIL-88B (a) Sc content (b) Fe content.

Figure 6.4. FTIR analysis of Fe and Sc containing MIL-88B catalysts.

Figure 6.5. TGA profiles of (a) (Fe)MIL-88B (b) (Sc)MIL-88B (c) (FeSc)MIL-88B.

Figure 6.6. Ammonia TPD of (Fe)MIL-88B including a 'blank' experiment conducted in the absence of ammonia.

Figure 6.7. Ammonia TPD of (FeSc)MIL-88B including ‘blank’ experiments conducted in the absence of ammonia.

Figure 6.8. Recycle reaction of (Fe)MIL-88B in DMSO at 120 °C. The reaction contained 200 mg of catalyst and 15 mL of 10 wt.% glucose stock solution. Insert: XRD of catalyst post Cycle 4.

Figure 6.9. Recycle reaction of (FeSc)MIL-88B in DMSO at 120 °C. The reaction contained 200 mg of catalyst and 15 mL of stock solution. Insert: XRD of catalyst post Cycle 4.

Figure 6.10. XRD fitting of $\text{Yb}_6(\text{BDC})_7(\text{OH})_4(\text{H}_2\text{O})_4$ (black) measured diffraction pattern (red) fitting (blue) difference. (Insert) SEM image of synthesised $\text{Yb}_6(\text{BDC})_7(\text{OH})_4(\text{H}_2\text{O})_4$.

Figure 6.11. TGA analysis of $\text{Yb}_6(\text{BDC})_7(\text{OH})_4(\text{H}_2\text{O})_4$.

Figure 6.12. Ammonia TPD pattern of $\text{Yb}_6(\text{BDC})_7(\text{OH})_4(\text{H}_2\text{O})_4$.

Figure 6.13. Glucose conversion in water on 10 mg of catalyst. Reaction conditions: 140 °C, 3 h, stock solution of 10 wt. % glucose in deionized water. *Reaction times vary for reactions containing $\text{Yb}_6(\text{BDC})_7(\text{OH})_4(\text{H}_2\text{O})_4$.

Figure 6.14. Glucose conversion in HCl on 10 mg of catalyst. Reaction conditions: 140 °C, 3 h, stock solution of 10 wt. % glucose in pH 2.5. *Reaction times vary for reactions containing $\text{Yb}_6(\text{BDC})_7(\text{OH})_4(\text{H}_2\text{O})_4$.

Figure 6.15. $\text{Yb}_6(\text{BDC})_7(\text{OH})_4(\text{H}_2\text{O})_4$ recycle reactions in water on 50 mg of catalyst. Reaction conditions: 140 °C, 24 h, 15 mL of 10 wt. % glucose stock solution. Blank* reaction conducted in 4 mL reaction vial.

Figure 6.16. XRD of (a) simulated pattern and (b) $\text{Yb}_6(\text{BDC})_7(\text{OH})_4(\text{H}_2\text{O})_4$ after four consecutive recycle reactions.

Figure 6.17. X-ray Powder Diffraction (XRD) patterns of (a) simulated ZIF-8 (b) (RT)ZIF-8 (c) (HT)ZIF-8.

Figure 6.18. BET isotherms of (a) (RT)ZIF-8 (b) (HT)ZIF-8.

Figure 6.19. FTIR analysis of ZIF-8 catalysts.

Figure 6.20. TGA profiles of ZIF-8 materials.

Figure 6.21. SEM imaging of catalysts (a) (RT)ZIF-8 (b) (HT)ZIF-8.

Figure 6.22. Glucose conversion in water on 40 mg of ZIF-8 catalysts or 24 mg of ZnCl_2 . Reaction conditions: 100 °C or 140 °C, 3 h, stock solution of 10 wt. % glucose in deionized water.

Figure 6.23. Glucose conversions vs. Time. Reaction conditions: 140 °C, 3 h, stock solution of 10 wt. % glucose in deionized water on 40 mg of catalyst.

Figure 6.24. Glucose conversion in 0.1M HCl on ZIF-8 catalysts. Reaction conditions: 100 °C or 140 °C, 3 h, stock solution of 10 wt. % glucose in 0.1M HCl.

Figure 6.25. Activity of (RT)ZIF-8 in a continuous flow reactor. 40 mg catalyst, 10 wt.% glucose in water stock solution, 100 °C, 0.14 mL/min.

Figure 6.26. XRD patterns of (a) UiO-66 (b) (10)MSBDC-UiO-66 (c) (20)MSBDC-UiO-66.

Figure 6.27. a) SEM image of UiO-66 b) zirconium EDX mapping of UiO-66. c) SEM image of (20)MSBDC-UiO-66 d) zirconium EDX mapping of (20)MSBDC-UiO-66 e) sulfur EDX mappings of (20)MSBDC-UiO-66.

Figure 6.28. Infrared (IR) spectra of UiO-66 and functionalised variants.

Figure 6.29. Nitrogen adsorption isotherm's of (a) UiO-66 (b) (10)MSBDC-UiO-66 (c) (20)MSBDC-UiO-66 .

Figure 6.30. TGA profiles of UiO-66 and functionalised UiO-66 materials.

Figure 6.31. Glucose conversion in water on UiO-66 catalysts. Reaction conditions: 140 °C, 3 h, stock solution of 10 wt. % glucose in deionized water.

Figure 6.32. Fitted diffraction patterns of UiO-66 catalysts before and after recycle reactions.

Figure 7.1. Catalytic performance of UiO-67 type materials. Reactions at 140 °C for 3 h. Glucose stock solution, 10 wt. %. Glucose to catalyst ratio was 30:1 by weight.

Figure 7.2. XRD powder analysis of catalysts post reaction in water at 140°C for 3 h (a) Nano-UiO-66 (b) (20)IPA-UiO-66 (c) (100)NO₂-UiO-66 (d) (100)NH₂-UiO-66 (e) (40)4-sulfbenz-UiO-66 (f) UiO-67 (g) (40)3-sulfoben-UiO-67(2eq).

Figure 7.3. Recycle reaction results (i) and XRD analysis of catalyst after 4 reaction cycles (ii) of selected catalysts (a) BTeC-UiO-66 (b) (50)MSBDC-UiO-66 (c) (50/50)MSBDC/Naphtha-UiO-66 (d) UiO-67 (e) UiO-67-SO₃H.

Figure 7.4. UiO-66 catalysts flow reactor results. Reactor temperature was maintained at 140 °C. Feedstock was 10 wt.% glucose in water.

Figure 7.5. Catalytic performance of selected UiO-66 and UiO-67 catalysts in 3 mL of 10wt. % glucose in DMSO. Reactions were conducted for 3 h at 140 °C with 10 mg of catalyst.

Figure 7.6. Diffraction patterns of catalysts post reaction in DMSO (a) BTeC-UiO-66 (b) (50)MSBDC-UiO-66 (c) (50/50)MSBDC/Naphtha-UiO-66 (d) UiO-67 (e) UiO-67-SO₃H.

Figure A1. Flow Reactor.

Figure A2. Brass heating block and reactor tubing.

Figure A3. Flow reactor power on.

Figure A4. Flow reactor LED lighting.

Figure B1. Deconvoluted UV-Vis spectra of aluminium oxide and gallium oxide.

Figure C1. XRD powder analysis of UiO-66 materials (a) Simulated UiO-66 (b) UiO-66 (c) UiO-66 with additional peaks.

Figure D1. XRD powder analysis pre and post hydrothermal treatment at 140 °C for 24 h (a) (50)MSBDC-UiO-66 (b) (50)MSBDC-UiO-66 post hydrothermal treatment (c) (100)MSBDC-UiO-66 (d) (100)MSBDC-UiO-66 post hydrothermal treatment.

Figure D2. XRD powder analysis of UiO-66 materials (a) Simulated UiO-66 (b) Nano-UiO-66 (c) Ultra-Nano-UiO-66 (d) Poorly Crystalline UiO-66.

Figure D3. XRD powder analysis of UiO-66 materials (a) Simulated UiO-66 (b) Defective-UiO-66.

Figure D4. XRD powder analysis of UiO-66 materials (a) (20)NO₂-UiO-66 (b) (50)NO₂-UiO-66 (c) (100)NO₂-UiO-66 (d) (20)NH₂-UiO-66 (e) (50)NH₂-UiO-66 (f) (100)NH₂-UiO-66.

Figure D5. XRD powder analysis of UiO-66 materials (a) Simulated UiO-66 (b) (10)IPA-UiO-66 (c) (20)IPA-UiO-66 (d) (30)IPA-UiO-66 (e) (40)IPA-UiO-66.

Figure D6. XRD powder analysis of UiO-66 materials (a) Simulated UiO-66 (b) (20)Naph-UiO-66 (c) (50)Naph-UiO-66 (d) (100)Naph-UiO-66.

Figure D7. XRD powder analysis of UiO-66 materials (a) Simulated UiO-66 (b) (20)4-Sulfoben-UiO-66 (c) (40)4-Sulfoben-UiO-66 (d) (20)3-Sulfoben-UiO-66 (e) (40)3-Sulfoben-UiO-66.

Figure D8. XRD powder analysis of UiO-66 materials (a) Simulated UiO-66 (b) (20)MSBDC-UiO-66-Nano (c) (50)MSBDC-UiO-66-Nano.

Figure D9. XRD powder analysis of UiO-66 materials (a) Simulated UiO-66 (b) (50)MSBDC-UiO-66.

Figure D10. XRD powder analysis of UiO-66 materials (a) Simulated UiO-66 (b) (50/50)MSBDC/Naptha-UiO-66.

Figure D11. XRD powder analysis of UiO-66 materials (a) Simulated UiO-66 (b) BTeC-UiO-66 (c) Hydroxyl-UiO-66.

Figure D12. XRD powder analysis (a) Simulated UiO-67 (b) UiO-67 (c) (20)3-Sulfobenz-1eq (d) (20)3-Sulfobenz-2eq (e) (40)3-Sulfobenz-1eq (f) (40)3-Sulfobenz-2eq.

Figure D13. FTIR analysis of nitro functionalised UiO-66.

Figure D14. FTIR analysis of amine functionalised UiO-66.

Figure D14a. FTIR analysis of amine functionalised UiO-66 around 3500 cm^{-1} .

Figure D15. FTIR analysis of sulfobenzoic acid functionalised UiO-66.

Figure D16. FTIR analysis of MSBDC functionalised UiO-66.

Figure D17. FTIR analysis of IPA functionalised UiO-66.

Figure D18. FTIR analysis of BTeC and Hydrox functionalised UiO-66.

Figure D18a. FTIR analysis of BTeC peak at around 1710 cm^{-1} .

Figure D19. FT-IR analysis of functionalised UiO-67.

Figure D20. XRD powder analysis of UiO-66 and UiO-67 catalysts after 4 consecutive recycle reactions in water.

List of Tables

- Table 2.1.** Heterogeneous acid catalysts for glucose isomerisation.
- Table 2.2.** Phosphate catalysts for the production of glucose derived HMF.
- Table 2.3.** Biphasic systems for HMF production from glucose.
- Table 3.1.** Summary of synthesized beta zeolites.
- Table 3.2.** Summary of zeolite Y materials.
- Table 3.3.** Summary of MIL-88B materials.
- Table 4.1.** BET surface areas and pore volumes of the beta zeolite catalysts.
- Table 4.2.** Metal content of beta zeolites.
- Table 4.3.** Acidity of beta zeolites.
- Table 4.4.** Catalytic performance of metal-containing beta zeolites in 3 mL aqueous solution. Reactant to catalyst ratio 30:1 (10 mg catalyst).
- Table 4.5.** Catalytic performance of metal-containing beta zeolites in 3 mL acid solution. Reactant to catalyst ratio 30:1 (10 mg catalyst).
- Table 4.6.** Catalytic performance of metal-containing beta zeolites in 3 mL aqueous solution considering a fructose feedstock. Reactant to catalyst ratio 30:1 (10 mg catalyst).
- Table 5.1.** Textural properties of Y zeolites determined by nitrogen adsorption.
- Table 5.2.** Elemental composition of Y zeolite catalysts.
- Table 5.3.** Acidity of Y zeolite frameworks.
- Table 5.4.** Sn and Ga content in post reaction solutions. Reactions consisted of 40 mg catalyst and 3 mL of stock solution (140 °C, 3 h).
- Table 5.5.** Glucose conversions using gallium nitrate and gallium oxide in water and 0.1 M HCl. Reaction conditions: 140 °C, 3 h, 3 mL of 10 wt. % glucose.
- Table 5.6.** Glucose conversion and product yields on 10 mg zeolite Y catalyst after 3 h at 140 °C.
- Table 5.7.** Conversions and product yields on zeolite Y catalysts for 10 wt.% fructose reactions in water after 3 h at 140 °C.

Table 5.8. L_{III} tin edge feature Energies (eV) in water in the absence of sugar.

Table 5.9. L_{III} tin edge feature Energies (eV) in water with glucose.

Table 6.1. Glucose isomerisation and dehydration reactions catalysed by Fe and Sc MIL-88B materials.

Table 6.2. ICP analysis of (FeSc)MIL-88B recycle reaction solutions.

Table 6.3. ICP analysis of recycle reaction solutions to quantify the amount of Yb leaching from Yb₆(BDC)₇(OH)₄(H₂O) during 24 h reactions at 140°C.

Table 6.4. Textural properties of ZIF-8 materials determined by nitrogen adsorption.

Table 6.5. ICP analysis of UiO-66 catalysts.

Table 6.6. Molar concentrations of elements within UiO-66 materials normalised in comparison to Zr.

Table 6.7. BET surface area and pore volume of UiO-66 catalysts.

Table 6.8. Zirconium and sulfur content in the reaction solution after 3 h reaction at 140°C.

Table 6.9. Glucose Conversions and Yields obtained from UiO-66 catalyst recycling.

Table 6.10. Recovery of UiO-66 catalysts after recycle reactions.

Table 6.11. Comparison of the zirconium and sulfur content of the UiO-66 catalysts before and after the reaction at 140°C for 3 h

Table 7.1. BET surface area and pore volume of Zr MOFs. (*degassed at 190°C)

Table 7.2. ICP analysis of S containing UiO-66 and UiO-67 materials normalised with respect to Zr.

Table 7.3. Reactions at 140 °C for 3 h. Glucose stock solution, 10 wt. %. Glucose to catalyst ratio was 30:1 by weight.

Table 7.4. Reactions at 140 °C for 3 h. Glucose stock solution, 10 wt. %. Glucose to catalyst ratio was 30:1 by weight.

Table 7.5. The effects of catalyst : glucose ratio. Reactions at 140 °C for 3 h. Glucose stock solution, 10 wt. %.

Table 7.6. Fructose dehydration by functionalised UiO-66 and UiO-67 catalysts. 140 °C, 3 h, 3 mL 10 wt % stock solution in water.

Table D1. Zr Coordination Numbers of UiO-66 and UiO-67 materials calculated from TGA data.

Chapter 1

General Introduction

Researchers within academia and industry alike are striving towards the development of renewable fuels and chemicals. This drive towards sustainability is fuelled by the current global dependence on finite fossil resources and the implications of global warming. It has been proposed that lignocellulosic biomass, a cheap and plentiful resource, could play a key role in the production of sustainable chemicals within the future “biorefinery”.¹⁻⁴ The simple sugars (hexoses) contained within renewable lignocellulosic biomass can be converted into commercially valuable products such as 5-hydroxymethylfurfural (HMF).⁵⁻⁷ A platform molecule, HMF can be transformed into numerous chemical products with potential applications in a wide verity of industries (**Figure 1.1**).⁸⁻¹¹

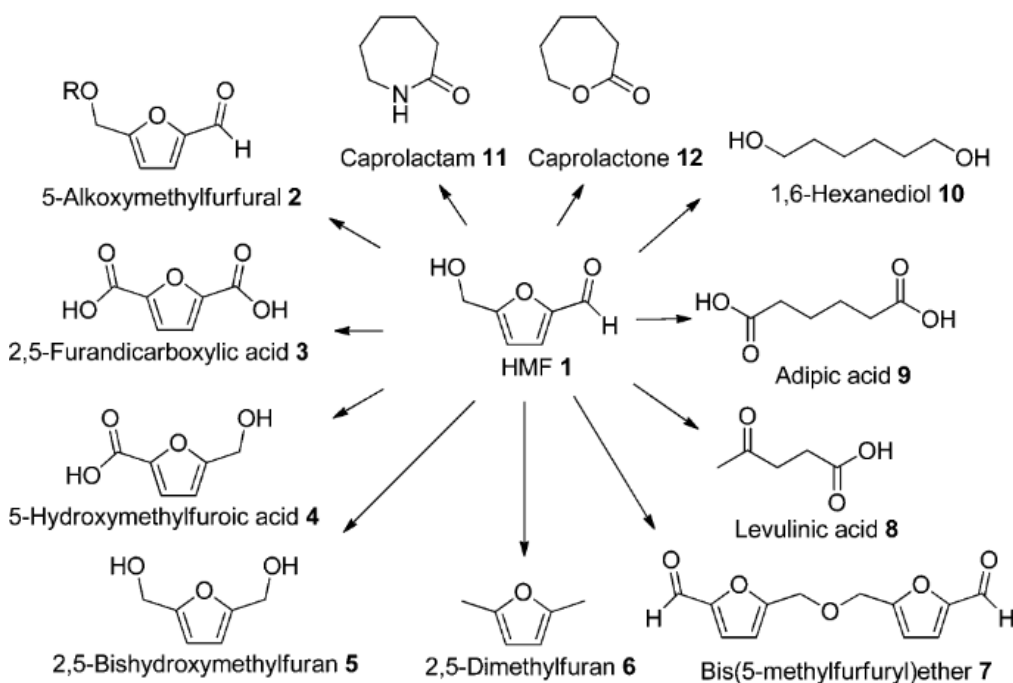


Figure 1.1. HMF as a platform molecule.¹¹

Of the hexoses contained within lignocellulosic biomass, the successful production of HMF from fructose has been well documented. Meanwhile, the effective production of HMF from glucose continues to present challenges.^{12,13} This is particularly true when considering the use of heterogeneous catalysts. HMF production from glucose may proceed firstly through the isomerisation of glucose to fructose (**Figure 1.2**).^{14,15} A bottleneck in the reaction system, it is this isomerisation step that must be developed to enable the energy efficient and cost effective production of HMF at an industrial level.

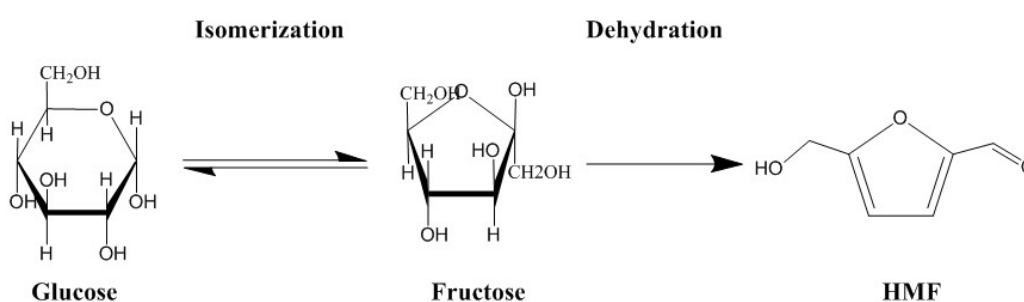


Figure 1.2. Reaction pathway from glucose to HMF via fructose.¹⁴

This thesis explores the development of heterogeneous catalysts for the production of glucose derived HMF. To begin, we explore the use of metal-containing zeolites as glucose isomerisation and dehydration catalysts in different solvents. Specifically, a number of different metal-containing beta zeolites are synthesised and tested as catalysts. Following this, we explore the development of metal-containing zeolite Y catalysts. Again, the catalytic performances of these zeolites are tested in different solvents and the activities of metal sites are studied in-situ for the first time using XANES analysis. Following our study of zeolites, we consider the use of metal-organic frameworks (MOFs) in reactions. Specifically, we begin by exploring the catalytic performances of several known frameworks; MIL-88B, $\text{Yb}_6(\text{BDC})_7(\text{OH})_4(\text{H}_2\text{O})_4$, ZIF-8, and UiO-66. Following these initial MOF studies, we focus on ‘fine-tuning’ the performances of UiO-66 and UiO-67 catalysts towards the isomerisation of glucose and production of HMF in water.

Literature Review

Summary

The production of value added platform molecules such as 5-hydroxymethylfurfural (HMF) from biomass resources remains at the forefront of academic research. The production of such renewable platform molecules at an industrial scale remains an important step towards improving the sustainability of the chemical sector. The production of glucose derived HMF may proceed via the isomerisation of glucose to fructose.^{14,15} As such, the first section of this literature review considers the isomerisation of glucose using chemical (chemo) catalysts. Several excellent reviews articles have also covered this topic in detail.¹⁶⁻²⁰ Due to their almost unequalled performance, many of these review articles have given specific attention towards the development and use of tin (Sn) containing beta zeolites as glucose isomerisation catalysts.¹⁶⁻²⁰ Indeed, the first section of this literature review also recognizes the significance of this catalyst and particular attention is given to the performance, structure, and synthesis, of Lewis acidic Sn-Beta. The second section of this literature review focuses on the production of glucose derived HMF. Again, given the significant amount of attention HMF has received in recent years, a number of excellent review articles have extensively covered the production of this valuable platform molecule.^{2,9,11,13,21} As such, the second half of this literature review provides an overview of some of the important developments in this field.

2.1 Glucose Isomerisation in Industry

Industrial scale glucose isomerisation is a multi-billion dollar industry that produces a substance generally referred to as ‘high fructose corn syrup’ (HFCS).²² Within this industrial process, fructose production is catalysed by the enzyme glucose (xylose) isomerase.^{22–25} This enzyme is typically immobilised and capable of generating a glucose conversion of ~50 % and a fructose yield of ~42 %.^{26–29} However, due to its inherent nature, this catalyst can not be regenerated. As such, the catalytic performance of this enzyme declines over time and must be replaced. To compensate for this, manufacturers typically utilise a series of packed bed reactors operating in parallel when producing HFCS.^{28,29} In such systems, a glucose feedstock is continuously pumped through a packed bed of immobilised glucose isomerase held at a constant temperature of around 50 – 58 °C.^{27–29} As the performance of the enzyme decreases with time on stream, the flow of feedstock to this reactor is proportionally slowed to give a higher residence time within the packed bed.²⁸ Meanwhile, a higher flow rate is directed towards a second reactor containing a fresher bed of enzymes.²⁸ A simplified schematic of this manufacturing process is shown in **Figure 2.1**.

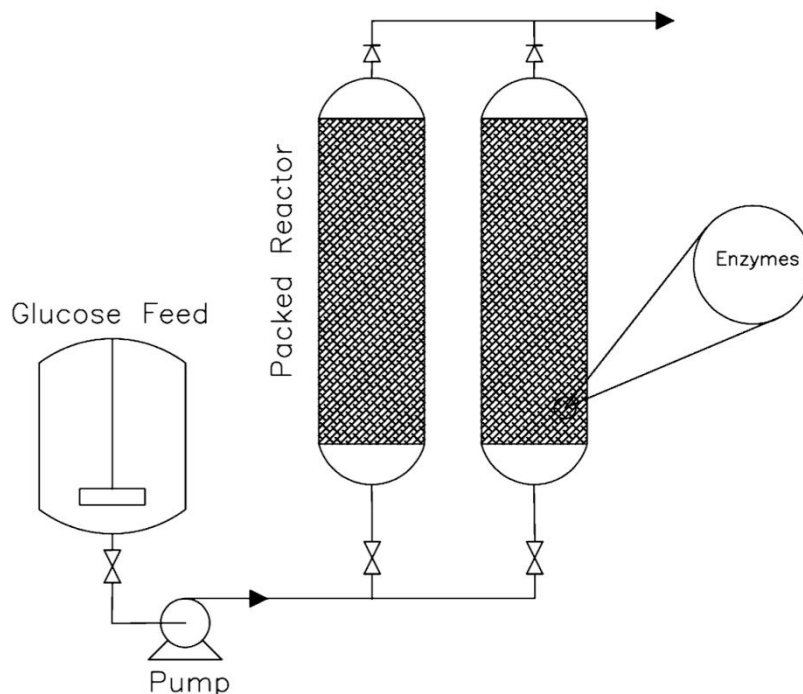


Figure 2.1. Simplified schematic of a typical reactor system used to produce HFCS in industry.

2.2 Base catalysed Glucose Isomerisation

Base catalysts may be used to promote glucose isomerisation via the Lobry de Bruyn–Alberda van Ekenstein reaction mechanism.³⁰ In the proposed reaction mechanism (**Figure 2.2**), glucose interacts with a base (deprotonation) to form an enediol / enolate intermediate that is subsequently converted to fructose following a hydride shift and protonation.^{30–32} Here, NMR studies have shown that a hydrogen ion can be sourced from the surrounding solvent for the protonation step.²⁶

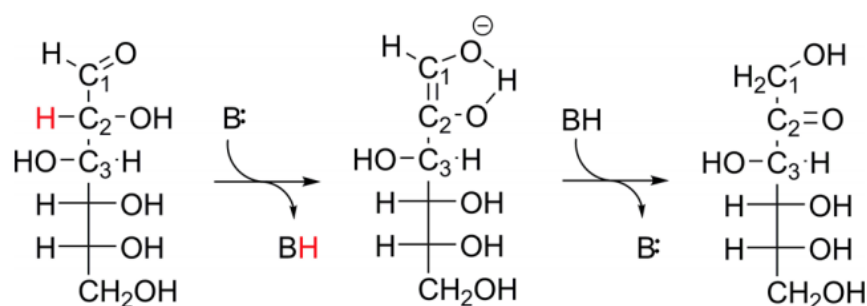


Figure 2.2. Fischer projections illustrating the base catalysed isomerisation of glucose to fructose via the Lobry de Bruyn–Alberda van Ekenstein reaction mechanism.³¹

Since Lobry de Bruyn–Alberda van Ekenstein, numerous studies have considered the use of basic catalysts for glucose isomerisation. For instance, amines^{31,33–37}, amino acids³⁸, resins^{39,40}, oxides^{39,41–45}, hydrotalcites^{46–48}, biochars⁴⁹, zeolites^{50,51}, and silicates⁵², have all been considered as basic glucose isomerisation catalysts in recent years. However, the performances of base catalysts and alkaline conditions may be limited as they can promote the formation of undesirable reactions at mildly elevated temperatures – resulting in losses and potential waste.^{17,32,53,54} With this being said, there are some exceptions to be found in literature. For example, exceptionally high fructose selectivity (~85 %) can be generated through the use of homogeneous sodium aluminate (NaAlO₂) as a basic catalyst.^{55–57} The exceptional performance of this catalyst stems from its ability to form sugar-complexes that facilitate an alternative reaction mechanism whilst also stabilising fructose yields.^{58,59} Indeed, the ability of the aluminate to stabilise fructose yields is also likely responsible for the exceptional performance of heterogeneous forms of this catalyst.⁵⁶ High fructose yields (50 %) have also been achieved using a

hydrotalcite catalyst containing magnesium (Mg) and aluminium (Al) in ethanol.⁴⁷ Here, the ethanol is thought to stabilise product yields whilst also shifting the reaction equilibrium towards fructose.⁴⁷ Moreover, the ability to stabilise the fructose formed in base catalysed reactions appears to be the key towards obtaining higher product yields.

The promising performance of other Mg containing catalyst has also been noted in literature within recent years.^{44,50,51} Namely, exceptionally high fructose selectivity (~100%) can be achieved in water alongside moderate glucose conversions (~35 %) when considering the use of Mg impregnated commercial zeolite Y (Na-Y) and desilicated versions of this catalyst.^{50,51} Notably the best results obtained here were achieved using mildly desilicated zeolite Y with a Mg loading of 5 %.⁵¹ Although leaching may be an issue with these catalysts, promising performances were observed in recycle reactions with intermediary catalyst regeneration.^{50,51} These results are of considerable interest as they indicate high fructose selectivity can be achieved in water-mediated reactions utilising a commercially available framework doped with Mg.

2.3 Acid catalysed Glucose Isomerisation

Glucose isomerisation can also be achieved through the use of Lewis acid catalysts.^{14,15,60} As such, researchers have explored the use of Lewis acid catalysts within various reaction systems for the isomerisation of glucose. **Table 2.1** provides an overview of some interesting heterogeneous acid catalyst systems reported in current literature. As seen in **Entry 1**, the large pore size and potential presence of extra-framework Al within commercial H-USY enables effective glucose isomerisation within a two-step reaction process that involves a sequential solvent change. Specifically, Saravanamurugan, *et al.* demonstrated that acidic zeolites (H-Y, H-USY, and H-Beta) can convert glucose to methyl fructose - via the formation of fructose - in alcoholic mediums.⁶¹ The conversion of the methyl fructose - back to fructose - can subsequently be achieved by adding water to the reaction mixture and reheating.⁶¹ Interestingly, it is also worth noting that in pure water the authors found H-USY to be an ineffective glucose isomerisation catalyst – thus highlighting the important of solvent selection.⁶¹ With regards to other zeolites, sodium variants were also able to promote glucose isomerisation using

this two-step reaction method.⁶¹ However, the yields of fructose obtained by these particular zeolites are much lower – as they do not appear to promote the production of methyl fructose within the reaction.⁶¹

Table 2.1. Heterogeneous acid catalysts for glucose isomerisation.

Entry	Catalyst	Solvent	Temp (°C)	Time	Glucose Conversion (%)	Fructose Yield (%)	Ref
1	H-USY	MeOH/ H ₂ O	120	1/1 hr	72	55	61
2	Cr(OH) ₃ / (Cr)MIL-101	EtOH/H ₂ O	100	24/24 hr	76.5	59.3	62
3	Modulated UiO-66	1-PrOH /H ₂ O	90	24/24hr	82	56	63
4	(Cr)MIL-101	H ₂ O	130	8 hr	72	20	64
5	UiO-66	H ₂ O	100	24 hr	63	5	64
6	NU-1000	H ₂ O	140	5	60	19	65
7	(Al) Biochars	Acetone/ H ₂ O	160	20 min	48.9	21.5	66
8	(Sn) Biochars	H ₂ O	160	20 min	~52.5	15.2	67
9	Ti-Beta	H ₂ O	110	90 min	26	14	53
10	Sn-Beta	H ₂ O	110	30 min	55	32	53

The work of Saravanamurugan, *et al.* has inspired others to consider similar two-step reactions. For instance, a recent study by Guo, *et al.* considers the use of a chromium (Cr) metal-organic framework (MOF) in a two-step reaction.⁶² Specifically, the authors demonstrate that Lewis acidic (Cr)MIL-101 can generate promising fructose yields (59.3 %) when combined with the sequential use of alcohol and aqueous solvents. Furthermore, the authors show that the performance of (Cr)MIL-101 can be significantly improved through the incorporation of Cr(OH)₃ nanoparticles within/on the materials structure (**Table 2.1, Entry 2**).

Here, the $\text{Cr}(\text{OH})_3$ nanoparticles facilitate fructose production via a base catalysed reaction involving a proton transfer (**Figure 2.2**).⁶² This fructose is then converted to ethyl fructoside via the Lewis acidic (Cr)MIL-101 structure in ethanol. The addition of water to the reaction mixture enables the ethyl fructoside generated in the first step to be hydrolysed back to fructose, ultimately resulting in a 59.3 % fructose yield.⁶² Moreover, the apparent role of the Lewis acidic MIL-101 catalyst here is to predominantly stabilise the fructose yields generated in the reaction by facilitating the formation of ethyl fructoside.

In similar work, de Mello and Tsapatsis considered the use of UiO-66 in a two-step reaction (**Table 2.1, Entry 3**).⁶³ Here, the authors show that modulated UiO-66 generates high fructose yields (56%) when reactions are preformed in 1-propanol (1-PrOH) and water. The authors also show that within 1-PrOH glucose isomerisation occurs via a 1,2-hydride shift - and a further 1,2-hydride shift generates mannose directly from fructose.⁶³ It is also worth noting that in comparison to modulated UiO-66, the authors report that defect free UiO-66 is considerably less active as a glucose isomerisation catalyst. This may be because glucose is unable to enter the structure of un-modulated (i.e. defect free) UiO-66.⁶³

In other work pertaining to the use of MOF catalysts; the application of (Cr)MIL-101, UiO-66, and NU-1000, in water generates considerably less fructose (**Table 2.1, Entries 4 & 5**).^{64,65} In this sense, the activity of these MOFs in different reaction solvents maybe somewhat comparable to acidic H-USY – which also expressed lower yields in water when compared with a two-step alcohol/water mediated reaction.⁶¹ Furthermore, in water-mediated reactions, UiO-66 may enable the production of mannose via an alternative reaction mechanism to that observed in alcoholic solutions. Specifically, work by Luo, *et al.* found that in water, UiO-66 can facilitate mannose production directly via the epimerisation of glucose.⁶⁴

Very recently a number of research groups have considered the use of biochars as glucose isomerisation catalysts. This is extremely interesting, as in the case of biochars, the catalysts itself may be generated from biomass waste. For instance, Yu, *et al.* have considered the use of Al-impregnated biochar catalysts generated from the pyrolysis of sawdust.⁶⁶ Here the authors suggest that Al sites contained

within the biochar may have contributed significantly to the activity of the catalyst by providing Lewis acidity – although there is some contribution from leached Al species.⁶⁶ One of the more promising catalysts observed in their study was able to generate a glucose conversion of 48.9 % along with a fructose yield of 23 % in water (**Table 2.1, Entry 7**).⁶⁶ Furthermore, this yield could be slightly improved through the use of organic/water solvent mixtures, and the use of such mixtures enabled high fructose yields to be generated in less time.⁶⁶ In other work involving the use of biochar catalysts, Yang, *et al.* investigated the use of tin (Sn) containing biochars.⁶⁷ Here the authors report a Sn biochar, containing both Lewis acid and Brønsted base sites, is able to generate a fructose yield of 15.2 % (**Table 1.1, Entry 8**).⁶⁷ It is worth noting that in each of these biochar examples, a microwave reactor system was utilised.

As seen in **Table 2.1**, titanium (Ti) and tin (Sn) containing beta zeolites have also been considered as glucose isomerisation catalysts in water. Of these, the Sn containing material is considerably more active. Indeed, the activity of Sn-Beta is somewhat comparable to the current enzyme technology used in industry.⁵³ As such, the activity of this zeolite (shown in **Figure 2.3**) will now be discussed in detail in order to better understand some of the characteristics that make Sn-Beta an effective glucose isomerisation catalyst.

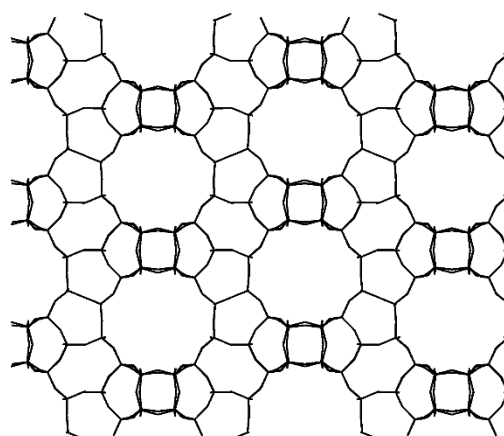


Figure 2.3. Beta zeolite framework. (CIF.⁶⁸)

2.4 Tin containing heterogeneous catalysts for Glucose Isomerisation

In 2010, the Davis group reported that the incorporation of Sn within the framework of beta zeolite yields a heterogeneous catalyst highly effective in the isomerisation of glucose.⁵³ The fructose yields achieved by Sn beta (Sn-Beta) rivals those produced by the immobilized enzyme technology currently used in industry. Interestingly, despite the performance of Sn-Beta, homogenous Sn chloride and Sn oxide are ineffective as glucose isomerisation catalysts in water.⁵³ This stark comparison in catalytic activity between framework Sn and homogeneous Sn species has also been observed in other reaction systems such as the Meerwein-Ponndorf-Verley (MPV) reaction.⁶⁹ Thus to fully utilize Sn for the isomerisation of glucose as well as other reactions, researchers are devoting efforts towards understanding the performance of Sn active sites. As such, Sn containing materials have quickly found themselves at the forefront of heterogeneous catalyst development for the purpose of lignocellulosic biomass utilization.

The application of Sn-Beta as a glucose isomerisation catalyst within laboratory batch reactors enables a fructose yield of approximately 30 % from either a 10 wt. % of 45 wt. % aqueous glucose feedstock (**Table 2.1**).⁵³ This is particularly interesting as the latter stock solution of 45 wt. % glucose is similar to that used in the immobilised enzyme technology currently employed in industry.⁵³ Furthermore, the recyclability and leaching tests employed by the same group have shown that Sn-Beta does not leach, and unlike enzyme catalysts, can be regenerated via calcination.⁵³

Of course the deployment of continuous flow reactors for material production holds several generic advantages over potential batch counterparts within industry. Despite this, there are few reports on the use of Sn-Beta within flow reactor systems. Indeed, only recently, Padovan, *et al.* tested the performance of Sn-Beta in such a manner.⁷⁰ Through their work the authors reveal that Sn-Beta, made using a post synthesis impregnation technique, rapidly deactivates within a flow system feeding an aqueous glucose feedstock. Furthermore, the activity of the catalyst could not be regenerated as it had been destroyed during the reaction. Interesting however, this was not the case when methanol was used as a reaction solvent. When feeding a glucose-methanol feedstock into the flow reactor, the rate of catalyst deactivation was far less severe, and further, the catalyst could be

successfully regenerated - thus implying that the catalyst may still be industrially relevant for other reactions. Moreover, the work of Padovan, *et al.* suggests that Sn-Beta is destroyed within aqueous flow systems. This conclusion is somewhat contrary to the results of the Davis group who show - albeit within batch systems - Sn-Beta to be highly recyclable.⁵³ Perhaps the reported differences in catalytic recyclability and stability may be related to the synthesis techniques employed by each group. For instance, Davis and co-workers utilised a “traditional” hydrothermal synthesis method to produce Sn-Beta; whilst Padovan, *et al* utilised a post synthesis method to produce the Sn-Beta tested in their study. However, more experimental work is needed before conclusions on the effect of synthesis methods can be made.

The performance of Sn-Beta as a glucose isomerisation catalyst, to some extent at least, can be attributed to the size of the Beta zeolite pore mouths. The large - 12 membered ringed - structure of this particular zeolite provides less mass transfer limitations and pore size limitations than other smaller zeolite frameworks such as MFI.⁷¹ Moreover, mass transfer limitations and pore size limitations make MFI zeolites less effective than Beta zeolites as glucose isomerisation catalysts.⁷¹ Indeed, pore size is not the only factor that defines the performance of Sn containing materials. The incorporation of Sn into highly ordered mesoporous silica materials, such as MCM41, yields a catalyst that is less active than hydrophobic Sn-Beta.⁵³ Indeed the hydrophobicity of the Beta structure has a significant impact on the performance of Sn-Beta as an isomerisation catalyst.¹⁷ Specifically, the hydrophobic framework prevents inhibition of active Sn sites by bulk water, thus enabling interaction with glucose.⁷² Furthermore, Sn sites are comparatively more Lewis acidic and hydrophobic than other metal sites, such as Ti, when introduced into the beta zeolite framework.⁷³

2.5 Tin Active Sites Within Beta Zeolite

In general, Sn can exist within the structure of Beta zeolite in two forms. Specifically, Sn can be incorporated into the structure of the zeolite in order to obtain tetrahedrally coordinated Lewis acid sites. Alternatively, basic extra-framework Sn oxide (SnO_x) particles may reside within the pore network of the zeolite.^{26,74} In order to understand the activity of Sn sites within Beta zeolite, the Davis group has conducted several studies.

In an initial study, Davis and co-workers utilised NMR techniques to confirm that framework Lewis acidic Sn sites facilitate glucose isomerisation via an intramolecular hydride shift.²⁶ In the same study, the group also suggest that extra-framework SnO_x nanoparticles contained within the zeolites pore network are considerably less active – or indeed inactive.²⁶ Specifically, the group showed that SnO_x particles within the framework of Beta zeolite generate comparatively lower glucose conversions and fructose yields.²⁶ However, this reported inactivity of SnO_x nanoparticles has since been reconsidered.⁷⁴ Later work by the same groups has found that SnO_x particles are able to facilitate glucose isomerisation via a base catalysed reaction in either water or methanol. This is only possible in aqueous solutions when SnO_x is contained within the hydrophobic structure of the siliceous Beta zeolite – hence indicating that exposure to bulk water inhibits the performance of SnO_x active sites.⁷⁴ Nevertheless, it is worth noting that despite the activity of SnO_x particles within hydrophobic environments, tetrahedrally coordinated framework Sn sites are considered to be responsible for the excellent activity of Sn-Beta catalysts.²⁶

In other work, the Davis group considered the effect of silanol groups on catalytic activity.⁷⁵ Their results show that reaction selectivity towards fructose and mannose can be adjusted by manipulating the silanol nests in close proximity to tetrahedrally coordinated Sn active sites. Specifically, when in proton form, silanol groups in close proximity to framework Sn promote reaction selectivity towards fructose and may facilitate mannose production via a second hydride shift (i.e. glucose to fructose to mannose).⁷⁵ However, if the same silanol groups are altered through sodium (Na^+) substitution, then reaction selectivity begins to favour glucose epimerisation toward mannose – which is achieved via an intramolecular carbon shift. Hence, the selectivity of the reaction can be tuned by modifying the

silanol groups in close proximity to Lewis acidic Sn active sites.⁷⁵ This effect of the silanol groups was also confirmed by computational analysis.⁷⁶ However, it is worth noting that this finding is in stark contrast with the group's earlier work. Specifically, the group previously reported that unmodified Sn-Beta in methanol catalyses mannose production via the epimerisation of glucose - rather than a series of hydride shifts.⁷⁴ However, the authors later explain that the samples used in the original paper were contaminated with potassium (K), and that this K promoted glucose epimerisation via a carbon shift – in the same way Na⁺ promotes glucose epimerisation.⁷⁵

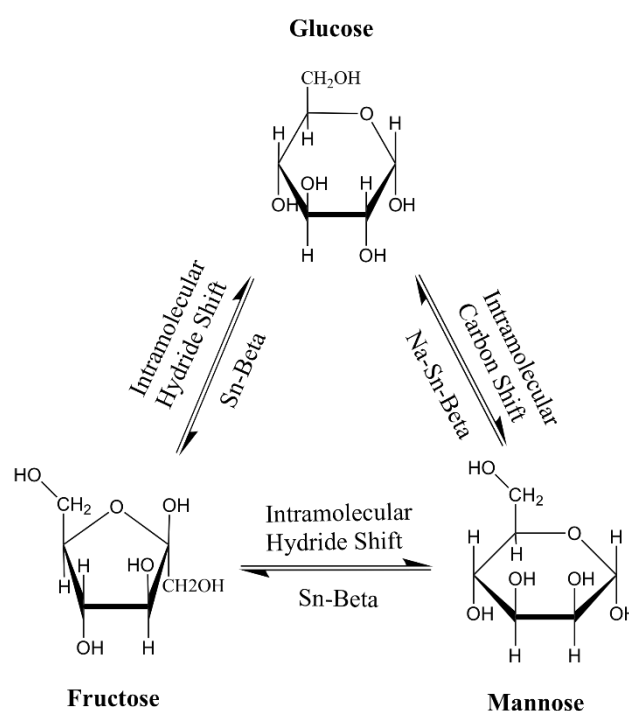


Figure 2.4. Reactions pathways towards fructose and mannose via framework Sn active sites as described by the Davis group.^{26,75}

Moreover, the Davis group has shown that both framework and extra-frame Sn active sites are able to promote glucose isomerisation. However, Lewis acidic framework Sn sites generate considerably higher glucose conversions and fructose yields than basic SnO_x sites. The fructose produced by Sn-Beta may react further to generate mannose. Indeed, fructose and mannose production catalysed by Sn-Beta typically proceeds via a series of intramolecular hydride shifts.⁷⁵ Interestingly however, reaction selectivity towards fructose and mannose can be tuned by altering silanol nests in close proximity to framework Sn sites. Specifically, when

the silanol nests are exchanged with Na⁺ or K⁺, reaction selectivity shifts towards mannose production.^{74,75} When this occurs, mannose is produced via an intramolecular carbon shift (epimerisation) rather than an hydride shift.⁷⁵ **Figure 2.4** illustrates the reaction pathways identified by Davis and co-workers.

2.6 Lewis Acid Tin Beta Active Sites and Isomerisation Mechanisms

The effectiveness of Sn-Beta as a glucose isomerisation catalyst is – in part - a result of Lewis acidic, single site, Sn atoms contained within the materials hydrophobic framework. The presence of these Lewis acid Sn sites enables an intramolecular hydride shift within the glucose molecule that subsequently results in fructose.^{26,77} Experimental analysis of the active material shows that framework Sn may exist in two different forms, with both forms potentially providing the characteristic Lewis acidity required for glucose isomerisation.^{77,78} Moreover, framework Sn within Beta zeolite can exist as fully embedded T-atoms coordinated to four silica atoms by way of oxygen Sn(-O-Si)₄, or as partially hydrolysed sites (Si-O)₃SnOH.⁶⁰ To determine which of these two forms of framework Sn plays a more prominent role in reactions, both experimental and computational techniques have been employed. Specifically, Boronat, *et al.* utilised acetonitrile as a probe molecule to evaluate the affinity of carbonyl groups towards fully embedded and partly hydrolysed framework Sn sites.⁷⁸ The output of both experimental and computational studies performed by Boronat, *et al.* agree that there is a stronger interaction between the electron density of the probe molecules carbonyl group and partly hydrolysed Sn sites. This suggests that partly hydrolysed Sn sites, (Si-O)₃SnOH, may provide greater/stronger Lewis acidity than fully embedded Sn. Moreover, the partly hydrolysed Sn sites are shown to play a more significant role in the specific reaction considered by the authors.⁷⁸ This conclusion was also confirmed by further experimental and theoretical results obtained by the Davis group - who considered the activation enthalpies at the partly hydrolysed Sn sites during the isomerisation of glucose to fructose.⁷⁷

With regards to the specific mechanism that accompanies this hydride shift, there is strong experimental evidence to suggest that a glucose molecule entering Sn-Beta “opens” in the presence of framework Sn.⁷⁷ Thus resulting in an acyclic form of the molecule. Following this, an intramolecular hydride shift occurs within the

acyclic glucose molecule as a result of direct interactions between the molecule and the Sn active site. Both computational and experimental results suggest that this intramolecular hydride shift is the rate limiting/determining step within the reaction.^{26,77} The resulting acyclic form of fructose, produced by the hydride shift, is stabilized whilst present within the structure of Sn-Beta.⁷⁷ Finally, this acyclic fructose molecule is closed, again via interactions with the framework Sn active site, thus completing the mechanism and producing a cyclic fructose molecule.⁷⁷

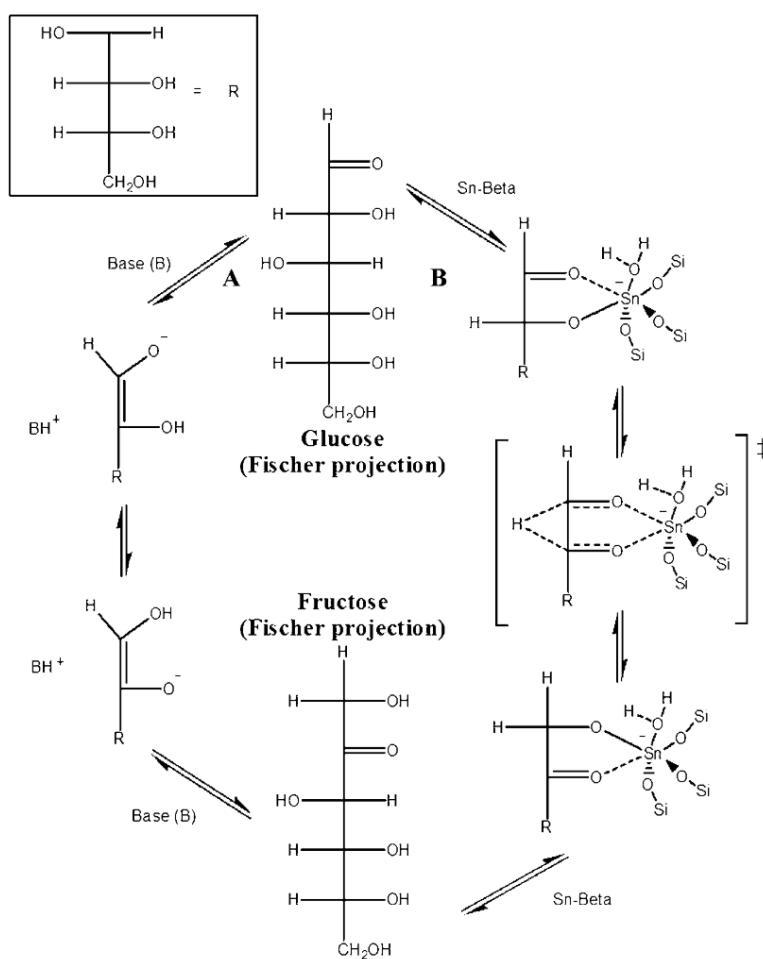


Figure 2.5. Glucose isomerisation pathways via a base catalyst and Lewis acidic Sn-Beta.²⁶

2.7 Synthesis methods towards active Tin Beta

The “traditional” incorporation of Sn within beta zeolite is achieved during the synthesis of an aluminium free BEA framework. In short, Sn is added to a mixture consisting of a silica source, an organic template, and hydrofluoric acid. Following thermal treatment of the mixture for 40 days, the resulting Sn-Beta zeolite consists of purely silica and Sn “T- atoms” bound by oxygen.^{53,79} As a final step the material is calcined in order to remove the organic template residing within the materials pore network.

The Sn source used during the synthesis of Sn-Beta impacts whether or not the Sn atoms are successfully incorporated into the framework of the zeolite. The necessity of having framework Sn within the zeolite is stressed by the inactiveness of homogenous Sn ions compared to Sn-Beta in aqueous reactions.⁵³ Tin chloride pentahydrate can successfully be used to prepare Sn-Beta.⁵³ However, the use of tin oxide as a metal source in the preparation of the same material results in a BEA framework containing SnO₂ nanoparticles that may facilitate an alternative reaction mechanism.^{77,78} Moreover, the extra-framework Sn particles resulting from the use of SnO₂ as a metal source are less effective as glucose isomerisation catalysts.^{26,53} It is also worth noting that the amount of Sn contained with the synthesis mixture can have an inverse effect on crystallisation time and morphology. With more Sn leading to longer synthesis times and impacting crystal shape/morphology.⁸⁰

Trichloromethyltin has also been experimented with as a metal source in the production of Sn-Beta. Results show the use of trichloromethyltin enables the successful incorporation of Sn into the zeolites framework. Thus an active isomerisation catalyst is produced following calcination of the material to remove the organic template. However, removal of the organic template from the synthesised material via acid washing rather than calcination results in a catalyst of decreased activity. In this material, the coordination of the framework Sn to a single methyl group found in the metal source is preserved.⁷⁷ Whereas calcination of the material sees the methyl group coordinated to the Sn site replaced, acid washing does not. The presence of this methyl group within the material does not greatly impact the overall pore volume, therefore it is unlikely to impede the movement of glucose through the framework. However, the resulting diminished

activity of CH₃Sn-Beta may suggest that the presence of the methyl group reduces the Lewis acidity of the Sn sites within the catalyst. However, to examine this further, more experimental analysis on CH₃Sn-Beta is needed.

The synthesis time of Sn-Beta can be significantly reduced through the use of seeding methods. In such methods, aluminium free Beta zeolite (often in the form of Nano-crystals) are synthesised and added to a Sn-Beta synthesis mixture.^{71,81-84} The presence of reaction seeds increases the hydrothermal growth kinetics of Sn-Beta crystals.⁸¹ With regards to the application of seeding to produce Sn-Beta for the isomerisation of glucose, Tsapatis and co-workers utilised a seeding method originally developed by Corma and co-workers to produce Sn-Beta within 22 days.^{71,82,84} More recently, Chang, *et al.* were successfully able to produce highly crystalline, highly inter-grown, Sn-Beta within as little as 52 h. This is a significant reduction in synthesis time when compared to the 40 days traditionally required to produce Sn-Beta - and is shorter than the 11-22 days reported when using other seeding methods.⁸¹ Furthermore, the Sn-Beta crystals produced by Chang, *et al.* were shown to effectively isomerize glucose.

Post-synthesis methods involving acid leaching and impregnation can be used to produce metal-containing Beta zeolites.⁸⁵⁻⁸⁸ Acid leaching (nitric acid) of commercial Beta zeolites results in the almost complete removal of aluminium (Al) from the material with little chance of producing extra framework Al, a common product of steaming techniques.⁸⁵⁻⁸⁷ The resulting silanol nests and vacant "T-sites", produced from the acid leaching step, can subsequently be filled with metal species to produce frameworks such as Sn-Beta.^{85,86} As demonstrated by Hammond and co-workers, the incorporation of framework metals within dealuminated Beta zeolite can be achieved through the application of solid-state ion exchange or wetted impregnation techniques.^{85,86} However, it is important to note that the silanol nests produced from acid dealumination exhibit Brønsted acidity that will remain in the final metal-containing zeolite unless they are effectively closed.⁸⁵ Overall, utilizing post-synthesis methods for the production of Sn-Beta provides four main advantages over more "traditional" hydrothermal synthesis routes, namely; faster synthesis of the active material (when not including the time to produce the parent material), the removal of highly toxic hydrofluoric acid from the synthesis procedure, the potential to introduce higher

quantities of metal species within the zeolite framework, and the ability to generate active catalysts of reduced size and hence higher surface area.⁸⁵⁻⁸⁷ Furthermore, the post-synthesis dealumination processes can be coupled with desilication techniques in order to produce mesoporous/hierarchical metal-containing Beta zeolites.⁸⁸⁻⁹⁰ Indeed, the development of mesoporous Sn-beta structures may reduce mass transfer limitations and the effects of fouling seen in microporous materials.⁹⁰

(Blank Space)

2.7 Glucose derived 5-hydroxymethylfurfural

Fructose can be readily dehydrated towards HMF. For instance, the production of fructose derived HMF can be readily achieved within autocatalytic systems at elevated temperatures.⁹¹ Within such systems, the natural formation of fructose derived formic acid at high temperatures has been found to improve HMF selectivity during reaction.⁹¹ Specifically, Ranoux, *et al.* reported a HMF yield of 43 % when considering a 30 wt.% fructose feedstock with no added catalyst (190 °C, 40 mins).⁹¹

With regards to added catalysts, both homogeneous and heterogeneous acid catalysts have been widely reported in literature for the production of fructose derived HMF. In addition to this a number of authors have considered the use of alternative reaction systems. For example, Román-Leshkov, *et al.* demonstrated the use of a biphasic reactor system containing an acid catalyst and phase modifiers as a means to improve HMF yields from fructose through the avoidance of undesirable reactions.⁹² A typical biphasic system approach consists of a batch reactor containing two immiscible phases; a catalyst rich aqueous phase and an organic layer for the purpose of continuous product extraction.⁹² Once removed from the systems reactive layer, HMF loss through undesirable (i.e. degradation, condensation, and rehydration) reactions are minimised whilst fructose conversions appear to increase.⁹²⁻⁹⁴ Within an optimised biphasic reactor system utilising hydrochloric acid as a catalyst and phase modifiers, Román-Leshkov, *et al.* achieved a fructose conversion of 89 % accompanied by a 85 % selectivity towards HMF.⁹² Incredibly, this was achieved using a 30 wt.% fructose feedstock and high HMF yields were also achieved when using a 50 wt.% feedstock. In addition, the authors of this study also proposed and simulated a means of product separation following reaction (**Figure 2.6**).⁹² With further regards to the use of biphasic reactor systems, it is also worth noting that counter current column reactors and co-current flow reactors have also been considered for the production HMF from fructose.⁹⁵⁻⁹⁷

Following from the work of Román-Leshkov, *et al.* the cost of producing HMF from fructose has been modelled by Torres, *et al.*⁹⁴ Modelling results, based on Román-Leshkov, *et al.* proposed extraction system (as shown in **figure 2.6**) as well as kinetic models reveals that fructose prices have a tremendous impact on

HMF production costs.⁹⁴ Moreover, the authors found that in order to minimise HMF production costs within the future biorefinery, the cost of fructose must fall and/or improvement must be made relating to selectivity/efficiency.⁹⁴ Indeed, later work by the same group attempts to address production costs through the use of an alternative biphasic system involving the use of an Extractive-Reactor.⁹⁸ Although simulations of this alternative system showed an improvement in HMF production cost in comparison to earlier work, fructose prices remained a major contributor to costs.⁹⁸

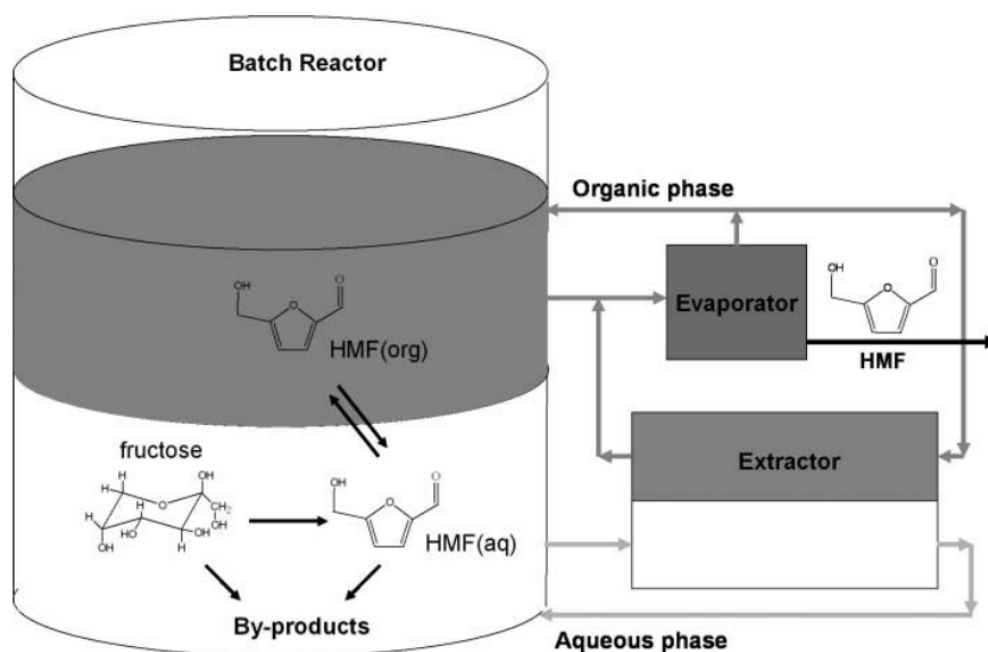


Figure 2.6. Combined biphasic reactor and product extraction system proposed by Román-Leshkov, *et al.* for the production of fructose derived HMF.⁹²

An alternative route towards HMF production is to begin with a glucose feedstock. Indeed, given the abundance and low cost of glucose, it is a preferred feedstock for HMF production.^{93,99} As previously mentioned, the production of glucose derived HMF may precede via the isomerisation of glucose to fructose.^{14,15} Subsequently, the fructose obtained from this initial reaction step may then be dehydrated towards HMF.^{14,15} Despite the potential advantages, the use of a glucose feedstock for the production of HMF continues to present challenges.^{13,100} Herein, examples that highlight some advances in the field of HMF production from glucose are described - with particularly emphasis on the use of “one-pot” reactions.

2.8 Ionic Liquid Systems for HMF Production

In 2007, Zhao, *et al.* demonstrated the potential to generate considerable HMF yields from glucose utilising a “one-pot” reaction.¹⁰¹ No doubt a considerable milestone in the field of HMF production, the authors showed metal chlorides in ionic liquids (ILs) to be exceptionally promising catalysts. Of the metal chlorides considered by the authors, chromium (Cr) chlorides were shown to be of considerable interest. Specifically, CrCl₃ enabled a glucose conversion > 90 % and a HMF yield of around 70 % in 1-ethyl-3-methylimidazolium chloride ([EMIM]Cl) at moderate temperature (100 °C).¹⁰¹ Here the authors propose that the exceptional performance of Cr ions may stem from a specific sugar-metal coordination involving the hemiacetal area of the cyclic sugar and a reaction pathway through fructose.¹⁰¹ Moreover, the authors show that in the absence of metal chlorides, negligible glucose conversions and product yields are obtained under chosen reaction conditions and other metal chlorides are less efficient in HMF production – although they may generate high glucose conversions.¹⁰¹

The exceptional performance of CrCl_x as a glucose isomerisation catalyst has prompted further investigation. Specifically, Pidko, *et al.* utilised a combination of experimental and computational techniques to gain a better understanding of the reaction mechanism involved and the formation of Cr-sugar complexes in ILs.¹⁰² In their study, the authors show that whilst the formation of single centred Cr complex's facilitates the opening and closing of hexose rings during the isomerisation process, the required hydride transfer step in the proposed reaction mechanism favours the formation of temporary Cr dimers.¹⁰² Here, both EXAFS experiments and DFT calculations suggest that Cr dimers facilitate a deprotonation step of the reaction mechanism, which is subsequently followed by a hydride shift.¹⁰² The overall reaction mechanism proposed by Pidko, *et al.* is shown in **Figure 2.7**.

Work towards the development of IL systems for the production of glucose derived HMF remains an active area in academic literature. Indeed, researchers have considered the use of; acidic ILs, zeolite / IL systems, metal oxide / IL systems, and resin / multi-IL systems, to name a few examples.^{103–107}

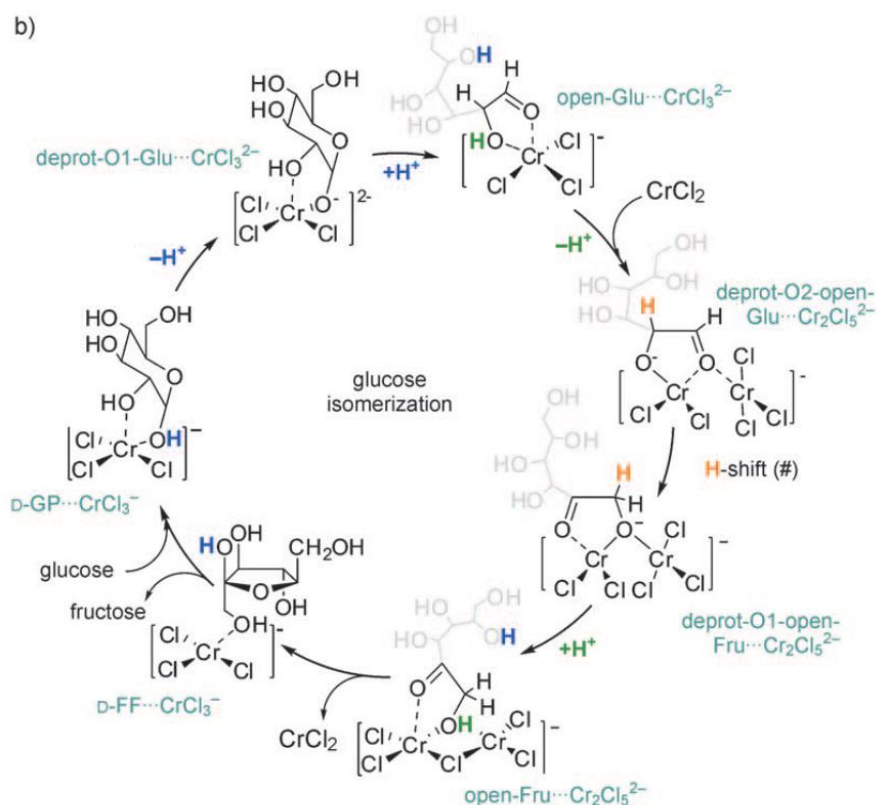


Figure 2.7. Cr ion / Ionic Liquid reaction mechanism proposed by Pidko, *et al.* based on EXAFS experiments and DFT calculations.¹⁰²

Despite the excellent performance of ILs in the production of HMF, the use of these solvents presents a number of challenges. For instance, ILs are generally considered expensive and the low vapour pressure of these potentially tailor made solvents complicates the separation of soluble products with low thermal stability when considering techniques such as distillation or evaporation.¹⁰⁸ Furthermore, the use of homogeneous catalysts such as CrCl_x may present a number of challenges relating to environmental/toxicity concerns and product separation.^{41,109} In order to overcome issues relating to product separation, researchers have investigated the use of supercritical CO_2 , nanofiltration membranes, and vacuum steam distillation systems for the extraction of HMF from ILs.^{103,110,111} Although such methods may address issues relating to production separation, they do not address issues relating to IL costs. To address this latter issue, researchers have begun to explore the use of inexpensive and available ILs for HMF production.¹¹² However, a potentially more holistic approach may seek to minimise the quantity of ILs used in the reaction. To this extent, Degirmenci and co-workers have explored the development of

heterogeneous catalysts consisting of ILs grafted on a silica support (SBA-15).^{12,100} By encapsulating metal chlorides within the grafted IL, the authors were able to effectively generate a microenvironment that somewhat mimics the metal chloride / IL system presented by Zhao, et al. However, despite the performance of these catalysts in different solvents including water, leaching of the encapsulated metal ions from the IL layer was problematic.^{12,100} As such, the use of ILs and homogeneous metal chlorides for HMF production still appears to present considerable challenges.

2.9 Heterogeneous Sulfates and Phosphates for HMF Production

A number of researchers have considered the use of sulphur containing catalysts for the production of glucose derived HMF. Interestingly, sulfur functionalised materials have also been identified as promising cellulose hydrolysis catalysts in water. For instance, early work identified sulfonated activated carbon as a particularly efficient and recyclable catalyst for cellulose hydrolysis – enabling a 40.5 % glucose yield (95 % selectivity) in water mediated reactions (24hr).¹¹³

Sulfated zirconia (SZ) catalysts have been considered for the production of glucose derived HMF in different solvents. Of particular interest here is the use of supported / modified SZ catalysts and their tuneability towards HMF production. For instance, the performances of $\text{SO}_4^{2-} / \text{ZrO}_2$, $\text{SO}_4^{2-} / \text{ZrO}_2 - \text{Al}_2\text{O}_3$, and zeolite supported SZ materials have been investigated as catalysts in DMSO.^{114,115} Specifically, Yan, *et al.* generated a HMF yield of 47.6 % (4 hr, 130 °C) using an optimised $\text{SO}_4^{2-} / \text{ZrO}_2 - \text{Al}_2\text{O}_3$ catalyst.¹¹⁴ Here, the authors demonstrate that the observed acidity and basicity of the catalyst can be tuned towards the production of fructose and HMF through the addition of Al.¹¹⁴ Meanwhile, in more recent work, Feng et al were able to generate a HMF yield of around 61 % using a SZ-zeolite (ZSM-5) catalyst in a solvent mixture consisting of DMSO, water, and sodium chloride (1.5 hr, 195 °C).¹¹⁵ Here the authors show that the Lewis and Brønsted acidity of the catalyst can be tuned by varying the SZ loading on the zeolite support.¹¹⁵ Furthermore, the authors also show that the performance of the SZ-zeolite catalyst is affected by the calcination temperatures used during material synthesis and may be substantially improved through the use of a biphasic reactor

system. Indeed, this is somewhat consistent with recent work by Zhang, *et al.* who demonstrate that calcination temperatures may influence the acidity and structure of zirconia and its performance as a glucose dehydration catalyst in a solvent mixture containing DMSO and water.¹¹⁶ Moreover, the calcination temperature of zirconia appeared to have a pronounced effect on the rate of reaction.¹¹⁶

The potential to tune sulfated metal oxides towards the production of glucose derived HMF has also been studied in water mediated reactions. For instance, Osatiashiani, *et al.* explored the catalytic performances of bulk SZ and SBA-15 supported materials.^{117,118} Here the authors found that sulfation effected crystal morphology in the bulk material as well as base and acid properties which drive catalytic performance in both the bulk and supported materials.^{117,118} Furthermore, the performance of SBA-15 supported materials may also be effected by the number/depth of grafted zirconia monolayers in the sulfur functionalised catalyst.¹¹⁸ Overall, fructose was found to be the main reaction product when considering a glucose feedstock along with bulk or supported SZ catalysts.^{117,118} In other work pertaining to the use of water-mediated reactions, Lopes, *et al.* considered the use of modified tin oxide catalysts.¹¹⁹ Here, as with the zirconia catalysts previously described, factors such as sulfur functionalisation, calcination temperature, and Al doping, were found to influence the performance of tin oxide as a catalyst for HMF production.¹¹⁹

Various phosphates have also been considered as glucose isomerisation and dehydration catalysts. Such materials may exhibit both Lewis and Brønsted acidity.^{120–125} Ordonsky, *et al.* studied the performance of several metal phosphates and their associated oxides as glucose isomerisation and dehydration catalysts.¹²¹ Here, the authors found niobium (Nb) and Zr phosphates to be of considerable interest and explored the possibility of tuning catalytically activity. Specifically, the ability to reduce the Lewis and Brønsted acidity of materials through silylation and Na⁺ ion exchange was investigated in detail. Moreover, silylation is shown to affect unsaturated/isolated Lewis acid metal sites resulting in reduced humin formation and improved selectivity, whilst Na⁺ ion exchange reduces Brønsted acidity at phosphate sites (P-OH to P-ONa) which subsequently impacts Lewis acidity at proximate Nb sites.¹²¹ Overall, the authors were able to generate a moderate glucose conversion and HMF yield in water (**Table 2.2, Entry**

1) that could be improved through the use of a biphasic reactor system (**Table 2.3, Entry 7**).

Table 2.2. Phosphate catalysts for the production of glucose derived HMF.

Entry	Catalyst	Solvent	Temp (°C)	Time	Glucose Conversion (%)	HMF Yield (%)	Ref
1	NbPO-f	H ₂ O	135	>400 min	~ 40	~ 18	121
2	ZrP-Cr	[Bmim]Cl	120	12h	94.7	43.2	126
3	SnPO	[Emim]Br	120	3h	94.1	58.3	127
4	ZrP	H ₂ O	240	240s	72.3	23.5	128
5	CaP ₂ O ₆	H ₂ O	220	5min	70	20	129
6	α -Sr(PO ₃) ₂	H ₂ O	220	5min	60	20.9	129
7	CePO ₄	DMSO	160	1h	97	61	125
8	FePO ₄	H ₂ O / acetone	160	100 min	65.4	35.3	122
9	H ₃ PO ₄ -SiO ₂ -FePO ₄	H ₂ O / acetone	160	100 min	99.9	76.3	122
10	SAPO-34	GVL / H ₂ O	170	40 min	100	93.6	123

Table 2.2 provides an overview of some other phosphate catalysts considered in literature for the production of glucose derived HMF. As seen, high HMF yields can be generated using a number of different catalyst and solvent combinations. For instance, cerous phosphate (CePO₄) is able to generate a HMF yield of 61 % in DMSO (**Table 2.2, Entry 7**).¹²⁵ Here, the performance of CePO₄ can be directly linked to its Lewis acidity - which is related to its crystal structure - and can be adjusted by changing the temperatures used during catalyst synthesis.¹²⁵ Furthermore, the performance of iron phosphate (FePO₄) can be greatly improved by supporting it on a functionalised silica and adding acetone to the reaction mixture (**Entries 8-9**).¹²² Meanwhile, an exceptionally high HMF yield of 93.6 % can be obtained from glucose when using silicoaluminophosphates (SAPO-34) as

a catalyst in a mixed solvent system containing water and γ -valerolactone (GVL) (**Entry 10**).¹²³ Moreover, exceptionally high HMF yields can be generated by SAPO-34 and supported FePO₄ catalysts in mixed solvent systems.^{122,123} Here, the Lewis and Brønsted acidity of the catalysts enable the production of HMF from glucose via an initial isomerisation step and the mixed solvent system improves product yields.^{122,123}

2.10 Metal-Organic Frameworks (MOFs) for HMF Production

As previously discussed, a number of researchers have begun to explore the development of MOF catalysts for glucose isomerisation. As such, these porous materials have also been considered for the production of glucose derived HMF. For instance, a number of research groups have considered the use of sulfonic acid functionalised Cr-MIL-101 as a glucose dehydration catalyst. Specifically, Su, *et al.* generated glucose conversions and HMF yields of approximately 100 % and 45 % respectively when considering the use of Cr-MIL-101-SO₃H in a mixed solvent system containing GVL and water (150 °C, ~220 min).¹³⁰ Furthermore, the authors also demonstrated the excellent performance of this catalysts when utilised in a flow reactor running the same solvent mixture and operating at the same reaction temperature.¹³⁰ This is particularly interesting considering the preferred use of flow reactors in industry and the relatively low quantity of flow data reported in literature. Meanwhile, in other work pertaining to the use of batch reactors, the performances of sulfonic acid functionalised Cr-MIL-101 catalysts has also been considered in THF solutions containing small quantities of water.¹³¹ However, the catalyst is shown to generate lower HMF yields within this solvent mixture.¹³¹ Overall, despite the promising use of functionalised Cr-MIL-101 catalysts for HMF production, the use of Cr may pose environmental/toxicity concerns and long reaction times are not ideal.

Several research groups have also considered the use of Zr based MOFs for HMF production. For example, researchers have considered the use of phosphate modified Nu-1000 and linker functionalised UiO-66 in various solvents.^{65,132} Here, phosphate modified Nu-1000 generates exceptionally high HMF yields in a solvent mixture containing water and 2-propanol.⁶⁵ Specifically, this modified

catalysts enables a glucose conversion of approximately 99 % and a HMF yield of 64 % by facilitating reactions via an initial isomerisation step towards fructose (140 °C, 7h).⁶⁵

2.11 Biphasic Reactors for HMF Production

As previously discussed, biphasic reactors may be used to increase HMF production when utilising a fructose feedstock. Unsurprisingly, such reactor systems may also be used to promote product yields in glucose fed systems. Indeed, biphasic reactor systems have been used in combination with many of the catalyst types already discussed in order to enhance HMF yields from glucose. Again, the use of a biphasic reactor facilitates the continuous extraction of product from the aqueous phase thus preventing loss through cascade reaction and/or degradation.⁹²⁻⁹⁴

Table 2.3 summarises a number of biphasic reactor examples that have been reported in literature for production of glucose derived HMF. As seen in **Entries 1-2**, Sn and Al chlorides are able to effectively promote HMF production in a biphasic system utilising 2-*sec*-butylphenol (SBP) as an extracting agent.¹⁴ Moreover, the reaction pathway is shown to proceed through the isomerisation of glucose to fructose - as evidenced by the presences of this intermediate product during reactions.¹⁴ The results presented here are of considerable interest as previous studies have shown SnCl₄ to be an ineffective glucose isomerisation catalyst.⁵³ Moreover, the Lewis acidic performances of the metal chlorides in the biphasic system is a result of a low pH environment caused by dissociation when considering SnCl₄ and through the addition of HCl in the case of AlCl₃.^{14,133}

The exceptional performance of Sn-Beta as a glucose isomerisation catalyst has no doubt inspired its use in biphasic systems. Here, the zeolite catalyst is complemented by HCl in an attempt to drive HMF production as shown in **Entry 3**.⁷⁹ Interestingly however, it is worth nothing that this catalyst combination is ineffective in monophasic aqueous systems.⁷⁹ In other work, researchers have considered the use of Beta zeolites containing extra-framework Fe and Cr metal sites as glucose isomerisation and dehydration catalysts (**Entries 4-5**).^{134,135} Here, the metal zeolites promote HMF production via Lewis and Brønsted acid catalysed reactions.^{134,135} Furthermore, these studies (along with others) highlight the

importance of optimising the ratio between Lewis and Brønsted acid site within the catalysts being considered.^{134,135}

As seen in **Entries 6-8**, HMF yields up to approximately 60 % may be generated using various phosphate catalysts.^{120,121,136} These catalysts exhibit both Lewis and Brønsted acidity which promoted the production of HMF from glucose via the formation of fructose.^{120,121,136} Interestingly, in the case of MnPO_4 , this acidity may stem from the partial dissolution and hydrolysis of the parent material during high temperature reactions to form catalytically active $\text{Mn}(\text{OH})_n^{(3-n)}$ and H^+ ions.¹³⁶ Following the reaction, the parent material (MnPO_4) may then precipitate out of solution during cooling, enabling it to be recovered and reused.¹³⁶ Indeed, this partial dissolution is somewhat similar to that observed when considering unsupported FePO_4 as a catalyst.¹³⁷

More recently, exceptional high HMF yields have been reported using a bifunctional activated carbon catalyst exhibiting both acid and base properties.¹³⁸ Specifically, Nahavandi, *et al.* achieved a 93 % HMF yield when using SO_3H -OAC in a biphasic reactor system (**Entry 9**).¹³⁸ In other work, exceptionally high HMF yields were also achieved using a new sulfonic acid functionalised Cr based condensation polymer (MOF).¹³⁹ As shown in **Entry 10**, Chen, *et al.* were able to generate a 80.7 % HMF yield in a biphasic reactor system using this new bifunctional catalyst containing both Lewis and Brønsted acid sites, $\text{PCP}(\text{Cr})\text{-SO}_3\text{H-Cr(III)}$.¹³⁹ However, as previously noted, the use of Cr based catalysts is not ideal for commercial systems.

Table 2.3. Biphasic systems for HMF production from glucose.

Entry	Catalyst	Aqueous Phase	Organic Phase	Temp (°C)	Time	Glucose Conversion (%)	HMF Yield (%)	Ref
1	SnCl ₄	NaCl _(aq)	SBP	170	45 min	90	52	14
2	AlCl ₃ , HCl	NaCl _(aq)	SBP	170	40 min	91	68	14
3	Sn-Beta, HCl	NaCl _(aq)	THF	180	70 min	79	57	79
4	Fe-Beta	NaCl _(aq)	THF	120	90 mins	95	61	134
5	Cr-Beta	NaCl _(aq)	THF	150	90 mins	87	72	135
6	Mesoporous zirconium phosphate	NaCl _(aq)	Diglyme	180	3h	N/A	63	120
7	NbPO ₄ -f	Water	MIKB	135	~ 450 min	~ 60	~ 36	121
8	MnPO ₄	NaCl _(aq)	THF	160	90 min	96	59	136
9	SO ₃ H-OAC	NaCl _(aq)	THF	160	3h	93	97	138
10	PCP(Cr)-SO ₃ H.Cr(II)	NaCl _(aq)	THF	180	4h	99.9	80.7	139

Conclusion

The drive towards efficient and cost effective HMF production remains a considerably active field within academic research. The potential to produce HMF from widely available glucose feedstocks is of considerable interest. The production of glucose derived HMF typically precedes via the production of fructose. As such, the development of catalytic systems capable of promoting this reaction is under investigation. The isomerisation of glucose may be catalysed via basic or Lewis acid catalysts. Within current literature, a number of studies have begun to identify particularly promising heterogeneous chemo-catalytic systems for this reaction. For instance, Sn-Beta has been identified as an exceptionally promising aqueous glucose isomerisation catalyst and can be combined with Brønsted acid catalysts in biphasic systems to facilitate HMF production. Meanwhile, zeolite Y has recently been reported as a promising catalyst within water (when modified with Mg) or when applied within a two-step reaction system involving a sequential solvent change. Indeed, the performances of these zeolites are highly promising and warrant further investigation.

In other recent work, a number of groups have begun to explore the use of MOFs as glucose isomerisation and dehydration catalysts in various systems. At present, the development of Cr and Zr MOFs has been explored and promising results have been achieved within literature. Indeed, the potential application of porous and tuneable MOFs within the field of catalysis in general has been highlighted and remains a growing interest.¹⁴⁰⁻¹⁴⁴ Moreover, the application of MOF catalysts is an exciting prospect and the tuneable nature of these materials means there is ample scope for development. As such, the development of MOF catalysts will also be explored within this thesis.

Experimental

Summary

The synthesis methods of all materials prepared for study within this thesis are outlined herein. A rapid synthesis method for the production of metal-containing beta zeolites is described along with the post-synthesis modification of commercial zeolite Y. With regards to metal-organic frameworks (MOFs), the synthesis details of UiO-66, UiO-67, MIL-88B, ZIF-8, and $\text{Yb}_6(\text{BDC})_7(\text{OH})_4(\text{H}_2\text{O})_4$ are given. The techniques used to characterise these materials are described as well as the methods used to test their catalytic performances in batch reactions. To test the performances of chosen catalysts within continuous flow, a purpose built flow reactor was utilised. The specifications of this reactor system are also included herein. Finally, a description is given of the equipment and methods used to collect Extended X-Ray Absorption Fine Structure (EXAFS) and X-ray Absorption Near Edge Structure (XANES) data from selected materials.

3.1 Zeolite Synthesis

Synthesis Of Metal-Containing Beta Zeolites

Metal-containing beta zeolites were synthesized using a seeding method adopted from the work of Chang, *et al.*⁸¹ In a typical procedure, 7.69 g of tetraethylammonium hydroxide (Sigma Aldrich, 35 wt.% in water) and 6.98 g of tetraethylorthosilicate (Sigma Aldrich) were added to a 45 mL teflon lined autoclave. The resulting solution was allowed to mix for 90 min. Following this a metal salt dissolved in 0.64 g of deionized water was added to the autoclave. The amount of metal added to each zeolite is summarized in **Table 3.1**. The subsequent solution was allowed to mix for several days until a mass loss of around 6 - 7 g was observed. Next, 0.89 g of hydrofluoric acid (Sigma Aldrich, 40 wt.%) was added to the autoclave. This was followed 84 mg of commercial beta zeolite

(Zeolyst CP814C* SiO₂/Al₂O₃ = 38) suspended in 0.431 g of deionized water. The resulting gel was mixed before the autoclave was sealed and heated at 140 °C for 72 h. Subsequently, the autoclave was quenched with water and the resulting zeolite was filtered, washed, and dried overnight at 100 °C. Finally the zeolite was calcined at 550 °C for 12 h in a muffle oven. The products of this synthesis procedure were denoted as (ZZ)XX-Beta, where XX refers to the metal introduced and ZZ refers to the weight percentage (wt.%) of the metal within the zeolite.

Table 3.1. Summary of synthesized beta zeolites.

Synthesised BEA Zeolite	Metal Source	Quantity of Metal Source (g)	Metal Source supplier
(0.5)Sn-Beta	Tin Pentachloride	0.031	Acros Organics
(1)Sn-Beta	Tin Pentachloride	0.061	Acros Organics
(2)Sn-Beta	Tin Pentachloride	0.126	Acros Organics
(1)Zr-Beta	Zirconium Oxychloride Octahydrate	0.072	Honeywell
(2)Zr-Beta	Zirconium Oxychloride Octahydrate	0.144	Honeywell
(1)Sn,(1)Zr-Beta	Tin Pentachloride & Zirconium Oxychloride	0.0605 (Sn) & 0.072 (Zn)	Acros Organics & Honeywell
(2)Zn-Beta	Zinc Chloride	0.882	Sigma Aldrich
(2)Yb-Beta	Ytterbium Chloride hexahydrate	0.094	Strem Chemicals UK
(2)Sr-Beta	Strontium Nitrate	0.192	Sigma Aldrich
(2)Ga-Beta	Gallium Nitrate	0.15	Fisher Scientific

Dealumination Of Commercial Zeolite Y

Dealumination of zeolite Y was performed based on methods adopted from literature.¹⁴⁵ For dealumination 5 g of zeolite Y (Alfa Aesar, SiO₂/Al₂O₃ mole ratio 30:1, H-Y) was added to a 100 mL round bottom flask. Subsequently 50 mL of 8 M nitric acid was added to the flask along with a magnetic stirring bar. The round bottom flask was then fitted with a condenser (cooled with tap water) and heated at 80 °C using a paraffin oil bath for 20 h. To stop the dealumination process the round bottom flask was quenched in water. The zeolite was recovered via filtration and washed with copious amounts of deionized water. Finally, the resulting solid was dried at 80 °C and denoted as DeAl-H-Y.

Post-Synthesis Addition Of Metals To Zeolite Y

For the preparation of tin (Sn) and gallium (Ga) containing zeolite Y, an adapted incipient wetness technique was used. Typically, a metal-containing precursor solution was made by dissolving 0.118 g of tin (IV) chloride pentahydrate (Sigma Aldrich) or 0.147 g of gallium (III) nitrate hydrate (Fisher Scientific) in 0.739 mL of deionized water. The metal precursor solution was added drop wise on 1 g of DeAl-H-Y. The resulting mixtures were stirred and then dried at 80 °C for 24 h. Finally the samples were calcined at 550 °C (using a ramp rate of 1 °C/min) for 5 h. The Sn and Ga modified zeolites were denoted as Sn-DeAl-H-Y and Ga-DeAl-H-Y, respectively. A summary of zeolite Y materials synthesised in this study is given in **Table 3.2**.

Table 3.2. Summary of zeolite Y materials.

Zeolite Y	Commercial Material	Dealumination	Metal Source
H-Y	Alfa Aesar	N/A	N/A
DeAl-H-Y	Alfa Aesar	8M Nitric Acid, 80°C, 20 hours	N/A
Sn-DeAl-H-Y	Alfa Aesar	(DeAl)H-Y	Tin Chloride
Ga-DeAl-H-Y	Alfa Aesar	(DeAl)H-Y	Gallium Nitrate

3.2 MOF Synthesis

Zirconium MOFs

UiO-66 was prepared by mixing 2.481 g of anhydrous zirconium tetrachloride (Alfa Aesar, $ZrCl_4$), 3.54 g of benzene-1,4-dicarboxylic acid (Sigma Aldrich, BDC), 100 mL of *N,N*-dimethylformamide (Fisher Scientific, DMF), and 20 mL of hydrochloric acid (37 % w/w, VWR, HCl). The synthesis mixture was then transferred into a large capacity acid digestion vessel (200 mL) and heated at 120 °C for 24 h. The resulting material was filtered, washed with methanol, and dried in air at 70 °C. Functionalised variants of UiO-66 were prepared by substituting fractions of benzene-1,4-dicarboxylic acid with alternative linkers during synthesis. It is worth noting that smaller autoclaves were typically used for the synthesis of various functionalised UiO-66 materials. The alternative linkers considered are shown in **Figure 3.1**.

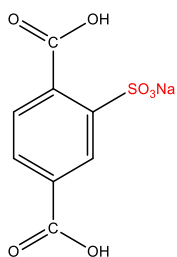
BTeC-UiO-66 was prepared by mixing 1.200 g of zirconium chloride, 1.300 g of benzene-1,2,4,5-tetracarboxylic acid (Sigma Aldrich), and 100 mL of water. The synthesis mixture was transferred into a teflon-lined autoclave and heated at 120 °C for 24 h. The autoclave was subsequently cooled and 30 mL of water was added to the resulting gel before it was reheated at 120 °C for a further 24 h under reflux.¹⁴⁶

Defective UiO-66 was prepared via the hydrothermal extraction of linker from standard UiO-66. As follows, 0.50 g of UiO-66 was treated in 10 mL of water at 240 °C for 24 h. The extracted linker was subsequently removed from the materials pore network by washing with DMF and then methanol. The washed material was dried in air at 70 °C.

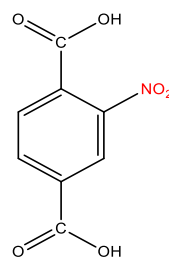
Nano UiO-66 materials were synthesised following the modified procedures developed by Taddei, *et al.*¹⁴⁷ Notably, a pre-solution was prepared by aging 1.75 g of $ZrCl_4$ in a solution of DMF (75 mL), water (1.6 mL) and acetic acid (7 mL). For the synthesis of Nano-UiO-66, 0.333 g of 1,4-benzenedicarboxylic acid was mixed with 20 mL of pre-solution aged for 48 h. The resulting mixture was transferred to a 45 mL teflon-lined autoclave and heated at 120 °C for 24 h. The resulting material was recovered, washed in methanol, and dried in air at 70 °C. An “Ultra” Nano UiO-66 material was synthesised following a similar procedure,

but here the pre-solution was aged for 96 h. Finally, a poorly crystalline-Nano-UiO-66 material was synthesised in the same way as Nano-UiO-66 but without acetic acid in the pre-solution and an increased water content of 3.2 mL.

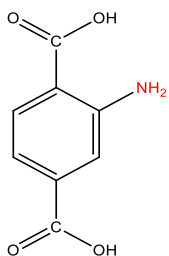
UiO-67 was prepared by mixing 0.805 g of zirconium chloride (Alfa Aesar), 1.082 g of biphenyl-4,4-dicarboxylic acid (Sigma Aldrich), 100 mL of N,N-dimethylformamide (Fisher Scientific), and 20 mL of hydrochloric acid (37 %, VWR). The synthesis mixture was then transferred to a teflon-lined autoclave and heated to 80 °C for 24 h. After cooling the solid product was recovered from the autoclave and washed with DMF and methanol before drying at 70 °C. Sulfonic acid functionalised UiO-67 was prepared by substituting biphenyl-4,4-dicarboxylic acid with monosodium 3-sulfo-benzoic acid (Sigma Aldrich). Both linkers are also shown in **Figure 3.1**.



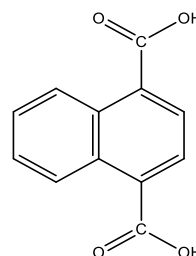
monosodium 2-sulfo-benzene-1,4-dicarboxylate acid



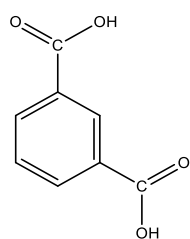
2-nitro-benzene-1,4-dicarboxylate acid



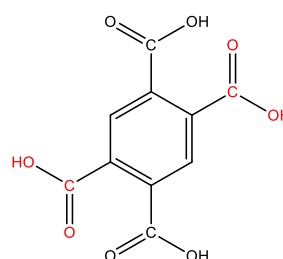
2-amine-benzene-1,4-dicarboxylate acid



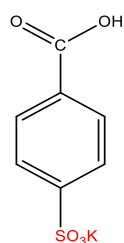
1,4-Naphthalenedicarboxylic acid



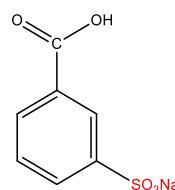
Isophthalic acid



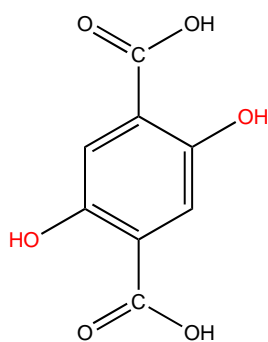
1,2,4,5-Benzenetetracarboxylic acid *



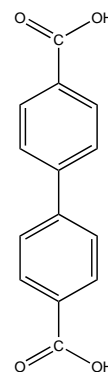
Potassium 4-Sulfo benzoic Acid



Sodium 3-Sulfo benzoate



2,5-Dihydroxyterephthalic Acid



Biphenyl-4,4'-dicarboxylic Acid (*)

Figure 3.1. Functionalised linker salts substituted during UiO-66 synthesis and (*) UiO-67 linker.

MIL-88B

Three variations of MIL-88B were prepared for study. These materials were synthesised using the same principle procedures reported in literature.^{148,149} Metal salt(s) were mixed in a beaker containing N,N-dimethylformamide (DMF) and 1,4-benzenedicarboxylic acid (BDC) for 20 min. The solution was then transferred to a PTFE lined autoclave and heated at 150 °C (or 110 °C) for 72 h. Solid materials were subsequently recovered via filtration and washed with ethanol before drying at 70 °C. The chemical quantities used in each synthesis procedure are summarized in **Table 3.3**.

Table 3.3. Summary of MIL-88B materials.

MOF	Metal Sources	Quantity of Metal Source(s) (grams)	DMF (mL)	BDC (grams)
Iron (Fe)MIL-88B	Iron (III) chloride	1.02(Fe)	20	0.284
Scandium (Sc)MIL-88B	Scandium (III) chloride	0.22(Sc)	9	0.14
Iron : Scandium (Fe:Sc)MIL-88B	Iron (III) chloride & Scandium (III) chloride	0.51(Fe) : 0.51(Sc)	20	0.284

Ytterbium MOF $Yb_2(BDC)_3(DMF)_2(H_2O)_2$

This material was prepared following the same principle procedure reported in literature.¹⁵⁰ Namely, 1 mmol of ytterbium (III) chloride hexahydrate, 1.5 mmol of BDC, 2.5 mL of DMF, and 2.5 mL of deionised water were mixed via stirring. The resulting mixture was sealed in a 20 mL Teflon-lined autoclave and heated at 100 °C for 20 h. Subsequently, the resulting material was collected via vacuum filtration, washed in DMF by stirring at room temperature overnight, collected via centrifuge and rewashed in ethanol, collected again and dried in air at 70 °C overnight.

Ytterbium MOF $Yb_6(BDC)_7(OH)_4(H_2O)_4$

This compound was prepared by mixing 0.20 g of finely ground $Yb_2(BDC)_3(DMF)_2(H_2O)_2$, 0.10 g of ytterbium chloride hexahydrate (Sigma Aldrich), and 10 mL of deionised water. The solution was stirred for 5 min before being sealed in a 20 mL teflon-lined autoclave and heated at 200 °C for 72 h. The resulting material was collected via filtration before being washed in DMF overnight to remove excess BDC. Subsequently the material was separated via centrifuge, rewashed in ethanol, and dried at 70 °C overnight.

ZIF-8 Room Temperature Synthesis

Two mixtures were prepared. For the first, 1.32 g (4.4 mmol) of zinc nitrate hexahydrate (Sigma Aldrich) was dissolved in 4 mL of deionized water. For the second, 11.37 g (138 mmol) of 2-methylimidazole (Sigma Aldrich) was dissolved in 40 mL of deionized water. The two solutions were then combined and mixed for 15 min. The resulting milky solution was transferred into centrifuge tubes and spun at 6500 rpm for 30 min. The recovered solid material was washed in acetone and separated again via a centrifuge. This washing was repeated a total of four times. Finally, the product was dried at 70 °C for 24 h and denoted as (RT)ZIF-8.

ZIF-8 Hydrothermal Synthesis

Two mixtures were prepared. For the first, 1.10 g of zinc nitrate hexahydrate (Sigma Aldrich) was dissolved in 5 mL of deionized water. For the second, 11.37 g (52 mmol) of 2-methylimidazole (Sigma Aldrich) was dissolved in 15 mL of deionized water. The two solutions were then combined and mixed for 5 min. After mixing, the solution was poured into a teflon-lined autoclave and heated at 140 °C for 24 h. Afterwards, the autoclave was quenched with tap water. A milky solution was recovered from the autoclave and centrifuged at 6500 rpm for 15 min. The resulting solid product was then washed four times with 10 mL of acetone and recovered via centrifuge. Finally, the product was dried at 80 °C for 24 h and denoted as (HT)ZIF-8.

3.3 Material Characterization Techniques

Powder X-ray Diffraction (XRD) data was collected using a Panalytical X'Pert Pro MPD equipped with monochromatic Cu K α 1 radiation source and a PIXcel solidstate detector. Nitrogen adsorption isotherms were measured at -196 °C on a Micromeritics ASAP2020 system. The samples were outgassed at temperature (110 – 300 °C) for 12 h prior to the sorption measurements. The Brunauer-Emmett-Teller (BET) equation was used to calculate specific surface area from the adsorption data obtained ($P/P_0=0.05-0.25$). The mesopore volume was calculated by the Barrett-Joyner-Halenda (BJH) method on the adsorption branch of the isotherm. The micropore volume was calculated from the t-plot curve at a thickness range between 3.5 and 5.4 Å. Infra-red spectra were recorded using a Perkin Elmer Paragon 1000 FT-IR Spectrometer in attenuated total reflection mode. Thermogravimetric analysis (TGA) was performed using a Mettler Toledo Systems TGA/DSC 1 instrument under a constant flow of air. Differential scanning calorimetry (DSC) curves were also recorded. Data was recorded from room temperature up to 900 °C at a ramp rate of 10 °C/min. Elemental analysis was performed by Medac Ltd (UK). Micrographs and elemental maps were obtained using a Zeiss Gemini or a Zeiss SUPRA 55-VP scanning electron microscope. Material acidity was measured via ammonia temperature programmed desorption (TPD). Here, 50 mg of catalyst was loaded into a reactor and calcined in an oxygen containing atmosphere (this calcination step was not included when measuring the acidity of MOFs). After cooling, ammonia was adsorbed onto the catalyst at 100 °C. The ammonia was then desorbed from the catalysts by heating the material to 550 °C (or 350 °C in the case of MOFs) at a ramp rate of 5 °C/min or 3 °C/min. The amount of ammonia desorbed from the catalyst was measured using a mass spectrometer.

3.4 Stability Testing

Material (catalyst) stability was tested at elevated temperatures in various solvents. For this, material was loaded into a 20 mL teflon-lined autoclave or reaction vial containing solvent (i.e. water, DMSO, etc.). The autoclave / vial was sealed and heated at a set temperature for a predetermined amount of time. Following this,

the autoclave / vial was quenched and the material recovered via filtration or centrifuge. The material was then dried and analyzed via XRD.

3.5 Batch Reactions

Batch Reactions

In a typical reaction, catalyst was added to a 4 mL glass vial. A magnetic stirrer bar was added to the vial along with 3 mL of stock solution consisting of D-(+)-Glucose (Sigma Aldrich) or D-(-)-Fructose (Sigma Aldrich) dissolved in a chosen solvent (i.e. water, DMSO, HCl). The concentration of the sugar solution was typically 100 mg/mL. The vial was crimp sealed and placed into a preheated oil bath for a predetermined amount of time. Following the reaction time, the vial was removed from the oil bath and quenched at 0 °C to stop the reaction.

Recycle Reactions

Recycle reactions were conducted using a 25 mL reactor obtained from Berghof (Berghof, BR-25). In a typical reaction, a chosen catalyst and a magnetic stirring bar were placed into the reactor's teflon vessel. 15 mL of solution consisting of 10 wt.% glucose was then added to the teflon vessel. The teflon vessel was then placed into the reactor. The reactor was sealed and pressurized to 10 bar using an inert gas (i.e. helium) and placed into a preheated aluminum block. This block was heated using an IKA heating/stirring plate. After a predetermined amount of time the reactor was removed from the heating block and quenched at 0 °C to stop the reaction. The reactor was then depressurized and opened. The reactor content was then centrifuged in order to separate solid and liquid components. A sample of the liquid component was drawn from the centrifuge tube using a clean needle and syringe. Excess solution was then removed from the catalyst. The catalyst was then washed and recovered again using a centrifuge. The recovered catalyst was added back into the 25 mL reactor along with fresh stock solution. The reaction was then repeated under the same conditions in order to test the recyclability of the catalyst. This process was repeated until up to 4 reaction cycles were completed.

3.6 Flow Reactor

The activity of catalysts under continuous flow was explored using a purpose built reactor unit. As seen in **Figure 3.2** (and **Appendix A**), this unit consisted of a Shimadzu High Performance Liquid Chromatography (HPLC) pump (Shimadzu LC-20AT) feeding a tubular reactor. The reactor itself was comprised of a 15.5 cm stainless steel tube (4.1 mm inner diameter) contained within a brass-heating block. This block was heated by four cartridge heaters (400 W) that enabled a maximum temperature of >500 °C to be reached. The reactor temperature was monitored using a thermocouple attached to the outer wall of the reactor tube. Temperature was controlled via a Eurotherm controller (Eurotherm 3216) whilst a second Eurotherm controller acted as a high temperature watchdog. Both the reactor and the heating block were contained within a stainless steel case fitted with a safety interlock (Allen Bradley Guard meter). The unit was also fitted with five mass flow controllers (Bronkhorst EL-Flow Select) and a gas manifold consisting of manual valves (Swagelok). These controllers and valves provided the option to introduce high or low-pressure gas (air, nitrogen, or hydrogen) into the reactor feed. Downstream of the reactor tube a peltier module (RS) was used to cool liquid exiting the reactor. Pressure within the system was controlled by a manual backpressure/needle valve (Swagelok) located downstream of this peltier module. Sampling of the reaction mixture was achieved using a 10-port Vici valve (Vici EUHA) that fed directly into 10 sample vials. These vials were housed in an aluminium block cooled by another peltier module.

Prior to each reaction, the reactor tubing was firmly packed with a mixture of catalyst and inert material. Typically, the reactor tubing was first packed with 1 cm of glass wool. Next 3 cm of glass beads (200 – 300 nm) were loaded into the reactor. These beads helped to precondition the feedstock flow. A mixture of catalyst (250 nm) and silicon carbide (250 nm) was then added to the reactor tubing. The height of this mixture was 8 cm and contained either 40 mg or 80 mg of catalyst. The remainder of the reactor volume was filled with glass beads (200 – 300 nm). The top of the reactor was capped with a stainless steel frit (2 nm) to prevent material loss during reaction.

The voidage within the catalyst bed and hence the space-time (residence time) of a packed bed reactor may be calculated using **Equation 1**.

$$\epsilon = 1 - \frac{m}{p_p A H} \quad (1)$$

Where:

A is cross sectional area of catalyst bed

H is bed height

m is particle mass

p_p is particle density

Considering the above equation, the retention time through a packed bed consisting of mostly silicon carbide may be calculated as approximately 2 min for a flow rate of 0.14 mL/min. Moreover, a 10 wt. % feedstock flowing at 0.14 mL/min through a reactor bed containing 40 mg catalyst would result in a Weight Hourly Space Velocity (WHSV) of 21 h⁻¹. Increasing flow to 0.28 mL/min would therefore result in a retention time of 1 min or a WHSV of 42 h⁻¹.

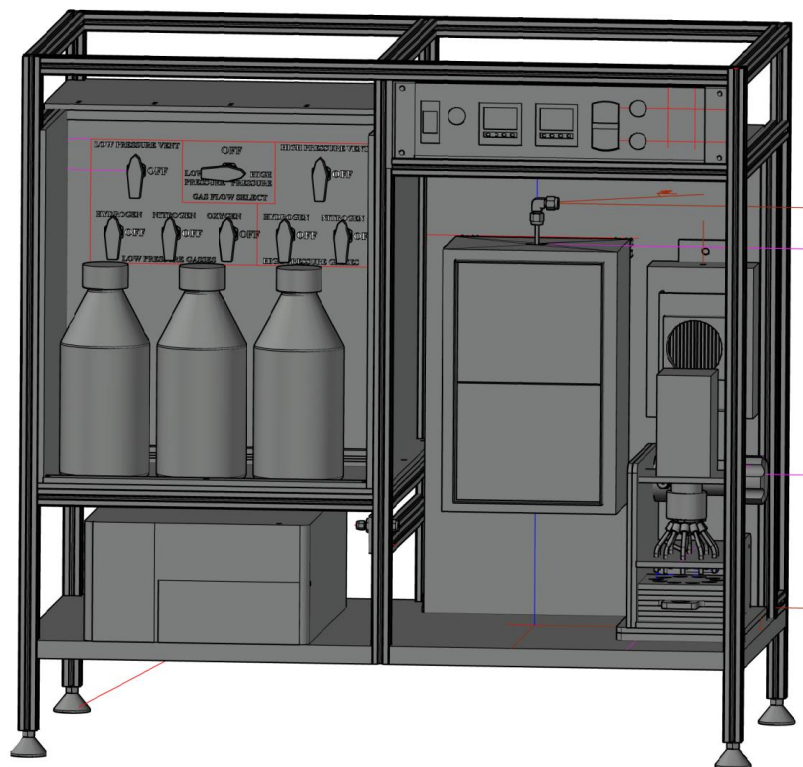


Figure 3.2. Flow reactor unit specifically designed, built, and utilized for the purpose of this project.

3.7 Reactions Analysis

High Performance Liquid Chromatography

For analysis, reaction samples were filtered into 2 mL glass vials using hydrophobic PTFE syringe filters. The 2 mL vials were sealed and placed into a Shumdzu High Performance Liquid Chromatography unit (HPLC) fitted with a Bio-RAD HPX-87P (or Bio-RAD HPX-87H) column. Sugars were quantified using an Evaporative Light Scattering Detector (ELSD) while HMF was quantified using a Photo Diode Array (PDA) detector. The mobile phase used was HPLC grade water (or 0.05 M sulfuric acid when using the Bio-RAD HPX-87H column). The mobile phase flow rate was set at 0.6 mL/min. The temperatures of the HPLC column oven, ELSD detector, and PDA cell were 50 °C, 65 °C and 40 °C respectively. Feedstock conversion, reaction selectivity and product yields were calculated using the following equations (**Equation 2 – 4**):

$$Conversion = \left(\frac{Mol_{H_0} - Mol_{H_1}}{Mol_{H_0}} \right) * 100 \quad (2)$$

$$Selectivity_A = \left(\frac{Mol_A}{Mol_{H_0} - Mol_{H_1}} \right) * 100 \quad (3)$$

$$Yield_A = \left(\frac{Conversion \times Selectivity}{100} \right) \quad (4)$$

Where:

Conversion is defined as the conversion of the hexose feedstock.

$Selectivity_A$ is defined as the reaction Selectivity towards product “A”

$Yield_A$ is defined as the Yield of product “A” at time T = 1

Mol_{H_0} is defined as the initial moles of hexose feedstock at time T = 0

Mol_{H_1} is defined as the moles of hexose feedstock at time T = 1

Mol_A is defined as the moles of product A at time T = 1

3.8 Extended X-ray Absorption Fine Structure (EXAFS) and X-ray Absorption Near Edge Structure (XANES) analysis

Extended X-Ray Absorption Fine Structure (EXAFS) and X-ray Absorption Near Edge Structure (XANES) analysis of synthesised materials were conducted at the European Synchrotron Radiation Facility (ESRF). This is an internationally funded facility located in Grenoble, France. All experiments conducted at the ESRF were performed within the UK's mid-range facility known as XMaS. This beamline has the capacity to perform experiments / analysis within an energy range of 2.4 keV to 15 keV. Experiments performed at the ESRF included; analysis of solid catalysts during reduction processes and in-situ analysis of catalysts during reactions.

Analysis Of Solid Materials During Reduction

To facilitate EXAFS and XANES analysis of catalysts during reduction processes, a purpose built sample cell was used (**Figure 3.3.**). This cell was equipped with four heating cartridges that enabled sample heating to a maximum temperature of 600 °C. The cell was also equipped with a gas inlet and exhaust. This enabled various gases to be passed through the sample during analysis. A manifold housing several Bronkhorst mass flow controllers was used to regulate gas flow to the sample cell. Sample heating and gas flow were controlled remotely during analysis.

In a typical procedure, material was loaded into the sample cell and pelletized using a purpose built press. The sample cell was then fitted with graphite windows before being loaded into the beamline chamber. Gas supplies were then connected to the cell as well as the power source of the four heating cartridges. The sample was then heated to a temperature of 400 °C for a period of 30 min before being allowed to cool. This ensured that the material was fully oxidised before the reduction sequence was initiated. After cooling, the first EXAFS / XANES analysis was performed. Upon completion of this first analysis, a hydrogen / helium mixture was passed through the sample at a flow rate of 10 mL/min. After 10 min another EXAFS / XANES analysis was performed on the sample. Following this, the cell was heated incrementally to a number of predetermined set points. At each set point, there was a temperature dwell of 10 min, following

which the sample was reanalysis before heating resumed. The set points used, and hence the temperatures at which EXAFS / XANES analysis were performed are as follows; 100 °C, 200 °C, 250 °C, 300 °C, 350 °C, 400 °C. After analysis at 400 °C the sample was allowed to cool once again to room temperature, at which point a final EXAFS / XANES analysis was performed.



Figure 3.3. Solid sample holder used for analysis at the ESRF.

In-situ Analysis Of Catalysts

XANES analysis was used to monitor the behaviour of catalysts during the aqueous isomerisation of glucose. To facilitate such experiments, a specialised sample cell was design and developed. The sample cell consisted of a circular area in which the stock solution and catalyst was contained. This area was sealed using kapton film. The cell was heated by four heating cartages installed within the sample cell holder. Heating of these cartages, and hence heating of the sample cell, was controlled by a eurotherm controller that could be programmed remotely. To ensure a homogeneous mixture was maintained during a reaction, the sample cell was continuous rotated. A motor located at the top of the sample probe provided this rotation. Throttling the electrical voltage to the motor controlled the rpm of the sample cell. An image of the sample holder described here is show in **Figure 3.4**.

In a typical procedure XANES analysis was first preformed on a chosen catalyst in deionised water (blank reaction). For this a catalyst and deionised water were loaded into the sample cell. The cell was then sealed using kapton film before being loaded into the XMAS beamline chamber. The cell was then continually rotated whilst heating to a set point of 140 °C (using a ramp rate of 1 °C/min). During this initial ramp sequence, XANES data was continually collected from the catalyst. XANES analysis was then preformed as the aqueous catalyst mixture dwelled at 140 °C. The cell was allowed to cool to room temperature before a final XANES analysis was conducted.

Following the “blank reaction”, XANES analysis of the catalyst was preformed in the presence of glucose. This enabled the behaviour of the catalyst to be studied during the isomerisation of glucose. To achieve this, 22 mg of catalyst, 22 mg of glucose, and deionised water were loaded into the sample cell. After sealing the sample cell with kapton film, the sample probe was loaded into the XMaS beamline chamber. XANES analysis of the sample at room temperature was then preformed as the sample cell rotated. Following this, XANES analysis was preformed as the sample was heated to 140 °C at a ramp rate of 1 °C/minute. XANES analysis was then again preformed as the catalyst dwelled at 140 °C. The

sample was allowed to cool to room temperature before a final XANES analysis was performed.



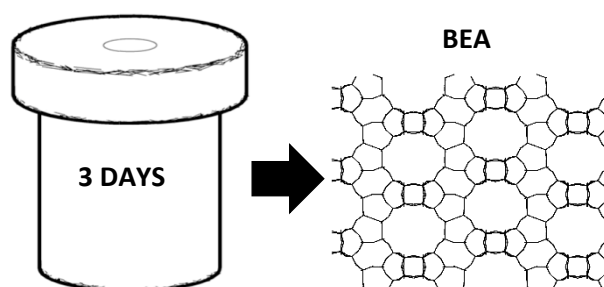
Figure 3.4. Liquid sample holder used in experiments at the ESRF.

Chapter 4

A Three-Day Crystallization of Metal-Containing Beta Zeolites and their Performances as Biomass Valorisation Catalysts.

Summary

In this chapter a rapid synthesis method is used to produce metal-containing beta zeolites. This method effectively reduces the synthesis times of metal-containing beta zeolites from 40 days to 3 days. Tin (Sn), gallium (Ga), zirconium (Zr), zinc (Zn) and ytterbium (Yb) were successfully introduced into the beta zeolite framework. Meanwhile, strontium (Sr) was not successfully introduced into the framework of beta zeolite. The acidity of each material synthesised in this study was quantified and their effectiveness as glucose isomerisation catalysts tested in batch reactions. (2)Sn-Beta was found to be the most effective glucose isomerisation catalyst tested in this study. (2)Sn-Beta was able to generate a glucose conversion of 64.2 % and a desirable product selectivity of 70.7 % (fructose, mannose, and HMF). The presence of 0.1 M HCl was found to significantly reduce the catalytic performance of the metal-containing beta zeolites. The activity of (2)Sn-Beta was also examined in a purpose built continuous flow reactor. The activity of this catalyst quickly declined in the flow reactor and subsequent calcination was found to partially damage the zeolite framework. However, following 8 h time on stream and subsequent calcination, the zeolite appeared to retain some of its Lewis acidic Sn sites.



Graphical Abstract: Rapid synthesis towards beta (*BEA) zeolites. (CIF.⁶⁸)

4.1 Introduction

Metal-containing beta zeolites have generated considerable interest within the catalytic community in recent years. This is largely due to the exceptional catalytic activity of tetrahedrally coordinated metal sites within the zeolite framework. For example, Sn containing beta zeolites (Sn-Beta) have shown remarkable promise as reduction and isomerisation catalysts.^{53,69,71,151} As a glucose isomerisation catalyst, the performance of Sn-Beta in water is almost comparable to the enzyme technology currently used in industry.⁵³ As such, Sn-Beta is now widely considered as a benchmark catalytic material within the field of glucose isomerisation. The development of such catalysts, which avoid the many drawbacks associated with biological (enzyme catalysed) processes, is an important step towards the economical production of value added chemicals from biomass feedstocks.

Despite the excellent performance of Sn-Beta as an isomerisation catalyst, its implementation in industry is yet to be fully realised. This may be due – in part – to the lengthy synthesis times associated with catalyst production. Typically, the synthesis of Sn-Beta requires exceptionally long crystallisation times of up to 40 days.^{53,79} To address this issue, numerous research groups have focused on developing alternative routes towards the synthesis of Sn-Beta.^{70,81,84–87,152–155}

The issue of synthesis time may be addressed using a “rapid synthesis” technique. This technique was first described by Chang, *et al.* and enables the synthesis of Sn-Beta within 2 days.⁸¹ This is a dramatic reduction in time when compared to the 40 days typically required in the “traditional” synthesis of the material. Moreover, the resulting Sn-Beta is shown to be a highly active glucose isomerisation catalyst in water.⁸¹ Inspired by this work, we hereby explore the introduction of Sn and various other metals within the framework of beta zeolite using the “rapid synthesis” technique. Here, we chose to elongate the crystallisation time to 3 days and utilise a commercial beta zeolite as the seed material. The alternative metals considered are: zirconium (Zr), gallium (Ga), ytterbium (Yb), zinc (Zn) and strontium (Sr). The catalytic activities of these metal-containing zeolites are tested in the isomerisation and dehydration of hexoses in batch reactions. The solvents considered are water and 0.1 M HCl. Finally, the activity of Sn-Beta is tested in a continuous flow reactor.

4.2 Results and Discussion

Catalyst Characterization

The successful synthesis of beta zeolites was confirmed by X-ray Diffraction (XRD) analysis (**Figure 4.1**). The sharp peaks within each diffraction pattern alludes to the formation of highly crystalline structures. This high degree of crystallinity appears regardless of the metal ion introduced into the zeolite framework. Furthermore, the diffraction patterns indicate that the synthesised materials are significantly more crystalline than the commercial beta zeolite.

The successful introduction of metal ions within the beta framework may be largely influenced by the metal precursor used during synthesis. For example, the use of tin chloride or trichloromethyl tin enables the formation of tetrahedrally coordinated Sn sites within the zeolite framework whereas the use of tin oxide (SnO₂) does not.^{26,77,80} This is likely due to the stability of SnO₂ inhibiting the addition of Sn into the zeolite framework.^{26,80} In such instances, the unreacted SnO₂ will accumulate on the surface (or within the pores) of the siliceous beta zeolite.^{26,80} The unsuccessful introduction of Sn within the zeolite may be identified by additional Bragg peaks within the material's diffraction pattern. These additional peaks are the result of unreacted SnO₂ clusters.⁷⁸

As seen in **Figure 4.1**, the diffraction pattern of (2)Sr-Beta contains an additional Bragg peak ($2\theta = 26.6$). This suggests that Sr may not have been successfully incorporated into the zeolite framework and strontium oxide (SrO) might have accumulated within the materials pore network. The unsuccessful addition of Sr within the zeolite framework is likely due to the size and charge of the metal atom. Specifically, the large atom size of Sr and its charge of only 2+ may prevent the formation of stable tetrahedrally coordinated bonds within the zeolite structure.

The diffraction patterns of Sn, Zr, Zn, Ga and Yb materials compare well with the commercial zeolite (**Figure 4.1**). This suggests that these metals were successfully introduced into the zeolite framework as tetrahedrally coordinated single atom sites. Although, it is worth noting that (2)Yb-Beta does contain a single very small additional Bragg peak (around $2\theta = 34.3$) that is not found in the other materials.

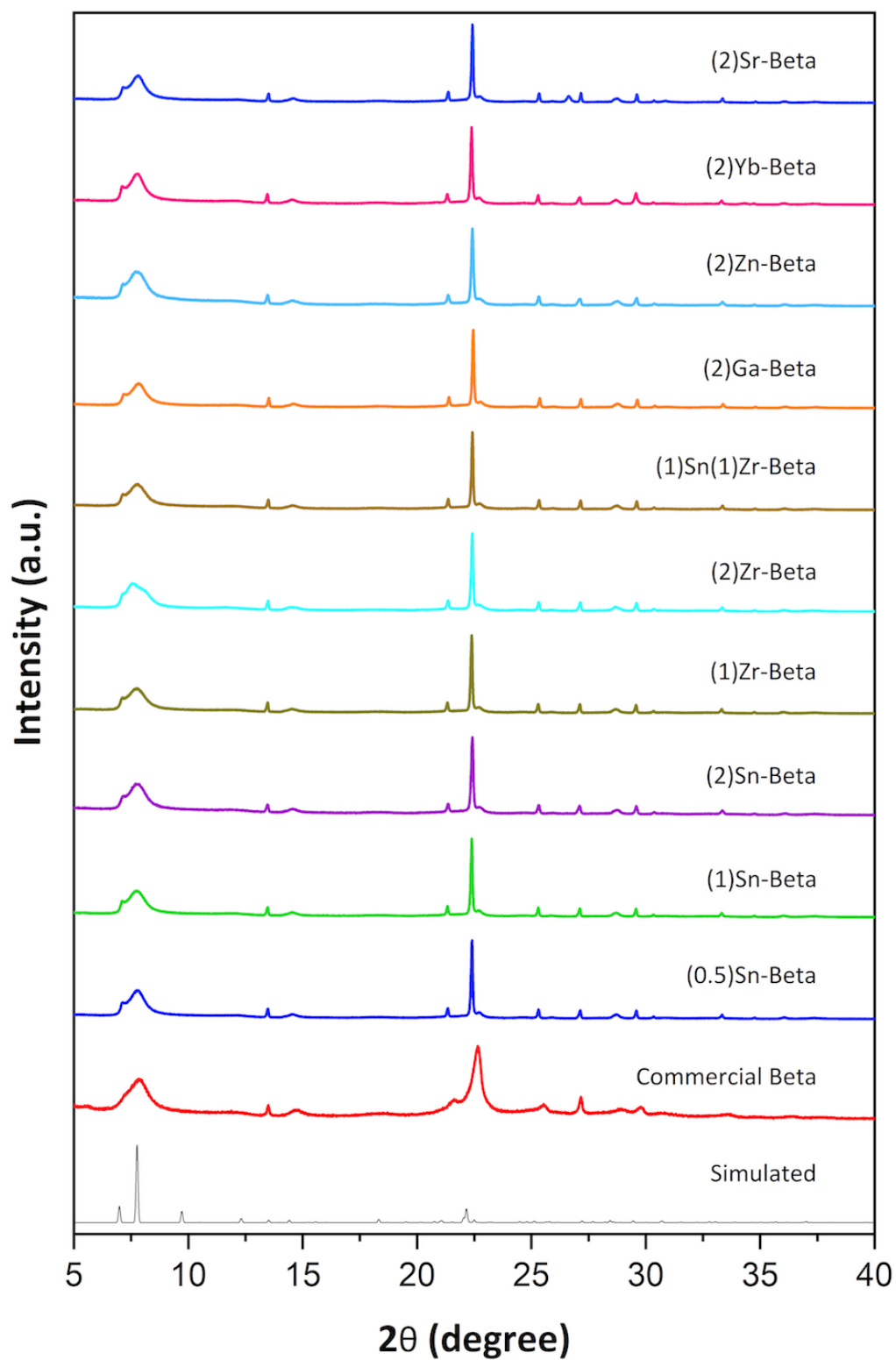


Figure 4.1: XRD patterns of synthesised metal-containing beta zeolites, commercial beta zeolite (CP814C), and simulated pattern⁶⁸.

Nitrogen adsorption analysis was used to quantify the surface areas and pore volumes of the beta zeolites synthesised in this study. The isotherms of beta zeolites containing 2 % metal (Sn, Zr, Zn, Ga, Yb and Sr) are shown in **Figure 4.2**. Consistent with literature the isotherms may be classified as type I.^{81,88,156} This indicates that the synthesised beta zeolites are microporous in nature. Interestingly, the isotherm generated by (2)Sn-Beta appears to have a wider hysteresis loop. This would indicate that the Sn containing materials have a higher mesoporous volume.

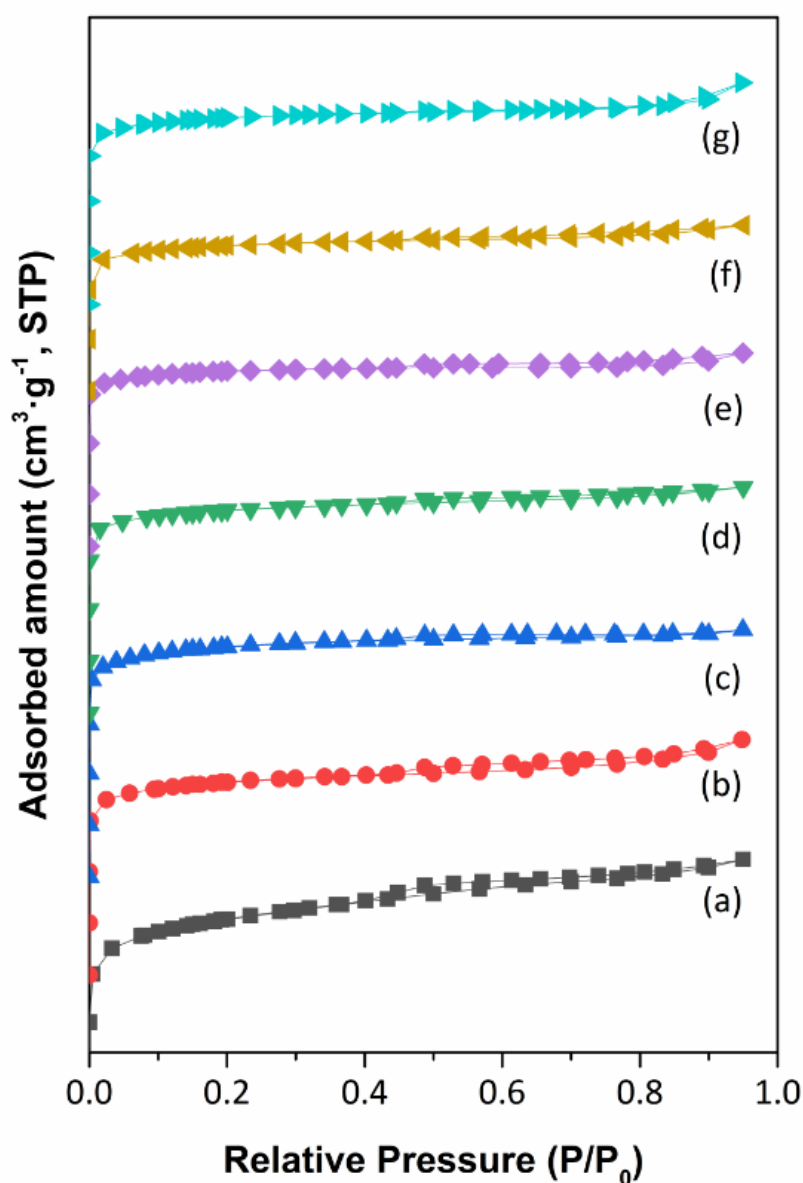


Figure 4.2. Nitrogen adsorption hysteresis loops of synthesised beta zeolites containing 2 % metal **(a)** Commercial Beta **(b)** (2)Sn-Beta **(c)** (2)Zr-Beta **(d)** (2)Ga-Beta **(e)** (2)Zn-Beta **(f)** (2)Yb-Beta **(g)** (2)Sr-Beta.

As shown in **Table 4.1**, increasing the quantity of Sn within the structure of the zeolite resulted in a decrease in BET surface area and micropore volume. This may suggest that not all of the Sn introduced into the zeolites has been successful incorporated into the framework and may reside within the materials pore network as SnO₂ nanoparticles. Furthermore, as suggested by the adsorption isotherms, the Sn containing materials encompass the greatest mesopore volume. (2)Zr-Beta, (2)Ga-Beta and (2)Yb-Beta have a greater surface area than (2)Sn-Beta. This may indicate that pore obstruction by extra-framework metal oxides is less prevalent in these materials. In contrast, the surface area of (2)Sr-Beta is the lowest measured. This suggests that (2)Sr-Beta contains the greatest quantity of extra-framework species. Indeed, this is consistent with the materials diffraction pattern, which clearly indicates the presence of additional peaks; likely caused by the presence of extra-framework Sr(OH)₂.

Table 4.1. BET surface areas and pore volumes of the beta zeolite catalysts.

Catalyst	BET Surface Area (m ² ·g ⁻¹)	Micropore Volume (cm ³ ·g ⁻¹)	Mesopore Volume (cm ³ ·g ⁻¹)
Commercial Beta	640	0.21	0.06
(0.5)Sn-Beta	545	0.20	0.03
(1)Sn-Beta	525	0.19	0.02
(2)Sn-Beta	507	0.18	0.03
(1)Zr-Beta	722	0.26	0.02
(2)Zr-Beta	585	0.22	0.02
(1)Sn(1)Zr-Beta	680	0.24	0.03
(2)Ga-Beta	529	0.20	0.02
(2)Zn-Beta	471	0.18	0.01
(2)Yb-Beta	518	0.20	0.02
(2)Sr-Beta	495	0.19	0.02

Scanning electron microscope (SEM) imaging was used to further observe the size and morphology of the synthesised beta zeolites. As seen in **Figure 4.3**, the commercial material consists of apparently spherical particles formed of highly inter-grown crystals. These crystals appear to be irregular and globular in nature. The overall size of the commercial beta zeolite particles is around 800- 1000 nm.

In comparison to the commercial zeolite, the Sn and Zr materials synthesised in this study appear to be highly cubic / square bipyramidal in nature. Meanwhile the Zn, Ga, and Sr zeolites may be described as square bipyramidal. In either case the rapid synthesis technique is shown to yield particles that are highly regular in shape. This is interesting considering the shape and roughness of the commercial zeolite used to seed the growth of these materials.

Like the commercial material, the synthesised beta zeolites are formed of highly inter-growing crystals. However, the synthesised materials are larger than the commercial zeolite. Specifically, all of the synthesised beta zeolites exhibit a particle size typically greater than 1000 nm. Surface defects are apparent on a number of the synthesised zeolites. With regards to (XX)Sn-Beta, the severity of these defects appears to increase with increasing amounts of Sn. Consistent with literature, this suggests that increasing the quantity of Sn inhibits the crystallization and morphology of the zeolite.⁸⁰

In comparison to published literature, the zeolites synthesised in this body of work appear to display a more consistent shape and morphology. For instance, the materials presented here are more regular in shape than those produced by Chang, *et al.* (who developed the rapid synthesis technique to produce Sn-Beta).⁸¹ This difference in shape/morphology is likely due to two contributing factors. Firstly, different seed materials were used. Here the commercial beta zeolite used for seeding contains Al whereas the seeding material used by Chang, *et al.* were dealuminated. Secondly, the crystallisation time employed here was 3 days whilst Chang, *et al.* used a 2 day (52 h or less) technique. Moreover, these two contributing factors appear to influence the morphology of materials produced during synthesis. Furthermore, the materials presented herein also appear to have a more consistent shape and morphology than some materials produced using a 40-day synthesis.⁷⁹

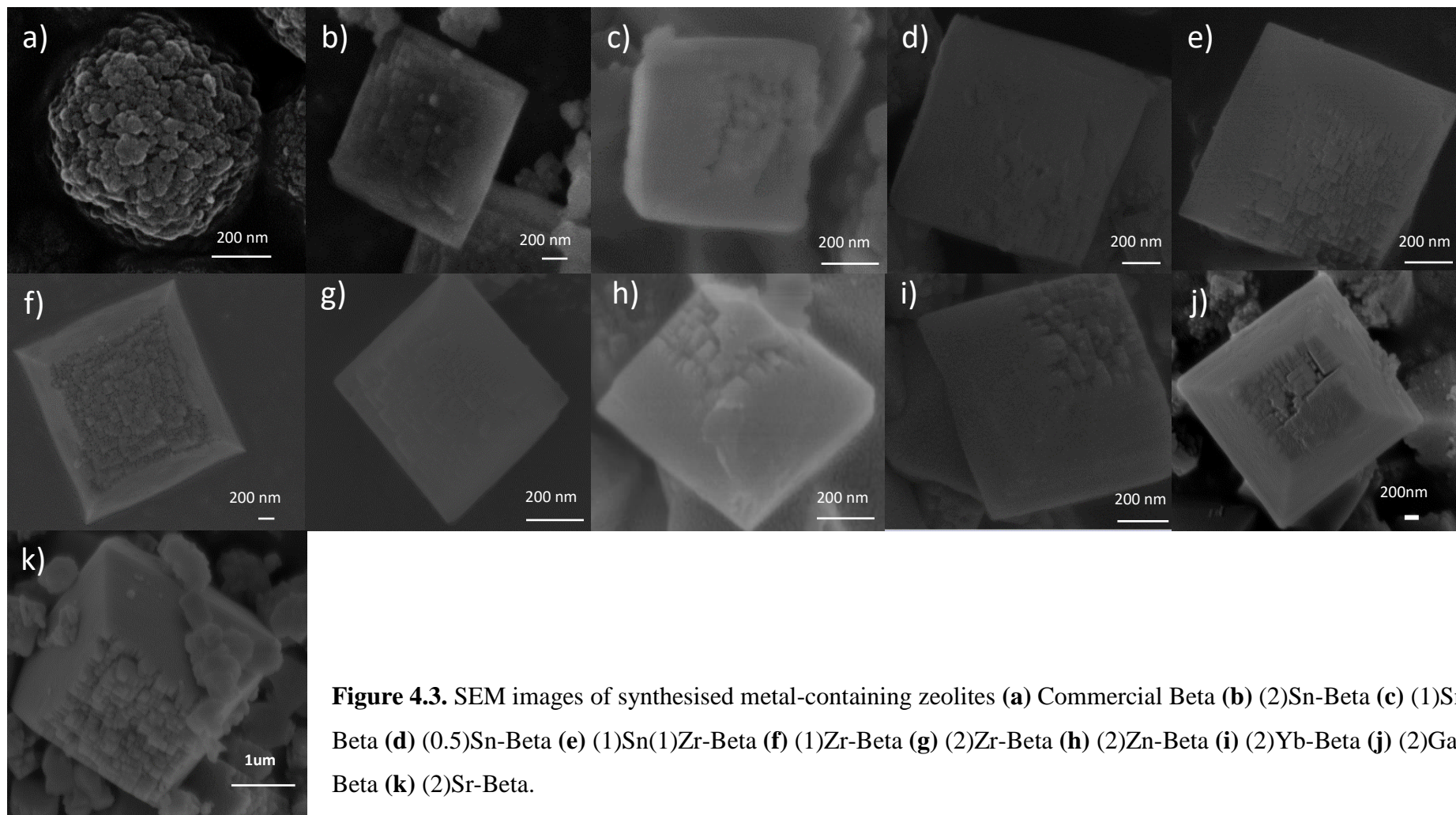


Figure 4.3. SEM images of synthesised metal-containing zeolites **(a)** Commercial Beta **(b)** (2)Sn-Beta **(c)** (1)Sn-Beta **(d)** (0.5)Sn-Beta **(e)** (1)Sn(1)Zr-Beta **(f)** (1)Zr-Beta **(g)** (2)Zr-Beta **(h)** (2)Zn-Beta **(i)** (2)Yb-Beta **(j)** (2)Ga-Beta **(k)** (2)Sr-Beta.

The successful incorporation of various metals within the framework of beta zeolite was assessed using UV-Vis DRS. As seen in **Figure 4.4**, the UV-Vis spectra obtained from (0.5)Sn-Beta contains three distinct peaks. Of these, the peak found at around 210 nm indicates the presence of tetrahedral (Lewis acidic) Sn sites within the zeolite framework.^{26,86} Meanwhile the peak at 285 nm indicates the presence of extra-framework (basic) SnO₂ within the materials pore network.²⁶ In comparison, the peak at around 210 nm is larger than that observed at 285 nm. This may indicate that the material contains considerably more Lewis acid Sn sites than basic SnO_x sites.

The UV-Vis spectrum of (1)Sn-Beta and (2)Sn-Beta also reveals the presence of peaks at around ~200 nm and ~270 nm. Again these peaks indicate the presence of tetrahedral (Lewis acid) and extra-framework (basic) Sn sites. Furthermore, the peak intensities suggest that these materials contain more Lewis acidic Sn sites than basic SnO₂. Overall, based on relative peak intensities, the ratio between Lewis acidic and basic Sn sites is greatest within (2)Sn-Beta. This may indicate that higher quantities of Sn within the synthesis mixture may promote the formation of tetrahedral metal sites. Indeed higher quantities of Sn within the synthesis mixture have been shown to slow crystallization times.⁸⁰ Perhaps this slower crystallization is key when attempting to increase the number of tetrahedral Sn sites within the zeolite framework.

The UV-Vis spectrums obtained from (1)Zr-Beta and (2)Zr-Beta are similar in shape. Deconvoluting these spectra reveals the presence of peaks at around 200 nm and 250 nm. Here the peak at ~200 nm indicates the presence of tetrahedrally coordinated Zr sites within the materials framework.^{88,157-159} The peak at ~250 nm indicates the presence of bulk ZrO₂ and ZrO₂ nano particles within the materials pore network.^{157,159} As seen in **Figure 4.4**, the relative peak intensities may suggest that (2)Zr-Beta contains a higher ratio of tetrahedrally coordinated Zr sites.

Two separate peaks can be clearly identified within the UV-Vis spectrum of (2)Zn-Beta. These peaks occur at around 200 nm and 235 nm. Here, the peak at 200 nm is indicative of framework Zn whilst the broader peak at 235 nm likely indicates the presence of extra-framework Zn within the materials pore network.¹⁶⁰

The UV-Vis spectrum of (2)Ga-Beta contains two distinct peaks. These occur at around 225 nm and 278 nm. As a comparison, UV-Vis data was also collected from Gallium Oxide (Ga_2O_3). The bulk oxide spectrum contains peaks at 207 nm, 243 nm and 256 nm. Hence, the differences observed here may indicate the successful introduction of Ga into the zeolite framework. However, there is likely some bulk metal oxides contained within the material. Solid state NMR may be useful here to distinguish between framework and extra-framework Ga sites within the synthesised material. The UV-Vis spectrum obtained from (2)Sr-Beta is extremely broad and dissimilar to the spectrum obtained from SrO.

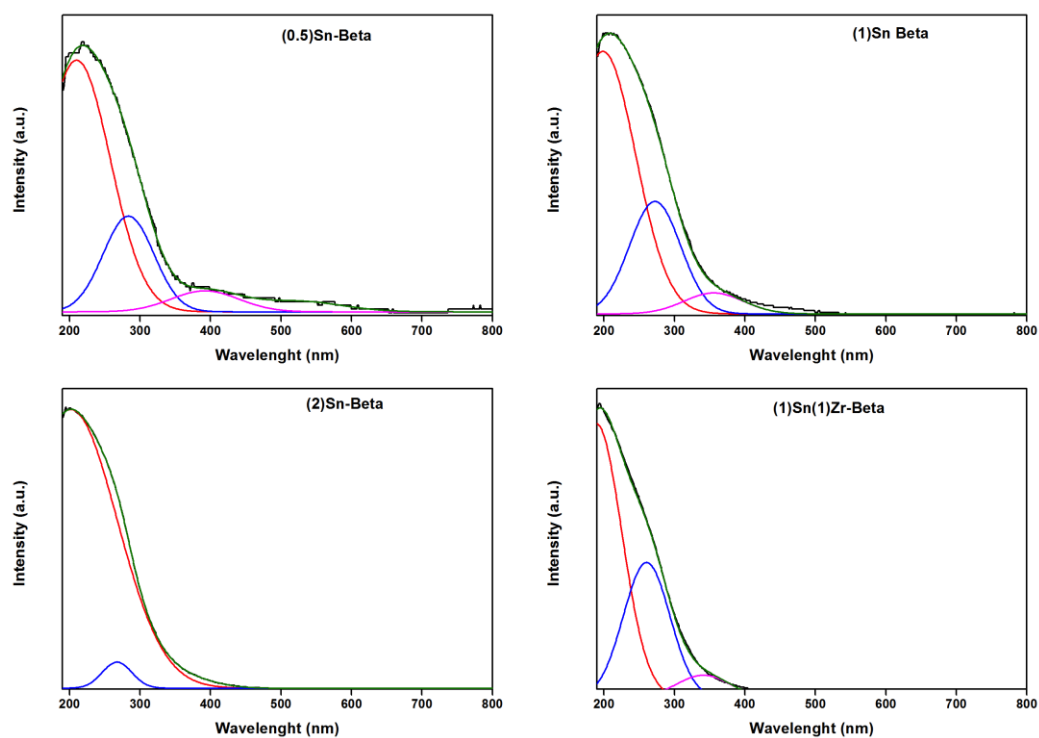


Figure 4.4. UV-Vis DRF analysis of metal-containing beta zeolites synthesised in this study along side chosen metal oxides for comparison.

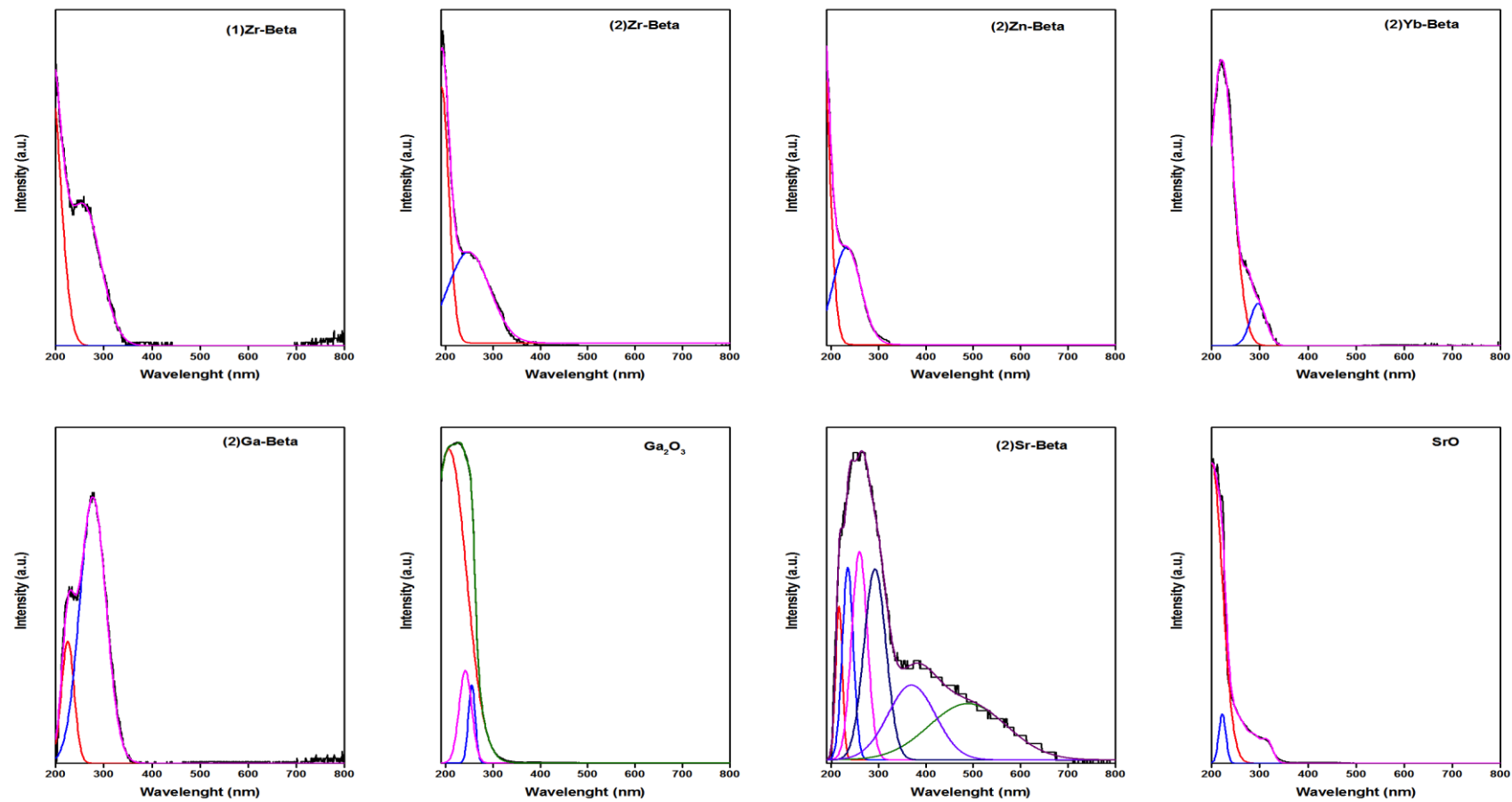


Figure 4.4 (Continued). UV-Vis DRF analysis of metal-containing beta zeolites synthesised in this study along side chosen metal oxides for comparison.

Inductively coupled plasma (ICP) analysis was used to quantify the successful introduction of metal species into the beta zeolites. As shown in **Table 4.2**, the quantity of Sn contained within (0.5)Sn-Beta is 0.44 wt.%. This is extremely close to the target amount of 0.5 wt.%. The actual amount of Sn contained within (1)Sn-Beta and (2)Sn-Beta was also close to target amounts. Specifically, the quantity of Sn contained within each of these materials was at least 80 % of target values.

The metal content of Zr, Ga and Yb containing materials is around 50 - 60 % of target values. This may suggest that Sn has a greater affinity towards the beta framework than these alternative metals. Indeed, the Sn content of (1)Sn(1)Zr-Beta is significantly higher than the materials Zr content. The Zn content of (2)Zn-Beta is 1.44 wt.%. This may infer that Zn has a greater affinity towards the beta framework than Zr or Ga, but is less readily introduced than Sn.

The Sr content of (2)Sr-Beta is 2.22 wt.%. This is significantly higher than the metal content of other synthesized zeolites considered in this study. However, as suggested by XRD, BET, and UV-Vis analysis, the Sr content of (2)Sr-Beta does not appear to form part of the materials framework. Instead, it likely resides within the materials pore network as SrO.

Table 4.2. Metal content of beta zeolites.

Catalyst	Elemental Composition						
	Al (wt.%)	Sn (wt.%)	Zr (wt.%)	Ga (wt.%)	Zn (wt.%)	Yb (wt.%)	Sr (wt.%)
Commercial Beta							
(0.5)Sn-Beta		0.44					
(1)Sn-Beta		0.87					
(2)Sn-Beta		1.69					
(1)Sn(1)Zr-Beta		0.65	0.38				
(1)Zr-Beta			0.62				
(2)Zr-Beta			1.14				
(2)Ga-Beta				1.16			
(2)Zn-Beta					1.44		
(2)Yb-Beta						1.02	
(2)Sr-Beta							2.22

The acidity of metal-containing beta zeolites was quantified using ammonia temperature programmed desorption (TPD). For this a homemade apparatus was used. Here ammonia desorption was recorded using a mass spectrometer. The heating rate applied during desorption was 5 °C/min. To verify the accuracy of the apparatus, the acidity of a commercially obtained ZSM-5 (Si: Al ratio 25:1) material was measured and compared to literature.

As shown in **Figure 4.5**, the ammonia desorption pattern of ZSM-5 contains two distinct peaks. These can be attributed to the presence of strong and weak acid sites within the material. Specifically, the low temperature peak correlates to the presence of weak acid sites within the material whilst the high temperature peak can be attributed to the presence of strong acid sites. Quantification of acidity was achieved through peak integration (**Table 4.3**). The acidity of strong and weak acid sites within ZSM-5 was found as 0.245 mmol.g⁻¹ and 0.258 mmol.g⁻¹ respectively. The total acidity of the material was hence calculated as 0.503 mmol.g⁻¹. This correlates well with the total acidity of other ZSM-5 materials reported in literature.^{161,162}

The commercial beta zeolite (Si: Al ratio 12.5:1) has a higher acidity than ZSM-5. The distribution of acid sites within the commercial beta zeolite also differs to ZSM-5. Specifically, the commercial beta zeolite contains a higher proportion of weak acid sites whereas the distribution of acid sites (strong and weak) within ZSM-5 is more even. Overall, the total acidity of the commercial beta zeolite was calculated as 0.759 mmol.g⁻¹. This value corresponds well with those reported in literature for the same material.¹⁶³⁻¹⁶⁶

With regards to the synthesised materials, the acidity of (0.5)Sn-Beta is significantly lower than the acidity of either commercial zeolite tested. However, increasing the Sn content within the zeolite from 0.5 % to 2 % is shown to increase acidity (0.011 mmol.g⁻¹ to 0.041 mmol.g⁻¹). This increasing acidity likely suggests that Sn is successfully being introduced within the Beta framework as tetrahedrally coordinated Lewis acid sites. Moreover, increasing the amount of Sn used during synthesis increases the quantity of Lewis acid Sn sites within the final material. In each of the Sn containing materials there is an even quantity of strong and weak acid sites. This suggests that Sn sites within the material exhibit varying degrees

of acid strength. Indeed, both computational and experimental methods have shown that Sn may reside within the Beta framework as either fully coordinated or partially hydrolysed single atom sites.^{77,78} Of these two sites, the partially hydrolysed site (open site) is responsible for glucose isomerisation (and may exhibit a greater Lewis acid strength).^{77,78,167} Hence, the distribution of acid strength within (XX)Sn-Beta may suggest that an even distribution of fully coordinated and partly hydrolysed Sn sites exists within the materials. However, further studies are required in order to fully evaluate this.

The acidity of (1)Zr-Beta was calculated as 0.02 mmol.g⁻¹. This acidity is predominantly a result of strong acid sites. Increasing the Zr content to 2 % increases material acidity to 0.034 mmol.g⁻¹. Again, strong acid sites within the material are contributing heavily towards overall acidity here. Moreover, this suggests that Zr atoms within the framework of Beta zeolite almost exclusively exist as strong Lewis acid sites. This is in stark contrast to Sn, which as described previously, contributes even quantities of strong and weak acid sites when introduced into the zeolite framework.

The total acidity of the bimetallic material, (1)Sn(1)Zr-Beta, is not equal to the sum of (1)Sn-Beta and (1)Zr-Beta. This is expected as ICP analysis revealed that the bimetallic material contained only 0.65 % Sn and 0.38 % Zr. With regards to acid site distribution, strong Lewis acid sites within (1)Sn(1)Zr-Beta contribute heavily towards acidity. This is expected given the difference in acidity between Zr and Sn atoms previously described.

The total acidity of (2)Ga-Beta was calculated as 0.057 mmol.g⁻¹. This is the highest acidity of any synthesised zeolite considered in this study. Within (2)Ga-Beta, strong and weak acid sites contribute 0.041 mmol.g⁻¹ and 0.017 mmol.g⁻¹ respectively towards overall acidity. Thus, although strong acid sites generate the bulk of the materials acidity, there is a significant quantity of weak acid sites present within the material. This suggests that Ga sites exhibit varying degrees of acidity within the zeolite. Also, this result may suggest that Ga has successfully been incorporated into the zeolite framework as tetrahedrally coordinated Lewis acid sites – a result that could not be fully confirmed by UV-Vis due to the lack of data available in current literature for comparison.

The total acidity of (2)Yb-Beta was calculated as 0.003 mmol.g⁻¹. This is significantly lower than the acidity of Sn, Zr and Ga materials. As such, it can be inferred that Yb does not exhibit significant Lewis acidity when introduced into the framework of beta zeolite. Furthermore, these results may suggest that Yb sites have not been successfully introduced into the zeolite framework. The acidity of (2)Sr-Beta was also significantly low. This is unsurprising as the previous characterisation techniques suggest that Sr atoms do not enter the framework of beta zeolite. Instead, Sr ions likely reside as extra-framework sites within the material's pore network.

Table 4.3. Acidity of beta zeolites.

Entry	Catalyst	Weak Site Acidity mmol/g	Strong Site Acidity mmol/g	Total Acidity mmol/g
1	Commerical ZSM-5	0.245	0.258	0.503
2	Commerical Beta	0.441	0.318	0.759
3	(0.5)Sn-Beta	0.005	0.005	0.011
4	(1)Sn-Beta	0.011	0.009	0.019
5	(2)Sn-Beta	0.021	0.020	0.041
6	(1)Zr-Beta	0.005	0.016	0.020
7	(2)Zr-Beta	0.006	0.028	0.034
8	(1)Sn(1)Zr-Beta	0.008	0.021	0.030
9	(2)Ga-Beta	0.017	0.041	0.057
10	(2)Yb-Beta	0.001	0.002	0.003
11	(2)Sr-Beta	0.001	0.007	0.008

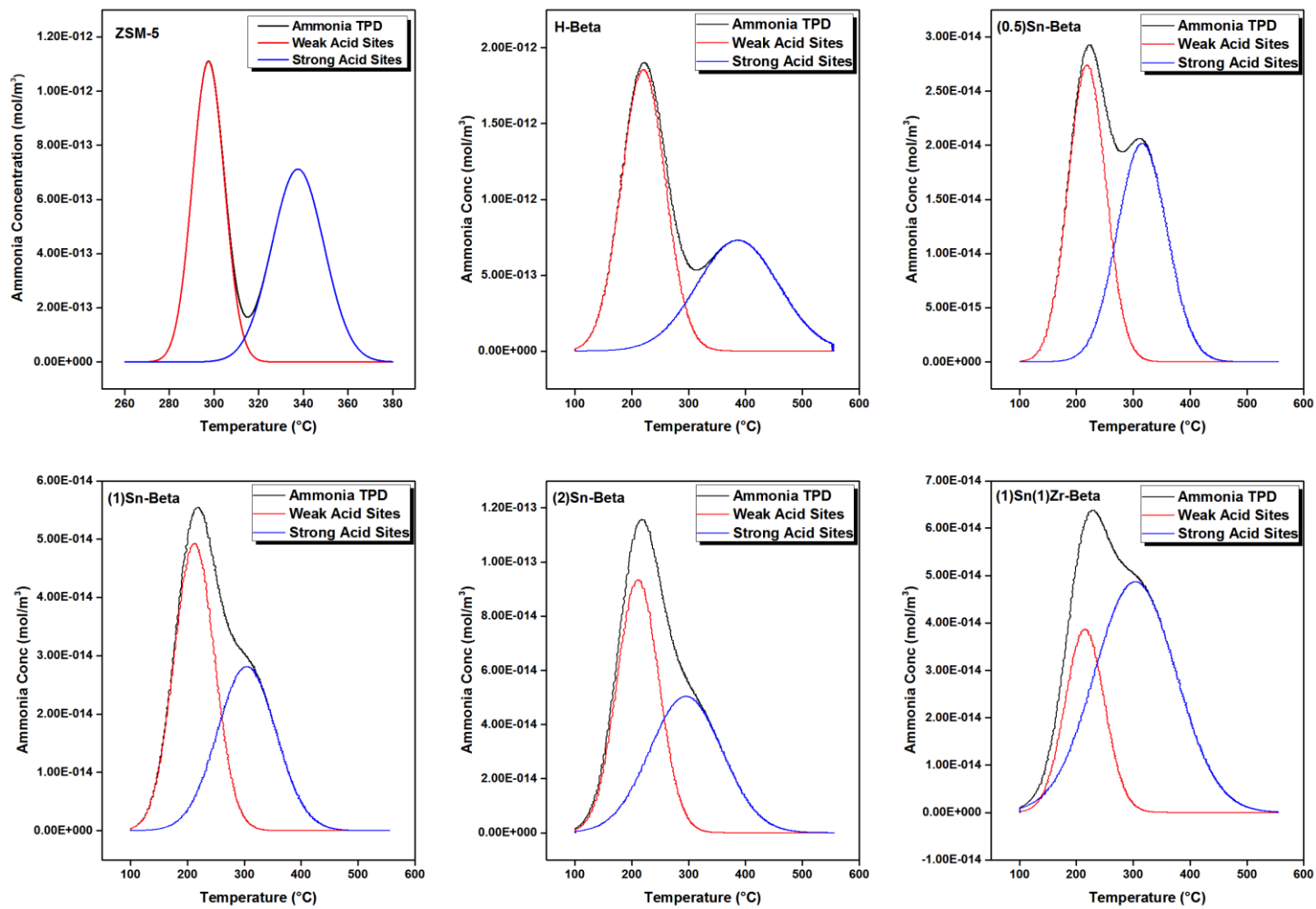


Figure 4.5. NH₃-TPD analysis of commercial and synthesised beta zeolites.

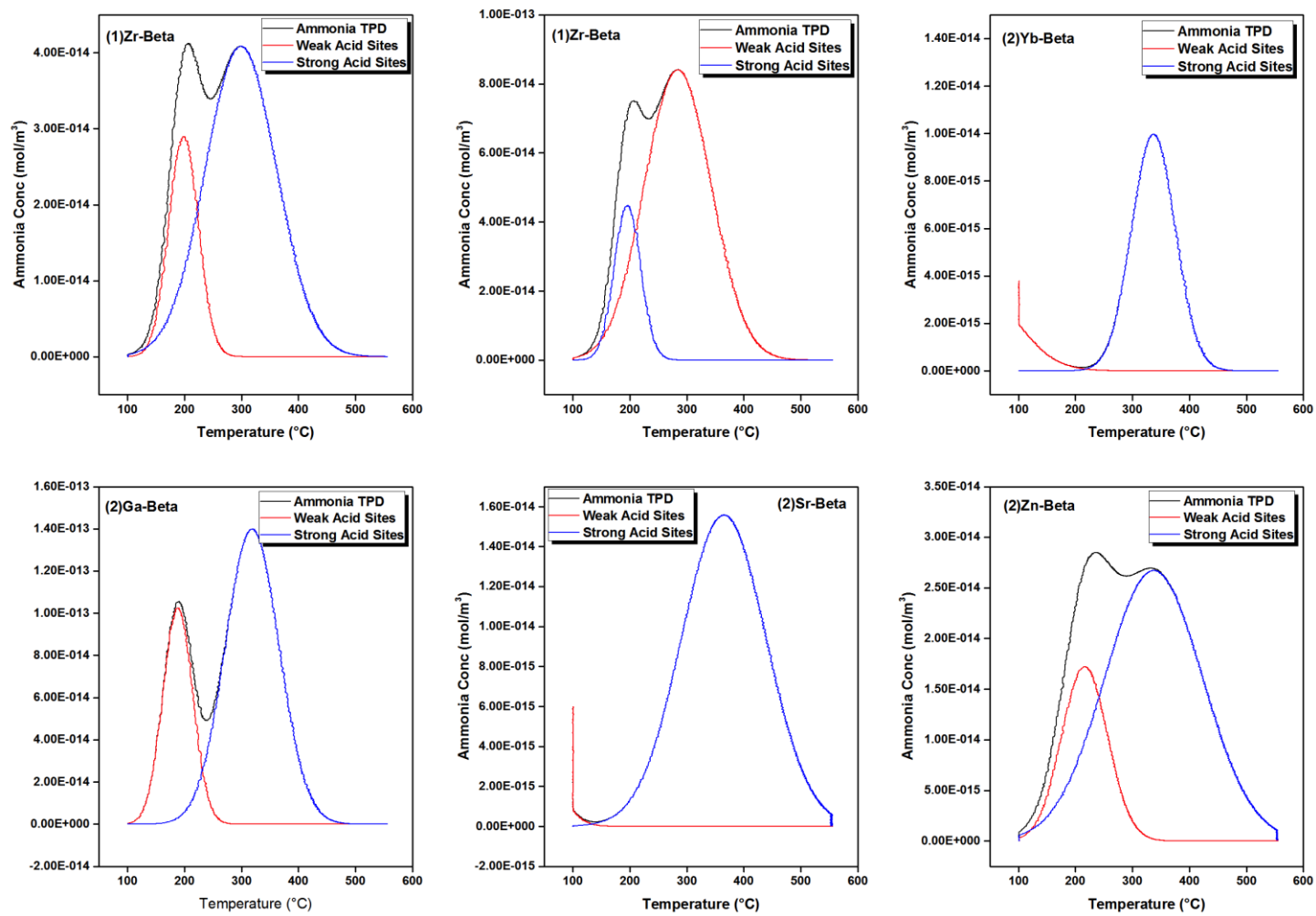


Figure 4.5 (Continued). NH₃-TPD analysis of commercial and synthesised beta zeolites.

Glucose Isomerisation and Dehydration towards HMF

As previously noted, Sn containing beta zeolites have been identified as exceptionally active glucose isomerisation catalysts in water. Therefore, the catalytic activities of materials synthesised in this study were first examined in aqueous solutions at moderated temperature. As a baseline for comparison, a blank reaction was also conducted under the same reaction conditions.

As seen in **Table 4.4**, the blank reaction generated a glucose conversion of around 5.7 % and a HMF yield of 2.5 %. Interestingly, trace amounts of fructose were also found in the post reaction solution. In comparison to the blank reaction, Sn containing beta zeolites generated considerably larger glucose conversions and product yields. Specifically, (2)Sn-Beta and (1)Sn-Beta generated glucose conversions of 64.2 % and 62.2 %, respectively. Each of these catalyst also generated a ~71 % selectivity towards desirable products (fructose, mannose and HMF). Within these product distributions, fructose was the dominant molecule. The comparable activities and product yields generated by (1)Sn-Beta and (2)Sn-Beta may suggest that the reaction is approaching equilibrium. The glucose conversion and total desirable product yield generated by (0.5)Sn-Beta is lower than that produced by other Sn beta zeolites. This is expected given the lower Sn content of (0.5)Sn-Beta. Moreover, the high activity of these materials provides further evidence that the rapid synthesis technique enables Sn to be successfully introduced into the zeolite framework as Lewis acid sites.

Each of the Sn containing materials also generated mannose in the reaction. Mannose itself has been reported in the literature as a product of Sn-Beta catalysed reactions.^{53,71} As shown in **Figure 4.6**, Sn-Beta may catalyse mannose production via fructose.⁷⁵ Alternatively, mannose may also be produced directly from glucose via an intramolecular carbon shift (epimerisation).^{74,75} Both experimental and computational studies have shown that silanol groups within Sn-Beta can influence the production of fructose and mannose.^{75,76} Specifically, silanol groups in close proximity to framework Lewis acidic Sn sites promote glucose isomerisation towards fructose via a intramolecular hydride shift.^{26,75,76} These sites also enable – to a much lesser extent - the isomerisation of fructose to mannose via a 1,2 intramolecular hydride shift.⁷⁵ However, when these same silanol groups are exchanged with sodium (Na⁺) or potassium (K⁺), the activation energy barrier

towards epimerisation appears to be lowered and mannose may be formed directly from glucose.⁷⁴⁻⁷⁶ Indeed, when this occurs, mannose may become the dominant product within the reaction. As the materials in this study do not contain Na⁺ or K⁺, and the quantities of mannose produced are low, we can infer that the mannose observed this study is formed via a series of intramolecular hydride shifts preceding through fructose.

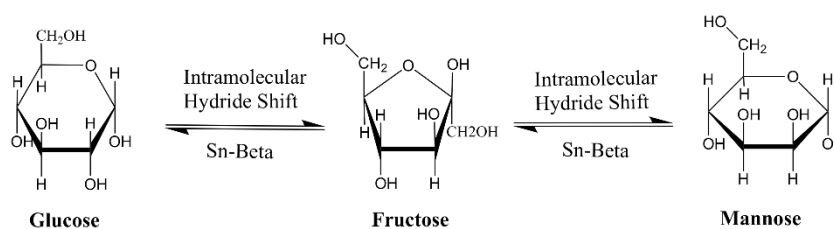


Figure 4.6. Reaction pathways towards fructose and mannose.

In comparison to (XX)Sn-Beta, Zr materials were found to be less active as glucose isomerisation catalysts. Specifically, (1)Zr-Beta and (2)Zr-Beta generated glucose conversions of 17.5 % and 22.4 % under the same reaction conditions. Furthermore, Zr materials generated significantly lower fructose yields than Sn equivalents and produced HMF yields similar to the blank reaction. These low HMF yields are somewhat surprising given the quantity of fructose found in the post reaction solution. To elaborate, the dehydration of fructose towards HMF is autocatalytic at elevated temperatures.⁹¹ Therefore it would be reasonable to expect Zr catalysts to generate greater HMF yields than the blank reaction - considering the higher quantities of fructose found in the reaction solution. The low HMF yields found within (XX)Zr-Beta catalysed reactions may suggest that Zr sites stabilises fructose within aqueous media. Or perhaps the Zr sites within the catalyst promote subsequent reactions that result in product (HMF/fructose) loss.

The difference in catalytic activity between Sn and Zr containing materials may be explained by a difference in acid site distribution. As previously discussed, Sn containing beta zeolites contain even quantities of strong and weak acid sites. In contrast, Zr containing materials predominantly consist of strong acid sites. Furthermore, the weak acid sites within these materials desorbed NH₃ at different temperatures. Specifically, the weak acid desorption peak of (2)Sn-Beta occurs around 211 °C, whilst the same peak occurs at around 197 °C in (2)Zr-Beta. This

indicates that the weak acid sites within (XX)Sn-Beta are stronger. Moreover, the superior activity and fructose yields generated by (XX)Sn-Beta are likely a result of the materials weak acid sites. Furthermore, strong correlations can also be drawn between material acidity and reaction selectivity towards mannose. For instance, mannose was found in the product distribution of Sn catalysed reactions and not those catalysed by (XX)Zr-Beta. This suggests that weak Lewis acid sites may promote mannose production.

The catalytic activity of (1)Sn(1)Zr-Beta is extremely similar to that of (0.5)Sn-Beta. As revealed by ICP analysis, the Sn content of (1)Sn(1)Zr-Beta was found to be 0.65 wt.%. This is extremely similar to the Sn content of (0.5)Sn-Beta. Therefore, the fact that these materials generate comparable glucose conversions and product yields is not surprising. Although, these similarities would suggest that the Zr content of the bimetallic material does not significantly contribute towards catalytic performance here. (2)Zn-Beta and (2)Yb-Beta generated low glucose conversions. Furthermore, although (2)Zn-Beta enabled a fructose yield of around 2.8 %, the HMF yields generated by (2)Zn-Beta and (2)Yb-Beta are lower than those obtained in the blank reaction. The poor catalytic performance of the materials may be explained by their lack of acidity. Indeed, the poor performance of (2)Sr-Beta may also be explained by insufficient acidity.

Although (2)Ga-Beta was found to be the most acidic zeolite synthesised in this study, it generated a considerably low glucose conversion and product yield. Specifically, (2)Ga-Beta generated a glucose conversion of 7.9 % and a HMF yield of 1.2 %. Furthermore, no fructose was found in the reaction mixture. This low activity is especially surprising given the considerable quantity of weak acid sites within (2)Ga-Beta. To explain the materials poor catalytic performance, the strength of weak acid sites may be considered. TPD analysis of (2)Ga-Beta shows a weak acid desorption peak at around 189 °C. Meanwhile the weak acid desorption peak within (2)Sn-Beta occurs at around 211 °C. This suggests that the weak acid sites within (2)Ga-Beta and (2)Sn-Beta have different strengths. Moreover, this may explain the difference in catalytic performance between the two materials. Interestingly, it is also worth noting that mannose was found in the product distribution of the (2)Ga-Beta catalysed reaction.

Table 4.4. Catalytic performance of metal-containing beta zeolites in 3 mL aqueous solution. Reactant to catalyst ratio 30:1 (10 mg catalyst).

Entry	Catalyst	Solvent	Hexose	Time (hr)	Temperature (°C)	Conversion (%)	Fructose Yield (%)	Mannose Yield (%)	HMF Yield (%)	Total Selectivity (Fructose, Mannose, HMF)
1	Blank	Water	Glucose	3	140	5.7	0.9	0.0	2.5	60.1
2	(2)Sn-Beta	Water	Glucose	3	140	64.2	24.3	3.9	17.2	70.7
3	(1)Sn-Beta	Water	Glucose	3	140	62.2	25.5	3.8	15.1	71.4
4	(0.5)Sn-Beta	Water	Glucose	3	140	54.3	24.5	2.8	11.9	72.2
5	(1)Zr Beta	Water	Glucose	3	140	17.5	7.9	0.0	2.1	56.7
6	(2)Zr- Beta	Water	Glucose	3	140	22.4	10.6	0.0	2.6	59.0
7	(1)Sn(1)Zr- Beta	Water	Glucose	3	140	52.4	22.3	2.7	12.0	70.7
8	(2)Zn-Beta	Water	Glucose	3	140	9.2	2.8	0.0	1.7	48.7
9	(2)Yb-Beta	Water	Glucose	3	140	7.0	1.0	0.0	1.4	34.2
10	(2)Sr-Beta	Water	Glucose	3	140	5.7	0.3	0.0	1.6	34.2
11	(2)Ga-Beta	Water	Glucose	3	140	7.9	0.0	2.0	1.2	40.6

Although autocatalytic at elevated temperatures, the dehydration of fructose to HMF is also readily catalysed by Brønsted acids.⁹¹ Within zeolites this acidity may be found in the form of bridging hydroxyl groups.¹⁶⁸ However, given the high fructose yields found in reactions catalysed by Sn and Zr beta zeolites, this acidity may not be enough to promote the dehydration step. As such, reactions were repeated in 0.1 M HCl in an attempt to drive HMF production.

As seen in **Table 4.5**, the blank reaction generated a glucose conversion of 18.2 % and a HMF yield of 4.03 %. Fructose and mannose were not found in the post reaction solution. The addition of (XX)Sn-Beta within the reaction increased glucose conversion. Specifically, (2)Sn-Beta generated a conversion of 34.79 % within 0.1 M HCl. Although this conversion is higher than the blank reaction, it is significantly lower than the glucose conversion generated in water (**Table 4.4, Entry 2**; 64.2 % glucose conversion). Furthermore, the Sn containing materials generated a HMF yield similar to the blank reaction and did not aid in the production of fructose or mannose. This suggests that the presence of HCl promotes the production of undesirable products such as humins whilst impeding the performance of Sn active sites. Indeed, Davis and co-workers also found that the combined use of Sn-Beta and HCl generated low HMF yields in monophasic water reactions.⁷⁹ However, these authors demonstrate that the performance of dual catalyst systems containing Sn-Beta and HCl can be dramatically improved through the use of biphasic reactors that prevent product loss.⁷⁹

The catalytic activities of Zr containing zeolites were also impeded by the presence of HCl. Again, this may suggest that HCl contributes towards the production of various by-products and/or impedes the reaction in another way. Indeed, similar results were found when using Zn, Yb and Sr catalysts within the reaction. In contrast, when combined with (2)Ga-Beta, the addition of HCl to the reaction mixture resulted in the production of trace amounts of fructose and mannose. This may suggest that HCl interacts differently with (2)Ga-beta.

Table 4.5. Catalytic performance of metal-containing beta zeolites in 3 mL acid solution. Reactant to catalyst ratio 30:1 (10 mg catalyst).

Entry	Catalyst	Solvent	Hexose	Time (hr)	Temperature (°C)	Conversion (%)	Fructose Yield (%)	Mannose Yield (%)	HMF Yield (%)
1	Blank	0.1M HCl	Glucose	3	140	18.20	0.00	0.00	4.03
2	(2)Sn-Beta	0.1M HCl	Glucose	3	140	34.79	0.00	0.00	4.81
3	(1)Sn-Beta	0.1M HCl	Glucose	3	140	29.74	0.00	0.00	4.72
4	(0.5)Sn-Beta	0.1M HCl	Glucose	3	140	25.44	0.00	0.00	4.33
5	(1)Zr Beta	0.1M HCl	Glucose	3	140	20.10	0.00	0.00	4.39
6	(2)Zr- Beta	0.1M HCl	Glucose	3	140	21.14	0.00	0.00	4.50
7	(1)Sn(1)Zr- Beta	0.1M HCl	Glucose	3	140	25.29	0.00	0.00	4.42
8	(2)Zn-Beta	0.1M HCl	Glucose	3	140	17.99	0.00	0.00	4.01
9	(2)Yb-Beta	0.1M HCl	Glucose	3	140	19.08	0.00	0.00	3.99
10	(2)Sr-Beta	0.1M HCl	Glucose	3	140	17.46	0.00	0.00	3.86
11	(2)Ga-Beta	0.1M HCl	Glucose	3	140	22.57	0.31	0.13	5.34

Fructose Dehydration towards HMF

To further examine the effectiveness of synthesised beta zeolites as dehydration catalysts, reactions were repeated using an aqueous fructose feedstock. As seen in **Table 4.6**, the blank reaction generated a fructose conversion of 17.8 % and a HMF yield of 15.1 %. The fructose conversions generated by Sn containing zeolites are significantly higher than the blank reaction. Interestingly, these conversions are remarkably similar to the glucose conversions found previously when using the same catalysts (**Table 4.4**). Furthermore, (XX)Sn-Beta generated significant glucose yields. This suggests that Sn sites are actively catalysing the reversible isomerisation of fructose to glucose (**Figure 4.7**). However, the glucose yields generated when starting from a fructose feedstock are lower than the fructose yields obtained when beginning from a glucose feedstock. This may suggest that the reaction pathway of fructose to glucose is more prone to the production of by-products than the forward reaction and may have a different activation energy barrier. Zr containing materials also facilitated the reaction pathway of fructose to glucose. However, less glucose was found in the post-reaction solutions catalysed by (XX)Zr-Beta.

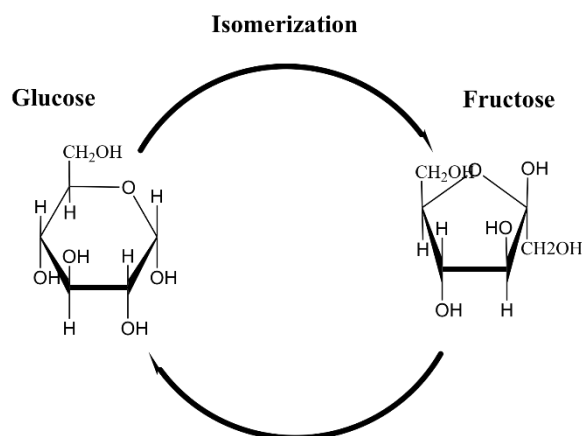


Figure 4.7. Reversible glucose isomerisation reaction.

Sn containing zeolites generated HMF yields slightly higher than the blank reaction. This may indicate that (XX)Sn-Beta contains some element of Brønsted acidity. Interestingly, Zr containing zeolites generated HMF yields similar to the blank reaction. In addition, the activities of Yb, Zn, and Sr containing materials were similar to the blank reaction, suggesting an absence of sufficient Brønsted and Lewis acid active sites within these zeolites.

Table 4.6. Catalytic performance of metal-containing beta zeolites in 3 mL aqueous solution considering a fructose feedstock. Reactant to catalyst ratio 30:1 (10 mg catalyst).

Entry	Catalyst	Solvent	Hexose	Time (hr)	Temperature (°C)	Conversion (%)	Glucose Yield (%)	Mannose Yield (%)	HMF Yield (%)
1	Blank	Water	Fructose	3	140	17.8	0.0	0.0	15.1
2	(2)Sn-Beta	Water	Fructose	3	140	65.4	14.2	7.1	20.3
3	(1)Sn-Beta	Water	Fructose	3	140	63.7	14.4	7.4	19.7
4	(0.5)Sn-Beta	Water	Fructose	3	140	55.0	11.3	7.3	17.5
5	(1)Zr Beta	Water	Fructose	3	140	25.0	1.5	0.9	15.2
6	(2)Zr- Beta	Water	Fructose	3	140	27.7	2.2	1.2	15.8
7	(1)Sn(1)Zr- Beta	Water	Fructose	3	140	56.8	10.1	6.6	19.2
8	(2)Zn-Beta	Water	Fructose	3	140	18.9	0.0	0.0	11.8
9	(2)Yb-Beta	Water	Fructose	3	140	17.9	0.0	0.0	13.0
10	(2)Sr-Beta	Water	Fructose	3	140	17.3	0.0	0.0	12.7

Flow Reactor

Within batch systems, Sn-Beta is a highly recyclable isomerisation catalyst. The catalyst has been shown to endure up to 3 reaction cycles in water with minimal activity loss and may be regenerated through calcination.⁵³ However, for the purpose of process intensification and scale up, the performance of Sn-Beta must be explored within continuous flow. To this end, Padovan, *et al.* recently reported the first use of Sn-Beta within a continuous flow reactor for the purpose of glucose isomerisation.⁷⁰ In this initial study, the authors considered the use of both water and methanol as reaction solvents. Interestingly, the combined use of Sn-Beta and water within a continuous flow system resulted in the destruction of the catalyst.⁷⁰ However, it is worth noting that the authors utilized a post-synthesis method to produce the Sn-Beta used in their study.⁷⁰

The performance of (2)Sn-Beta synthesised in this study was tested in a purpose built flow reactor. For this, 40 mg of (2)Sn-Beta was pelletized and sieved to give a uniform particle size of 250 nm. The catalyst was then mixed with glass beads (212 – 300 nm) and loaded into the reactor resulting in a bed length of 8 cm. A 10 wt.% glucose solution in water was then continuously pumped through the reactor at a flow rate of 0.14 mL/min resulting in a weight hourly space velocity (WHSV) of 21 h⁻¹. Meanwhile, the reactor was heated to a temperature of 140 °C.

The results from the flow reactor study are shown in **Figure 4.8**. As seen, the initial activity of (2)Sn-Beta is extremely high, facilitating a high glucose conversion (~60 %) combined with a ~29 % fructose yield. However, the activity of the catalyst is shown to rapidly decline over the course of 8 h. This decline in activity may be due to an accumulation of humins on the catalyst and is consistent with the results reported by Padovan, *et al.* Specifically, these authors found that the activity of Sn-Beta prepared via post synthesis techniques declines by approximately 50 % after 5 – 10 h time on stream.⁷⁰ However, the activity of the Sn-Beta tested in this study appears to begin stabilising following this initial loss in performance. Indeed, following this initial decline, the activity of the (2)Sn-Beta appears to begin stabilising, producing a glucose conversion of ~19 % and a fructose yield of ~10 % after 480 min of time on stream. To observe the effects of a typical regeneration process on the catalyst, it was washed in water, recovered, and dried. The catalyst was then calcined at 550 °C in order to remove humins

from the framework. The recovered and regenerated catalyst was subsequently denoted as (2)Sn-Beta*.

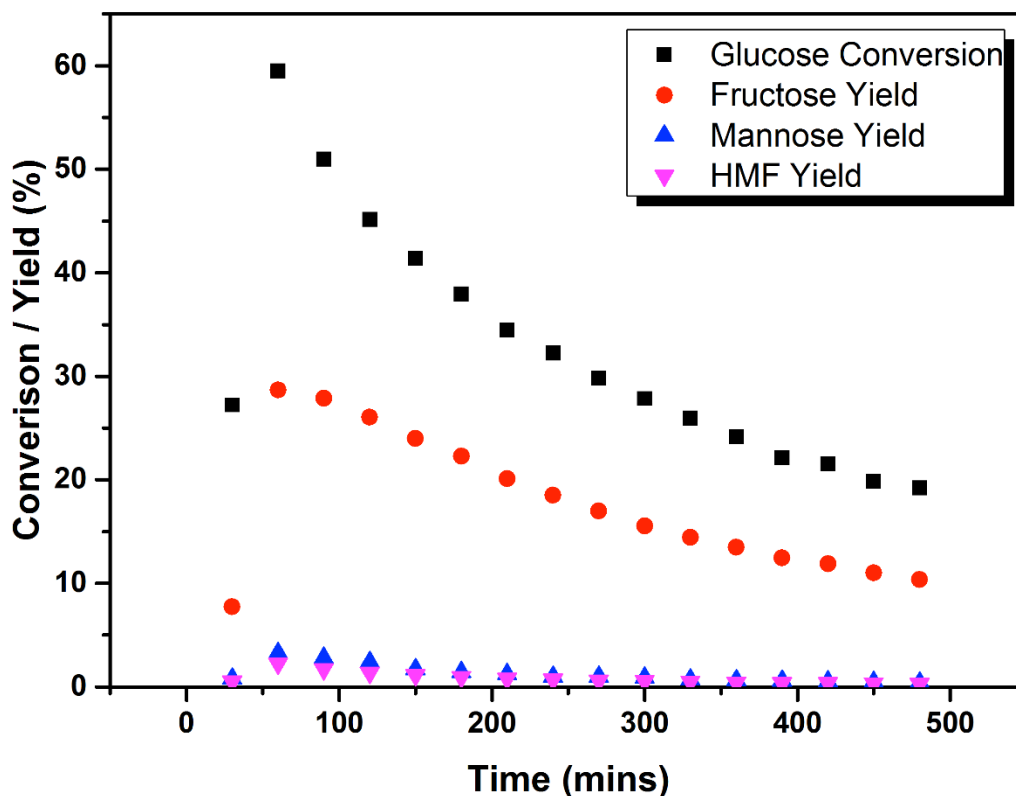


Figure 4.8. Activity of (2)Sn-Beta in a purpose built continuous flow reactor. 40 mg catalyst, 10 wt.% aqueous glucose feedstock, 140 °C, WHSV of 21 h⁻¹.

Following calcination, the recovered catalyst (2)Sn-Beta* was analysed via XRD. The results of this XRD analysis are shown in **Figure 4.9**. As seen, there are clear differences between the diffraction patterns of “fresh” (2)Sn-Beta and the “spent” calcined material. Most noticeably, the diffraction pattern of the recovered and calcined material contains large additional peaks. The presence of these peaks suggests that the reaction and calcination process has damaged the catalyst. However, despite this damage, the overall beta zeolite structure is still apparent. In comparison, Padovan, *et al.* reports the complete destruction of Sn-Beta after 30 h continuous time on steam in an aqueous medium.⁷⁰

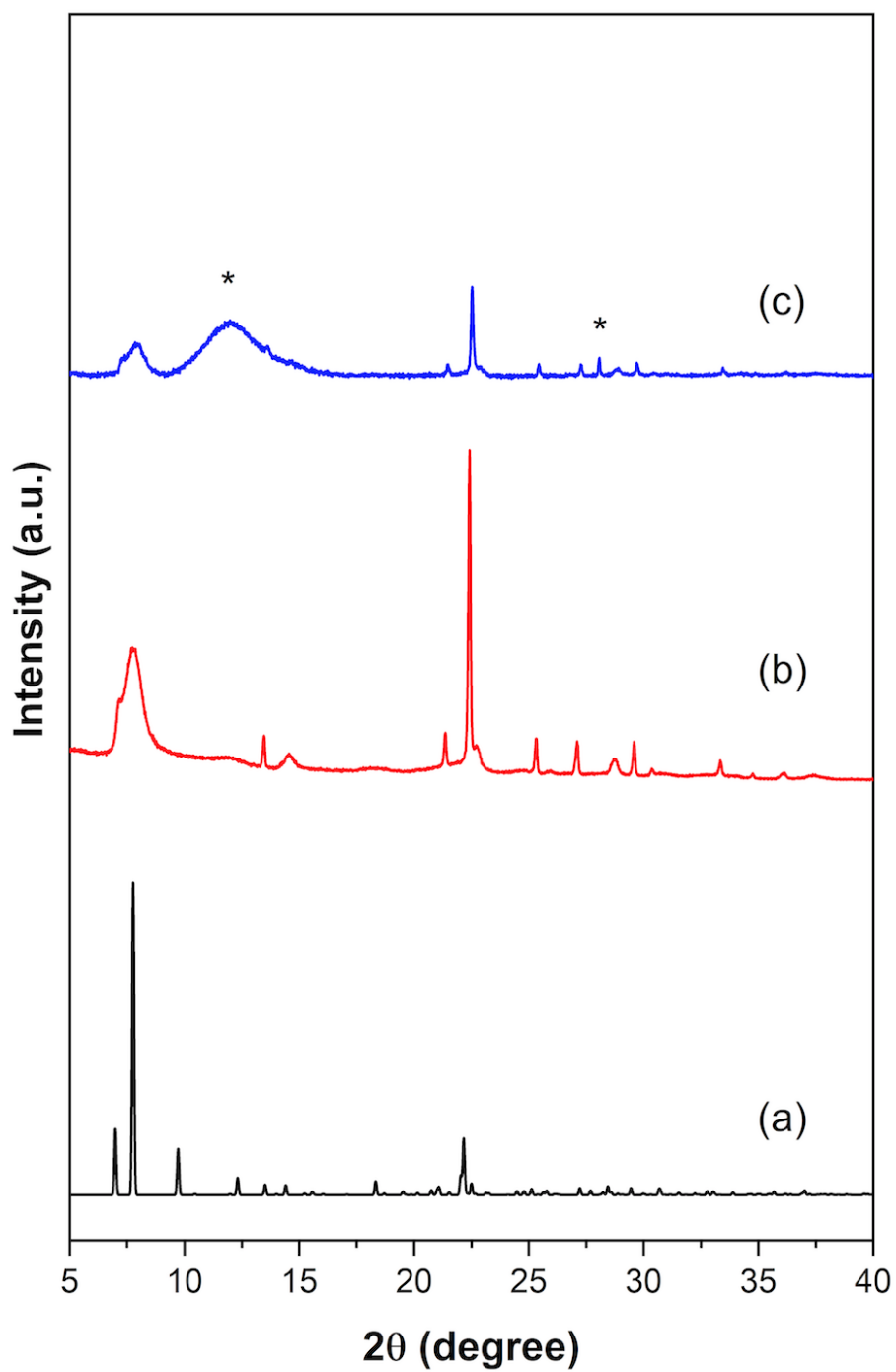


Figure 4.9. XRD patterns of (a) simulated pattern⁶⁸ (b) "fresh" (2)Sn-Beta and (c) "spent" (2)Sn-Beta* following use in the flow reactor and calcination.

The catalytic activity of (2)Sn-Beta* was tested in a batch reactor. For this, 10 mg of (2)Sn-Beta* was added to a 4 mL glass reaction vial along with 3 mL of glucose stock solution and a magnetic follower. The reaction mixture was then heated at 140 °C for 3 h. Quenching the reaction vial in an ice bath maintained at 0 °C stopped the reaction and products were analysis via HPLC. As seen in **Figure 4.10**, (2)Sn-Beta* is able to generate a glucose conversion of around 34.8 % along with a total product yield of around 17.5 % in 3 h. Although this catalytic activity is lower than ‘fresh’ (2)Sn-Beta, these results indicate that the regenerated material contains tetrahedrally coordinated, Lewis acidic, Sn active sites.

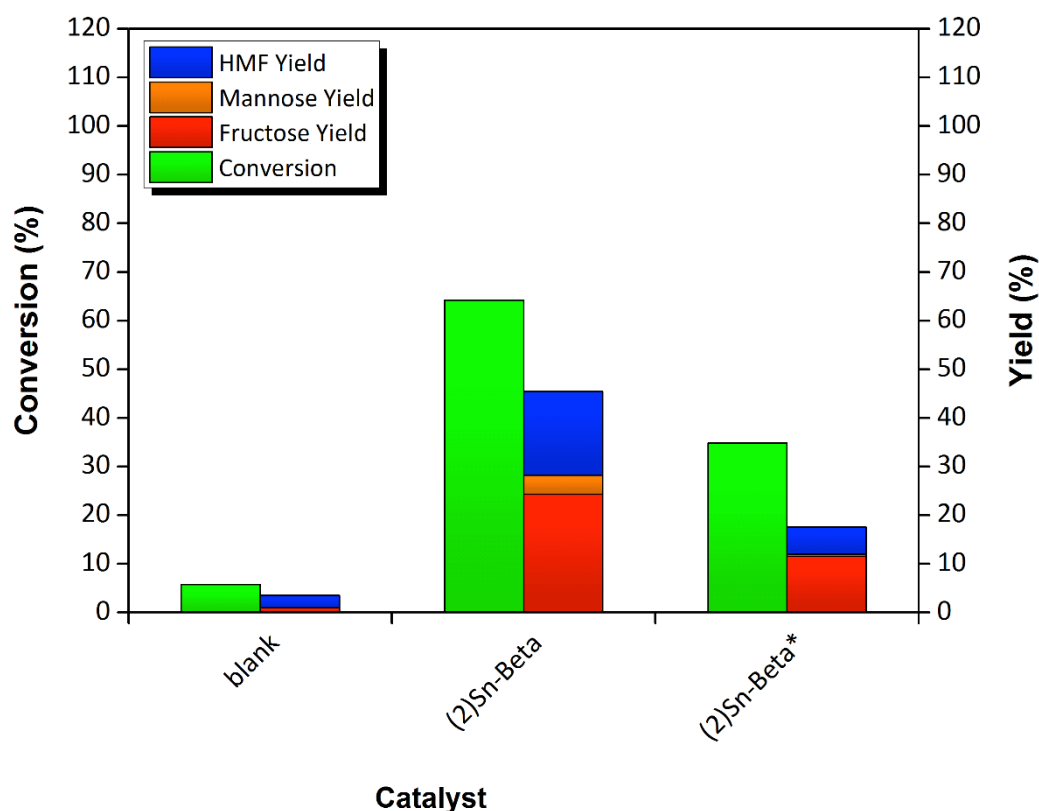


Figure 4.10. Catalytic activity of ‘fresh’ (2)Sn-Beta and ‘spent’ (2)Sn-Beta*. Reaction conditions: 10 mg of catalyst, 3 mL of 10 wt.% glucose in water, 3 h, and 140 °C.

4.3 Conclusions

Metal-containing beta zeolites have been produced using a rapid synthesis method. This method successfully reduces the time required to synthesis metal-containing beta zeolites from 40 days to 3 days. Tin (Sn), gallium (Ga), zirconium (Zr), zinc (Zn) and ytterbium (Yb) appeared to be successfully introduced into the beta zeolite framework. Meanwhile, strontium (Sr) was not successfully introduced into the framework of beta zeolite and may predominately reside as extra-framework sites within the materials pore network. The acidity of the zeolites was explored using NH₃-TPD analysis. The results of this analysis show that Ga, Sn and Zr containing materials are the most acidic. Furthermore, each of these materials have different acidity profiles as indicated by the peak positions within their respective desorption patterns.

The synthesised zeolites were tested as catalysts for the isomerisation and dehydration of glucose in water and HCl. As expected Sn-Beta, a well know isomerisation catalyst, facilitated the highest glucose conversion and product yield in water. Zr containing beta zeolites were also found to be of considerable interest as catalysts in water. The addition of 0.1 M HCl in reactions was found to impair the catalytic ability of each zeolite considered in this study with the possible exception of (2)Ga-Beta.

Reactions were repeated using a fructose feedstock in water. Glucose was observed in a number of reaction solutions. This suggests that the zeolites are able to catalyse the reversible isomerisation of fructose to glucose. The HMF yields generated in these reactions were low, and only marginally higher than the HMF yield generated in the fructose blank reaction. It has been well reported that Brønsted acids are able to catalyse fructose dehydration towards HMF. The low HMF yields generated in theses reactions may suggest that the synthesised metal-containing beta zeolites lack - or have low levels of - Brønsted acidity and/or promote side reactions.

The performance of (2)Sn-Beta was tested within a purpose built continuous flow reactor. The activity of the catalyst quickly declined but appeared to begin stabilising at lower conversions. XRD analysis of the recovered and calcined catalyst indicates that – although damaged – the beta zeolite structure is still

apparent. Furthermore, the calcined material retained some of the catalytic activity seen in the fresh catalyst – therefore suggesting the material still contains catalytically active Sn sites.

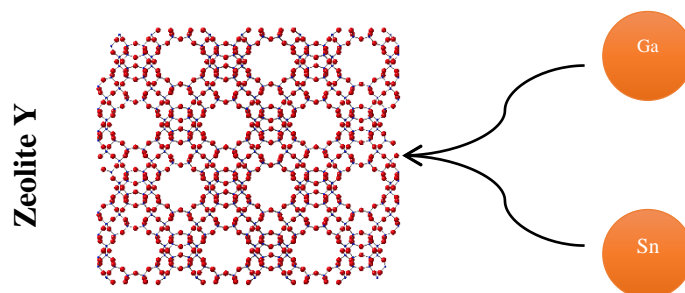
Finally, it is worth noting that metal-containing beta zeolites are highly effective catalysts within a number of important reactions other than glucose isomerisation. For example, Zr-Beta and Sn-Beta are highly effective Meerwein–Ponndorf–Verley (MPV) reaction catalysts whilst Sn-Zn-Beta may be used in the production of lactic acid.^{69,151,169–171} As such, the rapid synthesis method may be used to shorten the synthesis times required to produce various metal-containing beta zeolites of excellent morphology for numerous applications.

Chapter 5

Gallium and Tin Containing Zeolite Y for Glucose Isomerisation and 5-Hydroxymethylfurfural Production

Summary

In the previous chapter, various metal-containing beta zeolites were produced using a rapid synthesis method. Although this method does not negate the use of highly toxic hydrofluoric acid (HF), it does reduce the synthesis times of metal-containing beta zeolites from 40 days to 3 days. In this chapter, we attempt to employ glucose isomerisation catalysts that can be made in rapid succession without the use of HF. Specifically; we use a simple and scalable post-synthesis method to introduce tin (Sn) and gallium (Ga) into the framework of commercial zeolite Y. In water, Sn containing zeolite Y (Sn-DeAl-H-Y) is shown to generate a glucose conversion of ~36 % and a total desirable product yield of ~17 % (fructose, mannose, HMF). Meanwhile, Ga containing zeolite Y (Ga-DeAl-H-Y) is shown to generate a HMF yield of ~33 % when reactions are conducted in DMSO. The recyclability of Sn-DeAl-H-Y and Ga-DeAl-H-Y is considered and the activities of both materials were shown to remain significantly high in DMSO recycle reactions. The effect of catalyst to reactant ratio is explored as well as the use of a fructose feedstock. Finally, in-situ XANES analysis of Sn-DeAl-H-Y was conducted in real time using a purpose built reaction cell.



Graphical Abstract. Post-synthesis addition of Ga and Sn into the framework of zeolite Y. (CIF.⁶⁸)

5.1 Introduction

Sn-Beta is a highly effective glucose isomerisation catalyst in water.^{53,71} However, its application in industry has not yet been realised. This is likely due to the numerous drawbacks associated with the production of Sn-Beta. For instance, the traditional synthesis of this zeolite requires hydrofluoric acid (HF) and crystallization times of up to 40 days.^{53,79}

Zeolite Y is a commonly used catalyst within the petrochemical industry.¹⁷²⁻¹⁷⁵ Unlike beta zeolite, its structure contains sodalite cavities and supercage structures.^{174,176} Zeolite Y is typically hydrothermally unstable due to its high aluminium (Al) content.¹⁷⁷ However, the stability of this zeolite can be improved by removing Al from its framework.^{175,177} With regards to biomass valorisation, zeolite Y has shown promise as a glucose isomerisation catalyst.^{50,51,61,178} For example, Ultra-Stable zeolite Y (USY) is effectively able to generate high fructose yields when combined with the sequential use of alcohol and aqueous mediated solutions.⁶¹

Moreover, routes towards the development of industrial processes for the chemo-catalytic production of fructose and HMF remains at the forefront of current research. Furthermore, there is scope to pursue the development of zeolite Y catalysts. As such, to address current challenges, the implementation of tin (Sn) and gallium (Ga) containing zeolite Y is proposed hereafter. Recent work has shown that the introduction of these metals within the framework of zeolite Y yields catalysts of increased Lewis acidity with potential applications in the future bio-refinery.^{145,179,180} Thus, whilst utilising a simple and scalable catalyst synthesis method adopted from literature, we demonstrate the application of Sn and Ga containing zeolite Y in the isomerization of glucose and production of HMF within different solvents. Specifically, the catalytic performances and stabilities of these zeolites are tested in water, HCl, and DMSO. The recyclability of Sn and Ga materials is also explored in different solvents. Furthermore, the affect of catalyst to reactant ratio is studied as well as the use of a fructose feedstock. Finally, XANes analysis is employed to better understand the behaviour of Sn active sites during reactions.

5.2 Results and Discussion

Structure and Morphology

To achieve the post-synthesis introduction of framework metals in zeolites, an acid treatment of the parent material is a common prerequisite. Such treatments, often utilise nitric acid or ethylenediaminetetraacetic acid (H₄EDTA), to remove framework Al from the material.^{70,85–87,145,152–155,181} This results in the formation of vacant sites within the materials framework in the form of silanol nests which can later accommodate foreign metal species.^{85,86,145,152} Thus, for the preparation of Sn and Ga containing zeolite Y, we begin with a simple acid dealumination technique adapted from literature.¹⁴⁵

Acid dealumination was conducted using a heated solution of 8 M nitric acid. The ratio of zeolite to acid solution was 1 g : 10 mL and the stirring time was 20 h. The stability of zeolite Y is inversely effected by the amount of Al contained within its framework.¹⁷⁷ Hence, a commercial zeolite containing a high Silica : Alumina ratio (30 : 1 or Si : Al = 15 : 1) was specifically selected for use in this intensive dealumination process.

As shown in **Figure 5.1**, the diffraction pattern of DeAl-H-Y clearly exhibits the inherent structure of the parent zeolite Y material. This confirms that the commercial material has withstood the dealumination process and should now contain vacant sites capable of accepting foreign metal species.^{85–87,145,152} The subsequent addition of Sn and Ga within DeAl-Y was achieved using a wetted impregnation technique. A wetted technique was specifically chosen here to aid the dispersion of Sn and Ga within the zeolite pore network.

The diffraction patterns of Sn-DeAl-H-Y and Ga-DeAl-H-Y are identical to that of the H-Y. This indicates that the introduction of Ga and Sn has not impacted the superficial structure of the zeolite. Furthermore, the diffraction patterns are void of any additional Bragg peaks that may indicate the presence of bulk extra-framework metal oxide clusters within the materials.¹⁵² Hence, the absence of additional Bragg peaks may provide a first indication that Sn and Ga have been successfully introduced into the zeolite Y framework as tetrahedrally coordinated Lewis acid sites.

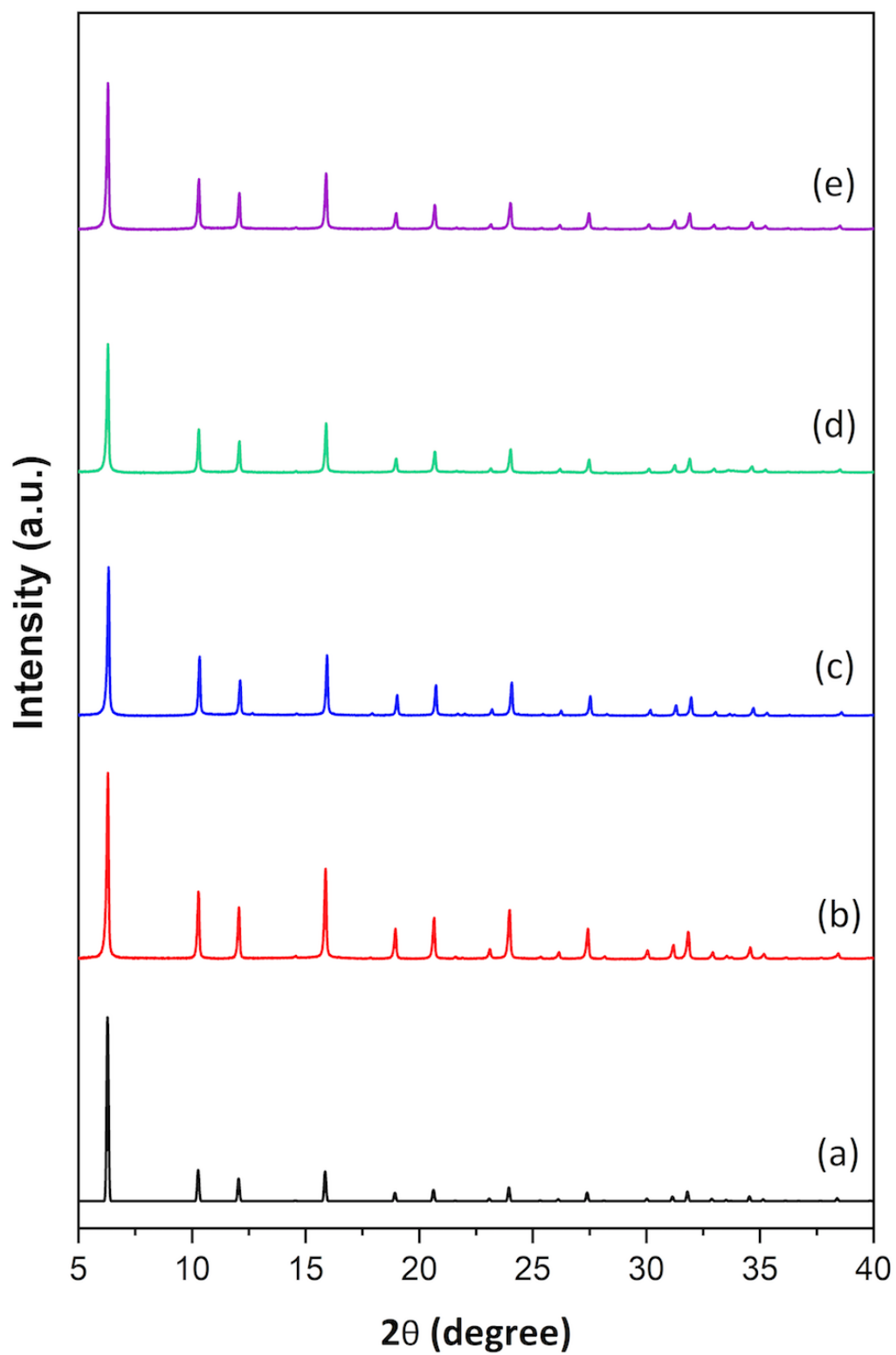


Figure 5.1. X-ray Powder Diffraction (XRD) patterns of (a) simulated pattern⁶⁸ (b) H-Y (c) DeAl-H-Y (d) Sn-DeAl-H-Y (e) Ga-DeAl-H-Y.

Nitrogen adsorption analysis was used to quantify the surface area and pore volumes of the materials considered in this study. The isotherms of each material are shown in **Figure 5.2** and indicate the presence mesoporous zeolite Y.^{145,182} Interestingly, the isotherms clearly indicate that dealumination and metal introduction greatly affect material pore volume. Specifically, the hysteresis loop appears to widen following dealumination, and narrow following the introduction of the metal species. This effect on pore volume is further quantified in **Table 5.1**.

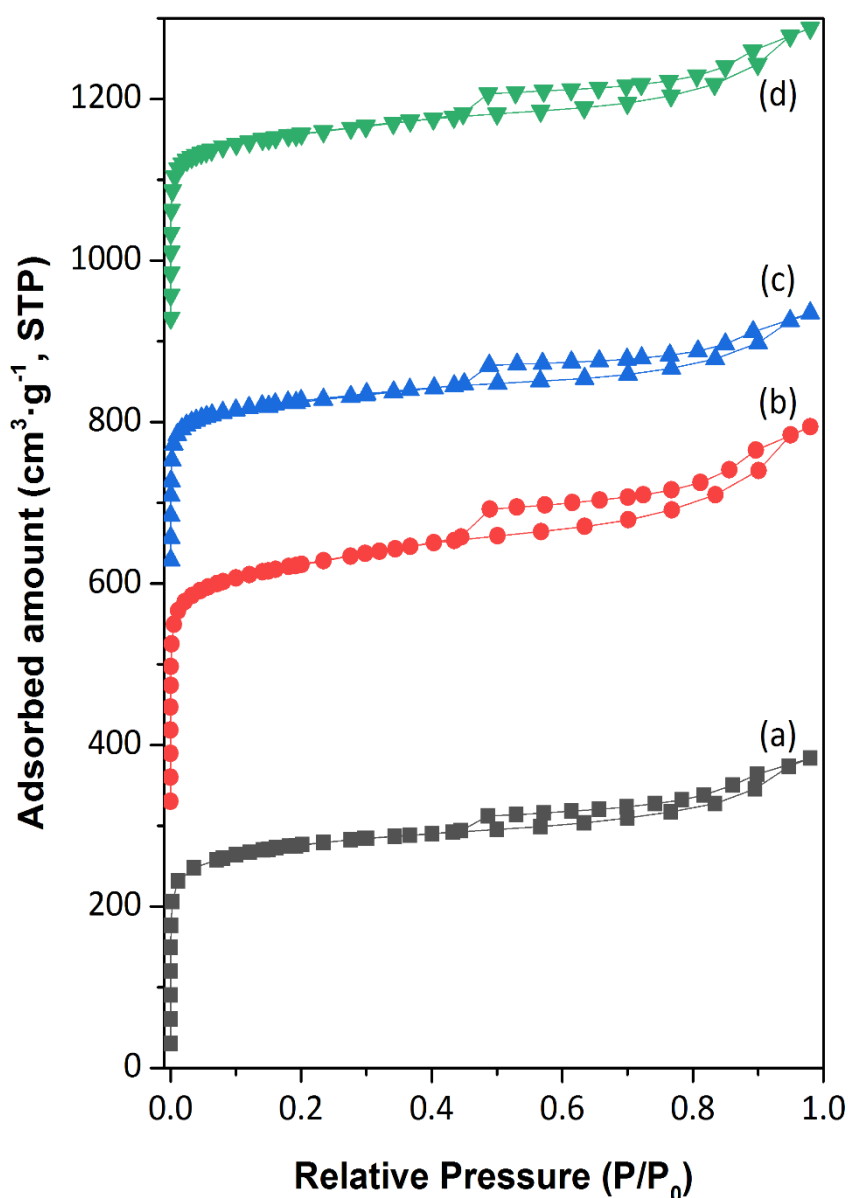


Figure 5.2. BET isotherms of (a) H-Y (b) DeAl-H-Y (c) Sn-DeAl-H-Y (d) Ga-DeAl-H-Y.

As shown in **Table 5.1**, DeAl-H-Y has a significantly larger surface area and mesoporous volume than H-Y. This change in tangible characteristics is presumably caused by the removal of Al from the materials framework. The specific increase in mesopore volume may suggest that dealumination has a preannounced effect on the zeolites supercage structures. By comparison, the dealumination process did not result in a dramatic increase in micropore volume.

Table 5.1. Textural properties of Y zeolites determined by nitrogen adsorption.

Catalyst	S_{BET} ($\text{m}^2 \cdot \text{g}^{-1}$)	V_{Micro} ($\text{cm}^3 \cdot \text{g}^{-1}$)	V_{Meso} ($\text{cm}^3 \cdot \text{g}^{-1}$)
H-Y	987	0.31	0.13
DeAl-H-Y	1155	0.33	0.23
Sn-DeAl-H-Y	807	0.24	0.14
Ga-DeAl-H-Y	916	0.27	0.17

The surface areas of Sn-DeAl-H-Y and Ga-DeAl-H-Y are the lowest measured. Hence, the introduction of Sn and Ga into the structure of DeAl-H-Y had a significant effect on surface area. Of these two metals, the addition of Sn reduced material surface area by the greatest amount. This may be due to the larger size of the Sn atom.

The addition of Sn and Ga also had a significant effect on material pore volume. The microporous volumes of Sn-DeAl-H-Y and Ga-DeAl-H-Y are significantly lower than those of DeAl-H-Y and H-Y. This reduction in micropore volume may be attributed to blockages. Indeed, small quantities of Sn and Ga that have been unsuccessfully introduced into the zeolite framework will likely reside within the materials pore network as extra-framework metal oxide species. As well as blocking micropores, these extra-framework species will likely reduce material surface area.

Sn-DeAl-H-Y and Ga-DeAl-H-Y have a lower mesoporous volume than DeAl-H-Y. This reduction in mesoporous volume may suggest that Sn and Ga have been successfully introduced into the zeolite framework at dealuminated sites. **Figure 5.3** illustrates the changes in material pore volume as a result of dealumination and metal introduction.

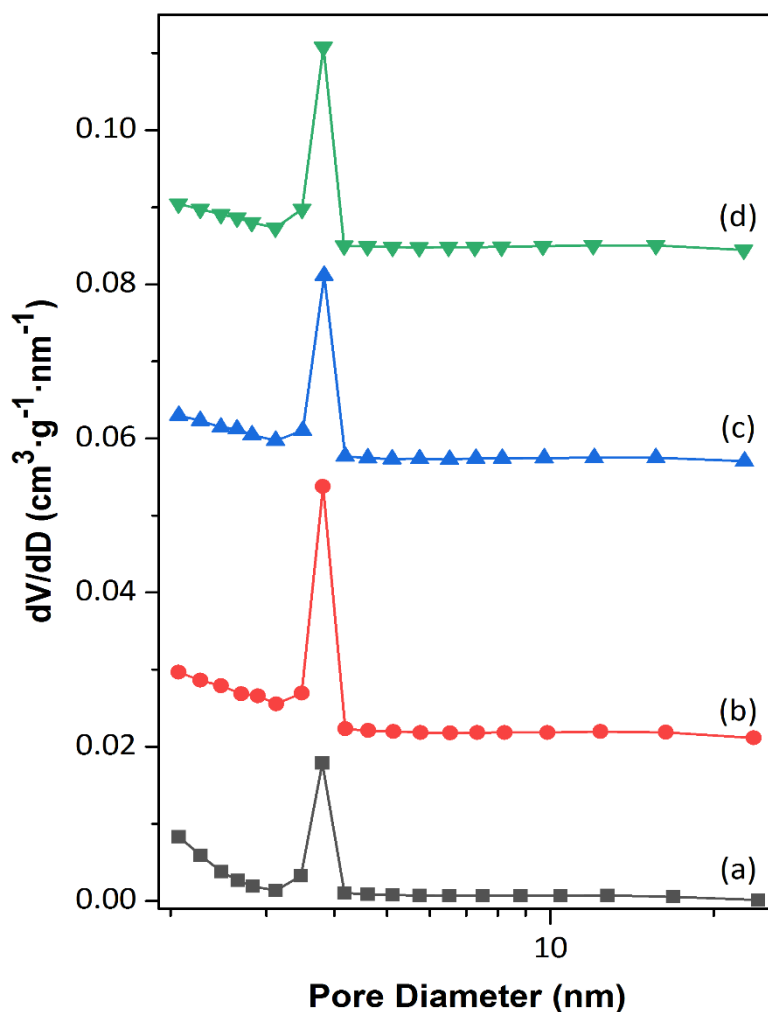


Figure 5.3. BJH Desorption of (a) H-Y (b) DeAl-H-Y (c) Sn-DeAl-H-Y (d) Ga-DeAl-H-Y.

UV-Vis DRS provides some indication of the successful dealumination of zeolite Y as well as the introduction of foreign metal species (**Figure 5.4**). The UV-Vis spectrum of H-Y reveals peaks at 200 nm, 220 nm and 270 nm. As a comparison, the deconvoluted UV-Vis spectrum of aluminium oxide displays two distinct peaks at 190 nm and 250 nm along with a much broader peak at 395 nm (**Appendix B**). Dealumination of H-Y generated a markedly different UV-Vis spectrum in comparison to H-Y and Al₂O₃. For instance, there is an apparent absence of a large peak at 270 nm in the UV-Vis spectrum of DeAl-H-Y. The UV-Vis spectrum of bulk tin oxide (SnO₂) contains peaks at 219 nm and 290 nm. In comparison, the UV-Vis spectrum of Sn-DeAl-H-Y contains an intense peak at ~207 nm and a smaller peak at 283 nm. The peak at 207 nm indicates the presence of tetrahedrally coordinated (Lewis acid) Sn sites within the framework of Sn-DeAl-H-Y.^{18,86,145}

Meanwhile, the smaller peak at 283 nm may indicate the presences of hydrated Sn sites or octahedrally coordinated Sn in the form of extra-framework (basic) SnO₂.^{86,87,154} The UV-Vis spectrum of Ga-DeAl-H-Y is notably different to that of the dealuminated material and more comparable to Ga₂O₃ spectrums reported in literature and in **Appendix B**.^{183,184} Moreover, this may indicate the existence of framework and extra-framework Ga species within Ga-DeAl-H-Y.

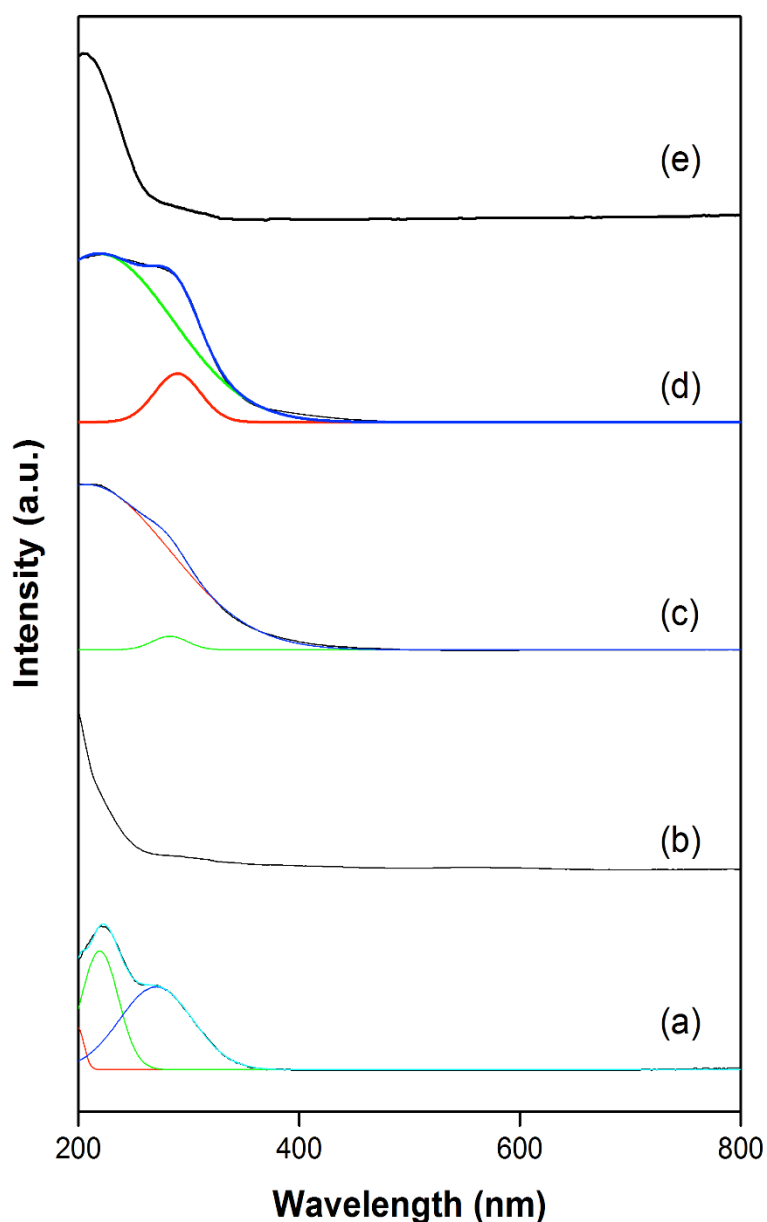


Figure 5.4. UV-vis diffuse reflective spectra of catalysts (a) H-Y (b) DeAl-H-Y (c) Sn-DeAl-H-Y (d) SnO₂ (e) Ga-DeAl-H-Y.

Inductively coupled plasma (ICP) analysis was used to quantify the severity of dealumination and success of metal introduction. As shown in **Table 5.2**, the quantity of Al contained within H-Y is 2.3 wt.%. As such, the silica to aluminium molar ratio (Si : Al) within H-Y was calculated as 18.7 : 1. This is higher than the expected ratio of 15 : 1 reported by the manufacturer. The Al content of DeAl-H-Y is 0.28 wt.%. This is significantly lower than the Al content within H-Y and therefore confirms the successful dealumination of the parent material. Furthermore, as shown by XRD analysis, this extensive dealumination did not destroy the intrinsic structure of the zeolite.

The Sn content of Sn-DeAl-H-Y is 2.9 wt %. Meanwhile the Ga content of Ga-DeAl-H-Y is 2.3 wt%. These values are lower than expected (4 wt.%) and may suggest that the introduction of foreign metal species is somehow impaired. It may also suggest that the wetted impregnation method used in preparation of these materials is not completely effective. Moreover, the Sn and Ga materials have a silica to metal molar ratio of 64.8 : 1 and 48.0 : 1, respectively. This may suggest that vacant silanol sites within the dealuminated structure have a higher affinity towards Ga than Sn.

Table 5.2. Elemental composition of Y zeolite catalysts.

Catalyst	Al (wt %)	Sn (wt %)	Ga (wt %)	Si/Al ratio	Si/Sn ratio	Si/Ga ratio
H-Y	2.3	N/A	N/A	18.7 : 1	N/A	N/A
DeAl-H-Y	0.28	N/A	N/A	159.5 : 1	N/A	N/A
Sn-DeAl-H-Y	0.26	2.9	N/A	164.2 : 1	64.8 : 1	N/A
Ga-DeAl-H-Y	0.28	N/A	2.3	152.5 : 1	N/A	48.0 : 1

SEM images of the zeolites considered in this study are shown in **Figure 5.5**. As seen, H-Y consists of discrete crystals that are largely plate like or trigonal in shape. Furthermore, the particle sizes are non-uniform but appear to fall within the range of approximately 1000 nm. Close inspection of the parent material also shows that large surface defects are prevalent. Dealumination did not result in the destruction of the crystals and nor did the process of wetted impregnation. Large crystal structures (approximately >600 nm) are still present following the

dealumination and impregnation process. Again, close inspection of the materials reveals the extent of surface defects - with surface voids apparent.

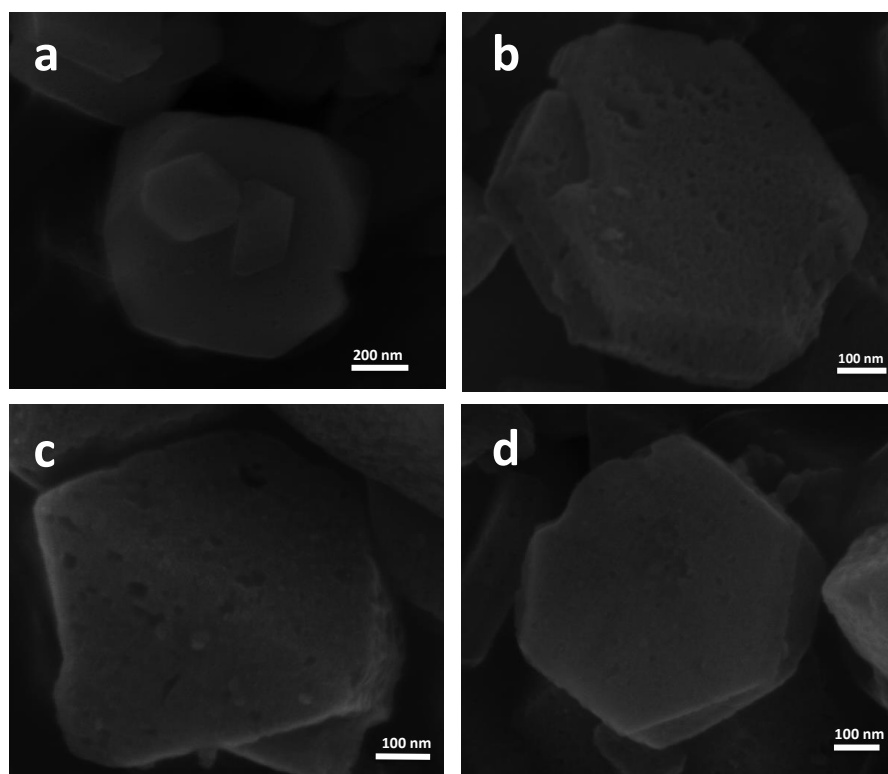


Figure 5.5. SEM imaging of catalysts (a) H-Y (b) DeAl-H-Y (c) Sn-DeAl-H-Y (d) Ga-DeAl-H-Y.

Material acidity was quantified using ammonia temperature programmed desorption (NH₃-TPD). For this a homemade apparatus was used. Here, ammonia desorption was recorded using a mass spectrometer. The heating rate applied during desorption was 5 °C/min. As discussed in the previous chapter, the accuracy of this equipment was verified by measuring the acidity of commercial ZSM-5 and beta zeolite. These results were then compared to literature.

As shown in **Figure 5.6**, the ammonia desorption pattern of H-Y contains two distinct peaks. These can be attributed to the presence of strong and weak acid sites within the material. Specifically, the low temperature peak correlates to the presence of weak acid sites within H-Y whilst the high temperature peak can be attributed to the presence of strong acid sites. Peak areas were quantified by integration and the results are shown in **Table 5.3**. As seen, H-Y contains mainly strong acid sites and the total acidity of the material was calculated as 0.447 mmol

/ g. This value compares well with those reported in literature and thus further confirms the accuracy of the NH₃-TPD system used.^{182,185}

The total acidity of DeAl-H-Y was calculated as 0.003 mmol / g. As expected this is significantly lower than the acidity of H-Y due to the removal of Al from the zeolite framework. As seen in **Figure 5.6**, the peak positions within DeAl-H-Y are different to those found in H-Y. Most noticeably, DeAl-H-Y does not contain a peak at 192 °C. This suggests that the material does not contain weak acid sites. Furthermore, the NH₃-TPD profile of DeAl-H-Y appears to indicate the presence of another peak at + 500 °C. This suggests that the dealumination process has changed the strength of the acid sites found within the zeolite.

Table 5.3. Acidity of Y zeolite frameworks.

Catalyst	First Peak Temperature (°C)	First Peak Acidity mmol/g	Second Peak Temperature (°C)	Second Peak Acidity mmol/g	Total Acidity mmol/g
H-Y	192	0.144	371	0.304	0.447
DeAl-H-Y	423	0.002	555	0.001	0.003
Sn-DeAl-H-Y	190	0.004	265	0.007	0.012
Ga-DeAl-H-Y	317	0.005	510	0.025	0.030

The introduction of Sn is shown to increase the acidity of the zeolite. This indicates that Sn has successfully been introduced into the zeolite framework as tetrahedrally coordinated Lewis acid sites. The total acidity of Sn-DeAl-H-Y was calculated as 0.012 mmol / g. The peak positions within the NH₃-TPD profile of Sn-DeAl-H-Y are found at 190 °C and 265 °C. This indicates that the acid sites within Sn-DeAl-H-Y have a different strength to those contained in the parent material. This change in acid site strength is reasonable considering the replacement of Al with Sn.

The introduction of Ga into the structure of DeAl-H-Y is also shown to increase acidity. Again, this may indicate that Ga has successfully been introduced into the zeolite framework as tetrahedrally coordinated Lewis acid sites. The total acidity of Ga-DeAl-H-Y was calculated as 0.03 mmol / g. This is significantly higher than

the acidity of Sn-DeAl-H-Y, indicating that Ga imparts more acidity than Sn. Furthermore, the peak positions within the desorption pattern of Ga-DeAl-H-Y are different to those found in Sn-DeAl-H-Y. Again, this suggests a difference in acid strength between the materials.

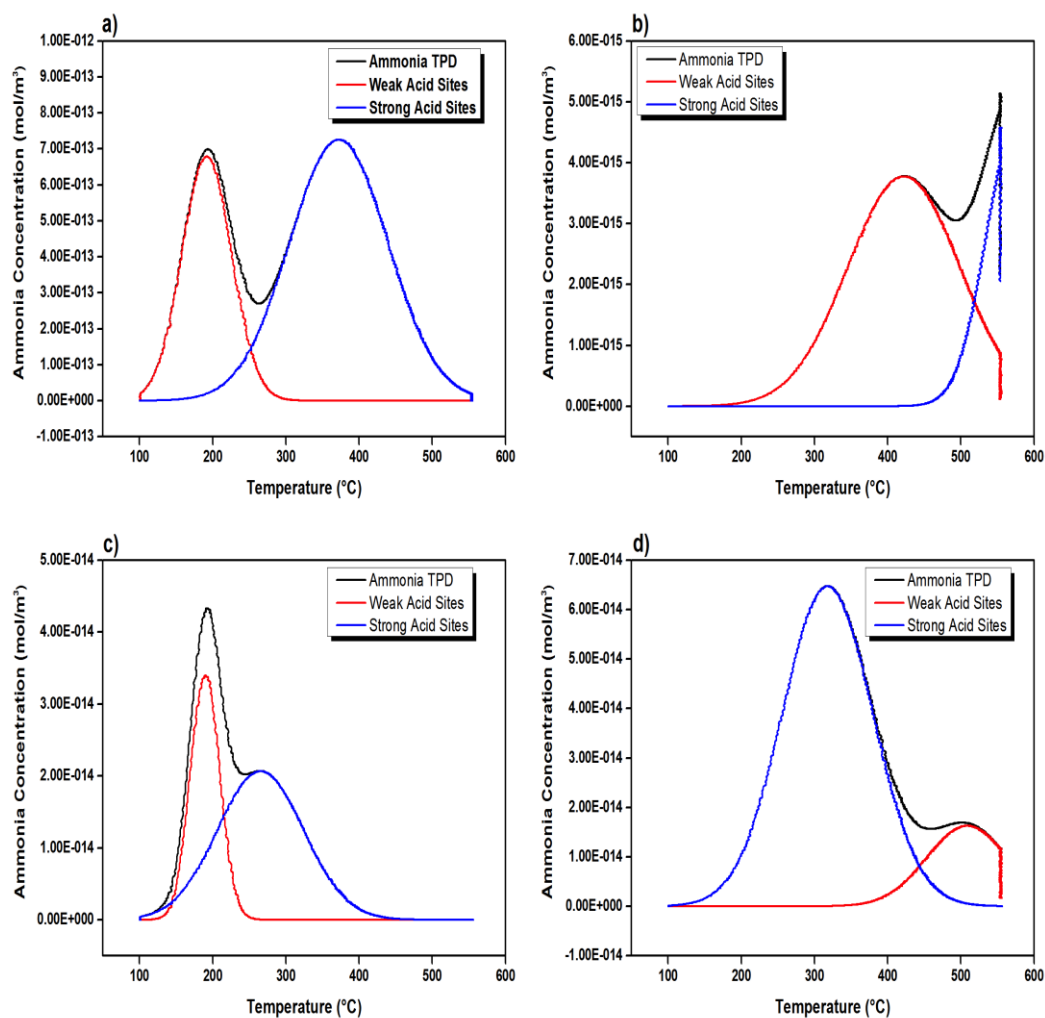


Figure 5.6. NH_3 -TPD profile of (a) H-Y (b) DeAl-H-Y (c) Sn-DeAl-H-Y (d) Ga-DeAl-H-Y.

Glucose Isomerisation and Dehydration towards HMF

The catalytic performances of the Sn and Ga containing zeolites were tested in the isomerisation of glucose and production of HMF. To provide a benchmark for easy comparison, the performances of H-Y and DeAl-H-Y were also tested in the same reactions. As an initial test, reactions were conducted in water. Not only is water the most ideal solvent choice in terms of being environmental benign, it is also the most favourable from an industrial standpoint.

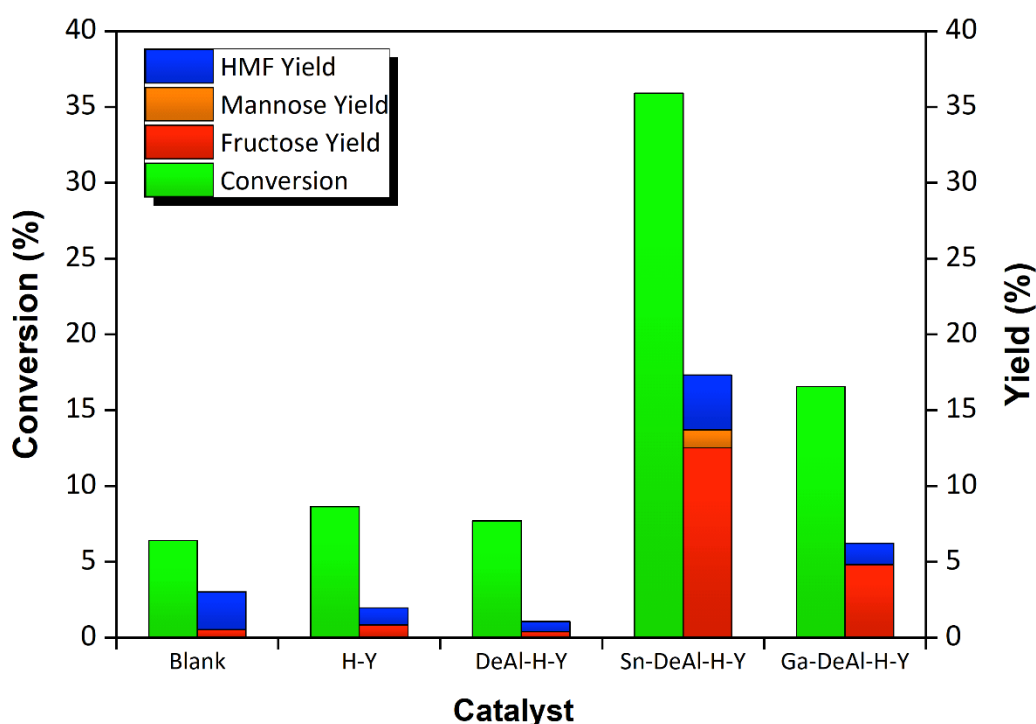


Figure 5.7. Glucose conversion in water on 40 mg zeolite Y catalysts. Reaction conditions: 140 °C, 3 h, stock solution of 10 wt. % glucose in deionized water.

Figure 5.7 illustrates the results from reactions conducted in aqueous solutions. The application of H-Y in the reaction did not significantly improve glucose conversions or product yields when compared to the blank reaction. This is likely due to a lack of Lewis acid sites exhibiting the required strength within H-Y. The reaction results also show DeAl-H-Y to be an ineffective catalyst for glucose isomerisation and HMF production in water. Again this is likely due to an absence of Lewis acid sites within the material. In contrast, the addition of Sn into the framework of the zeolite Y resulted in a substantial gain in catalyst activity and selectivity. Specifically, Sn-DeAl-H-Y generated a 35.9 % glucose conversion as

well as a noticeable gain in desirable product yields. In particular, a fructose yield of around 12.5 % was obtained using Sn-DeAl-H-Y. Considering the low activity of basic SnO₂ as a glucose isomerisation catalyst, the high activity of Sn-DeAl-H-Y further indicates the presence of tetrahedrally coordinated Lewis acid Sn sites within the materials framework.^{26,53,74,78,171} The introduction of Ga within the material also increased glucose conversion and product yields. However, this increase was not as dramatic as Sn-DeAl-H-Y. This is somewhat surprising given the higher acidity of Ga-DeAl-H-Y. However, the lower activity of Ga-DeAl-H-Y may be explained by acid site strength. As seen in **Table 5.3**, NH₃ desorption occurs at a much higher temperature in the Ga containing material. This suggests that Ga-DeAl-H-Y contains stronger acid sites than its Sn counterpart. Moreover, the difference in catalytic performance between Ga and Sn containing materials may be due to a difference in acid site strength.

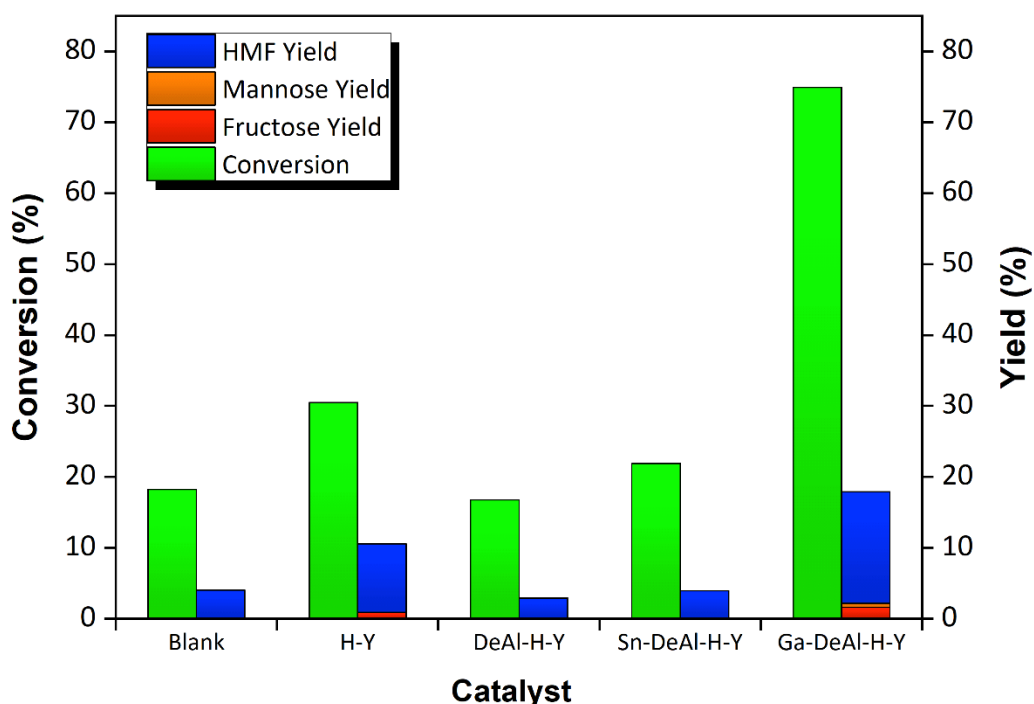


Figure 5.8. Glucose conversion in acidic medium (pH = 1.0) on 40 mg of zeolite Y catalyst. Reaction conditions: 140 °C, 3 h, stock solution of 10 wt. % glucose.

The HMF yields generated by Sn-DeAl-H-Y and Ga-DeAl-H-Y in water were low. This may indicate a lack of Brønsted acidity within the materials. To drive the production of HMF, reactions were repeated in 0.1 M (pH = 1) hydrochloric acid (HCl). The results from these reactions are shown in **Figure 5.8**. The presence

of HCl increased glucose conversion in the blank reaction to around 18.2 % although desirable product yields remained low. Interestingly, the addition of H-Y in the reaction generated a higher glucose conversion and product yield than Sn-DeAl-H-Y. Perhaps the high density of Cl⁻ ions in the acid solution swamps the Sn active sites, rendering them ineffective. Or perhaps the higher concentration of HCl increases the activation energy barrier in the presence of Sn and not Al or promotes more undesirable side reactions. Indeed, Davis and Co-workers reported a low HMF yield when considering a dual catalyst system containing Sn-Beta and HCl in water.⁷⁹ The addition of Ga-DeAl-H-Y significantly increased glucose conversions and HMF yields. Here, the fructose yield generated by Ga active sites is subsequently dehydrated towards HMF by the mineral acid solution.

Although the combination of HCl and Ga-DeAl-H-Y improved glucose conversions and HMF yields, overall selectivity towards desirable products remained relatively low. The accumulation of side products during the isomerisation of glucose and production of HMF is a common concern and often occurs regardless of the catalyst(s) considered in the reaction. To prevent the formation of side products, different reaction solvents and biphasic systems have been considered in literature. As such, we have chosen to repeat reactions in the aprotic organic solvent DMSO. The effect of DMSO on reactions is twofold. First, the use of this aprotic solvent has been shown to reduce the formation of humins.¹⁸⁶ Second, DMSO has been shown to catalyse the fructose dehydration step in the reaction pathway towards HMF.¹⁸⁷ As such, DMSO may enhance HMF yields when combined with heterogeneous acid catalysts.

As shown in **Figure 5.9**, a blank DMSO reaction generated a glucose conversion of around 60 %, although reaction selectivity towards fructose, mannose and HMF were extremely low. A similar trend was obtained when using H-Y and DeAl-H-Y in the reaction. However, the addition of Sn-DeAl-H-Y to the reaction resulted in a HMF yield of around 21.9%. Moreover, this HMF yield is higher than that produced in either water or HCl when using the same catalyst. The lack of fructose within the Sn-DeAl-H-Y catalysed reaction suggests that the dehydration step within the reaction mechanism is faster than the prerequisite isomerisation step. The use of Ga-DeAl-H-Y within the reaction generated a glucose conversion of around 77.6 % and a HMF yield of 33.1 %. This is the highest HMF yield

generated in this study. Again, the lack of fructose within the post-reaction solution suggests that glucose isomerisation is the rate-limiting step when using metal-containing zeolite Y catalysts in DMSO.

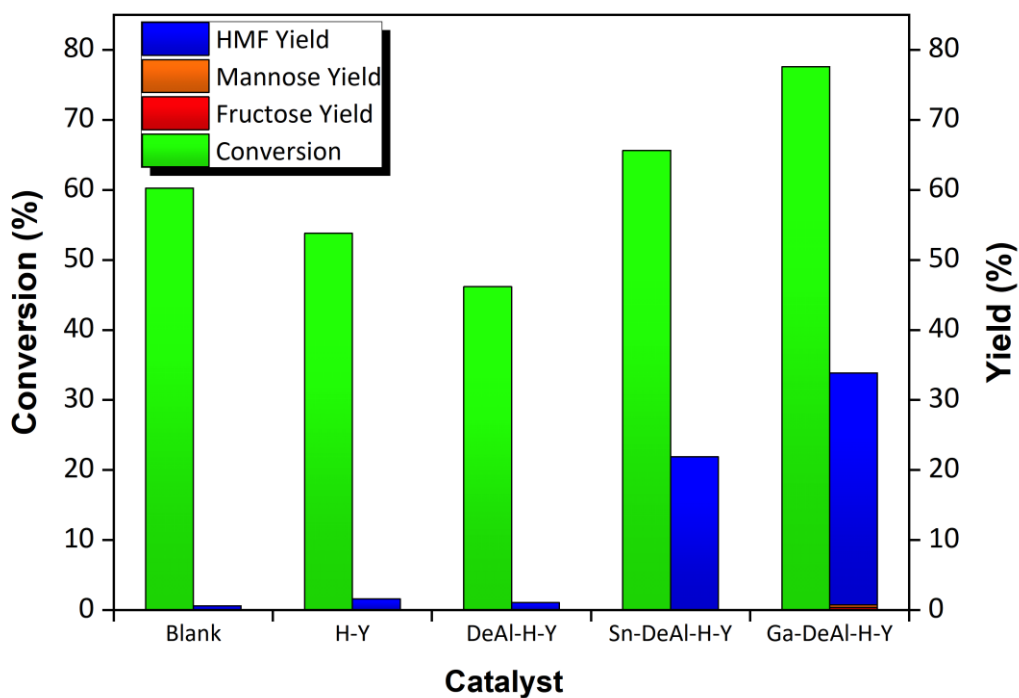


Figure 5.9. Glucose conversion in DMSO on 40 mg of zeolite Y catalyst. Reaction conditions: 140 °C, 3 h, stock solution of 10 wt. % glucose in DMSO.

Fructose Dehydration to HMF

To better access the implications of the rate determining isomerisation step, reactions were performed using an aqueous fructose feedstock. As observed in **Figure 5.10**, the blank reaction produced a fructose conversion of around 17.8 % as well a considerably high selectivity towards HMF (15.1 % HMF yield). The production of HMF from fructose has been documented as autocatalytic, with the autonomous production of acids (such as formic acid) from fructose at elevated temperatures catalysing the dehydration of the feedstock towards HMF.⁹¹ In comparison, the Sn and Ga containing materials generated fructose conversions of 53.5 % and 52.7 %, respectively. This is a significant increase when compared to the blank reaction. The resulting HMF yields generated by these metal-containing zeolites were also higher than the blank reaction by around 5 %. This may suggest that these zeolites exhibit mild Brønsted acidity. The addition of metal-containing zeolite Y catalysts to the reaction also resulted in the production of low quantities of glucose and mannose. The production of these sugars from fructose serves to highlight the isomerisation capabilities of these metal-containing zeolites.

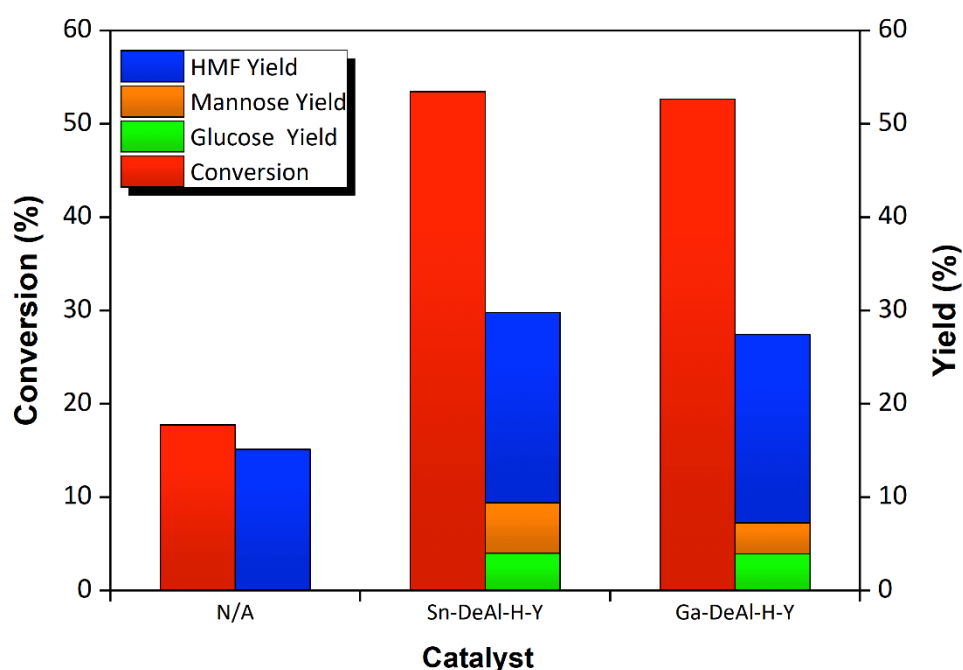


Figure 5.10. Fructose conversion in deionized water on 40 mg of zeolite Y catalyst. Reaction conditions: 140 °C, 3 h, stock solution of 10 wt. % fructose.

Catalyst Stability & Recycling

Catalyst stability is a crucial feature that must be considered when developing chemo-catalytic processes for industry. The stability of a catalyst can widely impact the economic feasibility of a chemical process, with continuous replacement of catalyst contributing tirelessly to operating costs. For this reason, the stability of Sn-DeAl-H-Y and Ga-DeAl-H-Y is now examined. Quantification of catalyst stability was achieved through ICP analysis of filtered reaction solutions. The results of which are shown in **Table 5.4**. Regardless of solvent, Sn-DeAl-H-Y is shown to have superior stability in comparison to Ga-DeAl-H-Y. The leaching of Sn is shown, surprisingly, to be highest in water; although the amount of Sn leached here is considered minimal. Overall, the amount of Sn leached from Sn-DeAl-H-Y is calculated as 0.54 % or less regardless of reaction solvent. In comparison, the quantity of Ga leached from the Ga-DeAl-H-Y is far greater. As shown, the stability of the Ga-DeAl-H-Y is greatest in water and DMSO. Here, Ga leaching from the material is calculated at around 10.5 % and 13.3 % respectively. The highest quantity of Ga leaching was thus seen in the mineral acid solution. The amount of Ga leached here was around 54.5 %.

Table 5.4. Sn and Ga content in post reaction solutions. Reactions consisted of 40 mg catalyst and 3 mL of stock solution (140°C, 3 h).

Catalyst	Reaction medium	Sn (ppm)	Ga (ppm)
Sn-DeAl-H-Y	Water	2.1	N/A
Sn-DeAl-H-Y	HCl (pH=1.0)	0.4	N/A
Sn-DeAl-H-Y	DMSO	0.5	N/A
Ga-DeAl-H-Y	Water	N/A	32.1
Ga-DeAl-H-Y	HCl (pH=1.0)	N/A	167.2
Ga-DeAl-H-Y	DMSO	N/A	40.7

It is well known that homogeneous Sn ions are unable to facilitate glucose isomerisation in water. Indeed, this was shown by the Davis group.⁵³ Furthermore, SnO₂ is only able to catalysis glucose isomerisation in water when contained within the hydrophobic structure of beta zeolite.⁷⁴ However, there are fewer studies on the use of homogeneous Ga species for glucose isomerisation. As such,

the performances of gallium nitrate ($\text{Ga}(\text{NO}_3)_3$) and gallium oxide (Ga_2O_3) were tested in water and HCl.

Table 5.5. Glucose conversions using gallium nitrate and gallium oxide in water and 0.1 M HCl. Reaction conditions: 140 °C, 3 h, 3 mL of 10 wt. % glucose.

Entry	Catalyst	Solvent	Conversion	Yield		
				Fructose	Mannose	HMF
1	Ga_2O_3	Water	6.6	1.0	0.0	2.7
2	$\text{Ga}(\text{NO}_3)_3$	Water	58.9	6.2	1.1	22.0
3	$\text{Ga}(\text{NO}_3)_3$	0.1 M HCl	94.8	0.9	0.4	10.3

As seen in **Table 5.5**, the addition of Ga_2O_3 to water mediated reactions does not significantly improved glucose conversions or product yields. However, the addition of $\text{Ga}(\text{NO}_3)_3$ to reactions conducted in either water or 0.1 M HCl significantly improved glucose conversions and product yields. Specifically, the addition of $\text{Ga}(\text{NO}_3)_3$ to water mediated reactions generates a glucose conversion of around 58.9 % along with a desirable product yield of 29.3 %. Meanwhile, the addition of $\text{Ga}(\text{NO}_3)_3$ to reactions conducted in 0.1 M HCl generates a 94.8 % glucose conversion along with a 10.3 % HMF yield. Although these conversions and yields are not identical to those generated by Ga-DeAl-H-Y, they do suggest that Ga ions leached from the zeolite may contribute to reaction results.

To access the reusability of the materials considered in this study, recycle reactions were also preformed. Given the superior stability of Sn-DeAl-H-Y in water, it was the first material considered for recycling. The catalyst was recycled a total of four times. After each recycle reaction, the catalyst was recovered and washed via centrifuge before being added back to fresh stock solution. As shown in **Figure 5.11**, the activity of Sn-DeAl-H-Y significantly declined following the initial reaction. Given the stability of Sn active sites within Sn-DeAl-H-Y, leaching is not likely to be the cause of deactivation. Instead deactivation may be attributed to an accumulation of humins on the catalyst. These carbon by-products may deposit on the catalyst surface or within the materials pore network, preventing the movement of glucose to catalytically active Sn sites. Such inhibition will result in the deactivation of the catalyst over time. To remove humin deposits, recycled Sn-

DeAl-H-Y was calcined at elevated temperatures. XRD and SEM analysis reveals that the zeolite Y structure is maintained following calcination (**Figure 5.11**). However, the performance of the catalyst was not regenerated following this high temperature treatment. Indeed, a similar occurrence was seen when the catalysts underwent only a single reaction before calcination. This may suggest that the calcination of humins has a detrimental impact on Sn active sites within the zeolite. Perhaps the burning of humins releases enough moisture to essentially steam the zeolite during calcination. This steaming effect may remove Sn active sites from the material's framework, ultimately rendering the catalyst inactive.

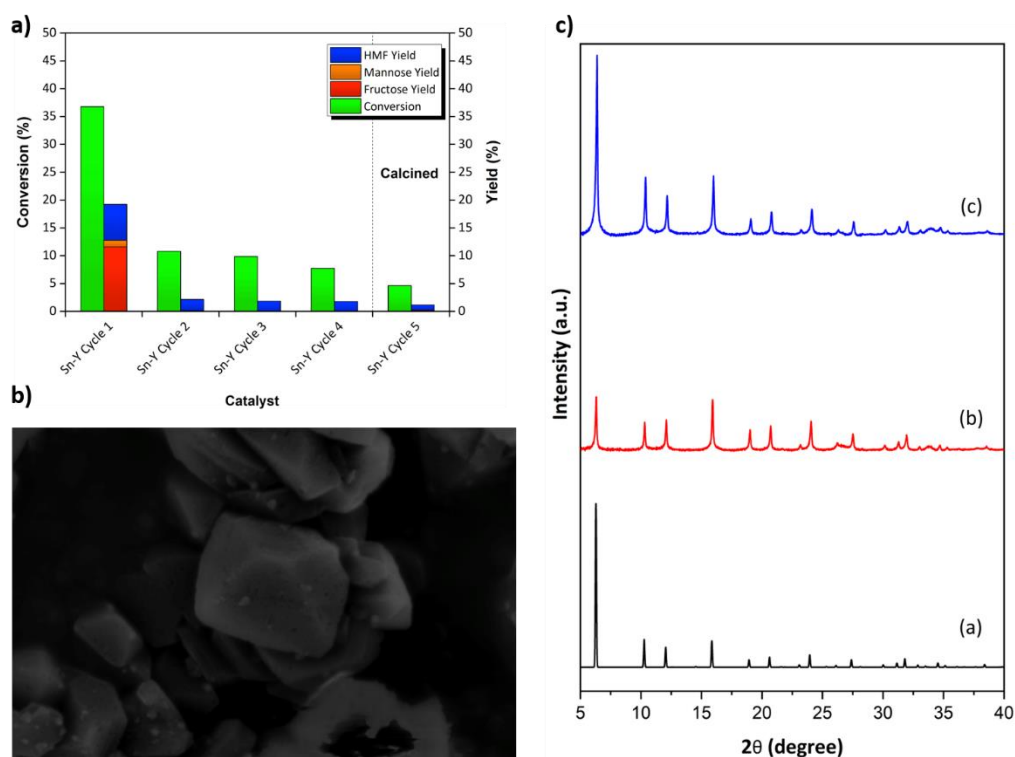


Figure 5.11. **a)** Glucose recycle reactions in water with Sn-DeAl-H-Y. Reaction conditions: 140 °C, 3 h, stock solution of 10 wt. % glucose in deionised water. **b)** SEM image of Sn-DeAl-H-Y post calcination. **c)** XRD of (a) simulated pattern⁶⁸ and XRD of spent Sn-DeAl-H-Y (b) before calcination (c) post calcination.

As previously noted, the use of DMSO as a reaction solvent effectively minimises the formation of humins. As such, recycle reactions were repeated using DMSO in an attempt to sustain activity and aid regeneration. In this instance, the catalyst underwent two reaction cycles before regeneration and further testing. As shown

in **Figure 5.12**, the activity of Sn-DeAl-H-Y remained high following the first reaction in DMSO. This indicates that preventing the formation of humins through a change of solvent may prolong the activity of Sn-DeAl-H-Y. To regenerate catalyst activity, calcination was once again considered. The subsequent calcination of recovered Sn-DeAl-H-Y was found to mildly improve the materials activity. This is in stark contrast to the observations made when using water as a reaction solvent; ultimately suggesting that the formation of humins within the reaction has a preannounced effect on catalyst activity and regeneration.

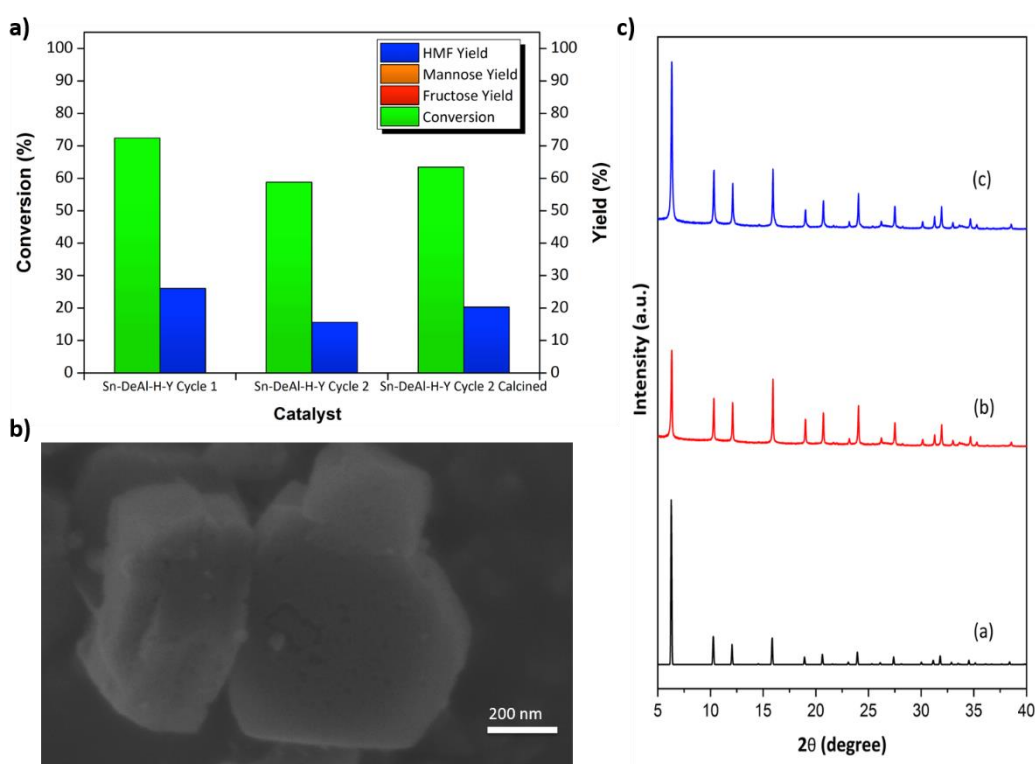


Figure 5.12. a) Glucose recycle reactions in DMSO with Sn-DeAl-H-Y. Reaction conditions: 140 °C, 3 h, stock solution of 10 wt. % glucose in DMSO. b) SEM image of Sn-DeAl-H-Y post calcination. c) XRD of (a) simulated pattern⁶⁸ and XRD of spent Sn-DeAl-H-Y (b) before calcination (c) post calcination.

For comparison, recycle reactions in DMSO were repeated using Ga-DeAl-H-Y. As seen in **Figure 5.13**, the decline in catalytic activity was minimal following the first recycle reaction. Again, this is likely due to DMSO preventing the formation of humins during the reaction. Calcination of the recovered material was also shown to regenerate the activity of Ga-DeAl-H-Y. XRD and SEM analysis of both

Sn-DeAl-H-Y and Ga-DeAl-H-Y following calcination shows that the structure of the zeolites has been preserved. However, as previously discussed, given the quantity of Ga leached during the reaction, it may be possible that homogenous reactions are contributing to glucose conversions and product yields when using Ga-DeAl-H-Y as a catalyst.

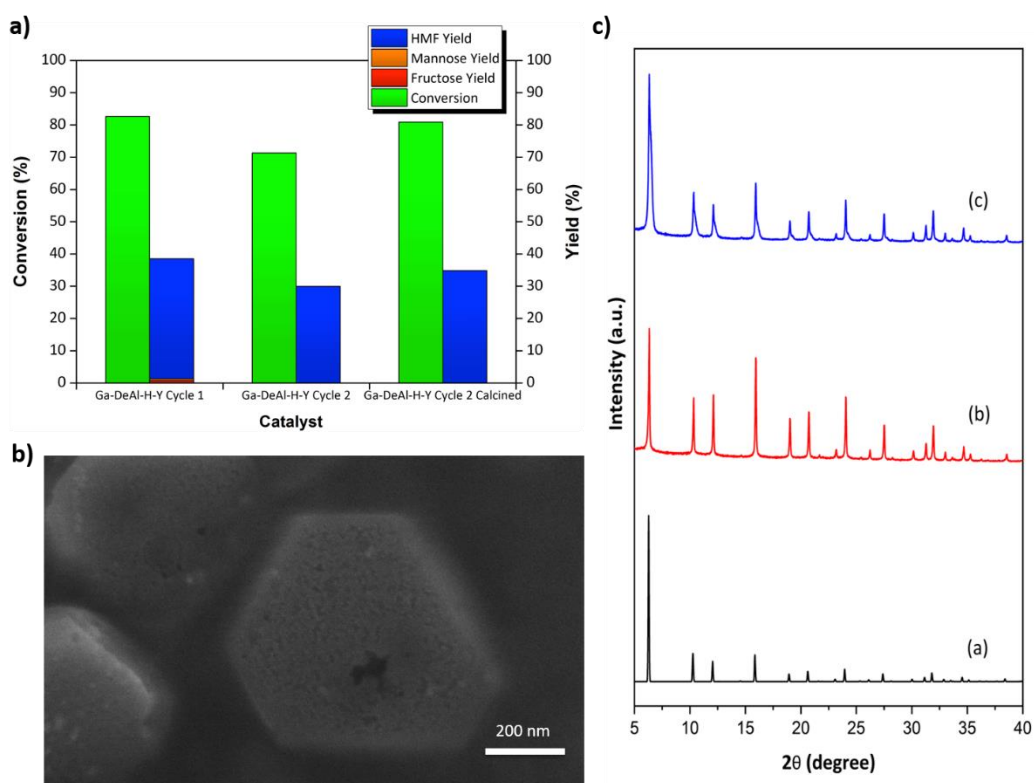


Figure 5.13. a) Glucose recycle reactions in DMSO with Ga-DeAl-H-Y. Reaction conditions: 140 °C, 3 h, stock solution of 10 wt. % glucose in DMSO. b) SEM image of Ga-DeAl-H-Y post calcination. c) XRD of (a) simulated pattern⁶⁸ and XRD of spent Ga-DeAl-H-Y (b) before calcination (c) post calcination.

Reactant to Catalyst ratio

The quantity of catalyst used in a reaction is an important consideration as it may impact the feasibility of potential scale ups. It is therefore usually beneficial to develop processes that require a small quantity of catalyst when compared to the starting amount of reactant. In this study, initial reactions were conducted using a reactant to catalyst ratio of 30:4 (i.e. 40 mg and a 10 wt. % hexose stock solution). Despite having a relatively low ratio, the Sn and Ga containing zeolites were shown to generate significant conversions and product yields within various solvents. Nevertheless, to further evaluate the effectiveness of the catalysts considered in this study, reactions were repeated using a catalyst : reactant ratio of 30:1. As seen in **Table 5.6**, decreasing the catalyst : reactant ratio decreased glucose conversions and product yield. Despite this, the impact of Sn and Ga within the zeolite framework is still largely evident even when considering lower quantities of catalyst.

Table 5.6. Glucose conversion and product yields on 10 mg zeolite Y catalyst after 3 h at 140 °C.

Entry	Reaction medium	Catalyst	Glucose conversion (%)	Fructose yield (%)	Mannose yield (%)	HMF yield (%)
1	Water	H-Y	6.6	0.3	0.0	1.6
2	Water	DeAl-H-Y	5.3	0.1	0.0	1.5
3	Water	Sn-DeAl-H-Y	18.6	6.1	0.4	2.6
4	Water	Ga-DeAl-H-Y	9.1	1.6	0.0	1.4
5	HCl (pH=1.0)	H-Y	21.2	0.2	0.0	6.0
6	HCl (pH=1.0)	DeAl-H-Y	16.6	0.0	0.0	3.9
7	HCl (pH=1.0)	Sn-DeAl-H-Y	16.8	0.0	0.0	3.9
8	HCl (pH=1.0)	Ga-DeAl-H-Y	37.1	0.0	0.0	10.0
9	DMSO	H-Y	42.9	0.0	0.0	0.6
10	DMSO	DeAl-H-Y	23.1	0.0	0.0	0.3
11	DMSO	Sn-DeAl-H-Y	56.4	0.0	0.0	8.2
12	DMSO	Ga-DeAl-H-Y	65.1	0.1	0.4	21.1

The effect of catalyst loading was also explored in fructose reactions. As seen in **Table 5.7**, both Sn-DeAl-H-Y and Ga-DeAl-H-Y generated a ~36 % fructose conversion in water when using a catalyst : reactant ratio of 30 : 1. This is significantly greater than the conversions generated using H-Y and DeAl-H-Y in the same reaction. Furthermore, the Sn and Ga containing materials generated small amounts of glucose and mannose within the reaction, thus indicating their prowess as isomerisation catalysts. Overall, the activity of Sn and Ga materials as isomerisation and dehydration catalysts is largely apparent even when considering lower quantities of catalyst in the reaction.

Table 5.7. Conversions and product yields on zeolite Y catalysts for 10 wt.% fructose reactions in water after 3 h at 140 °C.

Entry	Catalyst	Fructose conversion (%)	Glucose yield (%)	Mannose yield (%)	HMF yield (%)
1	N/A	17.8	0.0	0.0	15.1
2	H-Y	20.4	0.3	0.0	14.7
3	DeAl-H-Y	17.7	0.0	0.0	15.1
4	Sn-DeAl-H-Y	35.1	1.1	1.7	19.1
5	Ga-DeAl-H-Y	36.4	2.1	1.8	16.8

XANES analysis

The catalytic performance of tetrahedrally coordinated Sn sites within the framework of zeolite Y must be better understood in order to develop the catalyst further. A better understanding of the behaviour of Sn within zeolite Y may be obtained through in-situ XANES analysis at the L_{III} edge during reactions. To the best of our knowledge, the values reported hereafter are the first relating to the real time behaviour of Sn active sites during reactions relative to the L_{III} edge.

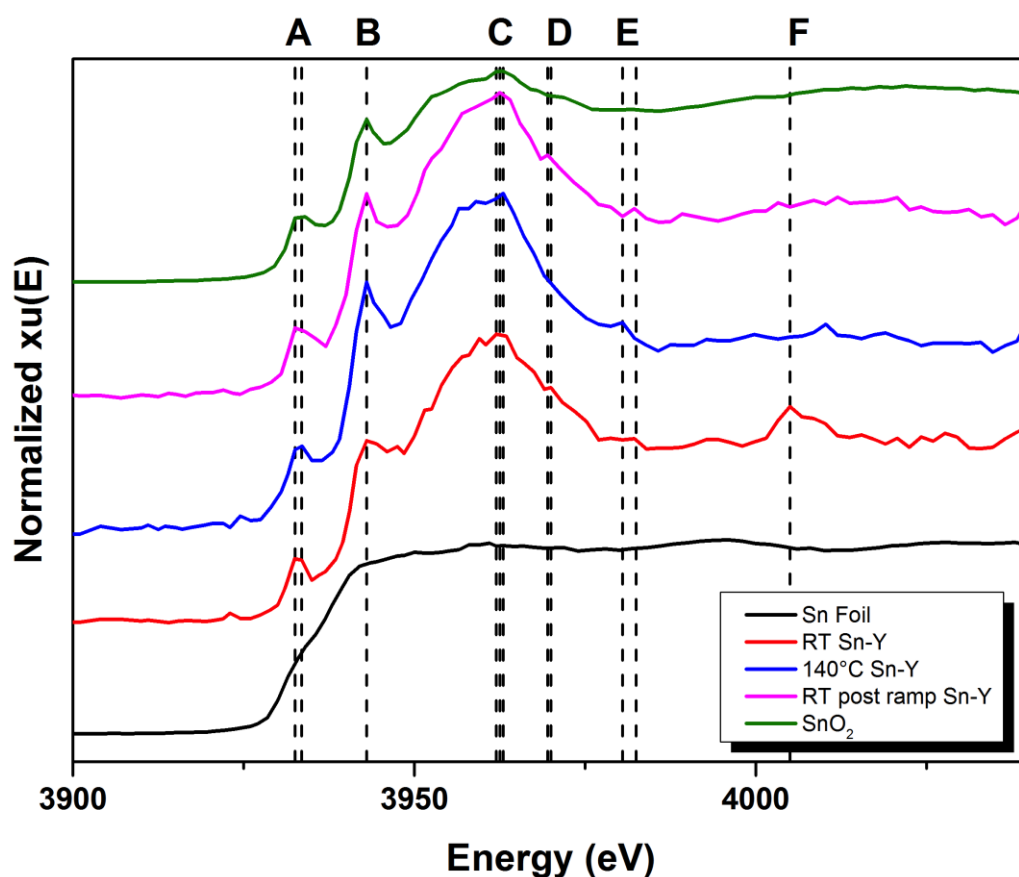


Figure 5.14. In-situ liquid cell results of Sn-DeAl-H-Y in water.

Table 5.8. L_{III} tin edge feature Energies (eV) in water in the absence of sugar.

Feature (eV) / Condition	A	B	C	D	E	F
Room Temperature	3932.5	3943.0	3962.0	3970.0	-	4005.0
At 140 °C	3933.5	3943.0	3963.0	-	3980.5	
Post reaction	3932.5	3943.0	3962.5	3969.5	3982.5	

XANES analysis at the L_{III} Sn edge was first performed in water in the absence of glucose (blank reaction). Scans were taken at room temperature (RT), 140 °C, and again after cooling, the results of which are shown in **Figure 5.14**. For comparison, results obtained from reference materials (tin foil and bulk tin oxide) at RT are also shown. The results obtained from these reference samples are within relatively good agreement with those reported in literature (5 eV difference).¹⁸⁸ When comparing the reference materials with Sn-DeAl-H-Y, we can clearly see that the Sn sites contained within the catalyst mostly resemble that of bulk SnO₂.

The XANES scans show several prominent features before and after the main edge peak. For convenience these have been labelled “A” – “F”. The energies of these peaks are given within **Table 5.8**. Within Sn-DeAl-H-Y, the relative intensities between pre-edge peaks “A” and “B” are greater than those observed in SnO₂. Heating the catalyst to 140 °C causes a 1 eV energy change at features “A” and “C”. In addition, features “D” and “F” become significantly less prominent as a result of heating whilst another peak (“E”) becomes more so. Upon cooling of the sample, further changes are observed at the L_{III} edge. Specifically, there are changes at the post-edge peak “E” and the relative intensity of “F” also changes. Overall, these results suggest that there are local changes at the materials Sn sites during heating and cooling.

XANES analysis was also conducted in the presence of water and glucose. These results are shown in **Figure 5.15** and **Table 5.9**. Again, the Sn sites within the structure of Sn-DeAl-H-Y produce a spectrum most comparable to that of the bulk oxide. Changes at the L_{III} edge were observed upon heating. Namely a 1 eV decrease in the energy was observed at the pre-edge feature “B” and a 1 eV increase was observed at “C”. These changes are different to those observed in the blank reaction, thus illustrating an interaction between glucose and Sn active sites. Furthermore, in comparison to the blank reaction, there is a complete absence of the post-edge peak “E” in the presence of glucose and the relative intensity of peak “F” is greatest upon heating.

As described in literature, L_{III} edge peaks can be used to observe interactions between Sn and organics.^{189,190} Thus, we now compare the relative peak intensities at the pre-edge and edge peaks from the blank reaction and glucose reaction

spectra. At room temperature, the relative height ratio between pre-edge peaks “A” and “B” is lower in the blank solution whilst the ratio between “B” and “C” is higher. However, upon heating the solutions to 140 °C, the relative ratio of “B” and “C” is higher within the reaction solution. This may indicate an interaction between glucose and Sn active sites during the reaction.

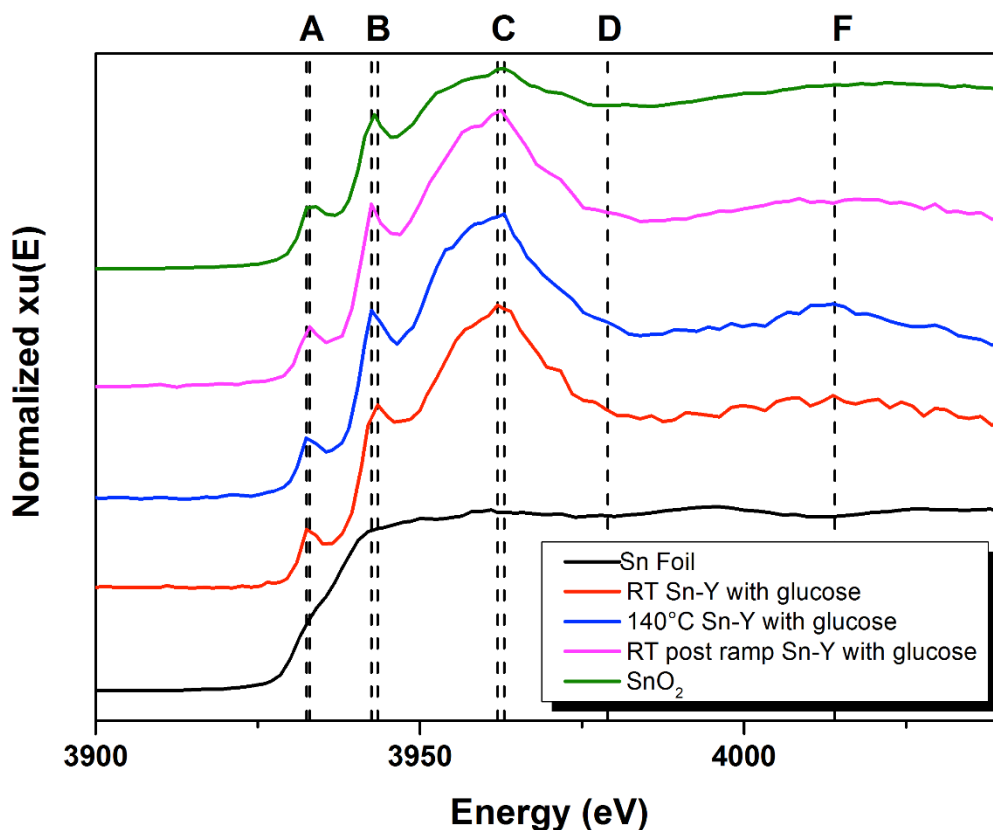


Figure 5.15. XANES spectra of Sn-DeAl-H-Y in water with glucose.

Table 5.9. L_{III} tin edge feature Energies (eV) in water with glucose.

Feature (eV) \ Condition	A	B	C	D	E	F
Room Temperature	3932.5	3943.5	3962.0	3979.0	-	4014.0
At 140 °C	3932.5	3942.5	3963.0	-	-	-
Post reaction	3933.0	3942.5	3963.0	-	-	-

5.3 Conclusions

Sn and Ga containing zeolite Y may be produced using a simple and scalable method. Both Sn-DeAl-H-Y and Ga-DeAl-H-Y have different acidity profiles as illustrated by NH₃-TPD analysis. Moreover, Ga-DeAl-H-Y is considerably more acidic than Sn-DeAl-H-Y. Of the materials considered, Sn-DeAl-H-Y was found to be the most stable and active catalyst for glucose isomerisation in water. Meanwhile, Ga-DeAl-H-Y was shown to generate the highest activity and HMF yield when reactions were conducted in DMSO. However, it should be noted that Ga leaching is an issue with this particular catalyst. Indeed, Ga ions leached from Ga-DeAl-H-Y during reactions may act as homogeneous acid catalysts; facilitating glucose conversions and increasing product yields.

To test the reusability of materials, recycle reactions were conducted. To begin, the recyclability Sn-DeAl-H-Y in water was considered. Here, the activity of the catalyst rapidly declined following the first reaction cycle and could not be regenerated. This decrease in catalytic performance was attributed to the formation of humins on Sn active sites. Moreover, we suspect that the moisture released by these insoluble humins during calcination may effectively steam the catalyst, removing active Sn sites from the materials framework and rendering it inactive.

In order to improve the recyclability of Sn-DeAl-H-Y, reactions were repeated in DMSO. As noted in the literature, this aprotic organic solvent is thought to minimise the formation of humins during reaction. Indeed, Sn-DeAl-H-Y demonstrated excellent activity over the course of two recycle reactions in DMSO and could be regenerated (to some extent) via calcination. Moreover, this result indicates that catalytic activity can be maintained by preventing the formation of humins.

The recyclability of Ga-DeAl-H-Y was also tested in DMSO. Like Sn-DeAl-H-Y, this catalyst demonstrated excellent activity over the course of the recycle reactions and its performance could be restored (to some extent) via calcination. However, as previously noted, the excellent performance of this catalyst may be significantly influenced by leached Ga ions. Indeed, Ga ions leached from the catalyst are likely contributing significantly toward the glucose conversions and product yields observed in these reactions.

XANES analysis of Sn-DeAl-H-Y was conducted during glucose isomerisation reactions in water using a purpose built sample holder. This is the first time a liquid reaction of this nature has been studied in real time using XANES analysis. The results of this analysis illustrate changes at the L_{III} Sn edge during heating and in the presence of glucose.

Chapter 6

Exploring Metal-Organic Frameworks for the Isomerisation of Glucose and Production of 5-Hydroxymethylfurfural.

Summary

Metal-organic frameworks (MOFs) are an emerging interest within the field of catalysis. The tuneable chemical and physical properties of these porous materials leads to the development of ‘designer catalysts’. In this chapter the use of MOFs for the isomerisation of glucose and production of HMF is explored. The MOFs considered are known frameworks previously reported in literature. In total, four different frameworks were studied - each with their own unique properties.

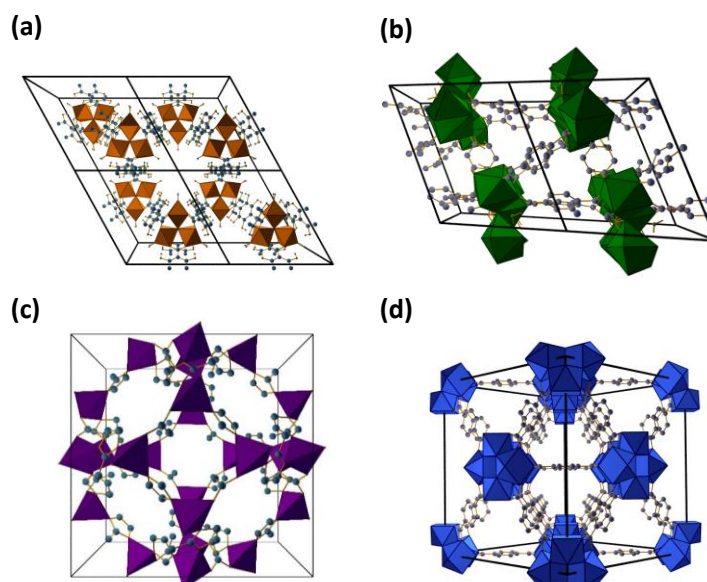
To begin, the application of iron (Fe) and scandium (Sc) MIL-88B in DMSO was considered. This non-toxic framework is a close relative to the chromium (Cr) MIL-101 catalysts already reported in literature for HMF production. The best catalytic results found in this study were obtained using a MIL-88B material containing a disproportional mixture of Fe and Sc active sites. However, each of the materials considered in this initial study were found to be hydrothermally unstable and did not retain their activity during recycle reactions in DMSO.

Following this initial study, we focused on the development of water stable MOFs. As such, a ytterbium (Yb) framework with the molecular formula $\text{Yb}_6(\text{BDC})_7(\text{OH})_4(\text{H}_2\text{O})_4$ was considered for catalysis. The catalytic performance of this MOF was tested in water and HCl (pH 2.5). The catalytic performance of $\text{Yb}_6(\text{BDC})_7(\text{OH})_4(\text{H}_2\text{O})_4$ is significantly lower than homogenous $\text{YbCl}_3 \cdot 6\text{H}_2\text{O}$; and its selectivity towards target products is reduced after only one recycle reaction. ICP analysis shows that approximately 5 % of the catalysts Yb content is leached during each recycle reaction. Furthermore, a control experiment shows that this leached Yb may contribute towards the catalytic results observed in the

recycle reactions. In addition, the synthesis of $\text{Yb}_6(\text{BDC})_7(\text{OH})_4(\text{H}_2\text{O})_4$ has not yet been optimised, and at present, only a small amount of material can be made using a synthesis process that requires multiple steps.

To address issues related to scale-up, the catalytic performance of ZIF-8 was considered. An extremely well known framework, ZIF-8 can be made in continuously flow and is commercially available. Moreover, the catalytic activity of ZIF-8 was found to be extremely promising in batch reactions. However, the activity of this catalyst quickly diminished within a flow reactor.

Finally, UiO-66 was considered as a catalyst for the isomerisation and dehydration of glucose. Not only is this framework hydrothermally stable, it has the added benefit of being non-toxic, making it an ideal choice for the development of truly green chemical processes. UiO-66 was found to be an excellent glucose isomerisation catalyst in water. The performance of this material was improved through the introduction of sulfonic acid functionalised linker. Furthermore, both UiO-66 and its functionalised variants were found to be stable during four consecutive recycle reactions in water. Overall, UiO-66 catalysts were found to be of considerable interest and are explored in greater detail in the **Chapter 7**.

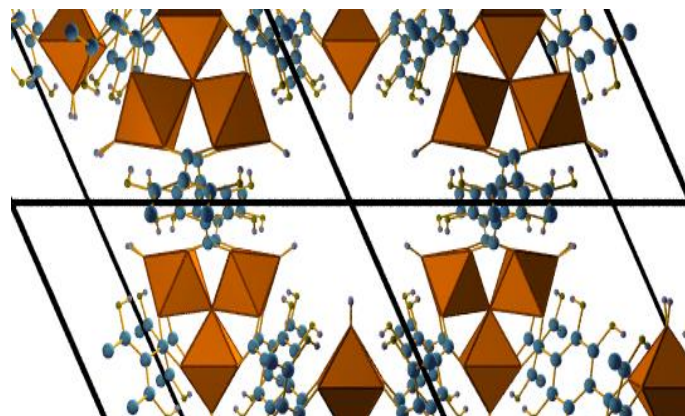


Graphical Abstract: The structures of the MOF catalysts considered in this chapter; MIL-88B (Top Left), $\text{Yb}_6(\text{BDC})_7(\text{OH})_4(\text{H}_2\text{O})_4$ (Top Right), ZIF-8 (Bottom Left)¹⁹¹, UiO-66 (Bottom Right)

Iron and Scandium MIL-88B as a non-toxic alternative to Chromium Containing MIL-101 for glucose isomerisation and HMF production.

Summary

Recent literature has shown that chromium (Cr) containing MOFs may be used to effectively catalyse the isomerisation of glucose and production of HMF. However, the use of Cr raises toxicity concerns that may hinder future process scale-up. In order to address these issues, the development of non-toxic catalysts is needed. In this study, we explore the use of non-toxic iron (Fe) and scandium (Sc) containing MIL-88B as alternative catalysts for fructose and HMF production. The best catalyst found in this study was a bimetallic material containing a disproportional mixture of Fe and Sc. Specifically, (FeSc)MIL-88B was able to generate a glucose conversion of 70 % and a desirable product yield of 29.6 %. Although the performances of selected catalysts drops during recycle reactions, the overall reaction yields presented in this study highlights the potential to develop non-toxic MOF catalysts for HMF production.



Graphical Abstract: MIL-88B structure.

6.1 Introduction

Metal-organic frameworks (MOFs) are a new class of materials that have attracted considerable attention in recent years. However, new MOFs have been developed at a rate that far surpasses research focusing on their potential applications. As a result, MOFs are now considered an emerging interest within numerous research fields including catalysis. Indeed, several recent review articles have attempted to highlight the potential benefits, opportunities, and pitfalls, of working with MOFs in a growing catalyst industry worth upwards of \$ 20 billion.^{168,192-195}

Relatively few research groups have considered the application of MOF catalysts in the isomerisation of glucose and production of HMF. Of these, many have chosen to focus their attention on the use of chromium (Cr) containing MIL-101 in organic solvents.^{62,130,131,196,197} Although promising yields and selectivities can be obtained from this catalyst, the use of Cr entails toxicity concerns and the application of organic solvents is not ideal.¹⁰⁹ The structure of MIL-101 is similar to that of MIL-88B (containing a trimer metal brickwork and BDC struts) and each material may be formed simultaneously during synthesis.¹⁹⁸⁻²⁰³ Furthermore, the metal centres contained within some MIL-88B materials, such as (Fe)MIL-88B, provide sufficient Lewis acidity to promote various reactions.^{204,205} As such there is scope to potentially develop non-toxic MIL-88B catalysts for the production of value-added products (fructose and HMF) from glucose.

In this study, MIL-88B is explored as a glucose isomerisation and dehydration catalyst. Both Fe and Sc variants of this non-toxic framework are considered as well as a bimetallic material. Given the instability of MIL-88B in water, reactions were conducted in DMSO. An aprotic solvent, DMSO is known to promote HMF production whilst also suppressing humin formation.^{186,187,206} Reactions were conducted at two different temperatures, 120 °C and 140 °C. The choice of these two reaction temperatures is based on the stability of MIL-88B. To assess the reusability of promising catalysts, recycle reactions were performed.

6.2 Results and Discussion

Structure and Morphology

Conformation of the MIL-88B structure was obtained by powder X-ray diffraction (XRD) analysis. As shown in **Figure 6.1**, there are no additional peaks within the diffraction patterns of these synthesised materials. This suggests an absence of bulk extra-framework metal species and uncoordinated BDC linker within each of the MIL-88B samples. MIL-88B is a ‘breathing’ framework – meaning its structure (unit cell) may expand or contract as a result of external influences such as the presence of different solvents or gases.^{200,207} Furthermore, the size of the materials unit cell may be influenced by the presence of different metals within its framework. To quantify this effect, the diffraction pattern of each material was fitted (GSAS software package). As seen in **Figure 6.1**, (Sc)MIL-88B was found to have a larger unit cell volume than (Fe)MIL-88B. This is unsurprising given the larger size of Sc atoms. Following this trend, the mixed metal material was found to have a larger unit cell volume than (Fe)MIL-88B.

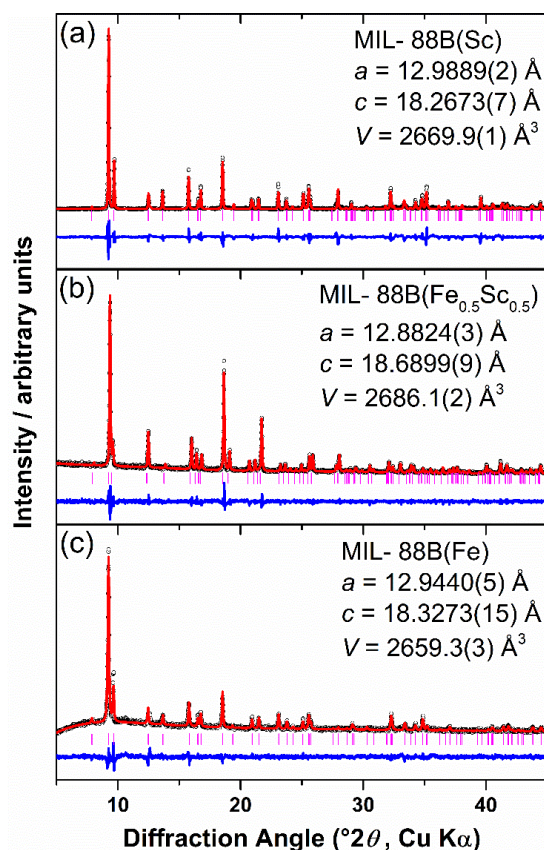


Figure 6.1. Fitted diffraction patterns of synthesised MIL-88B materials.

For synthesis, equimolar quantities of Fe and Sc were used to obtain a bimetallic framework. However, it may be possible that higher quantities of one metal species may be incorporated into the MIL-88B structure during synthesis – resulting in a MOF with unequal quantities of Fe and Sc. To ensure the presence of both metals within (FeSc)MIL-88B, the material was analysed using Energy-dispersive X-ray spectroscopy (EDX) mapping. As seen in **Figure 6.2**, EDX mapping of (FeSc)MIL-88B suggests that the material contains both Fe and Sc. This is a good indication that both metals have been successfully incorporated into the material's framework.

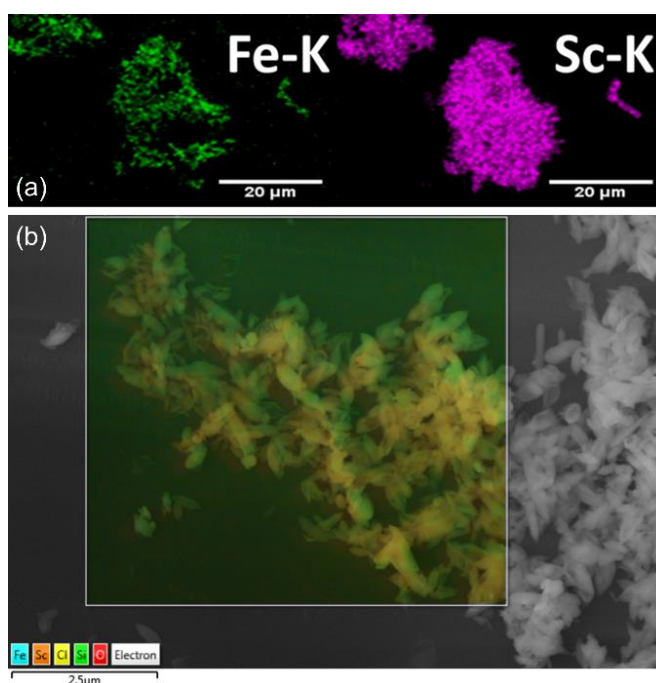


Figure 6.2. EDX mapping of (FeSc)MIL-88B.

To further quantify the amount of Fe and Sc within the bimetallic material, inductively coupled plasma (ICP) analysis and X-ray photoelectron spectroscopy (XPS) analysis was used. ICP analysis of (FeSc)MIL-88B reveals that the bulk material contains significantly more Sc than Fe (3.1:1 ratio). Furthermore, XPS analysis reveals that the material's surface is Sc rich, containing approximately 6 times more Sc than Fe (**Figure 6.3**). The majority of this Sc is octahedrally coordinated which suggests that it is part of the MIL-88B framework (**Figure 6.3a**). However, at least some of the Sc at the materials surface is extra-framework.

XPS analysis also shows that the material contains both Fe^{2+} and Fe^{3+} . This may suggest that the catalyst also contains both framework and extra-framework Fe.

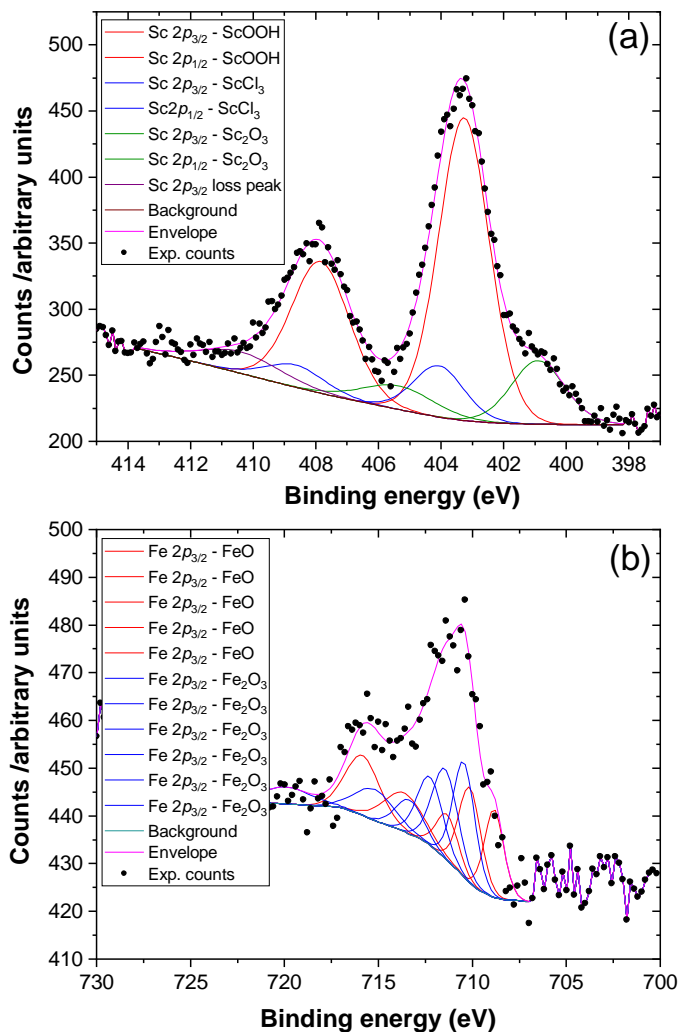


Figure 6.3. X-ray photoelectron spectroscopy (XPS) analysis of (FeSc)MIL-88B (a) Sc content (b) Fe content.

As seen in **Figure 6.4**, the FTIR spectrum obtained from (FeSc)MIL-88B contains a strong additional peak at around 1685 cm^{-1} which may be attributed to free C=O groups within the material's structure.²⁰⁸ In turn, this would suggest the presence of loose or partly coordinated linker within the material's framework. Furthermore, this peak is less apparent, or indeed absent, in the other FTIR spectra collected. As such, this indicates that (FeSc)MIL-88B may be considerably more defective than the pure metal materials. Meanwhile, there is an absence of a broad peak at around 3441 cm^{-1} in each FTIR spectra. This indicates that the materials do not contain large amounts of absorbed water.²⁰⁹

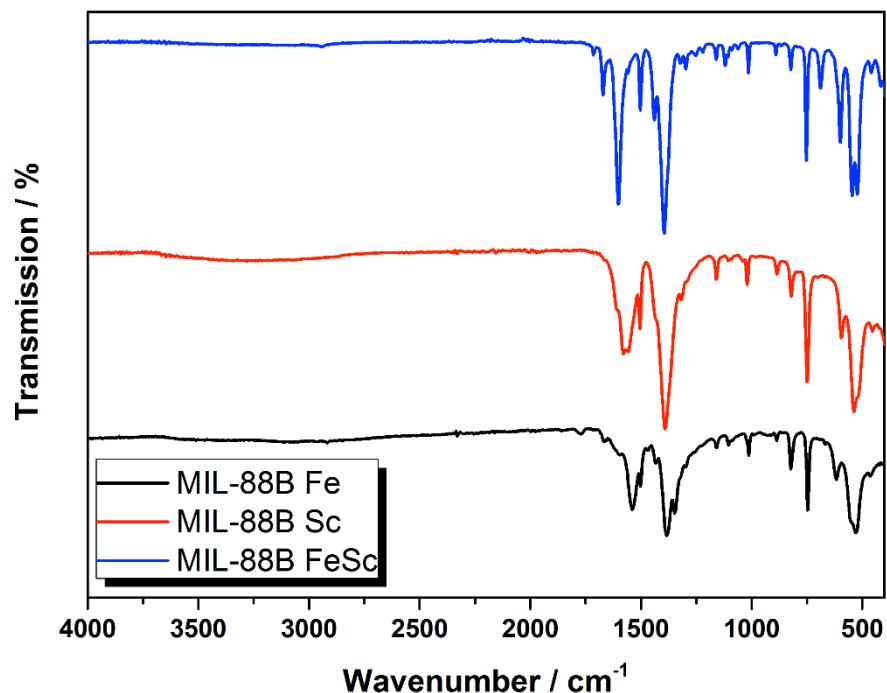


Figure 6.4. FTIR analysis of Fe and Sc containing MIL-88B catalysts.

Thermal gravimetric analysis (TGA) was used to determine the thermal stability of materials. As seen in **Figure 6.5**, the removal of residual organic solvent and water molecules from (Fe)MIL-88B occurs between 150 °C and 320 °C. Overall, it appears the amount of solvent/water removed from (Fe)MIL-88B is slightly larger than that removed from (Sc)MIL-88B. This may indicate that (Fe)MIL-88B has a great affinity towards solvent molecules.

The thermal decomposition of each material occurred above 400 °C. Interestingly, the TGA profile of (FeSc)MIL-88B shows a second prominent feature above this decomposition temperature. This secondary feature may be attributed to the decomposition of partly coordinated linker within the materials structure and suggests that (FeSc)MIL-88B contains a large number of defective sites. In comparison, this secondary feature is less apparent - or indeed absent - in the TGA profiles of Fe and Sc MIL-88B. Again this indicates that the bimetallic material is significantly more defective than the single metal MOFs.

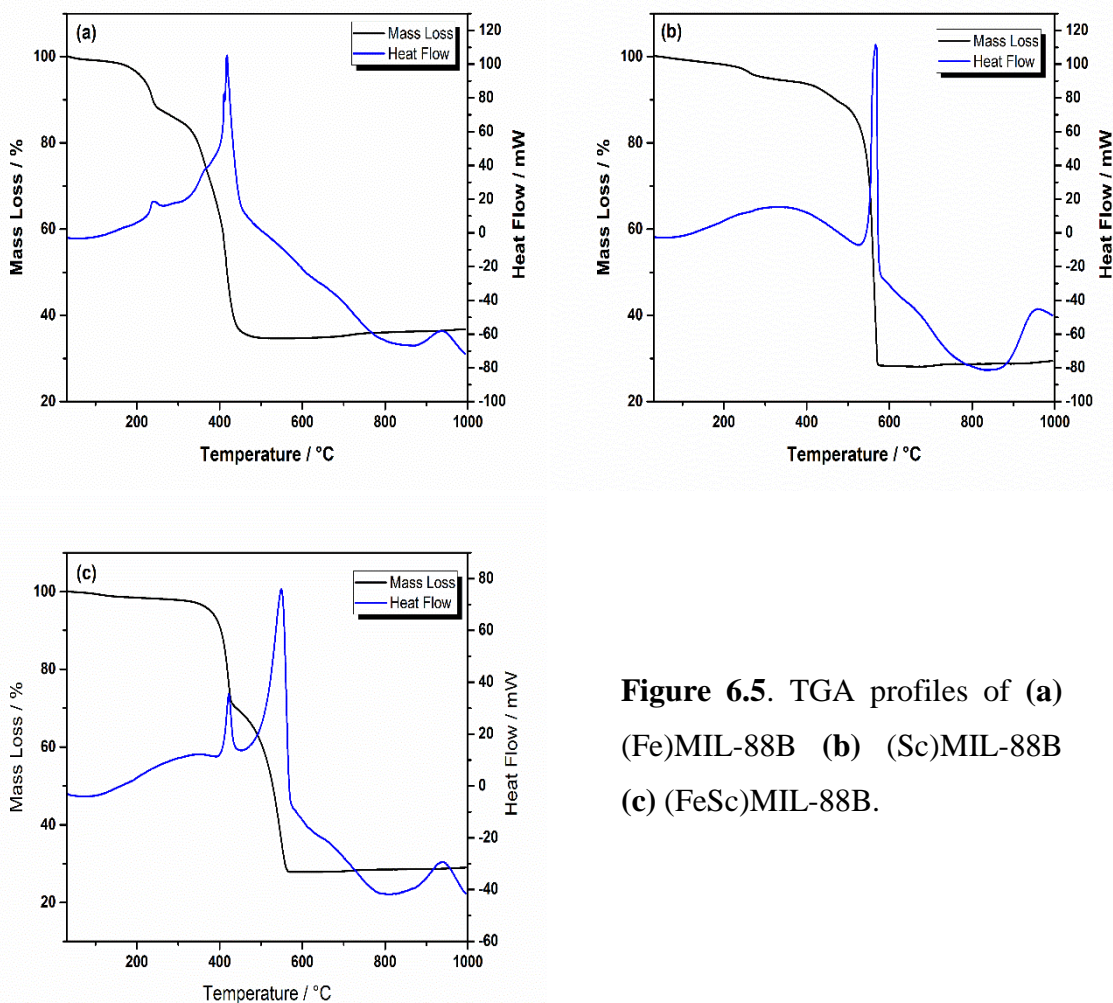


Figure 6.5. TGA profiles of (a) (Fe)MIL-88B (b) (Sc)MIL-88B (c) (FeSc)MIL-88B.

Ammonia temperature programmed desorption (TPD) was used to quantify the acidity of (Fe)MIL-88B and (FeSc)MIL-88B. This was done using a homemade apparatus. The accuracy of this equipment was verified by measuring the acidity of commercial ZSM-5, Beta zeolite, and H-Y (see zeolite chapters). The TPD studies were performed by dosing ammonia (in helium) onto 50-70 mg of catalyst contained within a quartz tube. In order to minimise physisorption, the quartz tube was maintained at 100 °C. The ammonia was then desorbed from the catalysts by heating the material to 350 °C at a ramp rate of 3 °C min⁻¹. To ensure the complete desorption of ammonia from the material, the temperature was then maintained at 350 °C for 6 h. The amount of ammonia desorbed from the catalyst was measured using a mass spectrometer and quantified at $m/z = 17$ (with the interference of water vapour taken into account.) A blank (baseline) experiment was also performed with fresh catalyst in the absence of ammonia.

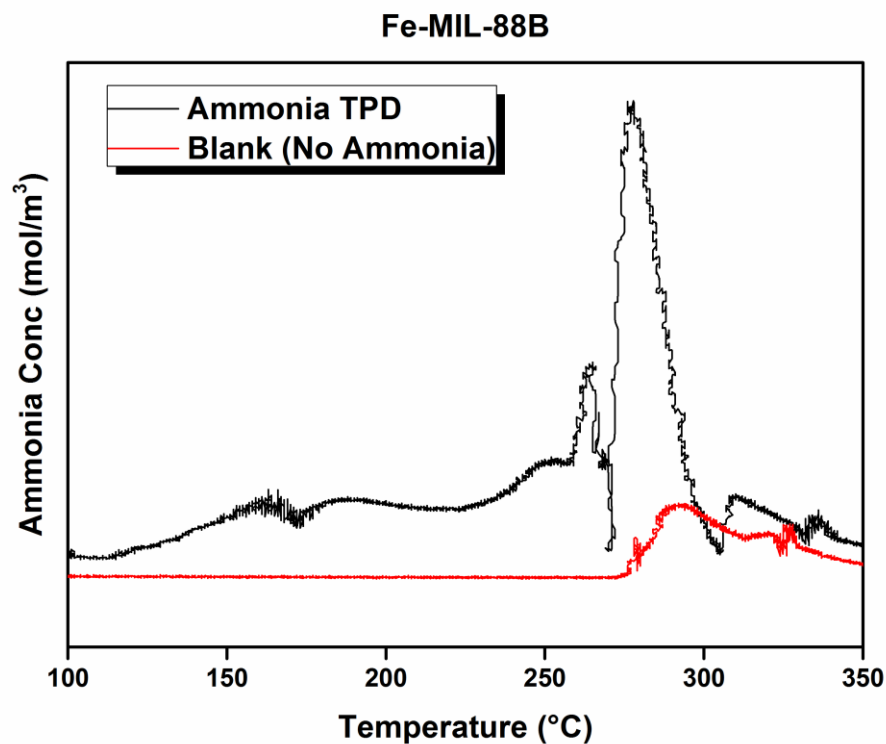


Figure 6.6. Ammonia TPD of (Fe)MIL-88B including a ‘blank’ experiment conducted in the absence of ammonia.

As seen in **Figure 6.6**, heating (Fe)MIL-88B in the absence of ammonia (blank) produces a signal on the mass spectrometer. This may be due to the removal of residual organic solvent or water from the material during heating. This signal may also indicate that the thermal decomposition of (Fe)MIL-88B begins at 300 °C. Regardless, the signal generated in the blank reaction is considerably smaller than that produced during the ammonia TPD measurement and is therefore regarded as negligible.

The ammonia TPD measurement of (Fe)MIL-88B produces numerous peaks. This abundance of peaks suggests that the material contains a number of different acid sites. To calculate the total acidity of (Fe)MIL-88B, the baseline (blank experiment) was subtracted from the ammonia TPD measurement. The resulting acidity of the material was calculated as 1.69 mmol g⁻¹.

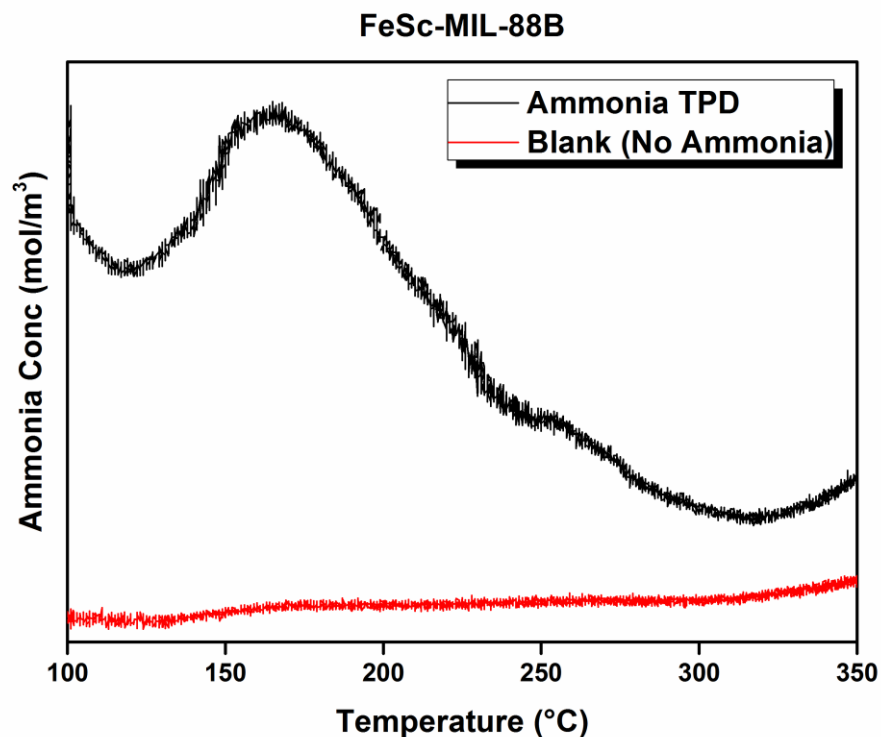


Figure 6.7. Ammonia TPD of (FeSc)MIL-88B including ‘blank’ experiments conducted in the absence of ammonia.

In comparison to (Fe)MIL-88B, heating (FeSc)MIL-88B in the absence of ammonia does not produce a signal on the mass spectrometer (**Figure 6.7**). This is not surprising as the TGA measurements suggests that the bimetallic material contains less residual solvent/water and is thermally stable at 350 °C.

The ammonia desorption pattern of (FeSc)MIL-88B is significantly different to that produced by (Fe)MIL-88B. Specifically, the ammonia TPD measurement of (FeSc)MIL-88B produces a large prominent peak at around 160 °C - and possibly smaller peaks between 200 °C and 300 °C. The large peak at 160 °C suggests that the material contains a large quantity of one particular acid site. Overall the acidity of (FeSc)MIL-88B is calculated as 0.36 mmol g⁻¹. Given that the bimetallic material contains significantly more Sc than Fe, one might assume that Sc is responsible for the majority of the materials acidity.

Glucose dehydration to HMF

The MIL-88B materials were tested as catalysts in the isomerisation of glucose and production of HMF. As Fe and Sc MIL-88B are hydrothermally unstable - reactions were conducted in DMSO. In total, two reaction temperatures were considered along with two different glucose: catalyst ratios. The results are shown in **Table 6.1**.

Consistent with literature, the blank reaction conducted at 120 °C generated a glucose conversion of only 1.6 % and no desirable products.²¹⁰ This confirms that DMSO does not contribute significantly toward catalytic reactions at lower temperatures. The addition of (Fe)MIL-88B in the reaction (30 : 1 wt./wt.) increased glucose conversion and product yields (**Table 6.1 Entry 2**). Specifically, (Fe)MIL-88B generated a glucose conversion of 18.9 % - along with fructose and mannose yields of 6.3 % and 0.3 %, respectively. This increase in glucose conversion confirms the catalytic activity of (Fe)MIL-88B. Meanwhile, the fructose yield confirms that Fe sites within the material are enabling glucose isomerisation – likely through a Lewis acid catalysed reaction pathway. The lack of HMF produced during the reaction suggests that (Fe)MIL-88B does not exhibit sufficient Brønsted acidity to promote fructose dehydration.

As seen in **Table 6.1 Entry 3**, (Sc)MIL-88 generated a glucose conversion of 9.0 % along with small quantities of fructose, mannose, and HMF. This glucose conversion and product yield is lower than that generated by (Fe)MIL-88B. Moreover, this suggests that (Sc)MIL-88B is less active as an isomerisation catalyst. This difference in activity may be related to the different metal sites present within each catalyst.

The glucose conversion and product yield generated by the bimetallic material is similar to that produced by (Sc)MIL-88 (**Table 6.1 Entry 4**). This is unsurprising as (FeSc)MIL-88B contains significantly more Sc than Fe - particularly at the material's surface. Moreover, these results may suggest that glucose reactions occur primarily on the outer surface of MIL-88B.

At a higher temperature of 140 °C, the blank reaction generated a glucose conversion of 60.3 % (**Table 6.1 Entry 5**). This is significantly higher than that obtained in the blank reaction conducted at 120 °C. Moreover, this indicates that

the activation energy barrier for glucose conversion in DMSO is sufficiently exceeded above 120 °C.

In comparison to the blank reaction conducted at 140 °C, the addition of (Fe)MIL-88B slightly decreased glucose conversions (54.2 %) whilst increasing fructose and mannose yields (**Table 6.1 Entry 6**). Interestingly, the fructose yield generated by (Fe)MIL-88B at 140 °C is comparable to that produced by the catalyst at 120 °C. Moreover, this may suggest that higher temperatures do not promote the isomerisation of glucose at Fe sites within the catalyst.

As seen in **Table 6.1 Entry 7**, (Sc)MIL-88B generated a glucose conversion of 28.8 % at 140 °C. This is approximately half of the conversion obtained in the blank reaction. However, the presence of the pure Sc material increased fructose, mannose and HMF yields. In comparison to (Fe)MIL-88B, the pure Sc material generated less fructose and more HMF. This suggests that the fructose yield produced by (Sc)MIL-88B is more readily converted to HMF. As such, we can infer that Sc and Fe sites within the MIL-88B structure interact differently with the fructose molecules produced during reaction.

As seen in **Table 6.1 Entry 8**, (FeSc)MIL-88B generated a glucose conversion of 53.3 % and a total product selectivity of 43.9 % at 140 °C. Within this product distribution - HMF was the most prominent molecule (17.8 % yield). The excellent performance of the bimetallic material suggests that there is a positive effect of having both Fe and Sc active sites. As previously noted, both Fe and Sc active sites promote the isomerisation of glucose. However, these metal sites appear to interact differently with the fructose molecules generated in the reaction. Perhaps the Fe sites stabilise the fructose molecules, thus preventing further reactions, whereas the Sc sites do not. Or perhaps Fe sites more readily promote side reactions and the production of undesirable by-products instead of HMF. The activity of (FeSc)MIL-88B may also be attributed to the high number of defective sites within the material. As previous noted, the bimetallic material is more defective than the single metal MOFs and therefore may contain more Lewis acid active sites.

Reactant to Catalyst ratio

To evaluate the effect of substrate to catalyst ratio, reactions were repeated using higher quantities of catalyst. Specifically, reactions were repeated using a glucose: catalyst ratio of 7.5:1. As seen in **Table 6.1 Entry 9**, increasing the amount of (Fe)MIL-88B within the reaction increased glucose conversions by around 5 % when reactions were performed at 120 °C. However, the reactions overall selectivity towards desirable products decreased significantly (34.6 % to 14.8 %). This suggests that higher quantities of (Fe)MIL-88B promotes undesirable side reactions at 120°C. In contrast, increasing the amount of (FeSc)MIL-88B within the reaction was found to increase both glucose conversion and product selectivity (**Table 6.1 Entry 10**). This difference in catalytic performance may be attributed to the presence of Sc active sites and a more defective structure. Moreover, we may infer that higher quantities of Sc - and/or a defective structure - minimises undesirable side reactions at 120 °C.

At 140 °C, increasing the quantity of (Fe)MIL-88B within the reaction did not significantly increase glucose conversions. However, increasing quantities of the catalyst did effect product distributions. For instance, with a glucose: catalyst ratio of 30:1, the main reaction product produced by (Fe)MIL-88B was fructose - and only small quantities of HMF were obtained (**Entry 6**). Meanwhile, higher quantities of (Fe)MIL-88B (7:1) within the reaction generates equal quantities of fructose and HMF (**Entry 11**). In comparison, increasing the quantity of (FeSc)MIL-88B within the reaction increases both glucose conversion and HMF yields (**Entry 12**).

(Blank Space)

Table 6.1. Glucose isomerisation and dehydration reactions catalysed by Fe and Sc MIL-88B materials.

Entry	Temperature (°C)	Catalyst	Glucose to Catalyst Ratio (wt./wt.)	Conversion (%)	Fructose Yield (%)	Mannose Yield (%)	HMF Yield (%)	Total Selectivity
1	120	none		1.6	0.0	0.0	0.0	0.7
2	120	(Fe)MIL-88B	30 : 1	18.9	6.3	0.3	0.0	34.6
3	120	(Sc)MIL-88B	30 : 1	9.0	1.0	0.4	0.1	16.3
4	120	(FeSc)MIL-88B	30 : 1	11.5	1.1	0.2	0.7	17.5
5	140	none		60.3	0.0	0.0	0.6	1.0
6	140	(Fe)MIL-88B	30 : 1	54.2	7.6	1.2	0.9	17.8
7	140	(Sc)MIL-88B	30 : 1	28.8	2.1	1.1	3.2	22.3
8	140	(FeSc)MIL-88B	30 : 1	53.3	3.6	2.0	17.8	43.9
9	120	(Fe)MIL-88B	7.5 : 1	24.2	3.2	0.0	0.4	14.8
10	120	(FeSc)MIL-88B	7.5 : 1	19.7	2.3	0.8	3.3	32.1
11	140	(Fe)MIL-88B	7.5 : 1	55.6	3.6	1.0	3.8	15.1
12	140	(FeSc)MIL-88B	7.5 : 1	70.7	3.3	1.4	24.9	42.0

Stability and recyclability

To access the reusability of (Fe)MIL-88B and (FeSc)MIL-88B, recycle reactions were conducted in DMSO at 120 °C. This temperature was chosen as the stability of the materials was found to be adversely effected by the higher temperature. After each reaction cycle, the catalysts were recovered via centrifuge and washed in DMSO before being added back to a fresh stock solution. As shown in **Figure 6.8**, the activity and product yield of (Fe)MIL-88B declined by approximately 10 % after the first reaction. The glucose conversion then began to rise in subsequent reaction cycles. This may suggests that (Fe)MIL-88B has been destroyed or rendered inactive, and a homogeneous catalyst may be contributing towards glucose conversions. To confirm this, the material was recovered at the end of the fourth reaction cycle, washed in DMSO, and analysed via XRD. As seen in **Figure 6.8**, the diffraction pattern of the recovered material appears different. This confirms that (Fe)MIL-88B has been damaged during the recycle reactions.

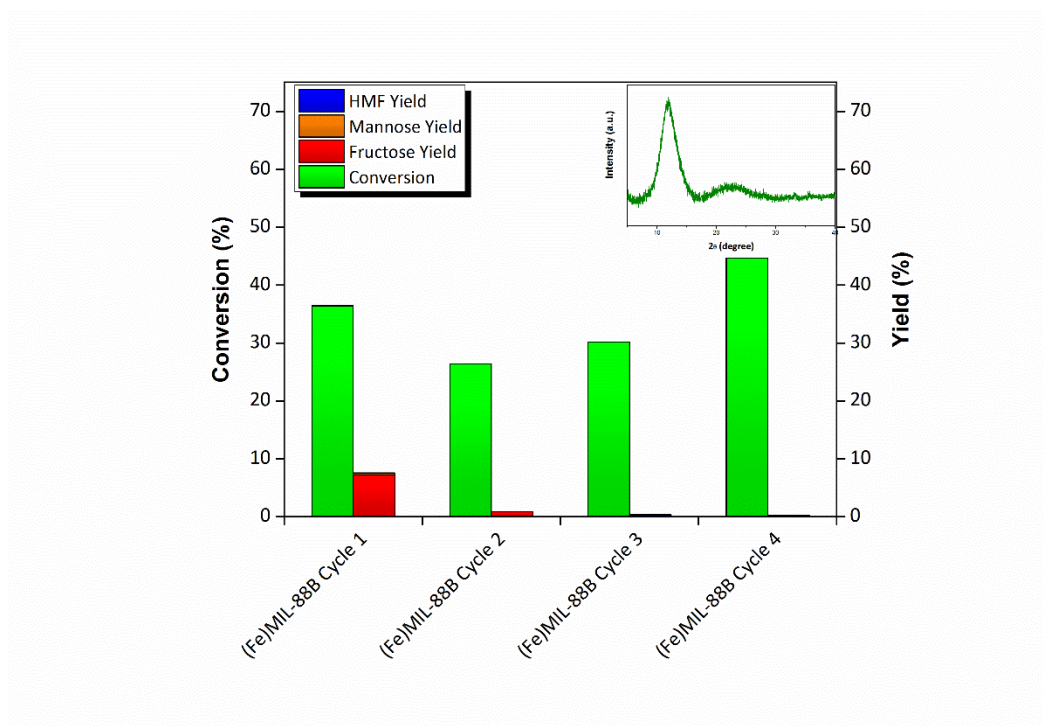


Figure 6.8. Recycle reaction of (Fe)MIL-88B in DMSO at 120 °C. The reaction contained 200 mg of catalyst and 15 mL of 10 wt.% glucose stock solution. Insert: XRD of catalyst post Cycle 4.

The recyclability of (FeSc)MIL-88B was also considered in DMSO at 120 °C. As seen in **Figure 6.9**, the activity of the catalyst declined following the first and third reaction

cycles. Indeed, this is different to the trend observed in the recycling of (Fe)MIL-88B. To confirm the stability of (FeSc)MIL-88B, the material was recovered at the end of the fourth reaction cycle and analysed via XRD. Furthermore, filtered reaction solutions were analysed via ICP in order to quantify metal leaching.

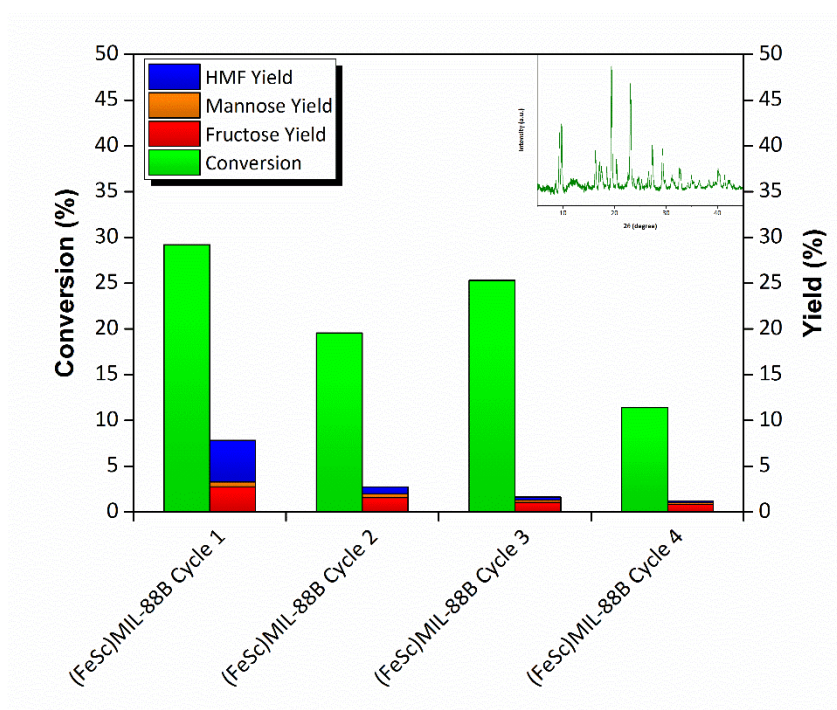


Figure 6.9. Recycle reaction of (FeSc)MIL-88B in DMSO at 120 °C. The reaction contained 200 mg of catalyst and 15 mL of stock solution. Insert: XRD of catalyst post Cycle 4.

As seen in **Figure 6.9**, the diffraction pattern of the recovered material contains peaks more indicative of MIL-88B. This confirms that (FeSc)MIL-88B has survived the reaction conditions better and is therefore more stable than (Fe)MIL-88B. However, as shown in **Table 6.2**, a large amount of Fe and Sc is leached from the material during the recycle reactions. In fact, during the course of the recycle reactions, approximately 51 % of the materials Fe is leached along with 30 % of the materials Sc. This may suggest that Sc ions have a greater stability within the MIL-88B structure. Furthermore, this also explains the observed instability of (Fe)MIL-88B in the recycle reactions described above.

Table 6.2. ICP analysis of (FeSc)MIL-88B recycle reaction solutions.

Catalyst	Fe		% of Fe	
	(ppm)	Sc (ppm)	leached	% of Sc leached
(FeSc)MIL-88B Cycle 1	259	290	38.68	17.32
(FeSc)MIL-88B Cycle 2	55	95	46.89	23.00
(FeSc)MIL-88B Cycle 3	22	62	50.17	26.70
(FeSc)MIL-88B Cycle 4	7	46	51.22	29.45

6.3 Conclusion

Sc and Fe can be successfully introduced into the framework of MIL-88B. These metals may also be used to synthesize a bimetallic MIL-88B structure. When this is done, the resulting material contains significantly more Sc than Fe, particularly at the surface. This suggests that Sc has a greater affinity towards the MIL-88B framework than Fe. Each of the MIL-88B materials considered in this study were found to be hydrothermally unstable.

The acidity profiles of (Fe)MIL-88B and (FeSc)MIL-88B are considerably different. Specifically, the acidity profile of (Fe)MIL-88B contains numerous peaks with different desorption temperatures. Meanwhile, the acidity profile of (FeSc)MIL-88B contains a single prominent desorption peak and possibly some smaller secondary peaks. With regards to catalysis, (Fe)MIL-88B generated the highest fructose yield observed in this study. Although this confirms the Lewis acidity of the materials Fe sites, it also suggests that the material lacks the Brønsted acidity required to drive HMF production. Furthermore, given the catalytic ability of DMSO (which can drive fructose dehydration towards HMF), the fructose yield within the reaction may suggest that the Fe sites stabilize this intermediate molecule – preventing further reaction towards HMF – or promotes side reactions and the formation of by-products. (FeSc)MIL-88B generated the highest HMF yield found in this study. This HMF yield can be attributed to a combined effect of having both Fe and Sc active sites as well as a highly defective structure. The catalytic activities of (Fe)MIL-88B and (FeSc)MIL-88B declined over the course of four consecutive recycle reactions. This was caused by the deactivation and/or destruction of the catalysts under reaction conditions. Moreover, the materials appear to degrade at 120 °C in DMSO and Sc sites within the framework are shown to be more stable than Fe sites.

Ytterbium Metal-Organic Frameworks

A ytterbium MOF catalyst for the isomerisation of glucose and production of HMF.

Summary

In the previous study, we considered the use of iron and scandium MIL-88B catalysts for the isomerisation of glucose. Although promising yields can be obtained from these catalysts, they are not hydrothermally stable and degraded during recycle reactions conducted in DMSO. As such, we now turn our attention towards water stable MOFs for the isomerisation of glucose and production of HMF. In this study, we consider the use of a ytterbium (Yb) MOF, $\text{Yb}_6(\text{BDC})_7(\text{OH})_4(\text{H}_2\text{O})_4$. The performance of this MOF was tested in both water and hydrochloric acid (pH 2.5). The time of reaction was varied between 1.5 h and 6 h. For reactions conducted in 3 h, $\text{Yb}_6(\text{BDC})_7(\text{OH})_4(\text{H}_2\text{O})_4$ generated a higher glucose conversion and desirable product yield (fructose, mannose, HMF) than reactions conducted in the absence of catalyst. However, the glucose conversions generated by $\text{Yb}_6(\text{BDC})_7(\text{OH})_4(\text{H}_2\text{O})_4$ were lower than those generated by $\text{YbCl}_3 \cdot 6\text{H}_2\text{O}$. In order to test the stability and reusability of $\text{Yb}_6(\text{BDC})_7(\text{OH})_4(\text{H}_2\text{O})_4$ in water, a series of recycle reactions were performed. The catalyst was able to generate a glucose conversion of around 28 % along with a HMF yield of 17 % in the first recycle reaction. However, the glucose conversions dropped following this first reaction, and the subsequent HMF yields generated were only marginally greater than those produced in the blank reaction. ICP analysis revealed that around 5 % of the catalysts Yb content was leached in each of the reaction cycles. In order to test the contribution of leached Yb ions in the reactions, a control experiment was conducted. This experiment suggests that leached Yb ions may contribute towards the glucose conversions and product yields obtained in the 24 h reactions.

6.4 Introduction

Several research groups have considered the use of ytterbium (Yb) catalysts for the production of glucose derived HMF. Specifically, researchers have considered the use of homogeneous Yb catalysts in water,²¹¹ ionic liquids (ILs),^{212,213} and biphasic reactors.^{14,214,215} However, there are some potential drawbacks associated with the aforementioned catalytic systems. For instance, it is well known that ILs are expensive and due to their low boiling point, make product separation considerably difficult. Moreover, the use of homogeneous catalysts in general presents difficulties in term of catalyst recovery. Many of these disadvantages can be overcome by developing heterogeneous catalysts.

In 2006 Weng, *et al.* discovered a new Yb MOF.²¹⁶ This particular framework consists of Yb clusters interlinked by terephthalic acid struts. The overall structure of this framework is described by the authors as $\text{Yb}_3(\text{BDC})_{3.5}(\text{OH})_2(\text{H}_2\text{O})_2$. As this MOF is made using a hydrothermal synthesis method, it should be water stable. Hence, it could potentially replace homogeneous Yb catalysts in the various reaction systems mentioned above.

In this study, we consider $\text{Yb}_6(\text{BDC})_7(\text{OH})_4(\text{H}_2\text{O})_4$ as a glucose isomerisation and dehydration catalyst. To begin, we utilise ammonia temperature programmed desorption (NH_3 -TPD) in order to quantify the acidity of this relatively unexplored MOF. The catalytic performance of the MOF is then tested in both water and hydrochloric acid (HCl). Reaction times were varied in order to optimise product yields and the reusability of the catalyst was explored in a series recycle reactions conducted in water.

6.5 Results and Discussion

Structure and Morphology

The successful synthesis of $\text{Yb}_6(\text{BDC})_7(\text{OH})_4(\text{H}_2\text{O})_4$ was confirmed by X-ray diffraction analysis (XRD). As shown in **Figure 6.10**, the diffraction pattern of the MOF does not contain any additional peaks. This suggests an absence of uncoordinated linker or bulk extra-framework Yb within the material's framework. The material was also analysed using a scanning electron microscope (SEM). As seen in **Figure 6.10**, SEM imaging reveals that the material does not contain obvious surface defects or inter-grown crystals.

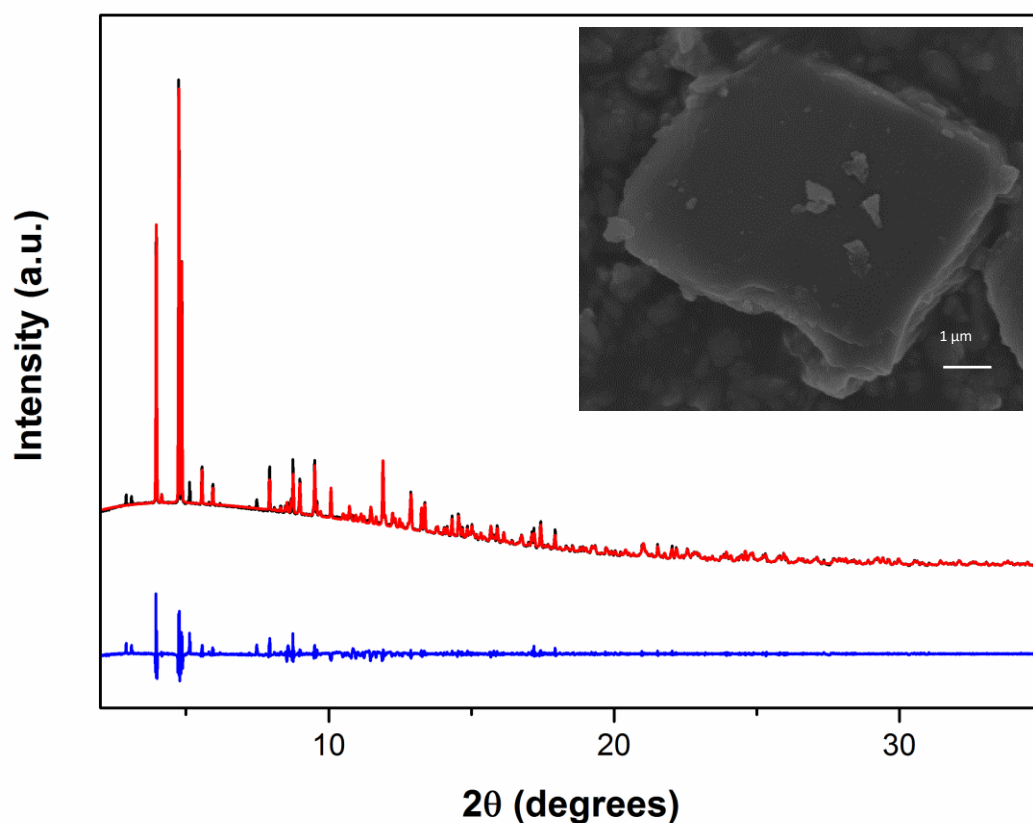


Figure 6.10. XRD fitting of $\text{Yb}_6(\text{BDC})_7(\text{OH})_4(\text{H}_2\text{O})_4$ (black) measured diffraction pattern (red) fitting (blue) difference. (Insert) SEM image of synthesised $\text{Yb}_6(\text{BDC})_7(\text{OH})_4(\text{H}_2\text{O})_4$.

Thermal gravimetric analysis (TGA) was used to determine the thermal stability of $\text{Yb}_6(\text{BDC})_7(\text{OH})_4(\text{H}_2\text{O})_4$. As seen in **Figure 6.11**, thermal decomposition begins above 480 °C. The final product of this decomposition - presumably ytterbium oxide (YbO) - accounts for approximately 49 % of the materials weight. This is close to the amount of YbO expected, based on the materials molecular formula, therefore suggesting that there are minimal defects within the synthesised $\text{Yb}_6(\text{BDC})_7(\text{OH})_4(\text{H}_2\text{O})_4$ structure.

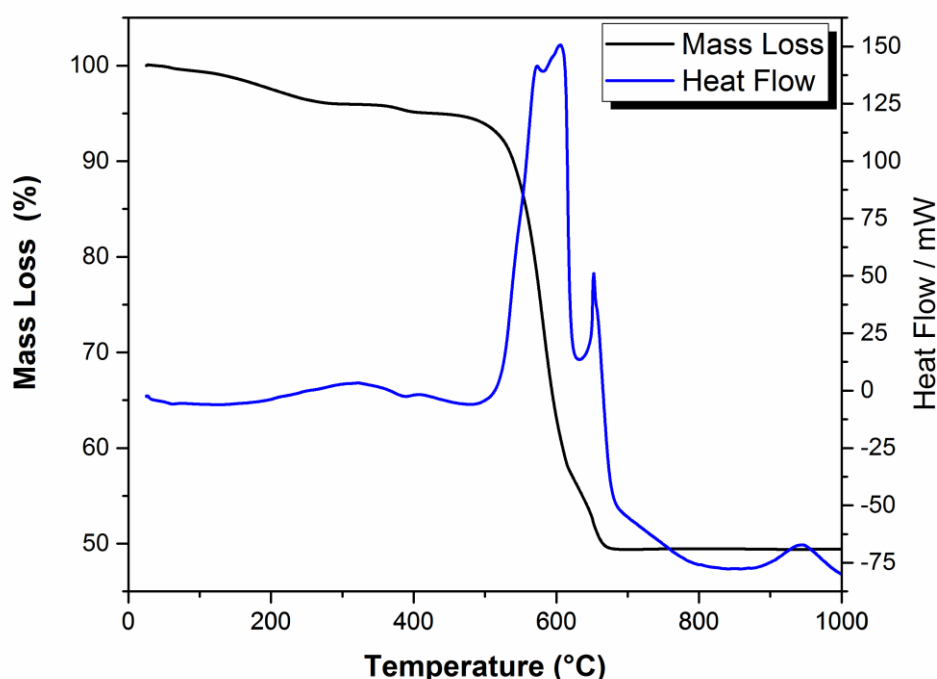


Figure 6.11. TGA analysis of $\text{Yb}_6(\text{BDC})_7(\text{OH})_4(\text{H}_2\text{O})_4$.

Ammonia temperature programmed desorption (TPD) was used to quantify the acidity of $\text{Yb}_6(\text{BDC})_7(\text{OH})_4(\text{H}_2\text{O})_4$. This was done using a homemade apparatus. The accuracy of this equipment was verified by measuring the acidity of commercial zeolites (see zeolite chapters). For the TPD measurement of $\text{Yb}_6(\text{BDC})_7(\text{OH})_4(\text{H}_2\text{O})_4$, 50 mg of catalyst contained within a quartz tube was heated to 200 °C at a ramp rate of 1 °C.min⁻¹. After 2 h, the catalyst was cooled to 100 °C and dosed with an excess of 0.02 vol.% ammonia in helium. The ammonia was then desorbed from the catalyst by heating the material to 400 °C at a ramp rate of 2 °C min⁻¹. To ensure the complete desorption of ammonia from the material, the temperature was then maintained at 400 °C. The amount of ammonia desorbed from the catalyst was measured using a mass spectrometer and quantified at $m/z = 15$ in order to avoid interference with desorbed

water. The acidity of the material was calculated as 0.39 mmol/g. As shown in **Figure 6.12**, the materials desorption pattern contains two distinct peaks. This suggests that the material contains two different acid sites. The second peak within the desorption pattern is significantly larger than the first. This suggests that the material contains more of one particular acid site.

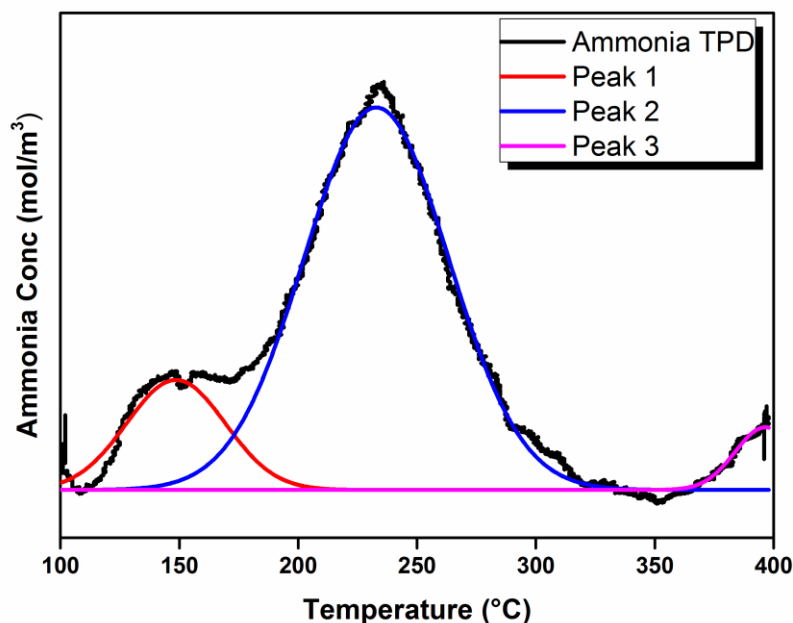


Figure 6.12. Ammonia TPD pattern of $\text{Yb}_6(\text{BDC})_7(\text{OH})_4(\text{H}_2\text{O})_4$.

Glucose dehydration to HMF

The catalytic performance of $\text{Yb}_6(\text{BDC})_7(\text{OH})_4(\text{H}_2\text{O})_4$ was tested in the isomerisation of glucose and production of HMF. To begin, reactions were conducted in water. This is an ideal solvent for the development of green chemical process as it is environmentally benign. It is also the solvent currently used in the enzymatic glucose isomerisation processes currently employed in industry.²⁹ As a baseline for comparison, reactions were also conducted in the absence of catalyst. Furthermore, reactions were also conducted the presence of $\text{YbCl}_3 \cdot \text{H}_2\text{O}$ and Yb_2O_3 .

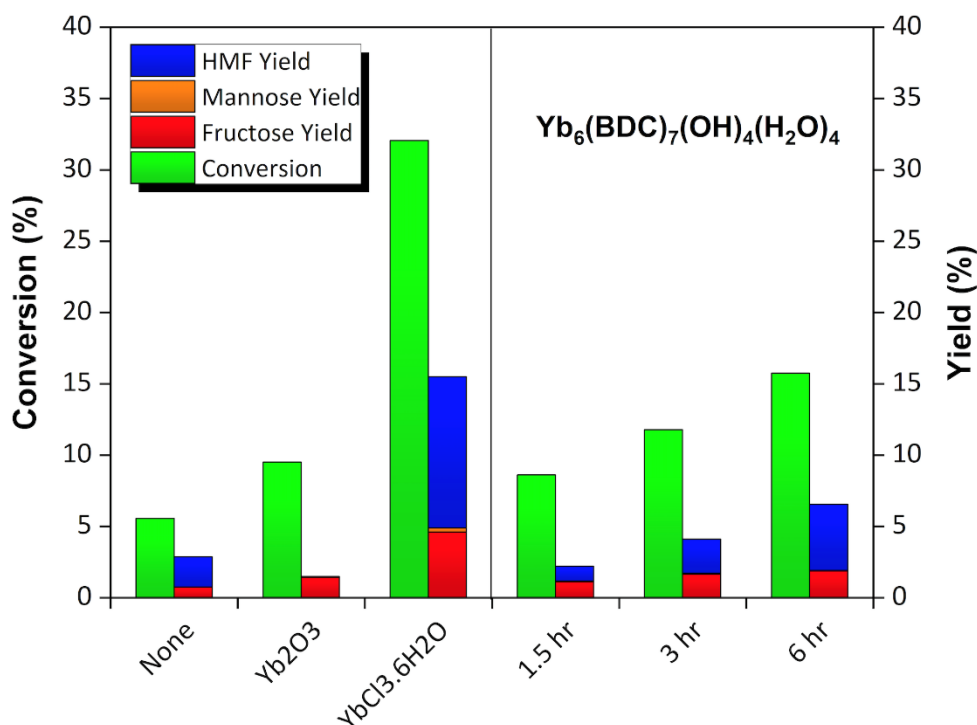


Figure 6.13. Glucose conversion in water on 10 mg of catalyst. Reaction conditions: 140 °C, 3 h, stock solution of 10 wt. % glucose in deionized water. *Reaction times vary for reactions containing $\text{Yb}_6(\text{BDC})_7(\text{OH})_4(\text{H}_2\text{O})_4$.

As seen in **Figure 6.13**, the blank reaction generated a glucose conversion of around 5 % along with small quantities of fructose and HMF (<3 %). The addition of Yb_2O_3 to the reaction increased glucose conversion to around 10 % whilst also slightly increasing HMF yields. Meanwhile, the addition of $\text{YbCl}_3.6\text{H}_2\text{O}$ to the reaction dramatically increased glucose conversions and product yields. Specifically, $\text{YbCl}_3.6\text{H}_2\text{O}$ generated a glucose conversion of around 32 % along with a desirable product yield (fructose, mannose, and HMF) of around 15 %. It is worth noting the striking difference in catalytic activity between Yb_2O_3 and $\text{YbCl}_3.6\text{H}_2\text{O}$. Base and acid catalysts generally facilitate glucose isomerisation via two different reaction mechanisms. Specifically, basic catalysts generally enable glucose isomerisation via the Lobry de Bruyn–Alberda van Ekenstein reaction mechanism which involves a proton transfer.^{30,31} Meanwhile, Lewis acid catalysts such as Sn-Beta, typically enable glucose isomerisation via an intramolecular hydride shift.²⁶ These different mechanisms may be responsible for the difference in catalytic activity observed between Yb_2O_3 and $\text{YbCl}_3.6\text{H}_2\text{O}$. However, detailed NMR studies are needed to confirm this.

The addition of $\text{Yb}_6(\text{BDC})_7(\text{OH})_4(\text{H}_2\text{O})_4$ to the reaction increased glucose conversions and product yields in comparison to the blank reaction. However, this heterogeneous acid catalyst is less effective than $\text{YbCl}_3 \cdot 6\text{H}_2\text{O}$. It is also worth noting that $\text{Yb}_6(\text{BDC})_7(\text{OH})_4(\text{H}_2\text{O})_4$ was activated at 200 °C for 2 h before the reactions. In order to optimise product yields, the reaction time was varied. As seen in **Figure 6.13**, increasing the reaction time from 1.5 h to 6 h increased glucose conversions and product yields. The highest glucose conversion obtained by $\text{Yb}_6(\text{BDC})_7(\text{OH})_4(\text{H}_2\text{O})_4$ was around 15 %. This was accompanied by a total desirable product yield of around 7 %. Again, this conversion and yield is significantly lower than that obtained by homogenous $\text{YbCl}_3 \cdot 6\text{H}_2\text{O}$ in water after only 3 h.

In an attempt to improve catalytic activity, reactions were repeated in HCl. The pH of this reaction solution was 2.5 before the addition of glucose and catalyst. The results of these reactions are shown in **Figure 6.14**.

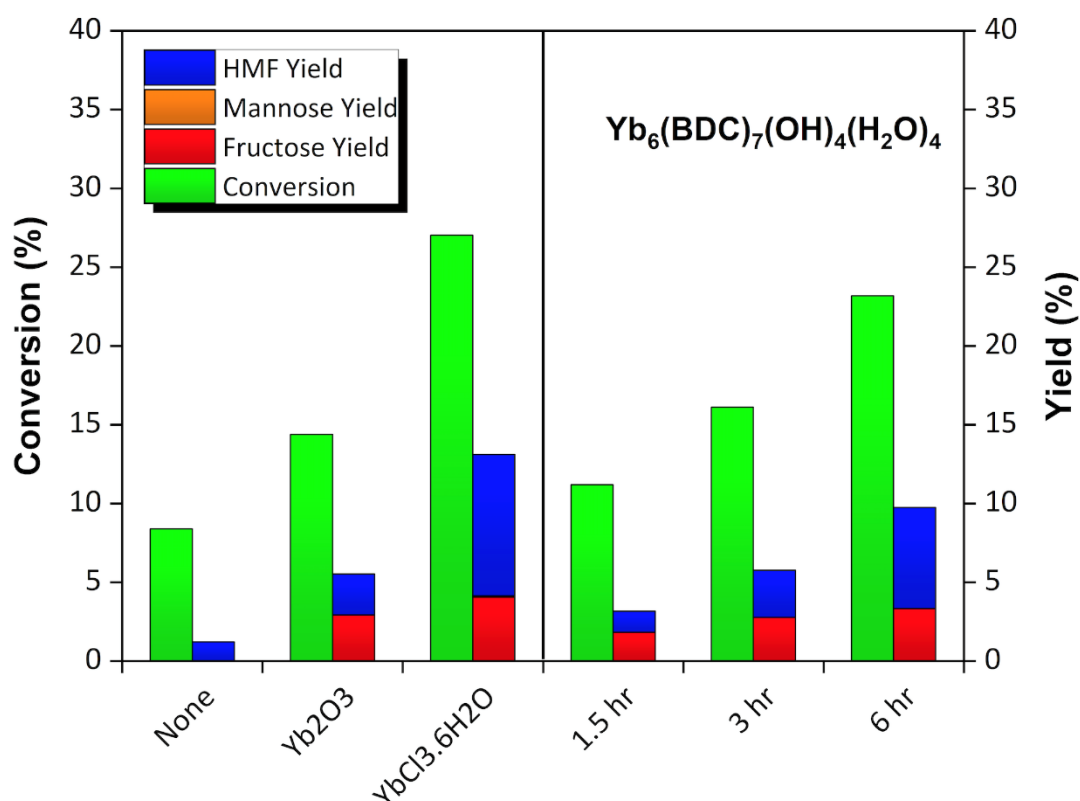


Figure 6.14. Glucose conversion in HCl on 10 mg of catalyst. Reaction conditions: 140 °C, 3 h, stock solution of 10 wt. % glucose in pH 2.5. *Reaction times vary for reactions containing $\text{Yb}_6(\text{BDC})_7(\text{OH})_4(\text{H}_2\text{O})_4$.

As seen in **Figure 6.14**, the blank reaction conducted in pH 2.5 generated a glucose conversion of around 8 % along with a HMF yield of approximately 1.2 %. This is a higher conversion obtained in comparison to the blank reaction conducted in water. Hence, the addition of HCl increased glucose conversions. The addition of Yb_2O_3 and $\text{YbCl}_3 \cdot 6\text{H}_2\text{O}$ to the reaction increased glucose conversions and desirable product yields. Again, Lewis acidic $\text{YbCl}_3 \cdot 6\text{H}_2\text{O}$ was found to be significantly more active than basic Yb_2O_3 . Interestingly, in comparison to reactions conducted in water, the addition of HCl appears to reduce the activity of $\text{YbCl}_3 \cdot 6\text{H}_2\text{O}$ whilst increasing the activity of Yb_2O_3 . This may suggest that the activity of these catalysts can be tuned by adjusting the pH of the reaction solution. However, separate studies are needed in order to fully investigate these effects.

The addition of $\text{Yb}_6(\text{BDC})_7(\text{OH})_4(\text{H}_2\text{O})_4$ to reactions conducted in HCl improved glucose conversions and product yields in comparison to the blank reaction. As before, glucose conversions and product yields increased with increasing reaction times. However, the heterogeneous Lewis acid catalyst was once again less active and less selective than homogeneous $\text{YbCl}_3 \cdot 6\text{H}_2\text{O}$. Indeed, the performance of $\text{Yb}_6(\text{BDC})_7(\text{OH})_4(\text{H}_2\text{O})_4$ during a 3 h reaction conducted in HCl is comparable to the performance of Yb_2O_3 under the same reaction conditions.

Stability and Recycling

In order to access the stability and reusability of $\text{Yb}_6(\text{BDC})_7(\text{OH})_4(\text{H}_2\text{O})_4$, a series of recycle reactions were performed in water. For this, reactions were scaled up by a factor of five and the reaction time was increased to 24 h in order to improve glucose conversions and product yields. The results of these recycle reactions are shown in **Figure 6.15**. For comparison, a blank reaction conducted under the same reaction conditions in the absence of catalyst is also shown.

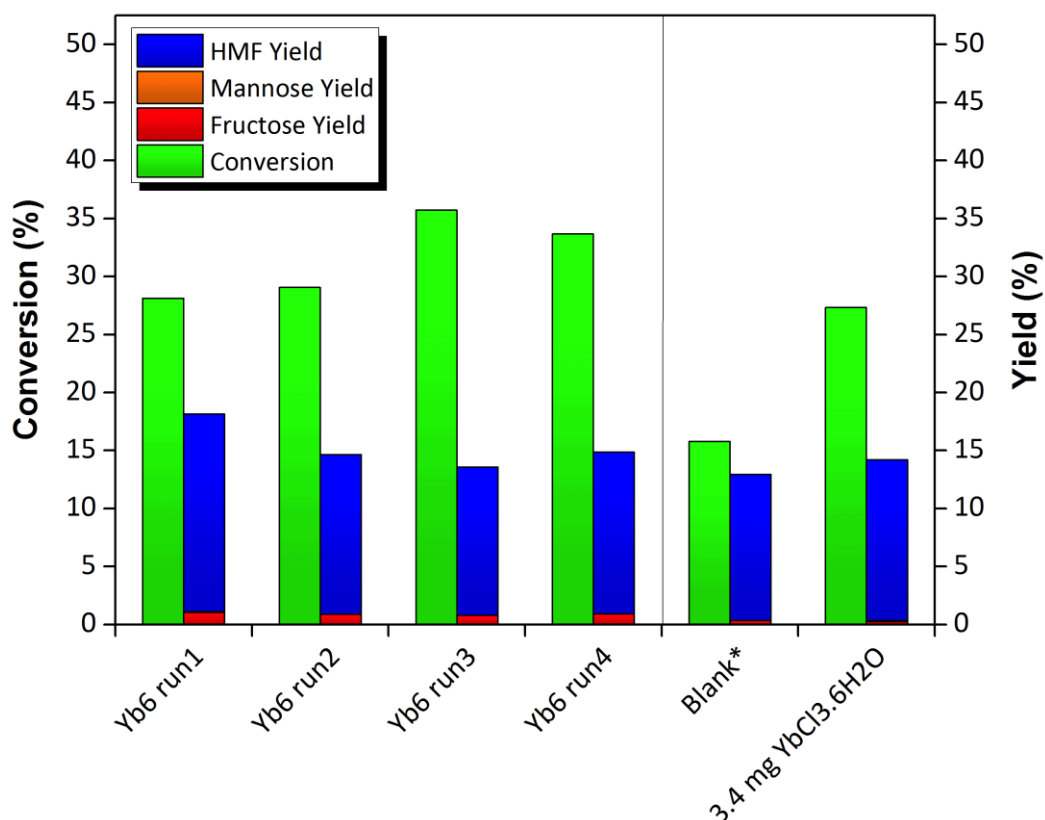


Figure 6.15. $\text{Yb}_6(\text{BDC})_7(\text{OH})_4(\text{H}_2\text{O})_4$ recycle reactions in water on 50 mg of catalyst. Reaction conditions: 140 °C, 24 h, 15 mL of 10 wt. % glucose stock solution. Blank* reaction conducted in 4 mL reaction vial.

As seen in **Figure 6.15**, the blank reaction generates a glucose conversion of around 15 % and a HMF yield of around 13 %. This high selectivity towards HMF indicates that an extended hydrothermal treatment of glucose may be used to generate this value-added platform molecule. However, heterogeneous catalysts are still required to reduce reaction times, improve yields, and facilitate process scale-up. The addition of $\text{Yb}_6(\text{BDC})_7(\text{OH})_4(\text{H}_2\text{O})_4$ to the reaction increases glucose conversions and HMF yields in comparison to the blank reaction. Specifically, $\text{Yb}_6(\text{BDC})_7(\text{OH})_4(\text{H}_2\text{O})_4$ generates a

glucose conversion of around 28 % along with a desirable product yield of around 18 %. Within this product yield, HMF is the dominant molecule. During the course of the recycle reactions, $\text{Yb}_6(\text{BDC})_7(\text{OH})_4(\text{H}_2\text{O})_4$ appears to remain active. However, the HMF yield generated by the catalyst declines following the first reaction cycle. Indeed, the HMF yield generated by the catalyst is similar to that obtained in the blank reaction. Moreover, selectivity towards desirable products is diminished after the first reaction cycle and it appears that the catalyst promotes the production of undesirable products (i.e. products not targeted in this study).

In order to assess the stability of $\text{Yb}_6(\text{BDC})_7(\text{OH})_4(\text{H}_2\text{O})_4$, material was collected following the fourth recycle reaction and analysed via XRD. As seen in **Figure 6.16**, the XRD pattern of the recovered material appears similar to that of $\text{Yb}_6(\text{BDC})_7(\text{OH})_4(\text{H}_2\text{O})_4$. Specifically, the diffraction pattern of the recovered material contains the same low angle peaks at around 5° .

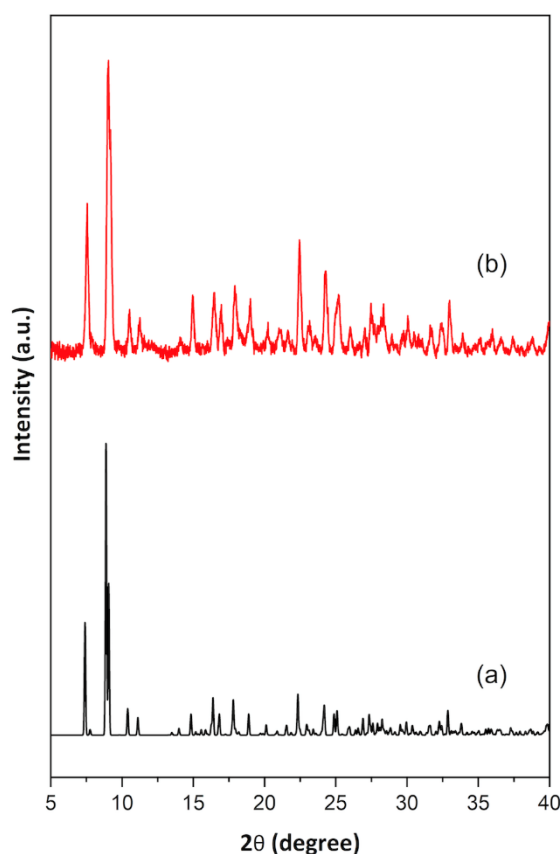


Figure 6.16. XRD of (a) simulated pattern²¹⁶ and (b) $\text{Yb}_6(\text{BDC})_7(\text{OH})_4(\text{H}_2\text{O})_4$ after four consecutive recycle reactions.

The stability of $\text{Yb}_6(\text{BDC})_7(\text{OH})_4(\text{H}_2\text{O})_4$ was also quantified by measuring the amount of Yb leached from the material during the recycle reactions. Here, Yb leaching was quantified via inductively coupled plasma (ICP) analysis. As seen in **Table 6.3**, approximately 5 % of the materials Yb content is leached during each recycle reaction. Given the high activity of $\text{YbCl}_3 \cdot 6\text{H}_2\text{O}$ (as previously discussed), it may be possible that leached Yb ions are contributing to the 24 h reactions.

Table 6.3. ICP analysis of recycle reaction solutions to quantify the amount of Yb leaching from $\text{Yb}_6(\text{BDC})_7(\text{OH})_4(\text{H}_2\text{O})_4$ during 24 h reactions at 140°C.

Reaction Cycle	Yb Leached (ppm)	Cumulative Yb Leached from Catalyst (%)
Run 1	81	5.45
Run 2	66	10.45
Run 3	66	15.89
Run 4	64	21.74

In order to quantify the contribution of leached Yb ions, a control experiment was conducted using a similar concentration of Yb. For this, approximately 3.4 mg of $\text{YbCl}_3 \cdot 6\text{H}_2\text{O}$ was added to a 15 mL solution of 10 wt.% glucose and heated to 140 °C for 24 h. In this reaction, the $\text{YbCl}_3 \cdot 6\text{H}_2\text{O}$ generated a glucose conversion of 27.32 % along with a HMF yield of 13.87 %. This glucose conversion and HMF yield is comparable to that generated by $\text{Yb}_6(\text{BDC})_7(\text{OH})_4(\text{H}_2\text{O})_4$ under the same reaction conditions. Specifically, under the same reaction conditions, $\text{Yb}_6(\text{BDC})_7(\text{OH})_4(\text{H}_2\text{O})_4$ generated a glucose conversion of 28.13 % along with a HMF yield of 17.04 %. This suggests that Yb ions leached from the heterogeneous catalyst may contribute towards glucose conversions and product yields in the 24 h reactions. Indeed, although $\text{Yb}_6(\text{BDC})_7(\text{OH})_4(\text{H}_2\text{O})_4$ generates a slightly higher HMF yield (~3 %), it appears that the solid catalyst may act as reservoir for highly active Yb ions in the extended 24 h recycle reactions.

6.6 Conclusions

In this study, $\text{Yb}_6(\text{BDC})_7(\text{OH})_4(\text{H}_2\text{O})_4$ is tested as a glucose isomerisation and dehydration catalyst in both water and HCl (pH 2.5). Although ammonia TPD studies indicate that the catalyst contains acid sites, the performance of the catalyst was lower than that obtained by homogenous Yb ions ($\text{YbCl}_3 \cdot 6\text{H}_2\text{O}$) in each of the reaction solvents considered. Furthermore, although the catalyst appeared to perform well during the course of four consecutive recycle reactions, further analysis suggests that the activity of the catalyst may – to some extent - be attributed to leached Yb ions. As such, it appears that $\text{Yb}_6(\text{BDC})_7(\text{OH})_4(\text{H}_2\text{O})_4$ acts as a reservoir for homogeneous Yb ions which may be responsible for a significant amount of the catalytic activity observed in the 24 h recycle reactions.

A room temperature and hydrothermal synthesis of ZIF-8 catalysts for glucose isomerisation in water.

Summary

In the previous section, a ytterbium (Yb) MOF was considered as a catalyst for glucose isomerisation and HMF production in water. However, leached Yb ions may significantly contribute towards the observed catalytic performance of this material in 24 h recycle reactions. Furthermore, the synthesis of $\text{Yb}_6(\text{BDC})_7(\text{OH})_4(\text{H}_2\text{O})_4$ has not yet been optimised. Indeed, the current synthesis method requires multiple steps, generates small yields, and does not appear to be scalable. In order to overcome these issues, a commercially available MOF is now considered for catalysis. In particular, ZIF-8 was synthesised and tested as a glucose isomerisation catalysts. The synthesis of ZIF-8 was achieved using two different methods. Of these, the hydrothermal synthesis (HT) method yields a material with exceptionally high surface area ($1967.2 \text{ m}^2 \cdot \text{g}^{-1}$). As a catalyst, ZIF-8 generates excellent fructose yields. Specifically, (HT)ZIF-8 generated a glucose conversion of 24 % and a fructose selectivity of 65 % at 100 °C in water. However, this selectivity fell dramatically when reactions were repeated at higher temperatures. Interestingly, greater quantities of mannose were generated at higher temperatures. In order to improve HMF yields, 0.1 M hydrochloric acid (HCl) was added to the reaction solution. At higher temperatures the presence of this mineral acid was found to improve desirable product yields. Unfortunately, despite the excellent performance of ZIF-8 catalysts in batch reactions, their activity does not translate well to flow reactors. Specifically, the activity of (RT)ZIF-8 quickly diminished in a flow reactor maintained at 100 °C.

6.7 Introduction

Zeolite imidazolate frameworks (ZIFs) are a type of MOF. As their name suggests, these materials contain imidazolate linkers and exhibit structural characteristics similar to zeolites. Specifically, the imidazolate linkers contained within ZIFs bond with tetrahedrally coordinated transitional metal ions at an angle typically seen in zeolites (145°).^{191,217} As such, ZIFs enable the incorporation of transitional metal ions and organic units within zeolite type structures.¹⁹¹

ZIF-8 was one of the earliest ZIF frameworks to be reported in literature. This particular material contains 2-methylimidazolate linkers and zinc (Zn) ions arranged in a SOD type (zeolite) structure.¹⁹¹ With regards to chemical and physical properties, ZIF-8 exhibits high surface area, porosity, excellent thermal stability, and excellent chemical stability.¹⁹¹ These properties have no doubt encouraged the study of ZIF-8 in numerous research fields including: catalysis, gas capture/separation, drug delivery, water treatment, and electrical energy storage.^{218–222}

The traditional synthesis of ZIF-8 requires the use of solvents such as DMF.¹⁹¹ However, the use of organic solvents is not ideal.²²³ As a result, researchers have striven to develop alternative ways to synthesis ZIF-8. These has led to the development of aqueous, mechanochemical, and electrochemical synthesis methods.^{223–230} The development of such methods has enabled the large-scale production of ZIF-8 by companies such as BASF and MOF Technologies, making it one of the first commercially available MOFs.

Herein, ZIF-8 is considered as a catalyst for the isomerisation of glucose and production of HMF. The ZIF-8 materials considered were prepared using two different synthesis methods. Specifically, materials were prepared hydrothermally and at room temperature. Reactions were initially conducted in water - the most environmentally benign solvent – at two different temperatures (100°C and 140°C). Subsequently, in an attempt to drive HMF production, reactions were also conducted in 0.1M HCl. Finally, the performance of a ZIF-8 catalyst was tested in a continuous flow reactor.

6.8 Results and Discussion

Structure and Morphology

The successful synthesis of ZIF-8 was confirmed by X-ray diffraction (XRD) analysis. As seen in **Figure 6.17**, the diffraction pattern of (RT)ZIF-8 matches the simulated pattern. This indicates that the room temperature synthesis of ZIF-8 was successful.²³¹ Furthermore, the lack of additional peaks within the diffraction pattern of (RT)ZIF-8 indicates that the material does not contain large quantities of extra-framework Zn or loose linker. The diffraction pattern of (HT)ZIF-8 also matches the simulated pattern and does not contain additional peaks.

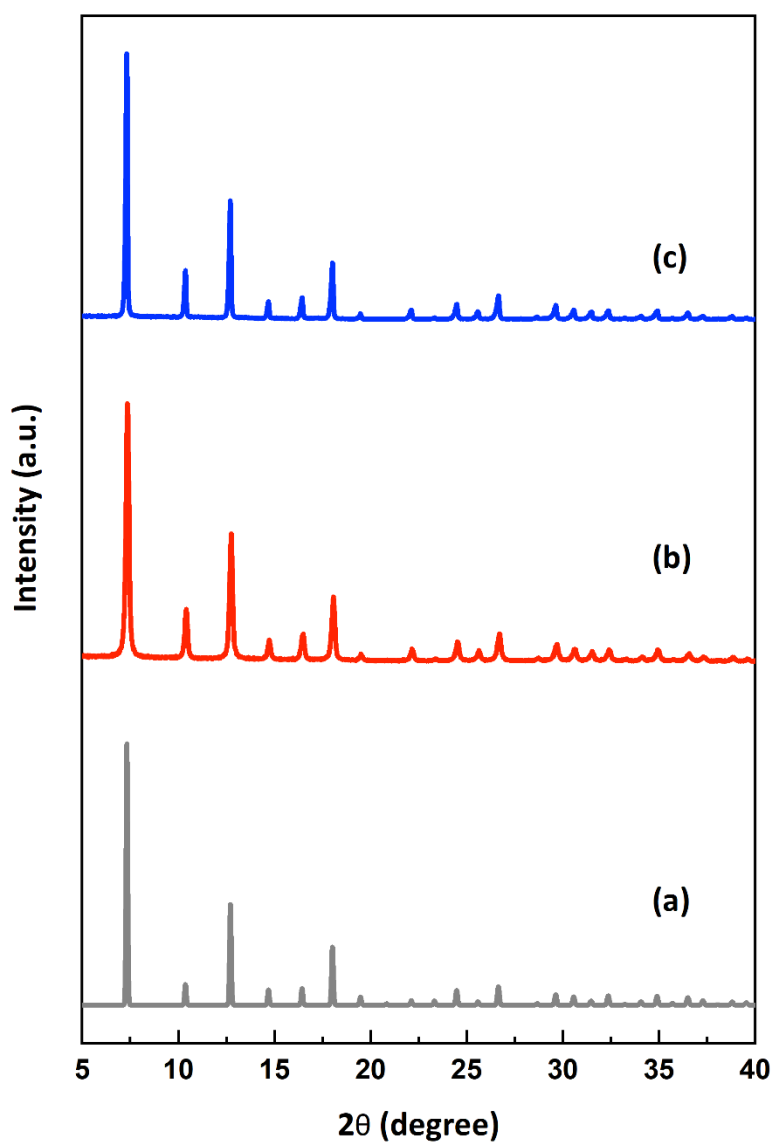


Figure 6.17. X-ray Powder Diffraction (XRD) patterns of (a) simulated ZIF-8 (b) (RT)ZIF-8 (c) (HT)ZIF-8.

Nitrogen adsorption was used to quantify the surface areas and pore volumes of the materials considered in this study. The isotherms are shown in **Figure 6.18**. Consistent with literature, the adsorption isotherms of (RT)ZIF-8 is indicative of type I.^{191,224,225,232} This suggests that the materials are microporous in nature. Meanwhile, the isotherm of (HT)ZIF-8 contains features similar to type IV.

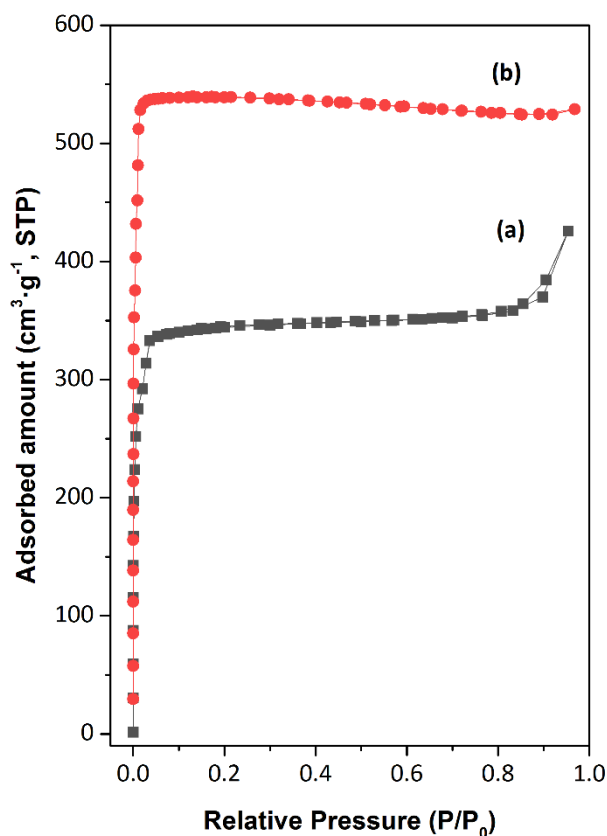


Figure 6.18. BET isotherms of (a) (RT)ZIF-8 (b) (HT)ZIF-8.

As seen in **Table 6.4**, the BET surface area of (RT)ZIF-8 is $1350.5 \text{ m}^2 \cdot \text{g}^{-1}$. This high surface area is typical of ZIF-8 materials reported in literature. Meanwhile, the surface area of (HT)ZIF-8 is $1967.2 \text{ m}^2 \cdot \text{g}^{-1}$. This surface area is unusually large. For instance, other hydrothermal synthesis methods reported in literature typically generate surface areas ranging from $1340 \text{ m}^2 \cdot \text{g}^{-1}$ to $1800 \text{ m}^2 \cdot \text{g}^{-1}$.^{228,229} In fact, the measured surface area of (HT)ZIF-8 is closer to that calculated from single crystal data. Specifically, the calculated surface area of ZIF-8 - based on single crystal data - is $1947 \text{ m}^2 \cdot \text{g}^{-1}$.¹⁹¹

Table 6.4. Textural properties of ZIF-8 materials determined by nitrogen adsorption.

Catalyst	S_{BET} ($\text{m}^2\cdot\text{g}^{-1}$)	V_{Micro} ($\text{cm}^3\cdot\text{g}^{-1}$)	V_{Meso} ($\text{cm}^3\cdot\text{g}^{-1}$)
(RT)ZIF-8	1350.5	0.53	0.05
(HT)ZIF-8	1967.2	0.83	N/A

Infrared (IR) spectroscopy analysis was used to further confirm the structure of the ZIF-8 materials. The results of this analysis are shown in **Figure 6.19**. The FTIR spectra generated by the materials (at lower wavelengths) are typical of ZIF-8.^{222,233} For instance, peaks at 421 cm^{-1} can be attributed to the stretching of Zn-N nodes.^{233,234}

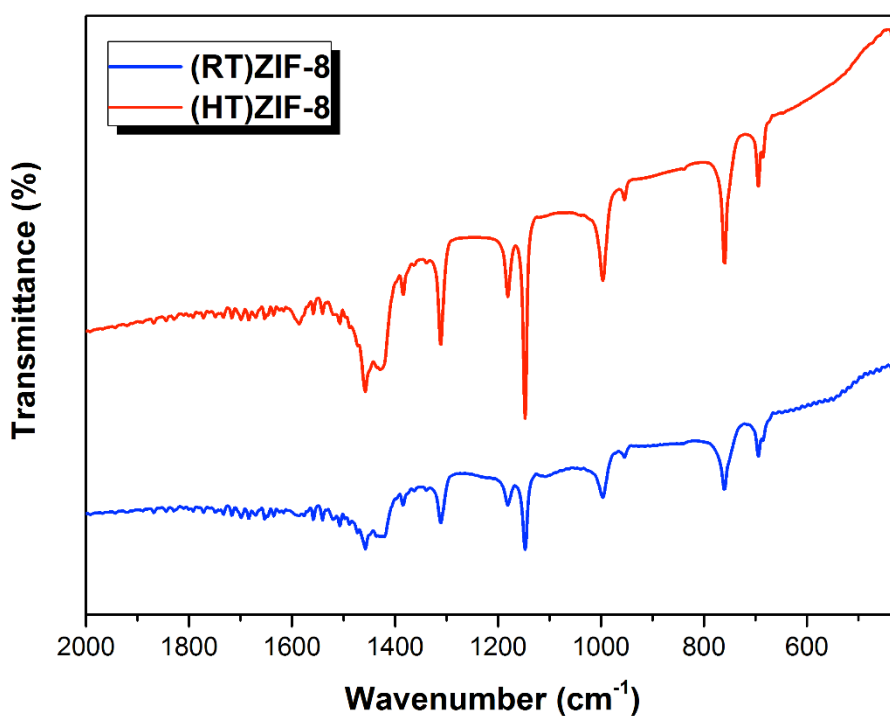


Figure 6.19. FTIR analysis of ZIF-8 catalysts.

Thermal gravimetric analysis (TGA) was used to determine the thermal stability of the ZIF-8 materials. As seen in **Figure 6.20**, the mass of (RT)ZIF-8 initially increased upon heating. This may be accredited to the oxidation of unreacted Zn within the materials structure. Residual water was removed from the materials at above $200\text{ }^{\circ}\text{C}$. Meanwhile, thermal decomposition begins above $400\text{ }^{\circ}\text{C}$ in each material and results in the formation of zinc oxide (ZnO). The quantity of ZnO produced accounts for around 38

% of the overall sample weights. This suggests that each sample contains approximately the same amount of Zn and organic linker.

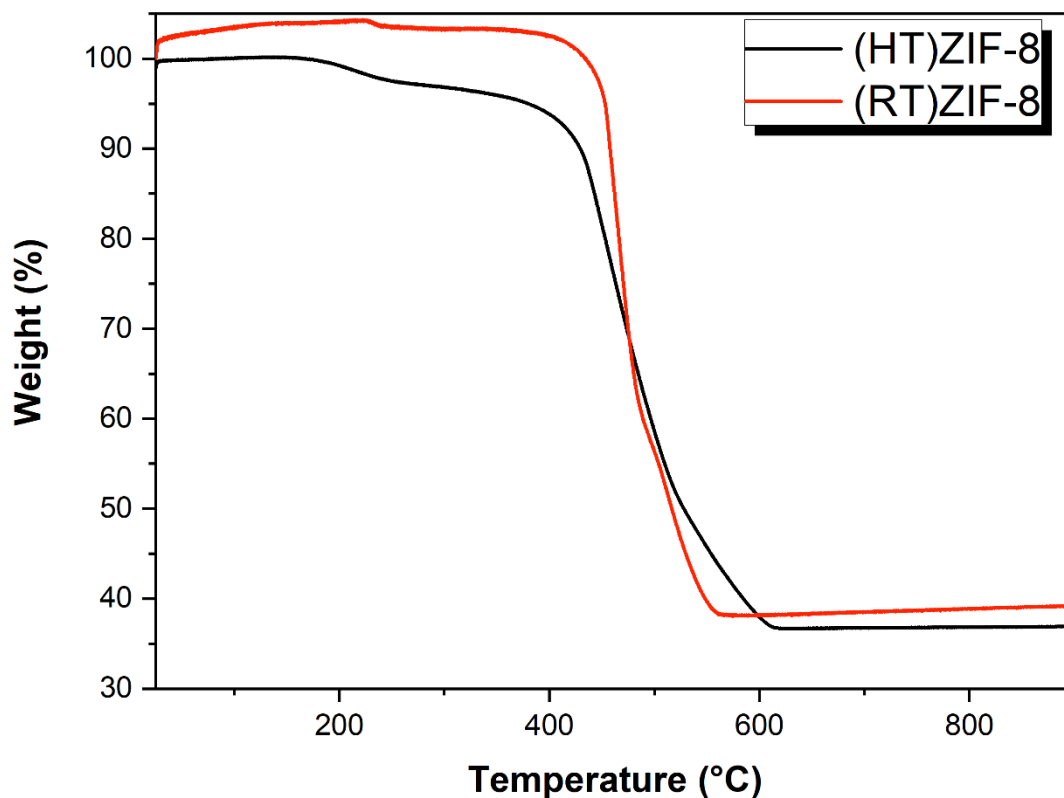


Figure 6.20. TGA profiles of ZIF-8 materials.

Scanning electron microscope (SEM) images of the ZIF-8 materials synthesised in this study are shown in **Figure 6.21**. As seen, the RT synthesis method yields particles of similar size and shape. The precise shape of these particles is difficult to view, however they do appear to be hexagonal or cubic in nature. Meanwhile, the HT synthesis method generates particles that are around 200 nm in size. These ZIF-8 materials are hexagonal/cubic in shape and appear to have a rough/uneven surface.

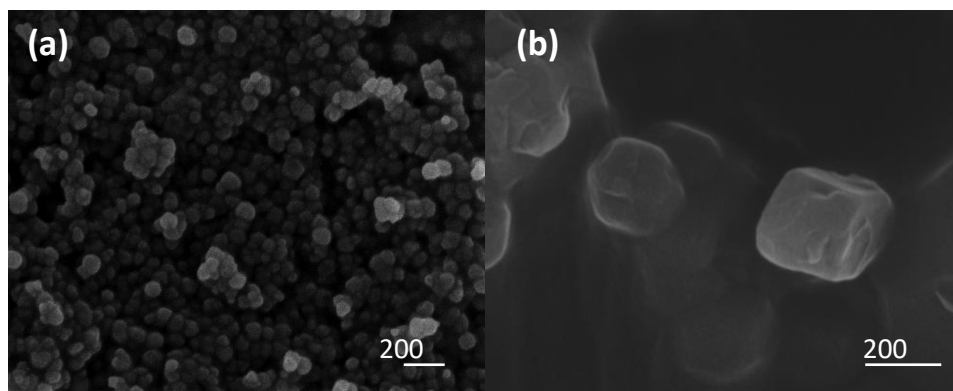


Figure 6.21. SEM imaging of catalysts (a) (RT)ZIF-8 (b) (HT)ZIF-8.

Glucose dehydration to HMF

The ZIF-8 materials were tested as catalysts in the aqueous isomerisation of glucose and production of HMF. As a benchmark for comparison, a blank reaction was performed at each of the chosen reaction temperatures (100 °C and 140 °C). All other reactions contained 40 mg of ZIF-8 catalyst or 24 mg of zinc chloride (ZnCl_2) unless otherwise stated.

As seen in **Figure 6.22**, the blank reaction conducted at 100 °C generated a glucose conversion < 1 % and negligible amounts of desirable products (fructose, mannose, HMF). This is expected considering the stability of glucose in water. The addition of 24 mg of ZnCl_2 (which should contain the same mass of Zn as 40 mg of ZIF-8) to the reaction marginally increased glucose conversions and fructose yields. Meanwhile, the addition of (RT)ZIF-8 to the reaction increased glucose conversions to 25.4 % and generate a desirable product yield of 15.6 % (~61 % selectivity). Within this product yield, fructose was the most abundant molecule. This suggests that Zn sites within the structure of ZIF-8 exhibit sufficient Lewis acidity to promote glucose isomerisation. Indeed, the Lewis acidity of ZIF-8 has previously been reported in literature and is specifically attributed to defective (low coordination) Zn sites within the materials structure.^{235–237} Furthermore, ZIF-8 is a hydrophobic framework.^{191,238} As such, the excellent catalytic performance of (RT)ZIF-8 may also be attributed to its hydrophobic nature. Specifically, the hydrophobicity of ZIF-8 likely minimises competition between reactants and solvent molecules at catalytically active sites. Moreover, the excellent performance of Sn-Beta as a glucose isomerisation catalyst has, in part, been attributed

to the hydrophobic nature of the zeolite structure - which prevents inhibition of active Sn sites by bulk water.⁷² Hence, the difference in activity observed between ZIF-8 and ZnCl₂ may be attributed to two factors; a difference in Lewis acidity, and a difference in hydrophobicity – with the ZIF-8 framework providing a more hydrophobic environment for reactions. The difference in performance between ZnCl₂ and ZIF-8 also suggests that leached Zn ions are not responsible for the observed catalytic activity of the MOF.

The addition of (HT)ZIF-8 to reactions conducted at 100 °C also increased glucose conversions and product yields. In fact, the glucose conversion and product yield generated by (HT)ZIF-8 is similar to that produced by (RT)ZIF-8. This is expected as TGA suggests that the materials contain approximately the same amount of Zn active sites. However, it is worth noting that the higher surface area of (HT)ZIF-8 may enable glucose conversions and product yields to be achieved faster.

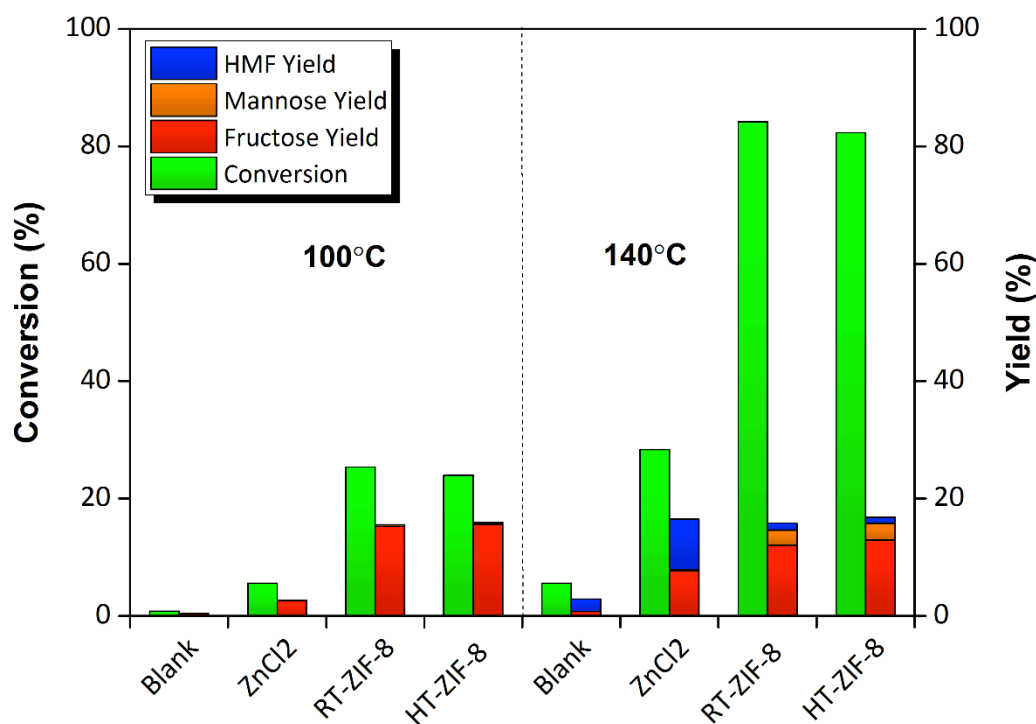


Figure 6.22. Glucose conversion in water on 40 mg of ZIF-8 catalysts or 24 mg of ZnCl₂. Reaction conditions: 100 °C or 140 °C, 3 h, stock solution of 10 wt. % glucose in deionized water.

In an attempt to improve glucose conversions and product yields, reactions were repeated at a higher temperature. As seen in **Figure 6.22**, a blank reaction conducted at 140 °C generated a glucose conversion of ~5 % as well as small quantities of fructose

and HMF. The addition of (RT)ZIF-8 and (HT)ZIF-8 to the reaction solution significantly increased glucose conversion and product yields. Specifically, the addition of (RT)ZIF-8 to the reaction resulted in a glucose conversion of ~84 %. This is significantly greater than the glucose conversion generated by the same catalyst at 100 °C and therefore highlights the temperature dependence of the reaction. Interestingly, the overall product yields generated by the ZIF-8 materials are comparatively similar to those produced at 100 °C. However, the product distributions are different. Specifically, the reactions at 140 °C generated higher quantities of mannose (2.6 % – 2.8 %) than reactions at 100 °C (0.3 %). This suggests that reaction selectivity is influenced by temperature. Indeed, higher temperatures appear to promote both fructose and mannose production. Meanwhile, mannose production appears to be suppressed at lower temperatures.

As previously seen, (RT)ZIF-8 and (HT)ZIF-8 generated almost identical glucose conversions and product yields in aqueous reactions. This is expected as the materials contain similar quantities of linker and Zn. However, the materials have significantly different surface areas. As such, it is reasonable to anticipate that (RT)ZIF-8 and (HT)ZIF-8 achieve their respective glucose conversions at different rates. To examine this, reaction times were varied. As seen in **Figure 6.23**, the results from these experiments indicate that (HT)ZIF-8 has a faster initial rate of reaction in comparison to (RT)ZIF-8. Moreover, this indicates that the higher surface area of (HT)ZIF-8 does impact the initial rate of reaction at shorter reaction times.

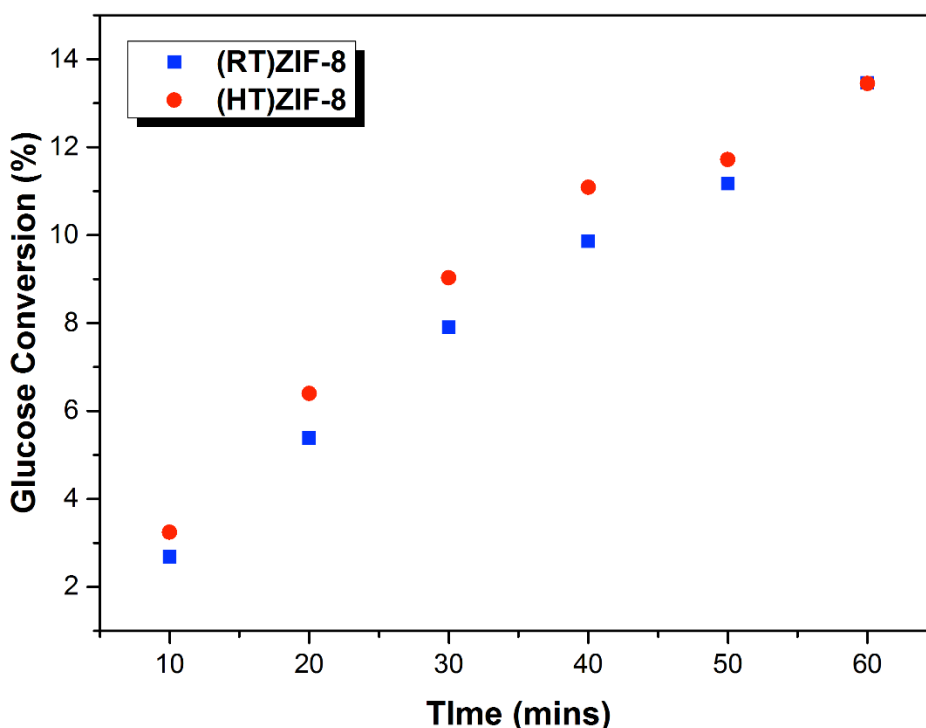


Figure 6.23. Glucose conversions vs. Time. Reaction conditions: 140 °C, 3 h, stock solution of 10 wt. % glucose in deionized water on 40 mg of catalyst.

The quantity of HMF produced by ZIF-8 is low. This indicates that ZIF-8 lacks the Brønsted acidity need to dehydrate fructose towards HMF. In an attempt to improve HMF yields, reactions were repeated in 0.1M HCl. As seen in **Figure 6.24**, the blank reaction at 100 °C generated a glucose conversion of around 5.7 % and negligible amounts of desirable product. The addition of ZIF-8 catalysts to the reaction increased glucose conversions and total product yield. However, these conversions and product yields are lower than those generated in water under the same reaction conditions. This indicates that the addition of HCl to the reaction hinders the performance of the catalyst. Perhaps the mineral acid effectively ‘swamps’ active sites within ZIF-8, resulting in poorer catalytic activity. The main product generated in the reactions was fructose. This indicates that the addition of the mineral acid does not effectively drive the reaction towards HMF. Indeed, it may suggest that Zn sites within the framework of ZIF-8 stabilise the fructose molecules generated in the reaction.

The blank reaction at 140 °C generates a glucose conversion of around 18 % and a HMF yield of around 4 %. As such, the mineral acid increases glucose conversions and the product yields at higher temperatures. The addition of ZIF-8 catalysts increased glucose conversions as well as fructose and mannose yields in comparison to the blank reaction – although HMF yields are lower. Overall, the conversions generated by ZIF-8 catalysts are slightly lower than those produced in water under similar conditions whilst product yields are higher. As such, the addition of 0.1M HCl is found to slightly improve reaction selectivity and overall desirable product yields at 140 °C.

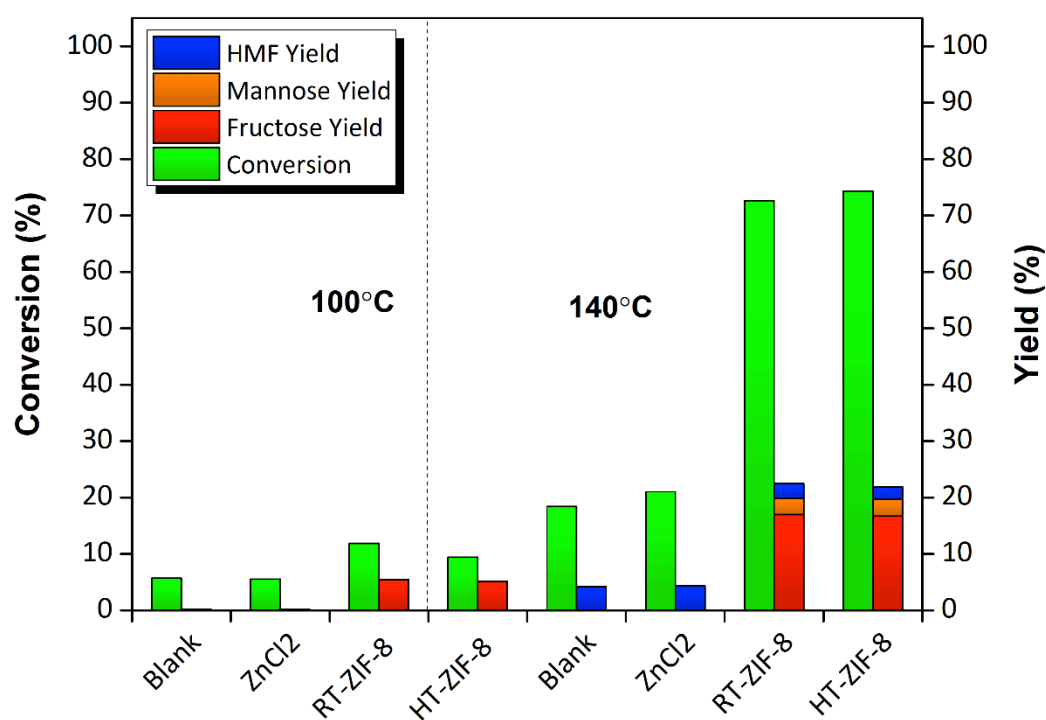


Figure 6.24. Glucose conversion in 0.1M HCl on ZIF-8 catalysts. Reaction conditions: 100 °C or 140 °C, 3 h, stock solution of 10 wt. % glucose in 0.1M HCl.

Catalyst Stability & Recycling

In order to test the stability and reusability of ZIF-8, its performance was tested in a purpose built flow reactor. For this, 40 mg of catalyst was pelletized and sieved to give a uniform particle size of 250 nm. The catalyst was then mixed with an inert material (silicon carbide) and loaded into the reactor resulting in a bed length of 8 cm. A 10 wt.% glucose solution in water was then continuously pumped through the reactor at a flow rate of 0.14 mL/min resulting in a weight hour space velocity (WHSV) of 21 h⁻¹. Meanwhile, the reactor was heated to a temperature of 100 °C.

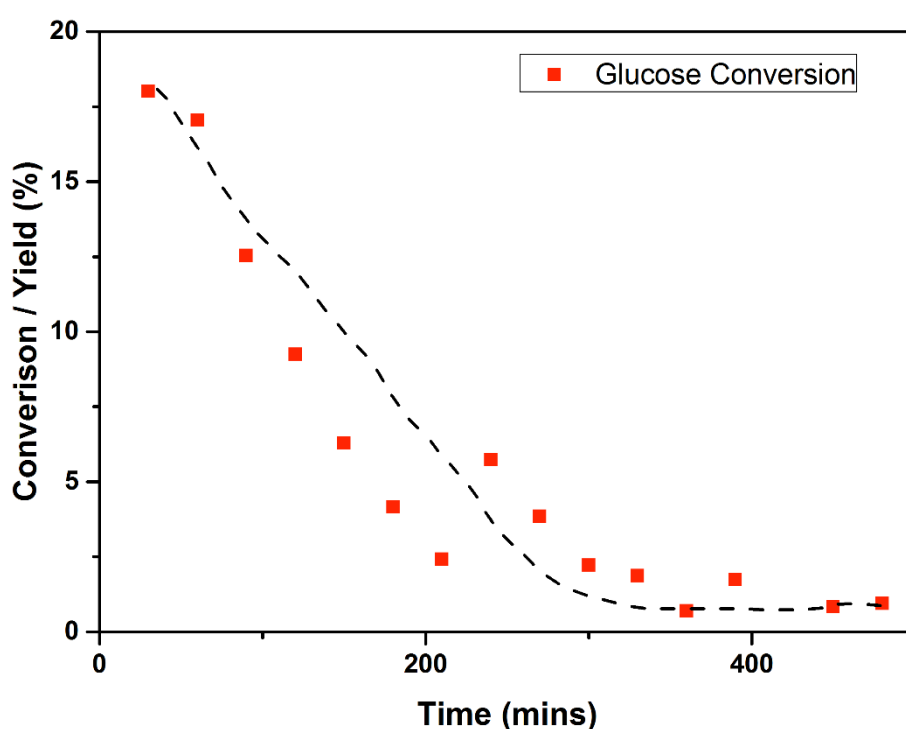


Figure 6.25. Activity of (RT)ZIF-8 in a continuous flow reactor. 40 mg catalyst, 10 wt.% glucose in water stock solution, 100 °C, 0.14 mL/min.

The performance of (RT)ZIF-8 is shown in **Figure 6.25**. As seen, the catalyst initial generates a glucose conversion of around 18 %. However, this initial activity quickly diminishes with increasing time on stream - ultimately resulting in a glucose conversion below 2 %. This clearly indicates that the catalyst is either destroyed/damaged during the reaction, or that the production of insoluble humins quickly deactivates the catalyst. Overall, the results of this study suggest that ZIF-8 may be unsuitable for aqueous glucose isomerisation in flow reactors.

6.9 Conclusions

ZIF-8 has been synthesised using a two different methods. Of these, the hydrothermal synthesis method yields a material with exceptionally high surface area. The synthesised materials were tested as catalysts for the isomerisation of glucose and production of HMF. Both ZIF-8 catalysts generated similar glucose conversions and product yields in water. This was not surprising as each catalyst contained similar quantities of Zn and organic linker. The main product generated in the reactions was fructose. This indicates that ZIF-8 exhibits sufficient Lewis acidity to promote glucose isomerisation in water. The effect of temperature on ZIF-8 catalysed reactions was also observed. Interestingly, higher temperatures were found to reduce reaction selectivity towards fructose. Furthermore, higher reaction temperatures appear to promote mannose and HMF production. Conversely, mannose production appeared to be suppressed at low reaction temperatures.

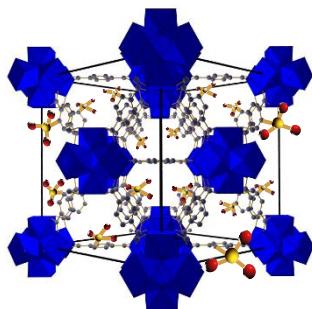
The ZIF-8 materials did not generate large HMF yields during reactions in water. This suggests that the ZIF-8 materials are not sufficiently Brønsted acidic. In order to drive HMF production, reactions were repeated in 0.1M HCl. Interestingly, the presence of this mineral acid reduced the activity of ZIF-8 catalysts at lower reaction temperatures (100 °C). Meanwhile, the mineral acid improved product yields at higher temperatures (140 °C). The main product generated in reactions containing ZIF-8 and 0.1M HCl was fructose. This indicates that the mineral acid does not dehydrate the fructose yields generated by ZIF-8 towards HMF. Perhaps the ZIF-8 material stabilises the fructose molecules produced, thus preventing further reaction.

In order gauge the suitability of ZIF-8 for potential scale-up reactions, the activity of the catalysts were tested in a purpose built flow reactor. The activity of (RT)ZIF-8 in the flow reactor was initially high but quickly diminished. This was potentially due to catalyst destruction, or deactivation caused by insoluble humin by-products.

Exceptionally Efficient and Recyclable Heterogeneous UiO-66 Catalysts for Glucose Isomerization in Water.

Summary

In the previous study, ZIF-8 was considered as a glucose isomerisation catalyst. Although this material generated promising reaction results, its framework contains a highly toxic organic linker and its performance rapidly declines in a flow reactor. In this study, we attempt to develop MOF catalysts that are both reusable and environmentally benign. For this we consider UiO-66, and a functionalised variant of this MOF, as glucose isomerisation catalysts in water. The UiO-66 framework was functionalised by replacing a fraction of the materials BDC linker with monosodium 2-sulfoterephthalate (MSBDC). The introduction of the functionalised linker appeared to improve the Lewis acidity observed at nearby defective Zr sites within the UiO-66 framework. A material containing 20 % MSBDC linker generated the highest glucose conversion and product yields observed in this study. Specifically, (20)MSBDC-UiO-66 generated a glucose conversion of around 36 % and a total desirable product yield of 29.6 %. However, it is worth noting that the BioRAD HPX-87H column used during analysis was unable to effectively separate isomerisation products (i.e. fructose and mannose). The stability and reusability of each catalyst considered in this study was confirmed via a series of recycle reactions. Overall, the results of this study highlight the potential to ‘fine-tune’ Zr MOFs for glucose isomerisation and HMF production in water.



6.10 Introduction

The number of metal-organic frameworks (MOFs) reported in literature has risen dramatically in recent years - with over 600 new MOFs published annually.²³⁹ With this, the number of water stable MOFs available to researchers has grown. The hydrothermal stability of a MOF is largely dependent on its vulnerability to hydrolysis.^{240,241} As such, numerous factors may influence the stability of a MOF in water. These factors may include; metal-ligand bond strength, kinetic stability, and hydrophobicity.²⁴⁰ This growing understanding of MOF stability has driven the development of water stable frameworks. Indeed, the use of high valence metals (i.e. Zr^{4+} , Fe^{3+} , Cr^{3+}) and the incorporation of azolate ligands (nitrogen containing ligands) can improve MOF stability in water.²⁴¹

UiO-66 is of considerable interest due to its stability in water and high mechanical strength. These attributes are a result of the frameworks Zr brickwork.²⁴² Specifically, UiO-66 consists of metal clusters containing six Zr^{4+} ions in octahedron geometry. These metal clusters are linked by terephthalic acid (BDC) struts - giving an overall chemical formula of $Zr_6O_4(OH)_4(CO_2)_{12}$ per cluster.^{242,243} The introduction of defective Zr sites (not fully coordinated) within the structure of UiO-66 results in Lewis acid properties.^{244,245} Furthermore, the Lewis acidity of UiO-66 may be “tuned” by altering the materials organic linker. For example, the introduction of electron-withdrawing groups on the material’s organic linker can improve the Lewis acidity observed at nearby defective Zr sites.²⁴⁶

In this study, UiO-66 is considered as a catalyst for the isomerisation of glucose and production of HMF. This non-toxic and environmental benign catalyst was synthesised using a simple, short, and well-reported procedure. In order to improve catalyst activity, a functionalised linker was introduced into the framework. This functionalised linker contained electron-withdrawing sulfonic acid groups. The maximum quantity of linker added into the framework was capped at 20 % in order to preserve material stability. To access the reusability of the catalysts considered, a number of recycle reactions were performed. All reactions were performed in water - the most environmentally benign solvent - at a moderate temperature of 140 °C.

6.11 Results and Discussion

Structure and Morphology

The successful synthesis of UiO-66 was confirmed by powder X-ray diffraction (XRD) analysis. As shown in **Figure 6.26**, there are no additional peaks within the diffraction pattern of UiO-66. This suggests an absence of bulk extra-framework metal and uncoordinated BDC linker within the materials structure. However, it is worth noting that several batches of UiO-66 were used in this study and some batches did exhibit additional Bragg peaks with their diffraction pattern. An example of a UiO-66 batch with additional diffraction peaks - presumably indicating the presence of loose linker within the material - is shown in **Appendix Figure C1**. Sulfonic acid functionalised UiO-66 was prepared by introducing MSBDC linker into the materials framework. However, high quantities of MSBDC linker can negatively impact the stability of UiO-66.²⁴⁷ As such, materials containing only 10 % and 20 % functionalised linker were prepared for study. Hereafter, these materials are referred to as (10)MSBDC-UiO-66 and (20)MSBDC-UiO-66, respectively. Powder XRD analysis shows that the addition of MSBDC does not alter the structure of UiO-66.

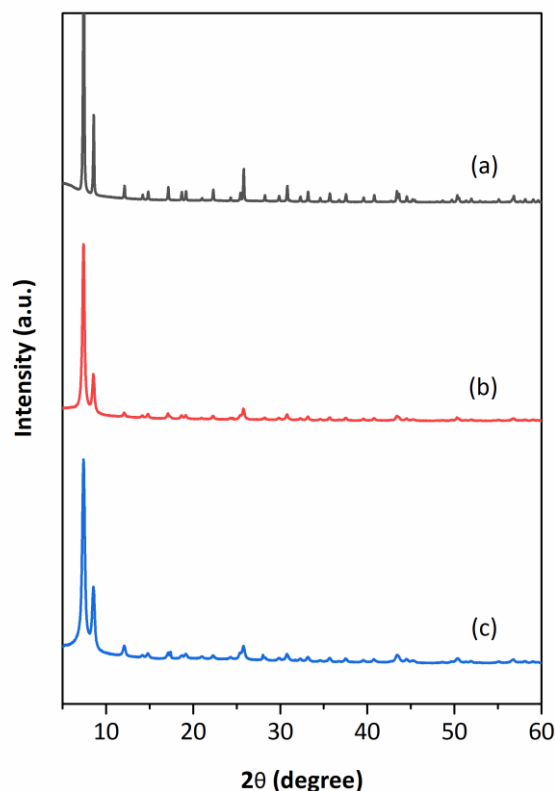


Figure 6.26. XRD patterns of (a) UiO-66 (b) (10)MSBDC-UiO-66 (c) (20)MSBDC-UiO-66.

The successful introduction of MSBDC linker within the structure of UiO-66 was confirmed by Energy-dispersive X-ray spectroscopy (EDX). Specifically, EDX mapping was used to confirm the presence of sulphur (S) within functionalised materials. As seen in **Figure 6.27**, both UiO-66 and (20)MSBDC-UiO-66 contain high quantities of Zr. Meanwhile, (20)MSBDC-UiO-66 also contains significant quantities of S. This high S content confirms the presence of MSBDC linker within the functionalised material.

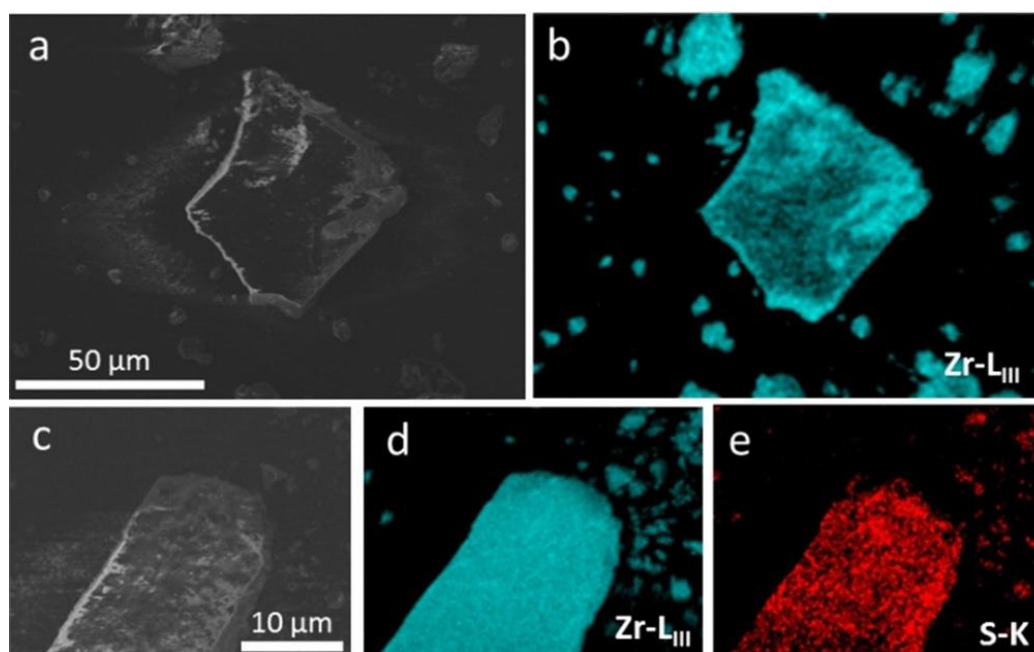


Figure 6.27. a) SEM image of UiO-66 b) zirconium EDX mapping of UiO-66. c) SEM image of (20)MSBDC-UiO-66 d) zirconium EDX mapping of (20)MSBDC-UiO-66 e) sulfur EDX mappings of (20)MSBDC-UiO-66.

To quantify the amount of S within the functionalised materials, and hence the amount of MSBDC linker, inductively coupled plasma (ICP) analysis was used. As seen in **Table 6.5**, (10)MSBDC-UiO-66 and (20)MSBDC-UiO-66 contains 1.19 wt. % and 2.09 wt.% S, respectively. Meanwhile, S was not detected in UiO-66. To give a more meaningful representation of these results, the molar concentration of S within each material was normalised in comparison to Zr. As seen in **Table 6.6**, (10)MSBDC-UiO-66 contains a Zr: S content of 1: 0.13 (wt.%/wt.%). Therefore indicating that 13 % of the materials organic linker content is MSBDC. The Zr: S content within (20)MSBDC-UiO-66 is calculated as 1: 0.23 (wt.%/wt.%) – indicating that 23 % of the materials

linker content is MSBDC. Overall, ICP analysis confirmed that each functionalised material contains quantities of MSBDC linker close to target amounts.

Table 6.5. ICP analysis of UiO-66 catalysts.

Catalyst	Carbon (wt. %)	Hydrogen (wt. %)	Nitrogen (wt. %)	Sulfur (wt. %)	Zirconium (wt. %)
UiO-66	30.77	3.20	<0.10	N/A	26.07
(10)MSBDC-UiO-66	30.02	3.04	0.81	1.19	26.85
(20)MSBDC-UiO-66	30.29	3.13	1.23	2.09	25.56

Table 6.6. Molar concentrations of elements within UiO-66 materials normalised in comparison to Zr.

Catalyst	Carbon	Hydrogen	Nitrogen	Sulfur	Zirconium
UiO-66	9.0	11.1	<0.02	N/A	1.0
(10)MSBDC-UiO-66	8.5	10.3	0.19	0.13	1.0
(20)MSBDC-UiO-66	9.0	11.1	0.31	0.23	1.0

Infrared (FTIR) spectroscopy of the synthesised materials confirmed the almost complete absence of DMF (**Figure 6.28**). The success incorporation of sulfonic acid groups within (10)MSBDC-UiO-66 and (20)MSBDC-UiO-66 was also confirmed through FTIR spectroscopy. Bandwidth peaks within the materials FTIR spectra at around 1090 cm^{-1} and 1220 cm^{-1} indicated the presence of $\text{O}=\text{S}=\text{O}$.^{248,249} The presence of these bonds further confirms that both (10)MSBDC-UiO-66 and (20)MSBDC-UiO-66 contain sulfonic acid functionalised linker.

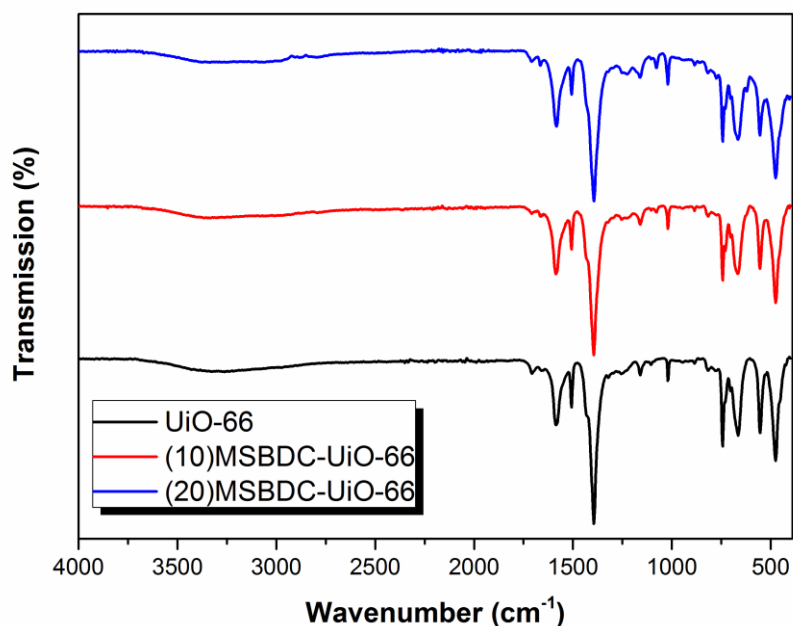


Figure 6.28. Infrared (IR) spectra of UiO-66 and functionalised variants.

Nitrogen adsorption analysis was used to quantify the surface areas and pore volumes of the UiO-66 materials considered in this study. As seen in **Figure 6.29**, the isotherm's of each material are different. The isotherm and hysteresis loop of UiO-66 is similar to those previously reported in literature.^{250,251} This adsorption isotherm is consistent with type I, indicating the presence of a microporous structure.

Increasing the quantity of MSBDC linker changes the materials hysteresis loop. Specifically, increasing the quantity of MSBDC linker appears to broaden the hysteresis loop. The hysteresis loops of (10)MSBDC-UiO-66 and (20)MSBDC-UiO-66 are consistent with type IV, suggesting that the introduction of functionalised linker results in an increasingly mesoporous structure.

This trend of increasing mesoporous volume is more clearly observed in **Table 6.7**. As seen, the pore volume of UiO-66 is mostly comprised of microporous channels. Interestingly, increasing the quantity of MSBDC linker within the material's framework dramatically increases mesoporous volume. Specifically, mesoporous volume is seen to increase with increasing quantities of MSBDC.

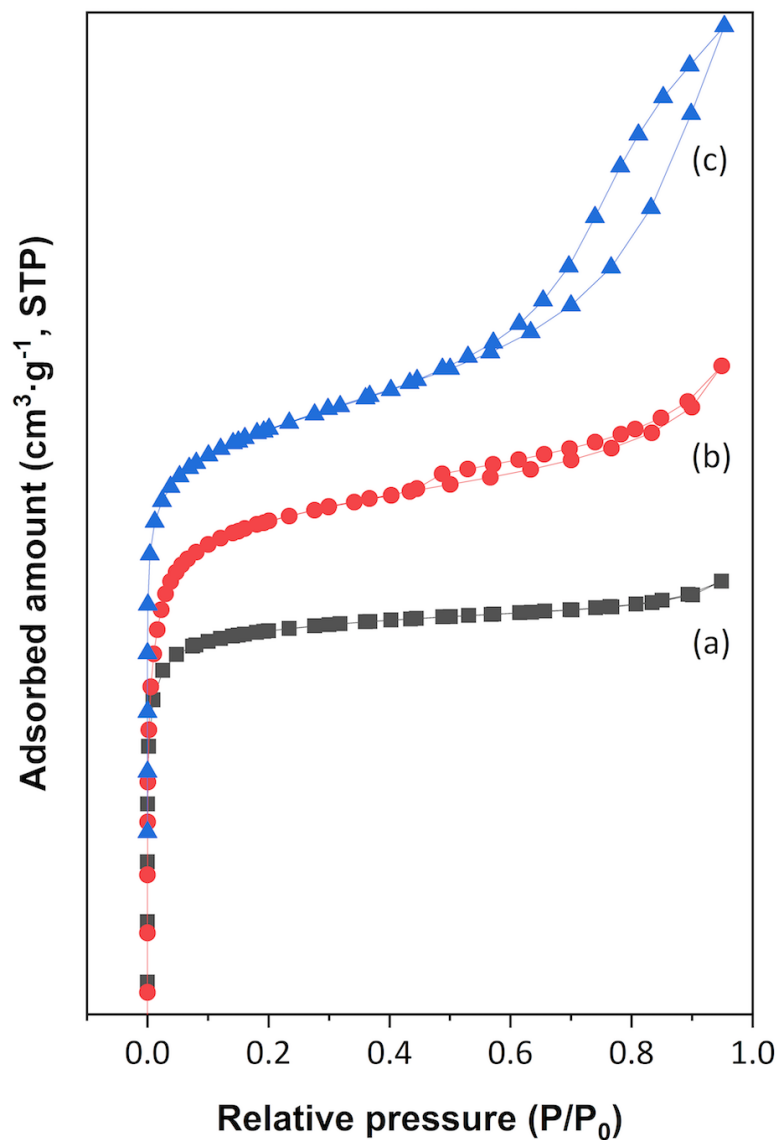


Figure 6.29. Nitrogen adsorption isotherm's of (a) UiO-66 (b) (10)MSBDC-UiO-66 (c) (20)MSBDC-UiO-66 .

Table 6.7. BET surface area and pore volume of UiO-66 catalysts.

Catalyst	BET Surface Area ($\text{m}^2 \cdot \text{g}^{-1}$)	Micropore Volume ($\text{cm}^3 \cdot \text{g}^{-1}$)	Mesopore Volume ($\text{cm}^3 \cdot \text{g}^{-1}$)
UiO-66	737	0.26	0.04
UiO-66-MSBDC(10)	1061	0.33	0.11
UiO-66-MSBDC(20)	823	0.22	0.29

Thermal gravimetric analysis (TGA) was used to determine the thermal stability of materials. As seen in **Figure 6.30**, thermal decomposition begins above 500 °C and results in the formation of zirconium oxide (ZrO). This is consistent with the reported decomposition temperature of 540 °C for UiO-66 and approximately 500 °C for sulfonic acid functionalised UiO-66 materials reported in literature.^{242,247} Extracted data from TGA indicates an MSBDC linker content of 14.6 % and 24.7 % for (10)MSBDC-UiO-66 and (20)MSBDC-UiO-66, respectively. Furthermore, the coordination number of Zr atoms within each material was determined from TGA. The coordination of the Zr atoms within the brickwork of UiO-66, (10)MSBDC-UiO-66, and (20)MSBDC-UiO-66, was found as 5.51, 5.11 and 5.63, respectively. As such, although close to perfect structures were obtained during synthesis, defective Zr sites are present within each material considered.

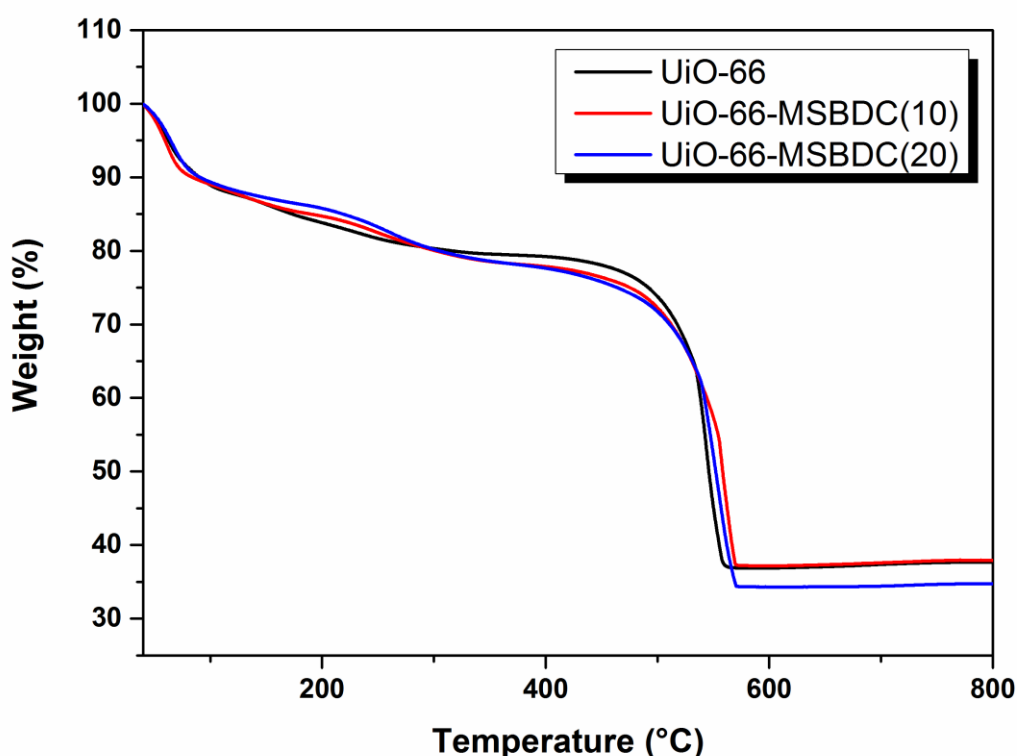


Figure 6.30. TGA profiles of UiO-66 and functionalised UiO-66 materials.

Glucose dehydration to HMF

The UiO-66 materials were tested as catalysts for the aqueous isomerisation of glucose and production of HMF. A green solvent, water is an ideal solution to perform such reactions. Reactions were performed at 140 °C using a 10 wt.% glucose feedstock. As a baseline for comparison, a blank reaction containing no catalyst was also performed. As seen in **Figure 6.31**, the presence of UiO-66 in the reaction increased glucose conversions and product yields in comparison to the blank reaction. Specifically, UiO-66 generated a glucose conversion of around 16 % and a total desirable product yield of around 11 %. Within this product distribution, fructose was the most prevalent molecule. This indicates that UiO-66 is acting as a glucose isomerisation catalyst. Moreover, the high fructose yield indicates that defective Zr sites within the UiO-66 framework are providing sufficient Lewis acidity to promote the isomerisation of glucose under moderate conditions. The HMF yield generated by UiO-66 is only marginally higher than that produced in the blank reaction. This suggests that UiO-66 does not exhibit the required Brønsted acidity needed to promote the dehydration of fructose towards HMF.

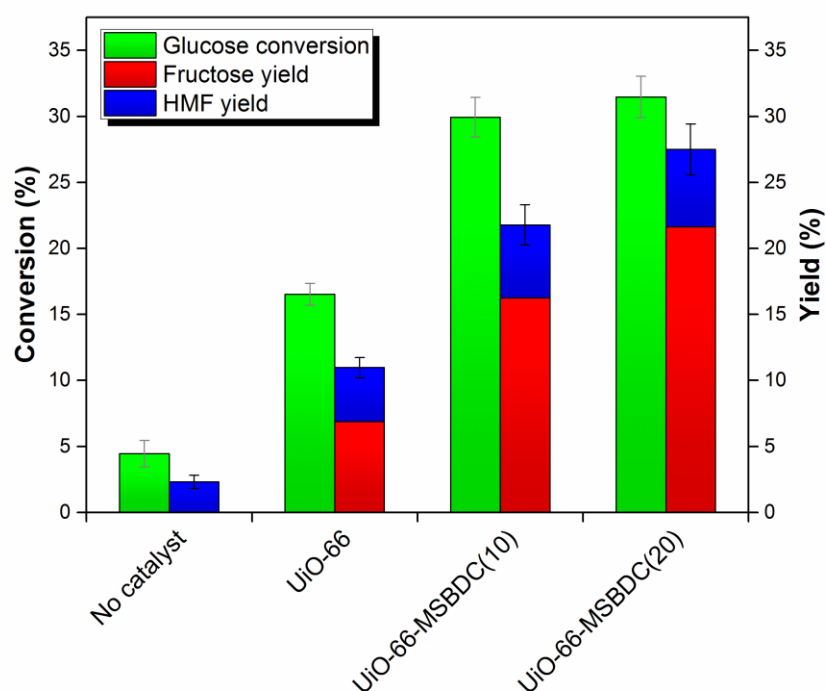


Figure 6.31. Glucose conversion in water on UiO-66 catalysts. Reaction conditions: 140 °C, 3 h, stock solution of 10 wt. % glucose in deionized water.

As seen in the **Figure 6.31**, the presence of MSBDC linker within the framework of UiO-66 increases both glucose conversion and desirable product yields. Overall, the material containing 20 % MSBDC linker produced the highest glucose conversion and desirable product yield found in this study. Specifically, (20)MSBDC-UiO-66 generated a glucose conversion of around 31 % and a total product yield of around 27 %. Within this product distribution, fructose was again found to be the dominant molecule. This suggests that the presence of electron withdrawing $-\text{SO}_3\text{H}$ groups within the UiO-66 framework enhances the materials Lewis acidity. Indeed, recent studies have concluded that the Lewis acidity of defective Zr sites within the framework of UiO-66 can be enhance by the presence of electron-withdrawing groups on the materials organic linker.²⁴⁶

Catalyst Stability & Recycling

The hydrothermal stability of UiO-66 and its functionalised variants were quantified through ICP analysis of the filtered reaction solutions. As seen in **Table 6.8**, Zr is leached form the framework of UiO-66 during the reaction at 140 °C. However, the amount of Zr leached is small and therefore indicates that the material is not destroyed during the reaction. This is expected given the reported hydrothermal stability of UiO-66. ICP analysis indicates that larger quantities of Zr are leached from the functionalised materials during the reaction. This is unsurprising as the introduction of sulfonic acid groups into the framework of UiO-66 is known to reduce material stability (as previously described). Never the less, the quantities of Zr leached from the functionalised variants is sufficiently small and therefore suggests that the MSBDC containing materials are not destroyed during reaction. ICP analysis also reveals that the filtered reaction solutions contain small quantities of S. This indicates that $-\text{SO}_3\text{H}$ groups may be stripped from the functionalised catalysts during reaction.

Table 6.8. Zirconium and sulfur content in the reaction solution after 3 h reaction at 140°C.

Catalyst	Sulfur (ppm)	Zirconium (ppm)
UiO-66	N/A	0.2
UiO-66-MSBDC(10)	<0.10	0.4
UiO-66-MSBDC(20)	<0.10	0.4

To access the reusability of the materials considered in this study, recycle reactions were also performed. For this, reactions were scaled up by a factor of five. After each reaction cycle the catalysts were recovered and washed via centrifuge before being added back to fresh stock solution. As seen in in **Table 6.9**, the glucose conversions and product yields generated by UiO-66 remained relatively consistent following an initial decline in activity. This initial decline in activity was also observed in the recycling of MSBDC functionalised materials. Overall, (20)MSBDC-UiO-66 was found to generate the highest glucose conversion and product yields over the course of four consecutive recycle reactions.

The initial declined in activity (and product yield) observed in the recycling of each catalyst may be attributed to a number of factors. Firstly, the decrease in yield may be attributed to a loss of small, highly active, catalysts particles that are difficult to recover following the first reaction cycle. Secondly, the production of insoluble humin by-products during the first reaction may block access to Zr active sites within the framework. Finally, in the case of MSBDC containing materials, $-\text{SO}_3\text{H}$ functional groups may be stripped from the organic linker during the first reaction – ultimately reducing the number of electro-withdrawing groups within the material and the Lewis acidity of nearby defective Zr active sites. In order to determine which of these effects are impacting product yields following the first reaction, the recovered catalysts were weighed and analysed via ICP and XRD analysis.

Table 6.9. Glucose Conversions and Yields obtained from UiO-66 catalyst recycling.

Catalyst	Reaction cycle	Glucose conversion (%)	Fructose yield (%)	HMF Yield (%)
UiO-66	1	19.1	5.7	4.9
	2	17.3	2.7	2.3
	3	16.4	2.6	2.3
	4	10.8	2.8	2.4
(10)MSBDC-UiO-66	1	33.2	18.6	7.6
	2	20.6	6.9	3.4
	3	20.3	7.2	3.5
	4	17.5	5.3	2.9
(20)MSBDC-UiO-66	1	35.9	21.7	7.9
	2	20.9	7.9	3.3
	3	19.5	9.5	3.4
	4	21.7	6.5	2.8

As shown in **Table 6.10**, the amount of UiO-66 recovered from the 4th recycle reaction is less than 50 mg – indicating a clear loss of catalyst during the recycle reaction. This mass loss is likely due to the incomplete recovery of small catalyst particles between reactions. As previously noted, this loss of catalyst likely contributed to the decline in catalytic activity following the initial reaction cycle. In contrast, the mass of MSBDC containing materials has increased over the course of four consecutive reactions. This increase in mass can be attributed to the accumulation of insoluble humins by-products on the catalyst surface. As previously mentioned, the accumulation of humins may block active Zr sites within the materials framework, leading to a decline in catalytic activity.

Table 6.10. Recovery of UiO-66 catalysts after recycle reactions.

Catalyst	Initial catalyst (mg)	Recovered catalyst after 4 th run (mg)
UiO-66	50.1	44.4
(10)MSBDC-UiO-66	51.2	75.1
(10)MSBDC-UiO-66	50.6	62.1

An initial ICP analysis of filtered reaction solutions suggests that $-\text{SO}_3\text{H}$ groups may be stripped from the fictionalised materials during reaction (**Table 6.8**). In order to quantify the loss of $-\text{SO}_3\text{H}$ during recycle reactions, the Zr and S contents of recovered functionalised catalyst were quantified using ICP analysis. This elemental analysis was then normalised towards Zr in order to determine the amount of functionalised linker within each material. As shown in **Table 6.11**, the quantity of $-\text{SO}_3\text{H}$ groups within each material decreased following the recycle reactions. Specifically, the functionalised linker content of (10)MSBDC-UiO-66 and (20)MSBDC-UiO-66 were reduced to 8 % and 13 %, respectively. This removal of functional groups likely changes the Lewis acidity exhibited by Zr active sites within the materials framework – ultimately contributing to a decline in catalytic activity.

Table 6.11. Comparison of the zirconium and sulfur content of the UiO-66 catalysts before and after the reaction at 140°C for 3 h

Catalyst	Before the reaction			After the reaction		
	S (wt. %)	Zr (wt. %)	Molar Ratio (S/Zr)	S (wt. %)	Zr (wt. %)	Molar Ratio (S/Zr)
(10)MSBDC-UiO-66	0.39	13.47	0.13/1	0.08	1.00	0.08/1
(20)MSBDC-UiO-66	0.53	12.49	0.23/1	0.13	1.00	0.13/1

To further confirm the stability of the catalysts, the recovered materials were analysed via XRD and their diffraction patterns fitted using GSAS software. As shown in **Figure 6.32**, the diffraction patterns of the recovered recycled materials are consistent with the UiO-66 framework. This indicates that the materials are stable and are able to endure

four consecutive heat treatments at 140 °C in water. However, as indicated by the GSAS fitting, the unit cell size of each material has increased following recycling. This expansion of the catalysts unit cell may be due to leaching or the accumulation of insoluble humins within the materials pore network.

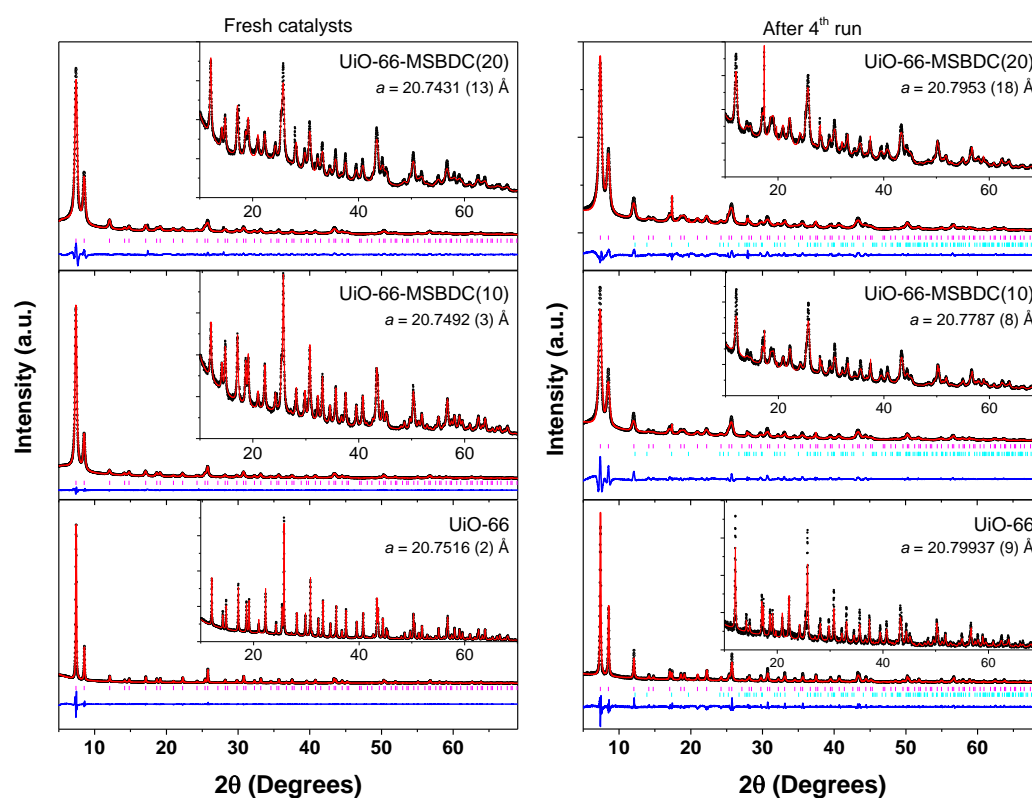


Figure 6.32. Fitted diffraction patterns of UiO-66 catalysts before and after recycle reactions.

6.12 Conclusions

Defects within the Zr brickwork of UiO-66 provide sufficient Lewis acidity to catalyse glucose isomerisation in water. Furthermore, the material is stable and retains its catalytic performance well over the course of four consecutive recycle reactions. The framework of UiO-66 can be functionalised by replacing the materials organic linker. The addition of MSBDC within the framework of UiO-66 improves glucose conversions and product yields. Interestingly, the addition of sulfonic acid groups within the framework of UiO-66 did not significantly increase HMF yields. Instead, the introduction of electron-withdrawing groups was found to improve the Lewis acidity observed at nearby defective Zr sites. Moreover, the introduction of MSBDC within the framework improves glucose conversions and fructose yields. As with UiO-66, the functionalised MOFs retained their catalytic activity well over the course of four consecutive recycle reactions. However, some of the materials sulfonic acid groups were stripped from the framework during these reactions. Furthermore, there was a significant build-up of insoluble humins on the catalyst during reaction. As such, catalyst deactivation over time may result from humin formation or functional group loss. Overall, the results obtained in this study highlight the potential to ‘fine-tune’ MOF catalysts towards fructose production in water.

Fine-Tuning Zirconium Organic Frameworks Towards the Isomerisation of Glucose and Production of 5-Hydroxymethylfurfural

Summary

As demonstrated in the previous chapter, the development of “designer catalysts” through the functionalisation of metal-organic frameworks (MOFs) may offer solutions towards the industrial scale production of 5-hydroxymethylfurfural (HMF). Herein, we expand upon our recent findings by fine-tuning the functionality of zirconium (Zr) MOFs towards the isomerisation of glucose and production of HMF. UiO-66 and UiO-67 MOFs were altered through linker substitution, size modulation, and post-synthesis treatment to promote surface defects. The functional groups introduced into the MOFs were sulfonic acid, carboxylic acid, hydroxyl groups, and naphthalene. The catalytic performances of these materials were tested in batch reactions. Preference was given to water mediated reactions with the foresight of developing non-toxic, and truly “green”, catalytic systems comparable to the enzymatic glucose isomerisation processes currently employed in industry. Sulfonic acid functionalised UiO-66 MOFs were found to be the most effective catalysts tested in this study. Specifically, (50)MSBDC-UiO-66 generated a glucose conversion of 37.3 % along with a 58.9 % selectivity towards desirable products (fructose, mannose, and HMF). We also show that defective sites and the introduction of naphthalene groups within the framework of UiO-66 promotes reaction selectivity towards mannose. Meanwhile, fructose dehydration towards HMF can be driven by the introduction of a BTeC linker that provides free carboxylic acid groups. The reusability of promising catalysts was explored through a series of recycle reactions. Both UiO-66 and UiO-67 catalysts remained active during the course four consecutive recycle reactions in water and maintained their inherent structure. Selected catalysts were also tested in a continuous flow reactor. Here, a number of UiO-66 catalysts demonstrate exceptional promise, generating stable glucose conversions and fructose yields with increasing time on stream.

7.1 Introduction

Metal-organic frameworks (MOFs) are an emerging interest within catalysis.^{140–144} The tuneable chemical and physical properties of these porous materials leads to the development of “designer catalysts”. Despite the potential application of MOFs within the field of biomass valorisation, relatively few research groups have considered their use in the production of fructose and HMF. Of these, several groups have focused their attention on the application of chromium (Cr) MIL-101 within organic solvents.^{62,130,131,196,197} Although promising yields and selectivity’s can be obtained from this catalyst, the use of Cr entails toxicity concerns and the application of organic solvents is not ideal.¹⁰⁹ More recent literature has begun to explore the use of Zr MOFs for fructose and HMF production. To this extent, NUS-6 enables high HMF yields to be obtained from a fructose feedstock.²⁵² Furthermore, NU-1000 and UiO-66 have shown promise as isomerisation catalysts. In particular, UiO-66 exhibits excellent activity as a glucose isomerisation catalyst when combined with the sequential use of alcohol and aqueous mediated reactions.^{63,65}

In the previous chapter we identified UiO-66 as a promising catalyst for the aqueous isomerisation of glucose and production of HMF. To improve catalytic activity and selectivity, we explored the use of a sulfonic acid functionalised variant of this MOF. Not only was the functionalised catalyst highly active, it was also shown to be highly recyclable. Stable in water under moderate conditions, UiO-66 can be produced in continuous flow using a commercially available linker that has the potential to be obtained from biomass feedstock.^{253,254} Moreover, the development of such catalytic systems that are robust, cheap, and environmentally benign, are favourable when working towards the production of HMF at scale. Herein, we continue our study of UiO-66 catalysts for the purpose of biomass valorisation, specifically focusing on glucose isomerisation and HMF production. We explore the effects of surface area, defective sites, and linker substitution on catalytic performance. Furthermore, the application of an isorecticular framework with an expanded structure, UiO-67, is explored as a glucose isomerisation and dehydration catalyst. The reusability of several highly promising catalysts is tested via a series of consecutive recycle reactions and through the use of a flow reactor. The effect of substrate to catalyst ratio is explored as well as the use of an alternative aprotic organic solvent, dimethyl sulfoxide (DMSO), and an alternative feedstock (fructose).

7.2. Results and Discussion

Structure and Morphology

Introducing high quantities of MSBDC linker into the framework UiO-66 can have an inverse effect on material stability.²⁴⁷ To ensure a stable structure for the purpose of heterogeneous catalysis, the quantity of MSBDC linker within UiO-66 was limited to 20 % in previous work.²⁵⁵ For our current study, we begin by exploring the limits of MSBDC linker substitution with respect to hydrothermal stability. Powder X-ray diffraction (XRD) analysis (**Appendix Figure D1**) reveals that materials containing both 50 % and 100 % MSBDC linker can be successfully made. However, upon completion of a hydrothermal stability test conducted at our upper reaction temperature (140 °C), (100)MSBDC-UiO-66 experiences a clear loss in crystallinity whereas (50)MSBDC-UiO-66 remains unchanged. As such, materials containing an MSBDC linker content of 100 % are not considered for catalysis in this study.

XRD analysis was also used to observe the crystallinity of all other materials prepared for study. For the standard UiO-66 material, it is worth noting that several batches of UiO-66 were used in this study and some batches did exhibit additional Bragg peaks with their diffraction pattern. An example of a UiO-66 batch with additional Bragg peaks - presumably indicating the presence of loose linker within the material - is shown in **Appendix Figure C1**. A simulated UiO-66 diffraction pattern from literature is also shown for reference.²⁵⁶ As shown in **Figure D2**, the diffraction patterns of Nano and Ultra-Nano UiO-66 reveal crystalline MOF structures. However, these diffraction patterns exhibit signs of peak broadening. This peak broadening is expected given the presumably smaller crystallite domain sizes contained within these samples. The production of a poorly-crystalline UiO-66 was also successful, and consistent with literature, only very broad peaks are present within the materials diffraction pattern (**Figure D2**).¹⁴⁷ Meanwhile, the diffraction pattern of defective UiO-66 appears to contain sharp peaks (**Figure D3**).

As seen in **Figure D4**, increasing quantities of amine functionalised linker reduces material crystallinity. In fact, a complete substitution of BDC linker for the amine functionalised variant results in a poorly crystalline material with only very broad diffraction features. The introduction of nitro groups within the framework of UiO-66 also reduces crystallinity (**Figure D4**). However, the extent of this reduced crystallinity

appears mostly independent to the quantity of nitro-functionalised linker introduced into the framework.

The crystallinity of UiO-66 appears to be unaffected by the introduction of varying amounts of isophthalic acid, sulfobenzoic acids, and naphthalene functionalised linker (**Figure D5, D6, and D7**). Although it is worth noting that a large additional peak is present within the XRD patterns of materials that contain 10 % and 30 % isophthalic acid (**Figure D5**). This additional Bragg peak appears at around 17° and is presumably caused by residual linker within the materials framework. The diffraction patterns produced by MSBDC containing Nano materials appear broadened but clearly resemble the inherent structure of UiO-66 (**Figure D8**). Similarly, diffraction patterns indicate the successful synthesis of (50)MSBDC-UiO-66 and (50/50)MSBDC/Naphtha-UiO-66 (**Figure D9 and D10**). The introduction of hydroxyl groups within the framework of UiO-66 did not appear to impact crystallinity. Meanwhile, the introduction of carboxylic acid groups resulted in a more amorphous material (**Figure D11**). For the UiO-67 materials considered in this study, the addition of sulfobenzoic acid appears to introduce some asymmetry in the low angle diffraction peaks, but overall crystallinity is maintained and compares well with the simulated pattern (**Figure D12**).²⁵⁶

The successful incorporation of functionalised linkers was confirmed by FTIR analysis. The incorporation of sulfonic acid groups in materials containing MSBDC linker was confirmed by new bands at 620 cm^{-1} , 1078 cm^{-1} , 1180 cm^{-1} , and 1223 cm^{-1} (**Figure D16**). These new signals correlate to the bending and stretching vibrations of the S=O and S-O bonds within the functionalized linker.^{248,249,257} Specifically, peaks at 1180 cm^{-1} and 1223 cm^{-1} correspond to S=O bond vibrations. Meanwhile, peaks at 1078 cm^{-1} and 620 cm^{-1} correspond to S-O bond vibrations. It is worth noting that additional peaks also appear in some MSBDC containing materials. For instance, the FTIR spectrum of (50/50)MSBDC/Naphtha-UiO-66 contains additional peaks at 1463 cm^{-1} , 1368 cm^{-1} , and 790 cm^{-1} .

New bands at 1530 cm^{-1} and 1346 cm^{-1} confirmed the successful incorporation of nitro groups within UiO-66. These new bands correlate respectively to the asymmetric and symmetric stretching of (NO) modes within the material (**Figure D13**).^{258,259} The presence of amine groups in (100)NH₂-UiO-66 was confirmed by the appearance of

new bands at 3457 cm^{-1} and $\sim 3376\text{ cm}^{-1}$ (**Figure D14 and D14a**). Here new bands correlate to the asymmetric and symmetric stretching of N-H nodes.^{259–263} The appearance of these bands, as well as the distinctive yellow colour of the material, was less prominent - and potentially absent - in materials containing less than 100 % amine functionalized linker.

The introduction of isophthalic acid (IPA) results in a prominent peak at 1659 cm^{-1} (**Figure D17**). It is worth noting that numerous other distinctive bands also appeared following the introduction of IPA. Specifically, these bands appear at 1092 cm^{-1} , 2452 cm^{-1} , 2771 cm^{-1} , and 2970 cm^{-1} . Meanwhile, literature reports the appearance of a broad band at around $1750\text{-}1700\text{ cm}^{-1}$ following the introduction of this functional linker.²⁶⁴

The FTIR spectra of UiO-66 and BTeC-UiO-66 contains a peak at 1710 cm^{-1} (**Figure D18 & D18a**). This peak within the BTeC material is indicative of a free carboxylic acid group on the linkers aromatic ring.^{265,266} Meanwhile, the same peak may suggest that UiO-66 contains some partly uncoordinated or loose linker.

The introduction of a single hydroxyl group on the linkers aromatic ring is reported to generate bands at low wavelengths ($450\text{-}750\text{ cm}^{-1}$), as well as a band at 3300 cm^{-1} and a strong peak at 1240 cm^{-1} .^{267,268} Here we also find that the introduction of hydroxyl groups generates a strong peak at $\sim 1230\text{ cm}^{-1}$ and a band at around 3240 cm^{-1} (**Figure D18**). Furthermore, the introduction of hydroxyl groups was also found to generate strong peaks at 869 cm^{-1} , 1459 cm^{-1} , 2446 cm^{-1} , 2771 cm^{-1} , 2928 cm^{-1} , and 2968 cm^{-1} . It is worth noting that similar peaks were also found in the IPA functionalized materials. Perhaps these additional peaks indicated the presence of trapped residual solvent or linker in the materials.

The introduction of 3-sulfobenzoic acid and 4-sulfobenzoic acid into the framework of UiO-66 generated a band at 1035 cm^{-1} (**Figure D15**). Furthermore, a small band appears at 615 cm^{-1} in the IR spectra of materials containing 3-sulfobenzoic acid. Meanwhile, the introduction of 4-sulfobenzoic acid produces additional bands at 1011 cm^{-1} and 1118 cm^{-1} . Presumably these bands can be attributed to the presence of sulfobenzoic acid within the framework of UiO-66. The presence of a band at 1035 cm^{-1} , as well as bands at 615 cm^{-1} and 692 cm^{-1} , are also present in sulfobenzoic acid functionalized UiO-67 materials (**Figure D19**). Furthermore, UiO-67 materials containing 3-

sulfobenzoic acid also appear to generate a band at around 756 cm^{-1} .

Nitrogen absorption analysis was used to assess the implications of linker functionality on material surface area. The BET surface areas of UiO-66 and defective UiO-66 are comparable ($737\text{ m}^2\cdot\text{g}^{-1}$ and $722\text{ m}^2\cdot\text{g}^{-1}$, respectively). Increasing amounts of MSBDC, IPA, and naphthalene-functionalized linker within the structure of UiO-66 was found to generally reduce surface area. This may be a result of functional groups or residual solvent blocking the materials' pore network. As expected, the BET surface area of Nano-UiO-66 was found to be significantly larger than that of UiO-66 ($1099\text{ m}^2\cdot\text{g}^{-1}$). However, the introduction of MSBDC linker within Nano materials reduced BET surface area and micropore volume whilst increasing mesopore volume. This reduction in micropore volume may indicate that functional groups are blocking the materials pore network. The introduction of sulfobenzoic acid within materials generally increased surface areas and micropore volumes in comparison to UiO-66.

The introduction of BTeC, hydroxyl, nitro, and amine functionalized linker within UiO-66 significantly reduced BET surface area. Indeed, these low surface areas are unexpected and are inconsistent with literature.^{258–261,263,266,269,270} The low surface areas reported here indicate that residual linker or solvent may be trapped within the materials. The surface area of UiO-67 was measured as $439\text{ m}^2\cdot\text{g}^{-1}$; significantly lower than that found in literature.²⁵⁰ Again, this may suggest that the material contains residual linker or solvent. The introduction of sulfobenzoic acid within UiO-67 generally increased surface area and micropore volume.

Table 7.1. BET surface area and pore volume of Zr MOFs. (*degassed at 190°C)

Entry	Catalyst	BET Surface Area (m ² .g ⁻¹)	Micropore Volume (cm ³ .g ⁻¹)	Mesopore Volume (cm ³ .g ⁻¹)
1	UiO-66	737	0.26	0.04
2	(10)MSBDC-UiO-66	1061	0.33	0.11
3	(20)MSBDC-UiO-66	823	0.22	0.29
4	(50)MSBDC-UiO-66	461.1	0.09	0.28
5	Defective UiO-66	722	0.25	0.09
6	Nano UiO-66	1099	0.33	0.21
7	Poorly Crystalline Nano	463	0.09	0.16
8	Ultra-Nano UiO-66	907	0.22	0.53
9	(20)MSBDC-UiO-66 Nano	687	0.15	0.34
10	(50)MSBDC-UiO-66 Nano	632	0.13	0.31
11	(20)3-sulfoben-UiO-66	723	0.22	0.03
12	(40)3-sulfoben-UiO-66	958	0.31	0.05
13	(20)4-sulfoben-UiO-66	1011	0.31	0.04
14	(40)4-sulfoben-UiO-66	1147	0.37	0.04
15	(20)NO ₂ -UIO-66*	159	0.05	0.02
16	(50)NO ₂ -UIO-66*	85	0.03	0.01
17	(100)NO ₂ -UIO-66*	61	0.02	0.01
18	(20)NH ₂ -UIO-66	598	0.22	0.02
19	(50)NH ₂ -UIO-66	451	0.16	0.01
20	(100)NH ₂ -UIO-66	2	0.01	N/A
21	(10)IPA-UiO-66	762	0.25	0.02
22	(20)IPA-UiO-66	707	N/A	N/A
23	(30)IPA-UiO-66	723	0.25	0.02
24	(40)IPA-UiO-66	689	0.23	0.03
25	(20)Naphtha-UiO-66	983	0.37	N/A
26	(50)Naphtha-UiO-66	827	0.30	0.01
27	(100)Naphtha-UiO-66	530	0.19	0.02

28	(50/50)MSBDC/Naphth a-UiO-66	465	0.09	0.17
29	BTeC-UiO-66	7	0.00	0.00
30	Hydroxy-UiO-66	256	0.08	0.04
31	UiO-67	440	0.09	0.01
32	(20)3-sulfoben-UiO-67 (1eq)	471	0.1	0.01
33	(20)3-sulfoben-UiO-67 (2eq)	478	0.13	0.01
34	(40)3-sulfoben-UiO-67 (1eq)	469	0.10	0.01
35	(40)3-sulfoben-UiO-67 (2eq)	426	0.11	0.01

The sulfur content of relevant materials was quantified via inductively coupled plasma (ICP) analysis. The results of this quantitative analysis are shown in **Table 7.2**. In order to give a more meaningful representation of these results, S quantities were calculated in terms of molecular concentration and normalized with respect to Zr. As seen in **Entries 1-5**, MSBDC was successfully introduced into the framework of UiO-66 and Nano UiO-66. For instance, ICP analysis shows that (50)MSBDC-UiO-66 contains a sulfur content of 0.53 (M.Conc). This indicates that 53 % of the materials organic linker content is MSBDC, which is close to the target amount. Similar results were obtained for each of the MSBDC containing materials with the exception of (50/50)MSBDC/Naphtha-UiO-66. Here the materials S content is lower than expected (only 38 %). This suggests that the naphthalene functionalised linker is more readily introduced into the framework of UiO-66 than MSBDC. Interesting, the sulfobenzoic acid functionalized UiO-66 materials contain significantly less S than expected. For instance, (20)3-sulfoben-UiO-66 only contains 15 % functionalised linker whilst (40)3-sulfoben-UiO-66 only contains 11 % functionalised linker. This suggests that sulfobenzoic acid is not easily introduced into the framework of UiO-66. Perhaps only a limited amount of sulfobenzoic acid can be successfully introduced into the material. Indeed, a similar trend is observed within the sulfobenzoic acid functionalised UiO-67 materials, with each material containing significantly less functionalised linker than expected.

Table 7.2. ICP analysis of S containing UiO-66 and UiO-67 materials normalised with respect to Zr.

Entry	Catalyst	Sulfur (wt. %)	Zirconium (wt. %)	Sulfur (M. Conc.)	Zirconium (M. Conc.)
1	(10)MSBDC-UiO-66	1.13	23.59	0.14	1.00
2	(20)MSBDC-UiO-66	1.7	22.01	0.22	1.00
3	(50)MSBDC-UiO-66	4.05	21.6	0.53	1.00
4	(20)MSBDC-Nano- UiO-66	1.96	23.76	0.23	1.00
5	(50)MSBDC-Nano- UiO-66	3.49	23.48	0.42	1.00
6	(50/50)MSBDC/Naphth a-UiO-66	2.79	20.98	0.38	1.00
7	(20)3-sulfoben-UiO-66	1.64	31.79	0.15	1.00
8	(40)3-sulfoben-UiO-66	1.13	29.89	0.11	1.00
9	(20)4-sulfoben-UiO-66	1.38	29.8	0.13	1.00
10	(40)4-sulfbenz-UiO-66	1	29.72	0.10	1.00
11	(20)3-sulfoben-UiO-67 (1eq)	0.99	27.4	0.10	1.00
12	(20)3-sulfoben-UiO-67 (2eq)	1.1	26.63	0.12	1.00
13	(40)3-sulfoben-UiO-67 (1eq)	1.2	30.07	0.11	1.00
14	(40)3-sulfoben-UiO-67 (2eq)	1.67	29.22	0.16	1.00

Thermogravimetric analysis (TGA) enables the linker and Zr content of materials to be calculated. From this the defectiveness of the material can be determined (**Table D.1**). The ideal chemical formula of UiO-66 is $Zr_6O_4(OH)_4(BDC)_6 \cdot nH_2O$, with 6 linkers per Zr_6 cluster ($n = 6$). For a UiO-66 sample synthesized in this study the amount of BDC linker was calculated as 5.51, thus suggesting that the materials framework contains defective Zr sites. Similar values were found for sulfonic acid (MSBDC), nitro, amine, and naphthalene functionalised UiO-66 materials ($n = 5 - 6$). Interestingly, the introduction of IPA functionalised linker did not significantly increase defectiveness –

in fact the materials were less defective than standard UiO-66. This is somewhat surprising as the introduction of IPA linker should increase material defectiveness whilst also providing free, uncoordinated, -COOH groups. As such, the high coordination numbers of the Zr atoms within the IPA functionalised materials may suggest that the majority of this functionalised linker is bound to the outer surface of UiO-66. Or perhaps the linker has not been successfully introduced in the framework.

As expected, the post synthesis hydrothermal treatment of UiO-66 resulted in a defective material with a lower ligand content of 4.12. The synthesis of nano materials also resulted in the formation of highly defective structures. The linker content of Nano-UiO-66 and nano materials containing 20 % and 50 % MSBDC is calculated as 4.44, 4.08, and 4.87, respectively. In the case of Ultra Nano UiO-66, a linker coordination number of 2.13 was calculated. This is considerably low and may indicate the presence of unreacted Zr nanoparticles within the material, potentially in the form of amorphous zirconium chloride/oxide. Interestingly, the poorly crystalline nano material had a Zr coordination number similar to standard UiO-66. The introduction of sulfobenzoic acid into the framework significantly increased material defectiveness. Here, the introduction of 3-sulfobenzoic acid had a greater impact on material defectiveness than 4-sulfobenzoic acid. Overall, this defectiveness is expected as the introduction of sulfobenzoic acid should lower Zr coordination whilst also providing sulfonic acid functionality. The defectiveness of UiO-67 was calculated as 5.21 and the introduction of sulfobenzoic acid within this framework appeared to increase material defectiveness.

Glucose dehydration to HMF: UiO-66 Catalysts

The isomerisation of glucose to fructose can be catalysed by the presence of Lewis acid sites.^{10,18} In the case of UiO-66, defects at the Zr₆ clusters provide this.^{244,271,272} UiO-66 was found to generate a glucose conversion of 16.3 % and a total product yield (fructose, mannose, HMF) of 5.6 % when reactions were conducted in water (**Table 7.3, Entry 2**). Increasing the number of available defective Zr sites is expected to increase the catalytic activity of UiO-66 and result in greater fructose yields. Indeed, defective UiO-66 generated a glucose conversion of 21 % and a desirable product yield of 11 % (**Table 7.3, Entry 3**). Moreover, the defective material more than doubled fructose yields whilst increasing mannose yields by almost seven or eight-fold. This increase in mannose production is both interesting and unexpected. A product of glucose epimerisation or fructose isomerisation, mannose production has also been reported when utilising tin containing beta zeolites (Sn-Beta) as catalysts in the same reaction.^{74,75} The defective material did not significantly increase HMF yields within the reaction. This suggests that increasing the number of defective sites within the catalysts does not generate the Brønsted acidity required to promote fructose dehydration.

To examine the effects of crystal size and morphology on catalytic performance; Nano, Ultra Nano, and Poorly Crystalline Nano UiO-66 materials were considered. The use of Nano and Ultra Nano materials resulted in glucose conversions of 27.5 % and 29.8 % respectively; each considerably higher than that produced by UiO-66 (**Table 7.3, Entries 4 & 5**). This increase in activity can be attributed to the materials' higher number of defective Zr sites and larger surface areas. The catalytic activity of Poorly Crystalline Nano UiO-66 was only marginally lower than the other Nano materials considered despite its less crystalline nature. This may indicate that glucose does not enter the pores of UiO-66 and instead reactions are limited to the outer surface of the material. Indeed, recent work by de Mello and Tsapatsis suggests that glucose is able to enter the framework of modulated UiO-66, but is unable to enter the structure of unmodulated UiO-66 (i.e. UiO-66 that does not have missing Zr clusters).⁶³ With regards to product yields and distribution, the Nano and Ultra Nano materials generated higher quantities of fructose, mannose and HMF than UiO-66. Within these product distributions, similar quantities of mannose were produced. Given the defectiveness of

Nano materials, this provides further evidence that increasing the number of defective Zr sites within UiO-66 effectively promotes mannose production.

In our previous study we explored the use of sulfonic acid functionalised UiO-66 as an isomerisation catalyst in water.²⁵⁵ Consistent with literature, the introduction of electron withdrawing sulfonic acid groups was found to increase the Lewis acidity of UiO-66; ultimately resulting in greater glucose conversions and higher fructose/mannose yields.^{246,255} The addition of Brønsted acid sites may also facilitate the dehydration of fructose to 5-HMF. In this study, we continue to explore the effects of sulfonic acid groups on catalytic performance. As shown in **Table 7.3**, increasing the quantity of MSBDC linker within UiO-66 improves catalytic activity. The highest glucose conversion and product yield generated in this instance was produced by the material containing 50 % MSBDC. Specifically, (50)MSBDC-UiO-66 was found to generate a glucose conversion of 37.3 % and a desirable product yield of 22 %; making it the most selective material observed this study (**Entry 9**). Comparing the product distributions of MSBDC containing materials (**Entries 7-9**) to standard UiO-66 (**Entry 2**) reveals that the greatest increase in yield is seen across Lewis acid catalysed products, fructose and mannose, rather than Brønsted acid catalysed products (i.e. HMF). Again, this suggests that the presence of sulfonic acid groups primarily increases Lewis acidity, rather than promoting HMF production

Having examined the singular effects of surface area and sulfonic acid groups, the combined effects of such alternations were explored. As seen in **Table 7.3**, (20)MSBDC-Nano-UiO-66 (**Entry 10**) generated a higher glucose conversion and total product yield than (20)MSBDC-UiO-66 (**Entry 8**), plus a significantly higher conversion and yield than UiO-66 (**Entry 2**). Again the higher activity of the Nano material may be attributed its higher number of defective Zr sites and greater surface area. However, the effect of a smaller crystal size was less dramatic when considering materials containing 50 % MSBDC linker (**Entries 9, 11**). Here, although the Nano material generated a slightly higher glucose conversion (**Entry 11**), (50)MSBDC-UiO-66 generated a greater total product yield (**Entry 9**).

The introduction of sulfobenzoic acid linker within UiO-66 has a dual effect of increasing the number of defective Zr sites within the materials framework whilst also providing sulfonic acid functional groups. Therefore, the introduction of such linker

enables the combined effect of sulfonic acid groups and increased material defectiveness to be studied. Here we consider both 3-sulfobenzoic acid and 4-sulfobenzoic acid linkers to this end. As seen in **Table 7.3**, the introduction of sulfobenzoic acid increased both glucose conversion and product yields when compared to UiO-66. However, increasing the quantity of sulfobenzoic acid linker within the framework of UiO-66 from 20% to 40% resulted in a slight decline in catalytic activity. This is expected, as ICP analysis revealed that the 20 % containing material actually contains more sulfobenzoic acid than the 40 % material. This is unexpected and so far unexplained. However, we may infer that sulfobenzoic acid is not easily introduced into the framework, and perhaps a higher quantity of this linker in the synthesis mixture actually impairs its successful introduction into the UiO-66 structure.

Table 7.3. Reactions at 140 °C for 3 h. Glucose stock solution, 10 wt. %. Glucose to catalyst ratio was 30:1 by weight.

Entry	Catalyst	Conversion	Yield			Total	Desirable Product Selectivity (Fructose, Mannose and HMF)
			Fructose	Mannose	HMF		
1	None	5.6	0.8	0.0	2.1	2.9	51.8
2	UiO-66	16.3	1.6	0.5	3.5	5.6	34.3
3	Defective UiO-66	21.0	3.8	3.9	3.3	11.0	52.3
4	Nano UiO-66	27.5	4.2	5.3	4.0	13.5	48.9
5	Ultra Nano UiO-66	29.8	5.0	6.1	4.4	15.5	52.0
6	Poorly Crystalline Nano UiO-66	26.3	4.6	3.8	4.8	13.1	50.1
7	(10)MSBDC-UiO-66	25.5	4.6	3.9	4.0	12.6	49.2
8	(20)MSBDC-UiO-66	30.7	5.7	6.2	5.0	16.9	55.2
9	(50)MSBDC-UiO-66	37.3	8.1	7.3	6.5	22.0	58.9
10	(20)MSBDC-Nano-UiO-66	37.8	6.3	6.8	6.9	20.0	53.0
11	(50)MSBDC-Nano-UiO-66	39.1	6.4	6.8	7.7	20.9	53.4
12	(20)3-sulfoben-UiO-66	27.0	4.3	4.2	4.3	12.8	47.4
13	(40)3-sulfoben-UiO-66	24.5	4.0	3.7	3.6	11.3	46.2
14	(20)4-sulfoben-UiO-66	28.0	5.0	4.2	4.1	13.3	47.4
15	(40)4-sulofben-UiO-66	27.2	4.8	3.5	4.1	12.3	45.3

To further examine the tunability of UiO-66 catalysts towards the isomerisation and dehydration of sugars, we now consider the effects of functional groups other than sulfonic acid. Linkers containing strongly electron-withdrawing nitro groups were introduced into the UiO-66 framework at various ratios. Moderate electron-withdrawing groups in the form of carboxylic acid (BTeC) were also introduced into the UiO-66 framework and the use of isophalic acid (IPA) linker was examined. Furthermore, the effect of an electron-donating amine group was studied as well as the effects of a hydrophobic naphthalene group. The reaction results obtain from the use of nitro, BTeC, IPA, amine, and naphthalene functionalised UiO-66 are summarised in **Table 7.4**.

As shown in **Entries 1-3**, the introduction of nitro functionalised linker into the framework of UiO-66 did not appear to significantly improve glucose conversion. This is interesting as nitro groups are more electron-withdrawing than sulfonic acid groups; and should therefore impart a greater Lewis acidity on catalytically active Zr sites. As such, the lower activity of the nitro functionalised materials - in comparison to MSBDC materials - may suggest that strongly Lewis acidic Zr sites are unfavourable for glucose isomerisation.

To examine the effects of weaker electron-withdrawing groups on catalytic performance, a carboxylic acid functionalised UiO-66 material was considered. Here, all of the materials organic linker was functionalised by additional carboxylic acid groups that remain uncoordinated (BTeC-UiO-66). As seen in **Entry 4**, the presence of free carboxylic acid groups within the material generated a HMF yield of 7.3 %. This HMF yield suggests that free carboxylic acid groups within BTeC-UiO-66 are providing sufficient Brønsted acidity to catalyse HMF production. However, as with the nitro functionalised materials, the incorporation of carboxylic acid groups did not increase glucose conversion as dramatically as materials containing comparatively smaller quantities of sulfonic acid (MSBDC). In conclusion, the addition of functional groups that are both more and less electron-withdrawing than sulfonic acid, were less effective in generating higher glucose conversions and overall product yields through increased Lewis acidity. Indeed, the addition of BTeC linker appeared to mostly increase the Brønsted acidity of UiO-66.

In an attempt to combine the catalytic activity of highly defective materials with the Brønsted acidity (and hence dehydration capability) of free carboxylic acid groups, the use of an isophthalic acid (IPA) linker was considered. Due to the structure of IPA, its incorporation within UiO-66 should ensure the presence of free carboxylic acid groups and defective Zr sites. However, as seen in the TGA results, the introduction of IPA into the framework of UiO-66 did not significantly increase the number of defective sites. This may suggest that the majority of IPA linker is bound to the outer surface of these functionalised materials. As seen in **Entry 8**, replacing 10 % of framework BDC with IPA generates a glucose conversion of ~ 24 % and a total desirable product yield of ~ 11 %. However, the effect of the IPA linker on catalytic performance appears to be maximised at this lower level of incorporation. As seen in **Entries 9-11**, increasing the IPA content of UiO-66 from 10 % to 40 % did not significantly improve catalytic performance.

The effect of electron donating groups was observed through the introduction of amine functionalised linkers within the framework of UiO-66. As seen in **Entry 5**, the introduction of 20 % amine functionalised linker did not significantly improve glucose conversion when compared to standard UiO-66. Increasing the quantity of amine functionalised linker to 50 % did increase glucose conversion to ~19% (**Entry 5**), however increasing the amine content of the material further was found to reduce catalytic activity (**Entry 6**). This decline in activity may result from the electron-donating amine groups reducing the Lewis acidity of local Zr active sites within the material.

In current literature, tin containing beta zeolite (Sn-Beta) is widely considered as a benchmark catalyst for glucose isomerisation. The effectiveness of this zeolite, is in part, a result of the hydrophobic nature of the materials highly siliceous beta framework.^{17,72} Being hydrophobic by nature reduces competition between glucose and water molecules at Lewis acidic Sn active sites. Moreover, the materials hydrophobic nature prevents inhibition of Sn active sites by bulk water.^{17,72} To replicate this effect within the Zr MOFs considered here, a naphthalene functionalised variant was considered. A naphthalene functionalised linker was introduced into the framework of UiO-66 at a ratio of 20 %, 50 %, or 100 %, relative to BDC. The resulting catalytic performances of these materials are shown in **Entries 12 – 14**. As seen, the conversion of glucose by (20)Naphtha-UiO-66 is

comparable to that produced by UiO-66. However, the selectivity of the reaction towards fructose is improved, thus highlighting the benefits of hydrophobicity within the catalyst. More interesting than this, whilst fructose yields are improved by the presence of naphthalene, mannose yields remain comparable to that of the standard material. This suggests that the proximity of water to Zr active sites has a prominent impact on reaction selectivity, with the absence of water suppressing the reaction pathway towards mannose whilst promoting that towards fructose. Indeed, reaction yields resulting from increasing quantities of naphthalene functionalised linker follows this trend. To improve yields further, a combination of naphthalene and sulfonic acid functionalised linker was considered. The resulting activity of the dual functionalised material is shown in **Table 7.4, Entry 15**. Overall, the bi-functional material effectively doubled the glucose conversion produced by UiO-66. However, this glucose conversion was lower than that produced by (50)MSBDC-UiO-66. Furthermore, the presence of sulfonic acid groups within the material and its more defective structure meant that the reaction pathway towards mannose was no longer suppressed to the same extent. Overall, the total product yield (fructose, mannose and HMF) generated by the bi-functional material was less than that produced by (50)MSBDC-UiO-66, but more than that produced by any of the mono-functionalised naphthalene materials.

The introduction of hydroxyl groups was also considered. As seen in **Table 7.4 Entry 16**, the introduction of free hydroxyl groups within UiO-66 increased glucose conversions and product yields. Indeed, Hydrox-UiO-66 generated a glucose conversion of 23.80 % along with a 51.6 % selectivity towards desirable products. This activity and selectivity clearly highlights the benefits of having free –OH groups within the material.

Table 7.4. Reactions at 140 °C for 3 h. Glucose stock solution, 10 wt. %. Glucose to catalyst ratio was 30:1 by weight.

Entry	Catalyst	Conversion	Yield			Desirable Product Selectivity	
			Fructose	Mannose	HMF	Total	
1	(20)NO ₂ -UiO-66	16.8	1.6	0.3	4.7	6.6	39.3
2	(50)NO ₂ -UiO-66	19.9	2.1	0.6	5.6	8.3	41.7
3	(100)NO ₂ -UiO-66	21.9	3	1.2	5.5	9.7	44.3
4	BTeC-UiO-66	20.9	2.01	0.31	7.34	9.7	46.2
5	(20)NH ₂ -UiO-66	16.7	2.2	1.4	3.9	7.5	44.9
6	(50)NH ₂ -UiO-66	19	1.9	1.2	5.2	8.3	43.7
7	(100)NH ₂ -UiO-66	15.9	0.9	0.2	5.5	6.6	41.5
8	(10)IPA-UiO-66	23.6	2.8	3.7	4.7	11.2	47.5
9	(20)IPA-UiO-66	23.6	2.7	3.6	4.5	10.8	45.8
10	(30)IPA-UiO-66	23.1	2.7	3.8	4.6	11.1	48.1
11	(40)IPA-UiO-66	24.4	3.1	4.1	4.9	12.1	49.6
12	(20)Naphtha-Uio-66	17.95	4.67	0.76	3.15	8.6	47.8
13	(50)Naphtha-Uio-66	18.22	5.52	0.88	3.14	9.5	52.4
14	(100)Naphtha- UiO-66	21.16	6.61	1.22	3.73	11.6	54.6
15	(50/50)MSBDC/Naphtha-UiO-66	32.71	7.14	5.35	5.41	17.9	54.7
16	Hydrox-UiO-66	23.80	5.24	2.17	4.88	12.29	51.6

Glucose dehydration to HMF: UiO-67 Catalysts

UiO-67 contains of the same Zr_6 brickwork as UiO-66 and may be functionalised through linker substitution in the same way. As such, the catalytic activity of several sulfobenzoic acid containing UiO-67 materials were explored in the aqueous isomerisation of glucose and production of HMF.

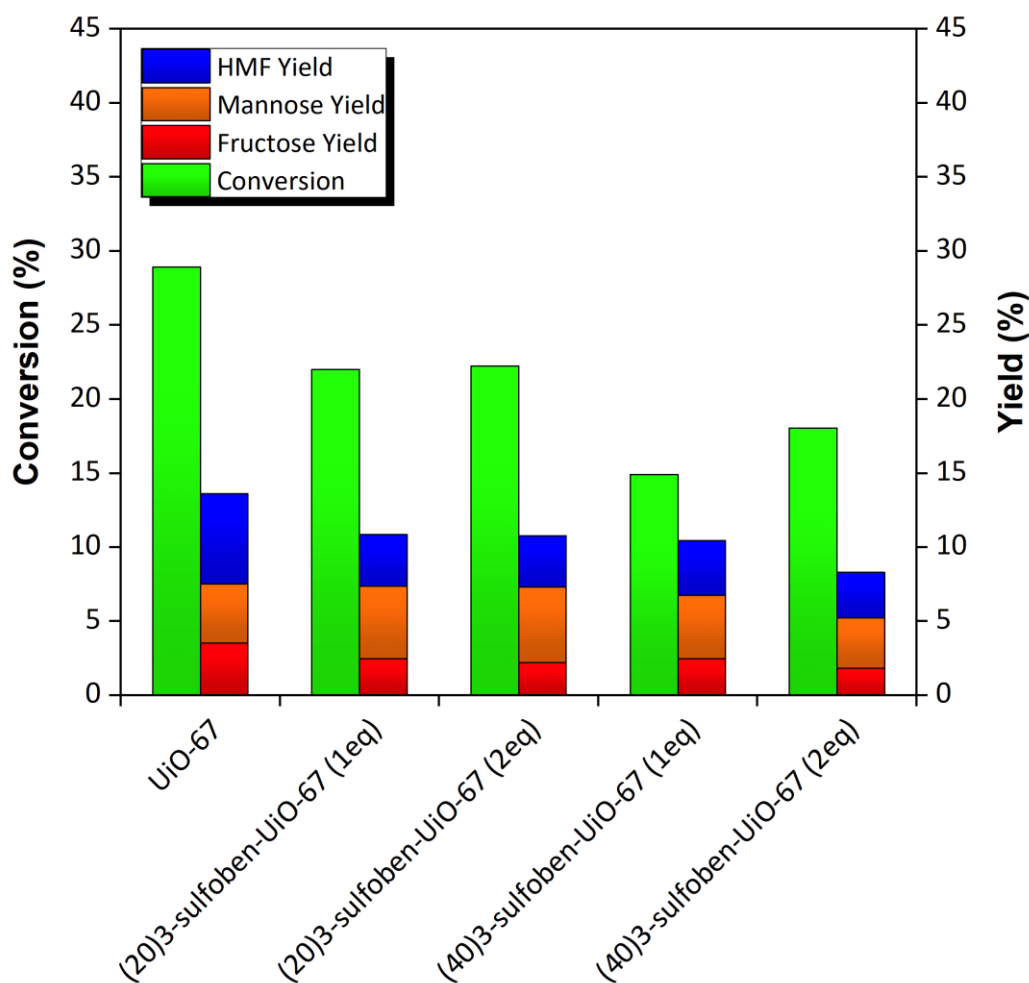


Figure 7.1. Catalytic performance of UiO-67 type materials. Reactions at 140 °C for 3 h. Glucose stock solution, 10 wt. %. Glucose to catalyst ratio was 30:1 by weight.

As shown in **Figure 7.1**, UiO-67 enables a glucose conversion of around 28 %. This is higher than that produced by UiO-66 under the same reaction conditions. The superior performance of UiO-67 may be due to a difference in pore size, with the larger pore diameter of UiO-67 enabling glucose to enter the material

framework more easily. Within the pore network of UiO-67, the glucose molecule will be exposed to additional defective Zr sites. The introduction of sulfobenzoic acid into the framework of UiO-67 was shown to reduce glucose conversions whilst improving reaction selectivity – particularly towards isomerisation products. Moreover, we can conclude that the introduction of sulfobenzoic acid into the framework of UiO-67 improves reaction selectivity towards Lewis acid products, and in particular, mannose. This may be due to an increased number of defective Zr sites within the functionalised materials, the presence of sulfonic acid groups, or a combination of both factors. On the other hand, HMF yields declined following the addition of sulfobenzoic acid. This may suggest that the sulfonic acid groups of the linker are not providing sufficient Brønsted acidity to catalyse HMF production within the reaction system. Or perhaps, the lower HMF yields are a consequence of the improved reaction selectivity toward mannose rather than fructose.

Stability and Recyclability

To test the stability of the catalysts, materials were recovered post-reaction and analysed via XRD. As seen in **Figure 7.2**, the crystallinity of IPA and sulfobenzoic acid containing UiO-66 is preserved during reaction, as is the crystallinity of Nano UiO-66. The highly functionalised amine material remains poorly crystalline and the nitro material becomes even more poorly crystalline after exposure to the reaction conditions. Both the standard and functionalised UiO-67 materials experience a clear loss in crystallinity under reaction conditions. Furthermore, the diffraction patterns of the recovered UiO-67 materials contain strong, sharp, additional peaks – presumably indicating the removal of linker from the framework of these materials.

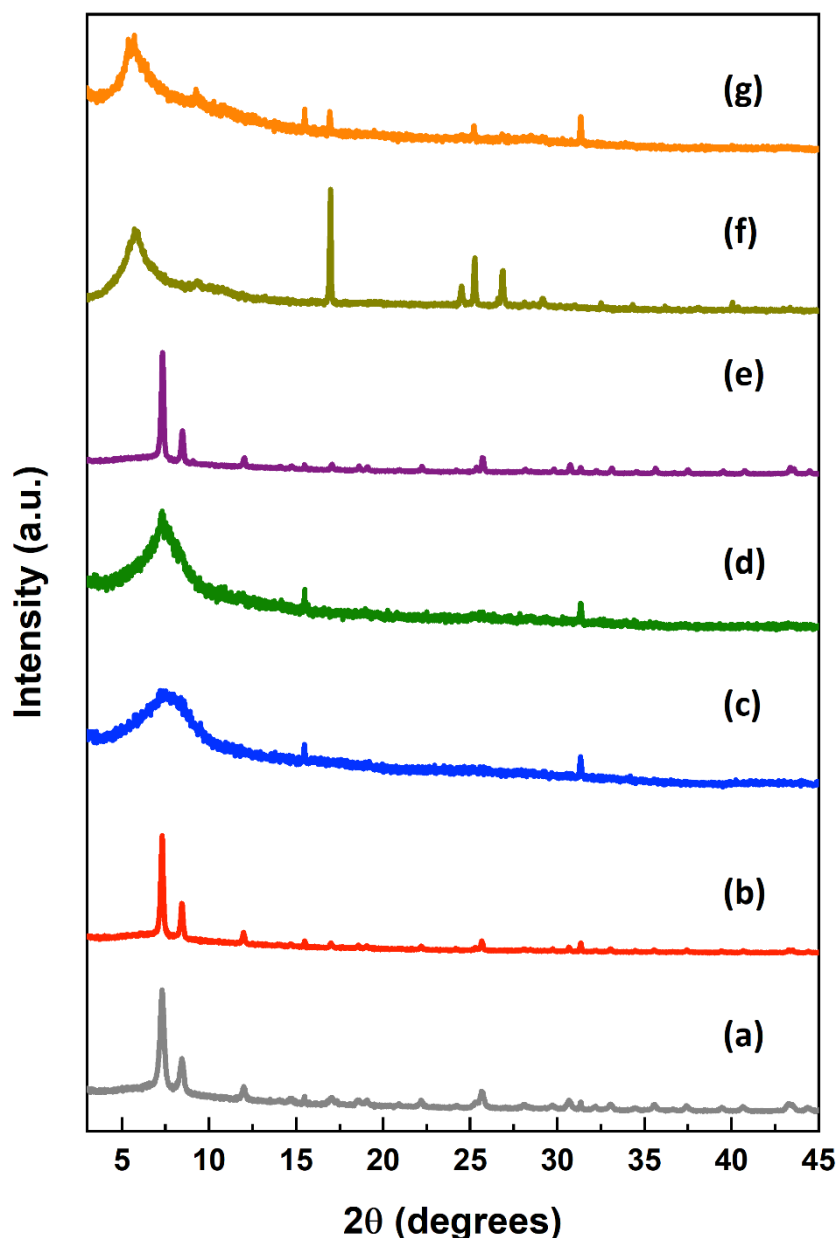


Figure 7.2. XRD powder analysis of catalysts post reaction in water at 140°C for 3 h (a) Nano-UiO-66 (b) (20)IPA-UiO-66 (c) (100)NO₂-UiO-66 (d) (100)NH₂-UiO-66 (e) (40)4-sulfbenz-UiO-66 (f) UiO-67 (g) (40)3-sulfoben-UiO-67(2eq).

Five different catalysts were selected for study in a series of recycle reactions. The materials were selected based on hydrothermal stability and catalytic performance. The reactions were conducted in a 25 mL reactor pressurized with an inert gas (helium). The reactant to catalyst ratio in each initial reaction was 30:1. Following recovery by centrifuge, the catalysts were washed and added back to the reactor along with fresh stock solution. The catalysts considered for recycling are as

follows; BTeC-UiO-66, (50)MSBDC-UiO-66, (50/50)MSBDC/Naphtha-UiO-66, UiO-67 and SO₃H-UiO-67. Each catalyst was cycled through a course of four reactions, after which the catalysts were dried and analysed by XRD to reassess material stability.

As seen in **Figure 7.3**, the activity of each catalyst dropped following the first reaction cycle. This initial decline in activity may be due to several factors. Firstly, smaller (highly active) particles contained within the bulk catalyst are hard to recover and may be lost from the system after the first reaction cycle. Secondly, as shown in our previous work, functional groups such as sulfonic acid may be stripped from the catalyst during reaction. Finally, insoluble carbon by-products, generally referred to as humins, may deposit on catalytically active Zr sites resulting in deactivation. Of the catalysts considered here, the activity of BTeC-UiO-66 appeared most resilient to catalyst recycling. However, the HMF yield generated by the catalyst declined significantly following the first reaction. This suggests that the carboxylic acid functional groups have been inhibited or removed from the material during the first reaction. The activity of (50/50)MSBDC/Naphtha-UiO-66 and (50)MSBDC-UiO-66 appears to stabilise at around 25 % following an initial drop in conversion. In either case, the activity of the MOFs remains higher than that of UiO-66 (**Table 7.3, Entry 2**). As illustrated by the diffraction patterns, the intrinsic framework of the UiO-66 materials remains following the four successive hydrothermal reactions (**Figure D20**).

In comparison to UiO-66, both the standard and functionalised UiO-67 materials also experienced a drop in glucose conversions and product yields over the course of the recycle reactions. Again, this can be attributed to a loss of functional groups, loss of catalyst, or an accumulation of humins. Furthermore, as illustrated in **Figure D20**, the diffraction patterns of the recovered UiO-67 catalysts contain large additional Bragg peaks. This presumably indicates a loss of framework linker during reactions.

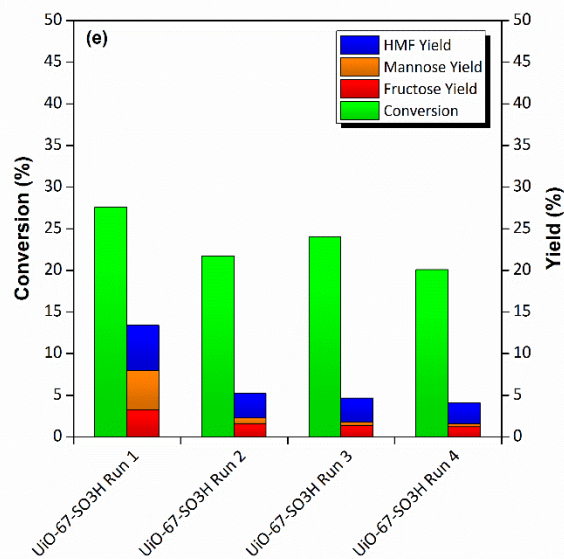
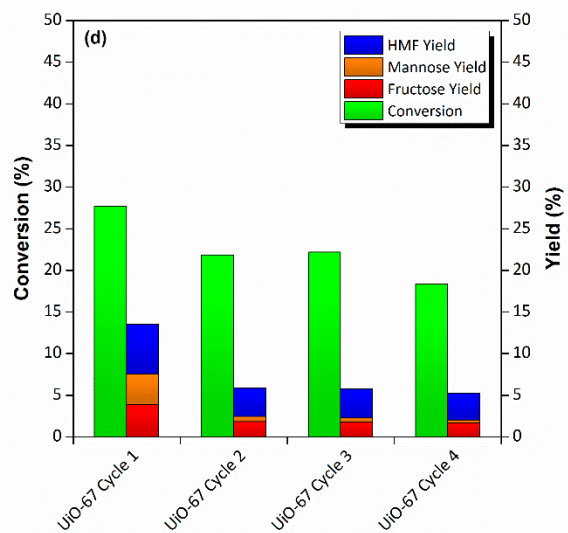
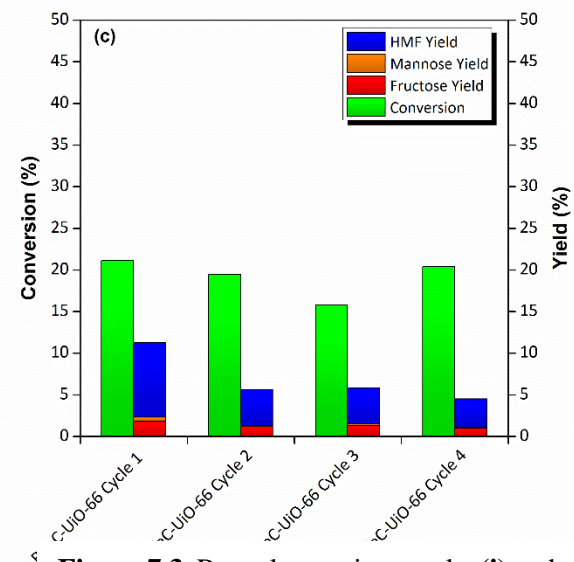
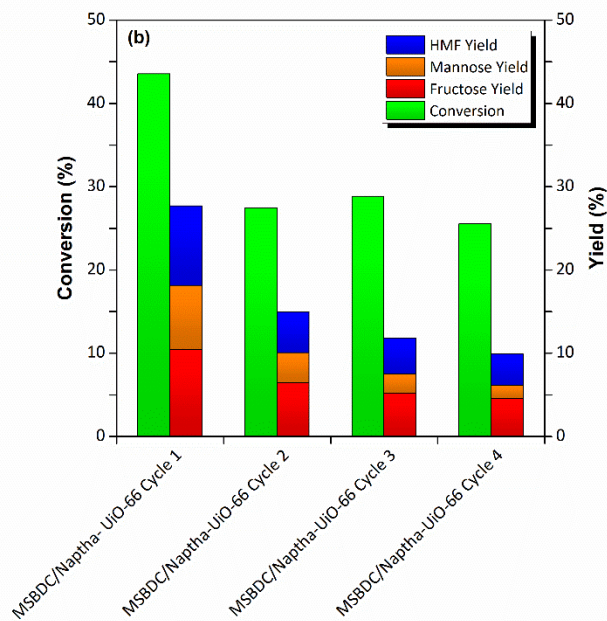
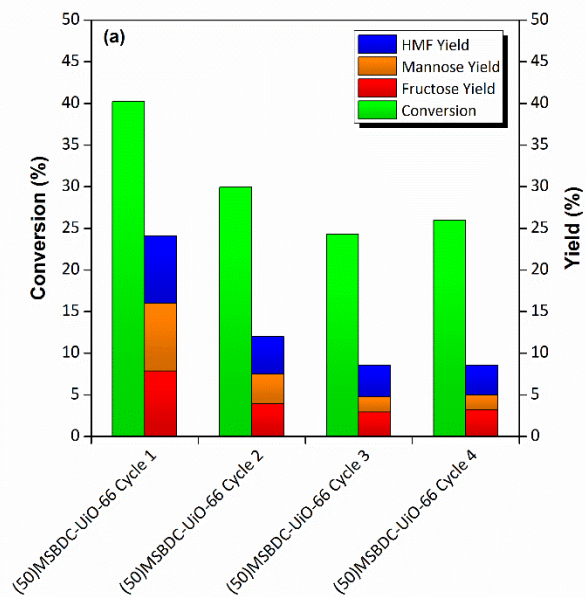


Figure 7.3. Recycle reaction results (i) and XRD analysis of catalyst after 4 reaction cycles (ii) of selected catalysts (a) BTc-UiO-66 (b) (50)MSBDC-UiO-66 (c) (50/50)MSBDC/Naphtha-UiO-66 (d) UiO-67 (e) UiO-67-SO₃H.

Flow Reactor Study

Within batch systems, UiO-66 and UiO-67 type MOFs are highly recyclable glucose isomerisation catalysts. However, for the purpose of process intensification and scale up, the performance of such catalysts must be explored within continuous flow. To this end, the performances of Zr MOFs synthesised in this study were tested in a purpose built flow reactor. For this, 80 mg of catalyst was pelletized and sieved to give a uniform particle size of 250 nm. The catalyst was then mixed with an inert material (silicon carbide) and loaded into the reactor resulting in a bed length of 8 cm. A 10 wt.% glucose solution in water was then pumped through the reactor at a constant flow rate whilst the reactor was heated to 140 °C. The results from this flow reactor study are shown in **Figure 7.4**.

At a low flow rate ($0.14 \text{ mL}\cdot\text{min}^{-1}$), UiO-66 generates an initial glucose conversion of 15 % and a fructose yield of 5 %. This initial conversion and fructose yield then declines slightly with increasing time on stream before finally stabilising. After 240 min on stream, the catalyst is able to generate a conversion of 13.5 % and a fructose yield of 4.5 %. Overall, this conversion and fructose yield is comparable to that seen at the start of the reaction. This suggests that the activity of UiO-66 has not experienced significant deactivation under these reaction conditions. Moreover, this suggests that UiO-66 is a highly promising catalyst for potential scale-up reactions.

At a higher flow rate of $0.28 \text{ mL}\cdot\text{min}^{-1}$, the activity of UiO-66 begins to decline after 150 min on stream. This decline in activity is interesting considering the observed stability of the catalyst at lower flow rates. The deactivation observed here is likely linked to a build up of humins on the surface of the UiO-66 catalyst. As previously discussed, the formation of these carbon by-products is common within glucose isomerisation reactions. Indeed, the deactivation seen in UiO-66, may be similar to that observed in Sn-Beta. This mode of deactivation was studied and modelled by Tsapatsis and co-workers.²⁷³ Here the authors found that their experimental data could be fitted using a number of deactivation models that take into consideration the formation of by-products, amount of catalyst, and the total amount of sugars. Moreover, the deactivation of UiO-66 may be due to changes to the catalyst, such as a loss of Zr active sites, within increasing time on stream. This mode of deactivation is generally referred to as aging and is typically seen in high

temperature gas reactions. However, due to the general fragility of MOFs, it may be possible that changes in the materials structure may occur with increasing time on stream.

The performance of (50)MSBDC-UiO-66 declined significantly at a flow rate of $0.14 \text{ mL}\cdot\text{min}^{-1}$. Specifically, following start-up, the glucose conversion achieved by the catalyst fell from 28.8 % to around 15.7 %. Interestingly however, the quantity of fructose generated in the reaction appears to stabilise at around 5 %. This fructose yield is comparable to that generated by UiO-66 under the same reaction conditions. This indicates that the effect of the electron-withdrawing groups has been nullified and the catalysts is performing like an un-functionalised UiO-66 material. This is plausible as previous work found that sulfonic acid groups may be stripped from MSBDC functionalised materials during reactions (See Chapter 6: UiO-66). As such, the deactivation of (50)MSBDC-UiO-66 observed here may be related to the loss of functional groups from the catalyst – resulting in a catalytic performance similar to UiO-66. Similar reasoning may be used to explain the performance of (50)MSBDC-UiO-66 at a flow rate of $0.28 \text{ mL}\cdot\text{min}^{-1}$.

At a flow rate of $0.14 \text{ mL}\cdot\text{min}^{-1}$, (50/50)MSBDC/Naphtha-UiO-66 generates an initial glucose conversion of around 36 %. This was accompanied by fructose and mannose yields of 9.3 % and 4.5 %, respectively. Following this initial activity, the performance of the catalyst declines before stabilising after 350 min of time on stream. This may suggest that sulfonic acid groups are stripped from the material upon start-up. Once stable, the catalyst is able to generate a glucose conversion of ~22 % and a total product yield of ~10.5 %. This catalytic activity is greater than that observed when using UiO-66 under the same reaction conditions. As such, the activity of the material suggests that although sulfonic acid groups have been removed, the material still contains hydrophobic naphthalene functionalised linker that improve catalytic performance. At a higher flow rate of $0.28 \text{ mL}\cdot\text{min}^{-1}$, the catalytic activity of the material appears extremely stable. This may suggest that sulfonic acid groups are removed from the material quicker when a higher flow rate is applied (i.e. loss of sulfonic acid groups occurs before $T = 30 \text{ min}$).

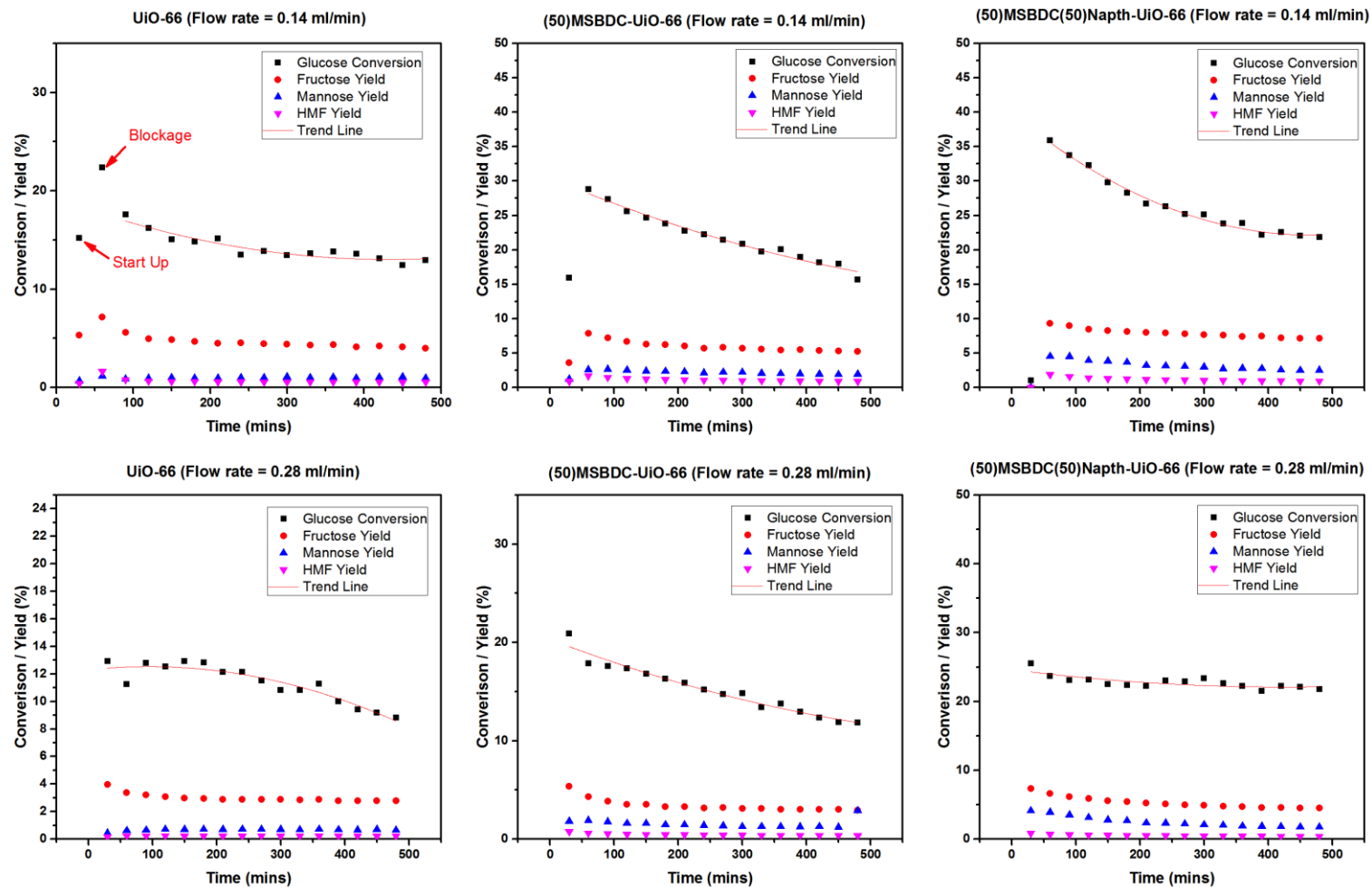


Figure 7.4. UiO-66 catalysts flow reactor results. Reactor temperature was maintained at 140 °C. Feedstock was 10 wt.% glucose in water.

Glucose to Catalyst Ratio

The effect of reactant to catalyst ratio was studied by increasing the amount of catalyst used in the reactions. The quantity of catalyst was increased four and eight fold in relation to the amount of catalyst used until this point in batch reactions. As shown in **Table 7.5**, glucose conversions grew with increasing quantities of catalyst. However, the net effect was detrimental to reaction selectivity. An excess of catalyst appeared to promote reaction pathways towards undesirable side products. Furthermore, the relationship between catalyst weight and activity is not linear - as doubling the amount of catalyst does not double glucose conversions. The accumulation of humins on the catalyst over time may have a more pronounced effect on catalytic activity when increasing the amount of catalyst used in the reaction.

(BLANK SPACE)

Table 7.5. The effects of catalyst : glucose ratio. Reactions at 140 °C for 3 h. Glucose stock solution, 10 wt. %.

Entry	Catalyst	Catalyst amount (mg)	Conversion (%)	Yield (%)			Product Selectivity (%)
				Fructose	Mannose	HMF	
1	BTeC-UiO-66	40	33.1	1.4	0.9	12.6	45.0
2	BTeC-UiO-66	80	40.4	0.7	0.9	12.3	34.4
3	(50)MSBDC-UiO-66	40	56.6	8.6	6.9	11.8	48.1
4	(50)MSBDC-UiO-66	80	61.9	8.1	6.2	12.0	42.4
5	(50/50)MSBDC/Naphtha-UiO-66	40	61.4	11.0	7.2	12.9	50.5
6	(50/50)MSBDC/Naphtha-UiO-66	80	71.3	9.0	5.7	14.4	40.9
7	UiO-67	40	43.4	5.7	5.4	7.0	41.4
8	UiO-67	80	57.4	5.7	4.8	8.9	33.8
9	UiO-67-SO ₃ H	40	42.1	5.1	7.2	6.7	45.2
10	UiO-67-SO ₃ H	80	53.5	5.4	7.4	7.8	38.4

Reactions in DMSO

As previously discussed, the activity of catalysts may be affected by an accumulation of humins. These insoluble carbon by-products may block active sites and cause an overall deactivation of the catalyst. The removal of humins may be achieved through simple calcination processes typically involving a temperature treatment of around $> 500\text{ }^{\circ}\text{C}$. However, when considering MOF catalysts, regeneration through calcination is difficult due to the comparatively low thermal stability of the materials. Therefore, to prevent deactivation via humins in MOF catalysed reactions, reaction selectivity must be tuned to avoid the production of these carbon products in the first instance. This can be achieved not only through catalyst modification but also through solvent selection. For instance, using DMSO as a reaction solvent has been shown to reduce the production of insoluble humins whilst also catalysing the production of HMF.^{186,187}

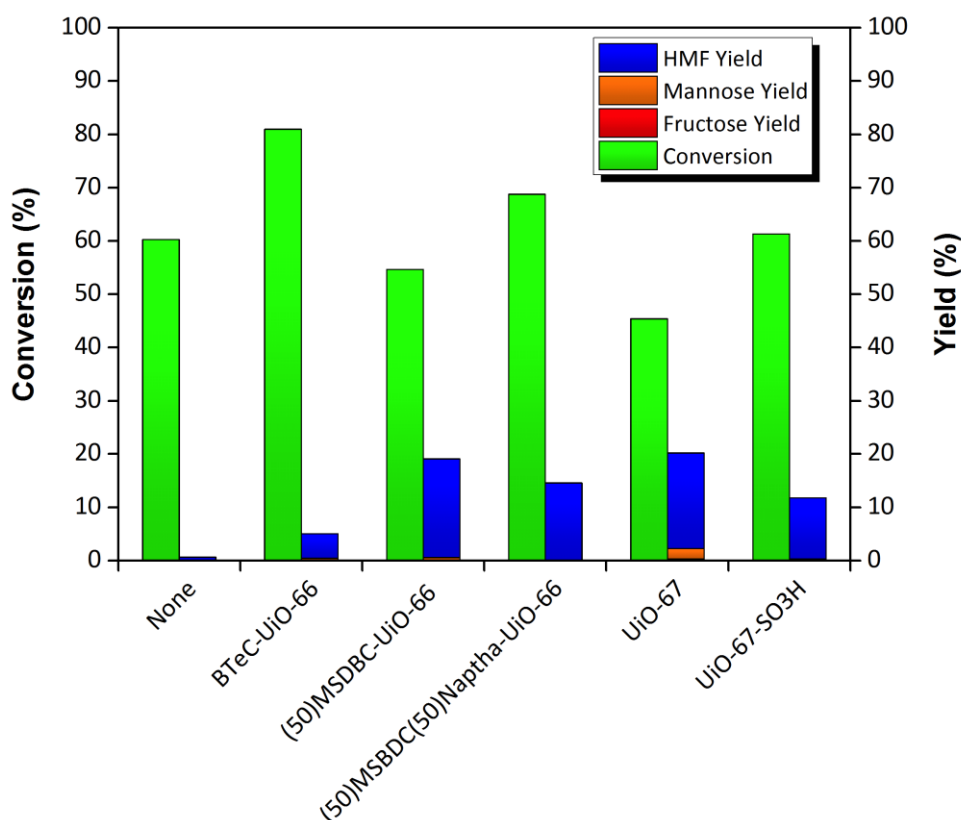


Figure 7.5. Catalytic performance of selected UiO-66 and UiO-67 catalysts in 3 mL of 10wt. % glucose in DMSO. Reactions were conducted for 3 h at $140\text{ }^{\circ}\text{C}$ with 10 mg of catalyst.

As seen in **Figure 7.5**, DMSO is able to generate a glucose conversion of around 60 %. However, as a catalyst DMSO is highly unselective towards desirable products fructose, mannose and HMF. The addition of Zr MOFs within the reaction increases glucose conversions as well as HMF yields. The lack of fructose within the reaction mixture illustrates the quick dehydration of this molecule towards HMF as a result of the combined use of catalyst and solvent. The highest HMF yield was generated by (50)MSBDC-UiO-66. This is unsurprising as (50)MSBDC-UiO-66 generated the highest fructose yield in water mediated reactions when applying the same glucose to catalyst ratio. To access the stability of the catalysts within this aprotic organic solvent, materials were recovered post-reaction, washed, and analysed via XRD. As shown in **Figure 7.6**, the structure of BTeC-UiO-66 sustained significant damage during reactions in DMSO. Meanwhile, the overall structure of other materials considered is persevered, suggesting that these catalysts are stable in DMSO at elevated temperature.

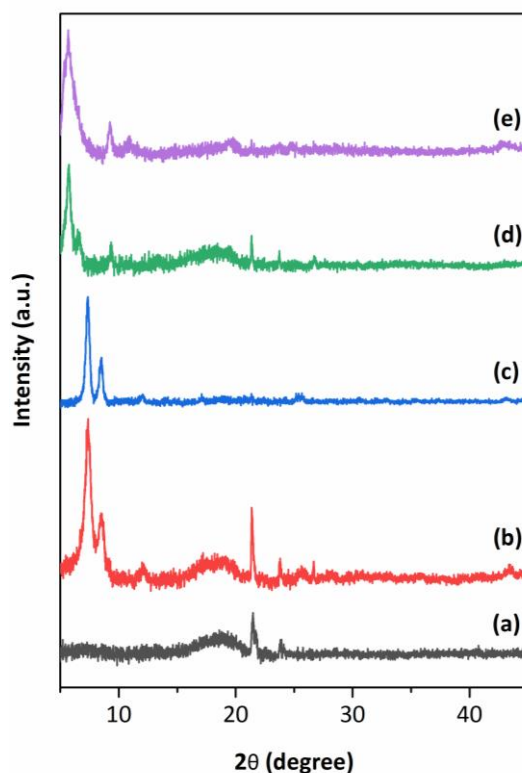


Figure 7.6. Diffraction patterns of catalysts post reaction in DMSO (a) BTeC-UiO-66 (b) (50)MSBDC-UiO-66 (c) (50/50)MSBDC/Naphtha-UiO-66 (d) UiO-67 (e) UiO-67-SO₃H.

Fructose Dehydration Reactions

To further evaluate the dehydration capabilities of the materials considered, and hence their Brønsted acidity, reactions were repeated using a fructose feedstock. The results of these reactions are shown in **Table 7.6**. The blank reaction generated a fructose conversion of 20.74 % and a HMF yield of 18.05 %. The autocatalytic nature of fructose dehydration in water has been previously reported in literature and is thought to be catalysed by the formation of formic acid in the reaction solution.⁹¹ UiO-66 generated a fructose conversion of 44.74 % along with a HMF yield of 33.20 %. This higher HMF yield suggests that UiO-66 is facilitating the dehydration of fructose to HMF. We expect that Brønsted acidity within UiO-66 may result from un-terminated -COOH groups within the material. Similar fructose conversions were also generated by UiO-67 and functionalised variants of both MOFs. In each MOF catalysed reaction, small quantities of glucose were found. Mannose was also generated in trace amount within the majority of MOF catalysed reactions. Meanwhile, fructose and mannose were not formed in the blank reaction. The isomerisation of glucose is a reversible reaction; therefore the small quantities of glucose found here serves to highlight the Lewis acidity of the UiO-66 and UiO-67 catalysts. BTeC-UiO-66 generated a HMF yield of 40.2%. This is the highest HMF yield generated in this series of reactions and suggests that the materials free -COOH groups provide sufficient Brønsted acidity to catalyse the dehydration of fructose to HMF. Interestingly however, the free -COOH groups within IPA functionalised UiO-66 was unable to effectively enhance HMF yields.

Table 7.6. Fructose dehydration by functionalised UiO-66 and UiO-67 catalysts. 140 °C, 3 h, 3 mL 10 wt % stock solution in water.

Entry	Catalyst	Conversion	Yield		
			Glucose	Mannose	HMF
1	None	20.74	0.00	0.00	18.05
2	UiO-66	44.74	0.52	0.23	33.20
3	Defective UiO-66	34.56	0.80	0.43	20.05
4	Nano UiO-66	42.18	0.92	0.45	20.54
5	(10)MSBDC-UiO-66	42.94	1.13	0.69	25.59
6	(20)MSBDC-UiO-66	44.49	1.21	0.62	24.67

7	(50)MSBDC-UiO-66	47.36	1.70	0.00	23.17
8	(20)MSBDC-Nano-UiO-66	46.02	1.39	0.62	22.20
9	(50)MSBDC-Nano-UiO-66	47.52	1.55	0.89	22.51
10	(20)3-Sulfoben-UiO-66	44.84	0.90	0.64	22.33
11	(40)3-Sulfoben-UiO-66	40.10	1.00	0.00	20.78
12	(20)4-Sulfoben-UiO-66	43.01	1.06	0.63	21.42
13	(40)4-Sulfoben-UiO-66	42.16	1.07	0.65	22.01
14	(20)NO ₂ -UiO-66	46.17	0.31	0.17	34.31
15	(50)NO ₂ -UiO-66	47.36	0.53	0.30	32.83
16	(100)NO ₂ -UiO-66	47.69	0.69	0.37	30.69
17	(20)NH ₂ -UiO-66	46.86	0.53	0.25	35.15
18	(50)NH ₂ -UiO-66	51.19	0.35	0.36	36.86
19	(100)NH ₂ -UiO-66	40.02	0.33	0.22	28.77
20	(10)IPA-UiO-66	36.15	0.60	0.27	22.70
21	(20)IPA-UiO-66	37.28	0.59	0.26	22.40
22	(30)IPA-UiO-66	35.80	0.59	0.23	21.10
23	(40)IPA-UiO-66	37.77	0.65	0.29	21.65
24	(50)Naphtha-UiO-66	37.14	1.18	0.56	22.06
25	(100)Naphtha-UiO-66	32.42	1.17	0.73	19.35
26	(50/50)MSBDC/Naphtha-UiO-66	46.47	1.70	0.91	25.13
27	BTeC-UiO-66	59.93	0.52	0.34	40.72
28	Hydrox-UiO-66	32.42	1.00	0.41	20.79
29	UiO-67	43.37	0.90	0.43	19.56
30	(20)3-Sulfoben-UiO-67(1eq)	37.85	0.62	0.20	22.60
31	(20)3-Sulfoben-UiO-67(2eq)	36.33	0.50	0.25	21.82
32	(40)3-Sulfoben-UiO-67(1eq)	37.28	0.60	0.23	22.63
33	(40)3-Sulfoben-UiO-67(2eq)	35.69	0.44	0.24	21.59

7.3 Conclusion

UiO-66 and UiO-67 MOFs can catalyse the isomerisation of glucose and production of HMF. Furthermore, the catalytic ability of these MOFs may be 'tuned' through the introduction of structural defects, size modulation, and the incorporation of functional groups. With regards to UiO-66, catalytic performance can be improved by increasing the number of defective Zr sites within the framework. These defective Zr sites are responsible for facilitating Lewis acid catalysed glucose isomerisation. Interestingly, increasing the number of defective sites within the framework of UiO-66 increases mannose as well as fructose production. The performance of UiO-66 can also be increased through size modulation. Specifically, nano UiO-66 materials are able to generate higher glucose conversions and desirable product yields than standard UiO-66. This improved catalytic performance can be attributed to the smaller size of the nano materials and their increased defectiveness. Catalytic performance could also be improved through the introduction of functional groups within the frameworks. Specifically, electron-withdrawing and donating groups were added to the UiO-66 framework. Of these, the introduction of sulfonic acid containing MSBDC had the greatest impact on catalytic activity. Here, the electron-withdrawing sulfonic acid groups are thought to enhance the Lewis acidity of nearby defective Zr sites responsible for catalytic activity. Furthermore, the introduction of $-COOH$ and naphthalene groups were also found to have a profound effect on catalytic performance. Naphthalene groups were found to enhance reaction selectivity towards fructose by enhancing the hydrophobicity of the UiO-66 framework. Meanwhile, the introduction of free $-COOH$ groups, through the incorporation of a BTeC linker, was found to enhance HMF yields – particularly when considering a fructose feedstock. With regards to UiO-67, the simultaneous introduction of defective sites and sulfonic acid groups within the structure of the material (through the incorporation of sulfobenzoic acid linker), enhanced reaction selectivity towards desirable products (fructose, mannose, HMF).

A number of UiO-66 and UiO-67 materials were tested in a series of recycle reactions. Each of these materials proved to be highly recyclable and stable within batch reactors. As such, the performances of some UiO-66 catalyst were further studied within a purpose built continuous flow reactor. Within this system the

performance of UiO-66, and a naphthalene/MSBDC functionalised material, proved to be highly stable with increasing time on stream. As such, these catalysts warrant further study and may be of considerable interest in potential scale-up reactions. On the other hand, the performance of (50)MSBDC-UiO-66 rapidly declines within a flow reactor before stabilising. Indeed, the performance of this catalyst stabilises with an activity comparable to standard UiO-66. This suggests that the materials sulfonic acid groups are removed (“stripped”) from the material within continuous flow.

Increasing the quantity of catalysts within the reaction increased glucose conversion and product yields. However, reaction selectivity towards desirable products is reduced. Meanwhile, the use of DMSO as a reaction solvent increased HMF yields within MOF catalysed reactions.

Overall, the results obtained in this extensive study suggest that the catalytic performances of MOFs may be ‘fine-tune’ towards glucose isomerisation and dehydration. The Zr frameworks considered in this study are highly recyclable and show considerable promise within flow reactor systems. As such, Zr MOFs may potentially offer an exciting solution towards the chemo-catalytic production of fructose and HMF in industry.

Conclusions

This thesis describes the development of several zeolite and metal-organic framework catalysts for the isomerisation of glucose and production of HMF. Studies were conducted in both batch and flow reactor systems. Considering the number of catalysts described in this work, numerous conclusions can be drawn. Detailed discussions and conclusions are provided in the individual chapters where results appear. As such, the conclusions presented herein will provide an overall highlight of the work conducted in this thesis.

With regards to zeolites, an initial study found that numerous metal-containing beta zeolites can successfully be produced using a rapid synthesis technique. This technique, adopted from Chang, *et al.*, successfully reduces the time required to synthesis metal-containing beta zeolites from 40 days to 3 days. We found that tin (Sn), zirconium (Zr), zinc (Zn), gallium (Ga) and ytterbium (Yb) can be successfully introduced into the beta zeolite framework. Meanwhile, strontium (Sr) could not be introduced as framework metal sites. Overall, the rapid synthesis method generated metal-containing beta zeolites of excellent size and morphology. The acidity of each of these materials was quantified using ammonia TPD analysis and their catalytic activity was tested in both water and HCl. Of the resulting materials, those containing Ga, Sn and Zr were found to be the most acidic. Furthermore, Sn-Beta was found to be the most effective glucose isomerisation catalyst in water. Specifically, Sn-Beta was able to generate a glucose conversion of 64.2 % and a desirable product selectivity of 70.7 % in a 3 h batch reaction conducted at 140 °C. The excellent performance of Sn-Beta is somewhat unsurprising. Indeed, Sn-Beta is widely regarded as a benchmark catalyst within the field of glucose isomerisation and has been extensively studied in current literature. Moreover, Chang, *et al.* also show that the rapid synthesis method yields highly active Sn-Beta catalysts for glucose isomerisation in batch

reactions. To explore the performance this catalyst in greater detail, Sn-Beta was tested within a purpose built flow reactor. Although the performance of this catalyst initially declined with increasing time on stream, the activity of the Sn-Beta appeared to begin stabilising at lower conversions and product yields. The inherent structure of the Sn-Beta recovered from the flow reactor was largely apparent following calcination – although the material had sustained some structural damage. Furthermore, the recovered and calcined material retained some of its catalytic activity when tested in a batch reaction. This suggests that the material recovered from the flow reactor and calcined still contains catalytically active Sn sites. With regards to reactions conducted in 0.1 M HCl, the presence of this mineral acid generally hindered glucose conversions and product yields.

Although the rapid synthesis method enables the production of metal-containing beta zeolites in only 3 days, it does not negate the use of highly toxic hydrofluoric acid during material preparation. As such, we considered the use of a post-synthesis technique in order to successfully introduce tin (Sn) and gallium (Ga) into the framework of zeolite Y. The resulting zeolites were found to be extremely promising glucose isomerisation catalysts in water. Interestingly, although the Ga containing material was found to be considerably more acidic, the Sn containing material generated the greatest glucose conversion and fructose yield in water. Specifically, Sn-DeAl-H-Y generated a 36 % glucose conversion along with a desirable product yield of 17 % in water-mediated reactions. As before, we attempted to improve HMF yields by introducing 0.1 M HCl into the reactions. However, the presence of this mineral acid was once again found to be detrimental to catalytic performance. As an alternative, we also considered the use of DMSO as a reaction solvent. Indeed, the presence of this aprotic solvent was found to significantly increase HMF yields, particularly when considering the Ga catalyst. Specifically, Ga-DeAl-H-Y enabled a 78 % glucose conversion along with a HMF yield of 33 % when reactions were conducted in DMSO. With regards to stability, Sn-DeAl-H-Y was found to be considerably more stable than Ga-DeAl-H-Y in each of the reaction solvents considered. In fact, a considerable amount of Ga was leached from Ga-DeAl-H-Y during reactions. Furthermore, these leached metal ions may contribute significantly toward glucose conversions and product yields. Thus, given the superior stability of Sn-DeAl-H-Y, it was selected for further study

in a series of recycle reactions. The activity of Sn-DeAl-H-Y rapidly declined following the first reaction cycle in water and could not be regenerated. This decrease in catalytic performance was attributed to the formation of humins on Sn active sites. Moreover, we suspect that the moisture released by these insoluble humins during calcination may effectively steam the catalyst, removing active Sn sites from the materials framework and rendering it inactive. As DMSO is known to prevent the formation of humins, recycle reactions were repeated in this aprotic organic solvent. Interestingly, the activity of both Sn-DeAl-H-Y and Ga-DeAl-H-Y remained high over the course of two consecutive recycle reactions in DMSO and could be regenerated via calcination. This suggests that humin formation on the catalyst surface during reactions conducted in water causes deactivation and may prevent regeneration.

With regards to the development of MOF catalysts, an initial study explored the application of iron (Fe) and scandium (Sc) MIL-88B materials. This MOF is a close relative to the chromium (Cr) containing MIL-101 catalysts that have previously been reported in literature for fructose and HMF production. However, unlike (Cr)MIL-101, Fe and Sc MIL-88B is non-toxic, making it a preferred alternative in the development of green chemical processes. The best catalyst observed in this initial study was a bimetallic material containing both Fe and Sc. The activity of this bimetallic material was attributed to its defective structure and the positive effect of having both metals within its framework. Unfortunately, each of the MIL-88B catalysts considered in this study were found to be hydrothermally unstable. As such reactions were conducted in a common aprotic solvent, DMSO. The materials degraded at 120 °C in DMSO and Sc sites within the framework are shown to be more stable than Fe sites. The catalytic activity of (Fe)MIL-88B and (FeSc)MIL-88B declined over the course of four consecutive recycle reactions conducted at 120 °C. This loss of activity was caused by the deactivation and/or destruction of the catalysts under reaction conditions.

Following our initial study of MIL-88B, we turned our attention towards the development of more hydrothermally stable MOF catalysts. Here, we first considered the use of a ytterbium framework, $\text{Yb}_6(\text{BDC})_7(\text{OH})_4(\text{H}_2\text{O})_4$. Reactions were conducted in both water and hydrochloric acid (pH 2.5) in an attempt to improve HMF yields. The performance of $\text{Yb}_6(\text{BDC})_7(\text{OH})_4(\text{H}_2\text{O})_4$ within the

reactions was lower than that of $\text{YbCl}_3 \cdot 6\text{H}_2\text{O}$. However, a positive trend was observed between reaction times and catalytic performance, with longer reaction times increasing glucose conversions and product yields. To examine the stability and reusability of this MOF, a series of recycle reactions were conducted. Here reaction times were extended to 24 h in order to promote glucose conversions and product yields. After the first recycle reaction, the performance of $\text{Yb}_6(\text{BDC})_7(\text{OH})_4(\text{H}_2\text{O})_4$ declined and the subsequent product yields generated were comparable to those produced in a blank reaction. Furthermore, ICP analysis revealed that approximately 5 % of the materials Yb content was leached in each of the recycle reactions, and a control experiment suggests that these leached metal ions may contribute to the glucose conversions and product yields observed. Indeed, it appears that $\text{Yb}_6(\text{BDC})_7(\text{OH})_4(\text{H}_2\text{O})_4$ may act as a reservoir for catalytically active homogeneous Yb ions within the 24 h recycle reactions.

Following our work on $\text{Yb}_6(\text{BDC})_7(\text{OH})_4(\text{H}_2\text{O})_4$, we considered the use of ZIF-8 as a catalysts for the isomerisation of glucose and production of HMF in water. Not only is ZIF-8 widely reported as being water stable, it is also commercially available. In our study, ZIF-8 was synthesised using two different methods. Of these, the hydrothermal synthesis method yields a material with exceptionally high surface area. Indeed, the surface area of (HT)ZIF-8 is comparable to the surface area calculated based on single crystal data (reported in literature). The activities of ZIF-8 catalysts were tested in water and 0.1 M HCl at two different temperatures (100 °C and 140 °C). In each of the reactions, both (RT)ZIF-8 and (HT)ZIF-8 generated comparable glucose conversions and product yields. This is not surprising as TGA suggests that the materials contain similar quantities of metal ions and organic linker. In water mediated reactions conducted at 100 °C, the ZIF-8 catalysts generated glucose conversions of around 25 % along with fructose yields of around 15 %. However, at a higher temperature of 140 °C, reaction selectivity towards desirable products (fructose, mannose, HMF) declined. For instance, at 140 °C in water, (RT)ZIF-8 generated a glucose conversion of 84 % and a total desirable product yield of around 16 %. As such, we can infer that lower temperatures improve reaction selectivity towards desirable products when considering ZIF-8 catalysts. Indeed, low temperature reactions appear to promote glucose isomerisation whilst higher temperatures appear to promote the production

of undesirable products. It is also worth noting that higher temperatures also appear to promote the production of mannose in the reaction. This may suggest that the activation energy barrier towards mannose is greater than the activation energy barrier towards fructose in ZIF-8 catalysed reactions. Interestingly, the addition of HCl to the reactions appeared to suppress the activity of the catalysts at lower temperatures whilst improving selectivity towards desirable products at higher temperatures. In order to test the reusability and stability of ZIF-8 catalysts in water, the performance of (RT)ZIF-8 was tested in a continuous flow reactor. Within the continuous flow reactor, the catalytic activity of (RT)ZIF-8 quickly diminished. This loss of activity may be attributed to catalyst destruction or deactivation caused by the production of by-products such as insoluble humins.

In a final exploratory MOF study, we consider the use of UiO-66 as a catalyst for glucose isomerisation in water. In this study, defective Zr sites within the framework of UiO-66 provide sufficient Lewis acidity to promote glucose isomerisation towards fructose. Furthermore, we found that glucose isomerisation could be improved by introducing sulfonic acid functionalised linkers into the catalysts framework. Specifically, the introduction of MSBDC linker within the framework of UiO-66 appeared to enhance the Lewis acidity at defective Zr sites. This enhanced Lewis acidity improved both glucose conversions and fructose yields. Interestingly, the presence of sulfonic acid groups did not significantly improve HMF yields within the reactions. A material containing 20 % MSBDC linker generated the greatest glucose conversion and product yield observed in this study. In order to test the stability and reusability of UiO-66 catalysts, a series of recycle reactions were conducted. In each of these recycle reactions; glucose conversions and product yields fell after the first reaction cycle. This initial loss of activity can be attributed to a number of factors: 1) a loss of small catalyst particles that are difficult to recover after the first reaction cycle, 2) a build-up of insoluble humin by-products on the catalyst that block Zr active sites, 3) a loss of sulfonic acid groups from the functionalised frameworks. However, after this initial loss of activity in the first reaction cycle, the performance of UiO-66 and its MSBDC functionalised variants remained high in subsequent reaction cycles. As such, the results of this study highlight the potential to “fine-tune” Zr MOF catalysts towards the isomerisation of glucose in water.

Given the excellent performance of functionalised UiO-66 catalysts in water, we expanded our study on Zr MOFs. Specifically, we considered the use of modified UiO-66 and UiO-67 materials as glucose isomerisation and dehydration catalysts. Here, the Zr frameworks were altered through linker substitution, size modulation and post-synthesis treatment to promote surface defects. As expected, increasing material surface area, and the number of defective Zr sites within UiO-66, increased glucose conversions and product yields. Interestingly however, increasing the number of defective sites within the framework of UiO-66 also promoted reaction selectivity towards mannose. In order to examine the effect of different functional groups on catalytic performance, several were introduced into the frameworks of the Zr MOFs. Specifically, the functional groups considered were sulfonic acid, carboxylic acid, hydroxyl groups, and naphthalene. Overall, a sulfonic acid functionalised UiO-66 material was found to be the most effective catalysts tested in this study. Specifically, (50)MSBDC-UiO-66 generated a glucose conversion of 37.3 % along with a 58.9 % selectivity towards desirable products. Furthermore, the introduction of free carboxylic acid groups (through the inclusion of BTeC linker) into the framework of UiO-66 improved HMF yields whilst the introduction of a hydrophobic naphthalene group enhanced glucose isomerisation. A number of functionalised UiO-66 and UiO-67 catalysts were tested in a series of recycle reactions conducted in water. Following an initial decline in activity, the performance of these catalysts remained high throughout the course of these recycle reactions. This suggests that the materials are highly recyclable. To further test the stability and reusability of promising materials, a purpose built continuous flow reactor was used. Here, a material containing both naphthalene and sulfonic acid functionalised linker was found to be the most promising catalyst when using a flow reactor. However, in the case of the bifunctional material, the sulfonic acid groups may be stripped from the catalyst during reactions, leaving the naphthalene groups and a high number of defective sites responsible for the majority of the catalytic activity observed in the flow reactor.

Future Work

This thesis explores the development of zeolite and metal-organic framework catalysts for glucose isomerisation and HMF production. Preference was given to the development of water stable catalysts, although alternative reaction solvents are also considered. The first two results chapters of this thesis focus on the development of zeolite catalysts. Meanwhile, the third and fourth results chapters focus on the development of MOF catalysts. Each of these chapters contain promising results, and have identified materials and trends that should be studied further. As such, this section provides a list of potential future works. These future works have been subdivided into different sections that relate to specific catalysts.

Metal-Containing Beta Zeolites

- The metal-containing beta zeolites are acidic, have excellent morphologies, and may be useful catalysts in a number of green chemical processes. As such, future work should test the application of these catalysts in different reactions such as the production of lactic acid.
- The activity of Sn-Beta initially declined within a continuous flow reactor operating at 140 °C for a period of 8 h. However, the catalyst recovered from the flow reactor still contained Lewis acidic Sn sites after 8 h time on stream and calcination. As such, the performance of this catalyst should be further studied within continuous flow systems. Furthermore, to better understand the nature of the Sn active sites within the catalyst before and after flow reactions; detailed NMR studies should be conducted.
- A number of studies have shown that the sequential use of alcohol and water mediated reaction solvents can improve product yields. As such, the metal-containing beta zeolites described in this chapter should be tested in such systems.

- Finally, NMR studies should be conducted to better understand the nature of the various metals sites introduced into the beta zeolite framework.

Metal-Containing Zeolite Y

- The second results chapter in this thesis describes the application of tin (Sn) and gallium (Ga) containing zeolite Y catalysts. The Sn containing material described in this chapter was extremely stable in water, however quickly deactivated during aqueous recycle reactions and could not be regenerated. We suspect that this deactivation in water is a result of humin formation. Furthermore, we suspect that moisture released from humins during regeneration processes (calcination) may effectively steam the catalyst, removing Sn active sites from its framework and rendering it inactive. In order to understand the aqueous deactivation of Sn-DeAl-H-Y in greater detail, NMR studies are needed. Specifically, NMR studies that describe the Sn active sites before and after reactions in water, as well as before and after calcination, may provide further insight into the causes of deactivation.
- The metal-containing zeolite Y catalysts generated promising HMF yields when reactions were conducted in DMSO. Furthermore, the catalysts were highly recyclable in this aprotic organic solvent and could be regenerated via calcination. In order to expand this study, the activities of these catalysts should be tested in a continuous flow reactor feeding a glucose/DMSO feedstock.
- In an attempt to improve product yields, the application of these catalysts should be considered in a reaction system involving the sequential use of alcohol and aqueous solvents. Indeed, recent studies reported in literature show that the performance of acidic zeolite Y catalysts can be improved in such systems.

MOF Catalysts

- A number of MOFs were considered as catalysts for the isomerisation of glucose and production of HMF. Of these, UiO-66 and UiO-67 materials were found to be of considerable interest. A material containing both naphthalene and sulfonic acid functional groups was found to be the most promising catalyst in a flow reactor. However, we suspect that the sulfonic acid groups may be stripped from the catalyst during reactions, and that the naphthalene groups – along with a defective structure - may be responsible for the majority of the materials catalytic activity. As such, future work should focus on studying naphthalene functionalised UiO-66 and UiO-67 catalysts for glucose isomerisation and HMF production within flow reactors. Here, factors such as catalyst loading and operating conditions should be studied in detail. Specifically, operating conditions should be optimised in order to enhance product yields and maximise catalyst lifespan.
- Future work should also include a number of kinetic studies. Specifically, the reaction kinetics of functionalised UiO-66 and UiO-67 catalysts should be explored in water. Furthermore, rates of catalyst deactivation should also be studied in future works.

References

- (1) Isikgor, F. H.; C. Remzi Becer. *Polym. Chem.* **2015**, *6*, 4497–4559.
- (2) Mukherjee, A.; Dumont, M. J.; Raghavan, V. *Biomass and Bioenergy* **2015**, *72*, 143–183.
- (3) Alonso, D. M.; Bond, J. Q.; Dumesic, J. A. *Green Chem.* **2010**, *12* (9), 1493.
- (4) Chandel, A. K.; Garlapati, V. K.; Singh, A. K.; Antunes, F. A. F.; da Silva, S. S. *Bioresour. Technol.* **2018**, *264* (June), 370–381.
- (5) Corma Canos, A.; Iborra, S.; Velty, A. *Chem. Rev.* **2007**, *107* (6), 2411–2502.
- (6) Saha, B.; Abu-Omar, M. M. *Green Chem.* **2014**, *16* (1), 24.
- (7) Wang, T.; Nolte, M. W.; Shanks, B. H. *Green Chem.* **2014**, *16* (2), 548–572.
- (8) Kucherov, F. A.; Romashov, L. V.; Galkin, K. I.; Ananikov, V. P. *ACS Sustain. Chem. Eng.* **2018**, *6* (7), 8064–8092.
- (9) Rosatella, A. A.; Simeonov, S. P.; Frade, R. F. M.; Afonso, C. A. M. *Green Chem.* **2011**, *13* (4), 754.
- (10) Yu, I. K. M.; Tsang, D. C. W. *Bioresour. Technol.* **2017**, *238*, 716–732.
- (11) Van Putten, R. J.; Van Der Waal, J. C.; De Jong, E.; Rasrendra, C. B.; Heeres, H. J.; De Vries, J. G. *Chem. Rev.* **2013**, *113* (3), 1499–1597.
- (12) Degirmenci, V.; Pidko, E. A.; Magusin, P. C. M. M.; Hensen, E. J. M. *ChemCatChem* **2011**, *3* (6), 969–972.
- (13) Xue, Z.; Ma, M.-G.; Li, Z.; Mu, T. *RSC Adv.* **2016**, *6* (101), 98874–98892.
- (14) Pagán-Torres, Y. J.; Wang, T.; Gallo, J. M. R.; Shanks, B. H.; Dumesic, J. A. *ACS Catal.* **2012**, *2* (6), 930–934.
- (15) Takagaki, A.; Ohara, M.; Nishimura, S.; Ebitani, K. *Chem. Commun.* **2009**, No. 41, 6276–6278.
- (16) Li, H.; Yang, S.; Saravanamurugan, S.; Riisager, A. *ACS Catal.* **2017**, *7* (4), acscatal.6b03625.
- (17) Román-Leshkov, Y.; Davis, M. E. *ACS Catal.* **2011**, *1* (11), 1566–1580.
- (18) Delidovich, I.; Palkovits, R. *ChemSusChem* **2016**, *9* (6), 547–561.
- (19) Caratzoulas, S.; Davis, M. E.; Gorte, R. J.; Gounder, R.; Lobo, R. F.; Nikolakis, V.; Sandler, S. I.; Snyder, M. A.; Tsapatsis, M.; Vlachos, D. G. *J. Phys. Chem. C* **2014**, *118* (40), 22815–22833.
- (20) Li, H.; Yang, S.; Riisager, A.; Pandey, A.; Sangwan, R. S.; Saravanamurugan, S.; Luque, R. *Green Chem.* **2016**, *18* (21), 5701–5735.

- (21) Zou, X.; Zhu, C.; Wang, Q.; Yang, G. *Biofuels, Bioprod. Biorefining* **2019**, *13* (1), 153–173.
- (22) Parker, K.; Salas, M.; Nwosu, V. C. *Biotechnol. Mol. Biol. Rev.* **2010**, *5* (5), 71–78.
- (23) Bhosale, S. H.; Rao, M. B.; Deshpande, V. V. *Microbiol. Rev.* **1996**, *60* (2), 280–300.
- (24) Zhang, Y.; Hidajat, K.; Ray, A. K. *Biochem. Eng. J.* **2004**, *21* (2), 111–121.
- (25) Vilonen, K. M.; Vuolanto, A.; Jokela, J.; Leisola, M. S. a; Krause, a O. I. *Biotechnol. Prog.* **2004**, *20* (5), 1555–1560.
- (26) Román-Leshkov, Y.; Moliner, M.; Labinger, J. A.; Davis, M. E. *Angew. Chemie Int. Ed.* **2010**, *49* (47), 8954–8957.
- (27) Douglas, W.; Shetty, J. K. *Curr. Opin. Microbiol.* **1999**, No. 2, 252–256.
- (28) Bread, I. *Enzymes in Industry*; 2007.
- (29) Liese, A.; Seelbach, K.; Wandrey, C. *Industrial Biotransformations*; WILEY-VCH Verlag GmbH & Co., 2006.
- (30) Stütz, A. E. *Glycoscience: epimerisation, isomerisation and rearrangement reactions of carbohydrates*; 2001; Vol. 215.
- (31) Carraher, J. M.; Fleitman, C. N.; Tessonnier, J. P. *ACS Catal.* **2015**, *5* (6), 3162–3173.
- (32) Graaff, W. N. P. Van Der; Pidko, E. A.; Hensen, E. J. M. In *Zeolites in Sustainable Chemistry*; Springer, 2016; pp 347–372.
- (33) Liu, C.; Carraher, J. M.; Swedberg, J. L.; Herndon, C. R.; Fleitman, C. N.; Tessonnier, J. P. *ACS Catal.* **2014**, *4* (12), 4295–4298.
- (34) Yang, Q.; Zhou, S.; Runge, T. *J. Catal.* **2015**, *330*, 474–484.
- (35) Yang, Q.; Runge, T. *ACS Sustain. Chem. Eng.* **2016**, *4* (12), 6951–6961.
- (36) Deshpande, N.; Cho, E. H.; Spanos, A. P.; Lin, L. C.; Brunelli, N. A. *J. Catal.* **2019**, *372*, 119–127.
- (37) Deshpande, N.; Pattanaik, L.; Whitaker, M. R.; Yang, C. T.; Lin, L. C.; Brunelli, N. A. *J. Catal.* **2017**, *353*, 205–210.
- (38) Yang, Q.; Sherbahn, M.; Runge, T. *ACS Sustain. Chem. Eng.* **2016**, *4* (6), 3526–3534.
- (39) Souzanchi, S.; Nazari, L.; Rao, K. T. V.; Yuan, Z.; Tan, Z.; Xu, C. (Charles). *Catal. Today* **2019**, *319* (March 2018), 76–83.
- (40) Lingjuan, L.; Xianghai, G.; Peng, B.; Shuo, Z. *Asian J. Chem.* **2014**, *27* (8), 2774–2778.
- (41) Kitajima, H.; Higashino, Y.; Matsuda, S.; Zhong, H.; Watanabe, M.; Aida, T. M.; Smith, R. L. *Catal. Today* **2016**, *274*, 67–72.

- (42) Ohyama, J.; Zhang, Y.; Ito, J.; Satsuma, A. *ChemCatChem* **2017**, *9* (14), 2864–2868.
- (43) Shen, F.; Fu, J.; Zhang, X.; Qi, X. *ACS Sustain. Chem. Eng.* **2019**, *7* (4), 4466–4472.
- (44) Gao, D.-M.; Shen, Y.-B.; Zhao, B.; Liu, Q.; Nakanishi, K.; Chen, J.; Kanamori, K.; Wu, H.; He, Z.; Zeng, M.; Liu, H. *ACS Sustain. Chem. Eng.* **2019**, *7* (9), 8512–8521.
- (45) Marianou, A. A.; Michailof, C. M.; Ipsakis, D. K.; Karakoulia, S. A.; Kalogiannis, K. G.; Yiannoulakis, H.; Triantafyllidis, K. S.; Lappas, A. A. *ACS Sustain. Chem. Eng.* **2018**, *6* (12), 16459–16470.
- (46) Yu, S.; Kim, E.; Park, S.; Song, I. K.; Jung, J. C. *Catal. Commun.* **2012**, *29*, 63–67.
- (47) Yabushita, M.; Shibayama, N.; Nakajima, K.; Fukuoka, A. *ACS Catal.* **2019**, *9* (3), 2101–2109.
- (48) Park, S.; Kwon, D.; Kang, J. Y.; Jung, J. C. *Green Energy Environ.* **2018**, No. xxxx.
- (49) Chen, S. S.; Yu, I. K. M.; Cho, D. W.; Song, H.; Tsang, D. C. W.; Tessonier, J. P.; Ok, Y. S.; Poon, C. S. *ACS Sustain. Chem. Eng.* **2018**, *6* (12), 16113–16120.
- (50) Graça, I.; Iruretagoyena, D.; Chadwick, D. *Appl. Catal. B Environ.* **2017**, *206*, 434–443.
- (51) Graça, I.; Bacariza, M. C.; Fernandes, A.; Chadwick, D. *Appl. Catal. B Environ.* **2018**, *224* (November 2017), 660–670.
- (52) Lima, S.; Dias, A. S.; Lin, Z.; Brandão, P.; Ferreira, P.; Pillinger, M.; Rocha, J.; Calvino-Casilda, V.; Valente, A. A. *Appl. Catal. A Gen.* **2008**, *339* (1), 21–27.
- (53) Moliner, M.; Roman-Leshkov, Y.; Davis, M. E. *Proc. Natl. Acad. Sci.* **2010**, *107* (14), 6164–6168.
- (54) Yun Yang, B.; Montgomery, R. *Carbohydr. Res.* **1996**, *280* (1), 27–45.
- (55) Haack, E.; Braun, F.; Kohler, K. Process for the manufacture of fructose, March 18, 1966.
- (56) Rendleman, J. A.; Hodge, J. E.; Icosse, D. *Carbohydr. Res.* **1979**, *75*, 83–99.
- (57) Marianou, A. A.; Michailof, C. M.; Pineda, A.; Iliopoulou, E. F.; Triantafyllidis, K. S.; Lappas, A. A. *ChemCatChem* **2016**, *8* (6), 1100–1110.
- (58) Shaw III, A. J.; Tsao, G. T. *Carbohydr. Res.* **1978**, *60*, 327–335.
- (59) Shaw, A. J.; Tsao, G. T. *Carbohydr. Res.* **1978**, *60* (2), 376–382.
- (60) Davis, M. E. *Top. Catal.* **2015**, 405–409.

- (61) Saravanamurugan, S.; Paniagua, M.; Melero, J. A.; Riisager, A. *J. Am. Chem. Soc.* **2013**, *135* (14), 5246–5249.
- (62) Guo, Q.; Ren, L.; Kumar, P.; Cybulskis, V. J.; Mkhoyan, K. A.; Davis, M. E.; Tsapatsis, M. *Angew. Chemie Int. Ed.* **2018**, *57* (18), 4926–4930.
- (63) de Mello, M. D.; Tsapatsis, M. *ChemCatChem* **2018**, *10* (11), 2417–2423.
- (64) Luo, Q. X.; Zhang, Y. B.; Qi, L.; Scott, S. L. *ChemCatChem* **2019**, *11* (7), 1903–1909.
- (65) Yabushita, M.; Li, P.; Islamoglu, T.; Kobayashi, H.; Fukuoka, A.; Farha, O. K.; Katz, A. *Ind. Eng. Chem. Res.* **2017**, *56* (25), 7141–7148.
- (66) Yu, I. K. M.; Xiong, X.; Tsang, D. C. W.; Wang, L.; Hunt, A. J.; Song, H.; Shang, J.; Ok, Y. S.; Poon, C. S. *Green Chem.* **2019**, *21* (6), 1267–1281.
- (67) Yang, X.; Yu, I. K. M.; Cho, D. W.; Chen, S. S.; Tsang, D. C. W.; Shang, J.; Yip, A. C. K.; Wang, L.; Ok, Y. S. *ACS Sustain. Chem. Eng.* **2019**, *7* (5), 4851–4860.
- (68) Baerlocher, C.; McCusker, L. B. Database of Zeolite Structures <http://www.iza-structure.org/databases/>.
- (69) Corma, A.; Domine, M. E.; Nemeth, L.; Valencia, S. *J. Am. Chem. Soc.* **2002**, *124* (13), 3194–3195.
- (70) Padovan, D.; Parsons, C.; Simplicio Grasina, M.; Hammond, C. *Green Chem.* **2016**, *18* (18), 5041–5049.
- (71) Lew, C. M.; Rajabbeigi, N.; Tsapatsis, M. *Microporous Mesoporous Mater.* **2012**, *153*, 55–58.
- (72) Gounder, R.; Davis, M. E. *AIChE J.* **2013**, *59* (9), 3349–3358.
- (73) Shetty, S.; Kulkarni, B. S.; Kanhere, D. G.; Goursot, A.; Pal, S. *J. Phys. Chem. B* **2008**, *112* (9), 2573–2579.
- (74) Bermejo-Deval, R.; Gounder, R.; Davis, M. E. *ACS Catal.* **2012**, *2* (12), 2705–2713.
- (75) Bermejo-Deval, R.; Orazov, M.; Gounder, R.; Hwang, S.-J.; Davis, M. E. *ACS Catal.* **2014**, *4* (7), 2288–2297.
- (76) Rai, N.; Caratzoulas, S.; Vlachos, D. G. *ACS Catal.* **2013**, *3* (10), 2294–2298.
- (77) Bermejo-Deval, R.; Assary, R. S.; Nikolla, E.; Moliner, M.; Roman-Leshkov, Y.; Hwang, S.-J.; Palsdottir, A.; Silverman, D.; Lobo, R. F.; Curtiss, L. a.; Davis, M. E. *Proc. Natl. Acad. Sci.* **2012**, *109* (25), 9727–9732.
- (78) Boronat, M.; Concepción, P.; Corma, A.; Renz, M.; Valencia, S. *J. Catal.* **2005**, *234* (1), 111–118.
- (79) Nikolla, E.; Román-Leshkov, Y.; Moliner, M.; Davis, M. E. *ACS Catal.* **2011**, *1* (4), 408–410.

- (80) Tolborg, S.; Katerinopoulou, A.; Falcone, D. D.; Sádaba, I.; Osmundsen, C. M.; Davis, R. J.; Taarning, E.; Fristrup, P.; Holm, M. S. *J. Mater. Chem. A* **2014**, *2* (47), 20252–20262.
- (81) Chang, C.-C.; Wang, Z.; Dornath, P.; Je Cho, H.; Fan, W. *RSC Adv.* **2012**, *2* (28), 10475.
- (82) Corma, A.; Nemeth, L. T.; Renz, M.; Valencia, S. *Nature* **2001**, *412* (6845), 423–425.
- (83) Koehle, M.; Lobo, R. F. *Catal. Sci. Technol.* **2016**, *6* (9), 3018–3026.
- (84) Corma, A.; Valencia, S. *US Pat. 5,968,463* **1999**, 1–5.
- (85) Hammond, C.; Conrad, S.; Hermans, I. *Angew. Chemie Int. Ed.* **2012**, *51* (47), 11736–11739.
- (86) Wolf, P.; Hammond, C.; Conrad, S.; Hermans, I. *Dalt. Trans.* **2014**, *43* (11), 4514.
- (87) Tang, B.; Dai, W.; Wu, G.; Guan, N.; Li, L.; Hunger, M. *ACS Catal.* **2014**, *4* (8), 2801–2810.
- (88) Tang, B.; Dai, W.; Sun, X.; Wu, G.; Guan, N.; Hunger, M.; Li, L. *Green Chem.* **2015**, *17* (3), 1744–1755.
- (89) Yang, X.; Bian, J.; Huang, J.; Xin, W.; Lu, T.; Chen, C.; Su, Y.; Zhou, L.; Wang, F.; Xu, J. *Green Chem.* **2017**, *19* (3), 692–701.
- (90) Al-Nayili, A.; Yakabi, K.; Hammond, C. *J. Mater. Chem. A* **2016**, *4* (4), 1373–1382.
- (91) Ranoux, A.; Djanashvili, K.; Arends, I. W. C. E.; Hanefeld, U. *ACS Catal.* **2013**, *3* (4), 760–763.
- (92) Roman-Leshkov, Y. *Science (80-.)*. **2006**, *312* (5782), 1933–1937.
- (93) Chheda, J. N.; Roman-Leshkov, Y.; Dumesic, J. a. *Green Chem.* **2007**, *9* (4), 342.
- (94) Torres, A. I.; Daoutidis, P.; Tsapatsis, M. *Energy Environ. Sci.* **2010**, *3* (10), 1560.
- (95) Moreau, C.; Durand, R.; Razigade, S.; Duhamet, J.; Faugeras, P.; Rivalier, P.; Ros, P.; Avignon, G. *Appl. Catal. A Gen.* **1996**, *145* (1–2), 211–224.
- (96) Rivalier, P.; Duhamet, J.; Moreau, C.; Durand, R. *Catal. Today* **1995**, *24* (1–2), 165–171.
- (97) Brasholz, M.; Von Känel, K.; Hornung, C. H.; Saubern, S.; Tsanaktsidis, J. *Green Chem.* **2011**, *13* (5), 1114–1117.
- (98) Torres, A. I.; Tsapatsis, M.; Daoutidis, P. *Comput. Chem. Eng.* **2012**, *42*, 130–137.
- (99) Huang, H.; Denard, C. a; Alamillo, R.; Crisci, A. J.; Miao, Y.; Dumesic, J. a; Scott, S. L.; Zhao, H. *ACS Catal.* **2014**.

- (100) Degirmenci, V.; Hensen, E. J. M. *Environ. Prog. Sustain. Energy* **2014**, *33* (2), 657–662.
- (101) Zhao, H.; Holladay, J. E.; Brown, H.; Zhang, Z. C. *Science (80-.)*. **2007**, *316* (5831), 1597–1600.
- (102) Pidko, E. A.; Degirmenci, V.; Van Santen, R. A.; Hensen, E. J. M. *Angew. Chemie - Int. Ed.* **2010**, *49* (14), 2530–2534.
- (103) Enomoto, K.; Hosoya, T.; Miyafuji, H. *Cellulose* **2018**, *25* (4), 2249–2257.
- (104) Sezgin, E.; Esen Keçeci, M.; Akmaz, S.; Koc, S. N. *Cellulose* **2019**, *26* (17), 9035–9043.
- (105) Zhang, M.; Su, K.; Song, H.; Li, Z.; Cheng, B. *Catal. Commun.* **2015**, *69* (1), 76–80.
- (106) Hou, Q.; Zhen, M.; Li, W.; Liu, L.; Liu, J.; Zhang, S.; Nie, Y.; Bai, C.; Bai, X.; Ju, M. *Appl. Catal. B Environ.* **2019**, *253* (December 2018), 1–10.
- (107) D’Anna, F.; Marullo, S.; Vitale, P.; Rizzo, C.; Lo Meo, P.; Noto, R. *Appl. Catal. A Gen.* **2014**, *482*, 287–293.
- (108) Kroon, M. C.; van Spronsen, J.; Peters, C. J.; Sheldon, R. A.; Witkamp, G.-J. *Green Chem.* **2006**, *8* (3), 246–249.
- (109) Dayan, A. D.; Paine, A. J. *Hum. Exp. Toxicol.* **2001**, *20* (9), 439–451.
- (110) Sun, X.; Liu, Z.; Xue, Z.; Zhang, Y.; Mu, T. **2015**, 2719–2722.
- (111) Sarwono, A.; Man, Z.; Idris, A.; Sada, A.; Muhammad, N.; Devi, C. *J. Ind. Eng. Chem.* **2019**, *69*, 171–178.
- (112) Hu, L.; Sun, Y.; Lin, L. *Ind. Eng. Chem. Res.* **2012**, *51* (3), 1099–1104.
- (113) Onda, A.; Ochi, T.; Yanagisawa, K. *Green Chem.* **2008**, *10* (10), 1033–1037.
- (114) Yan, H.; Yang, Y.; Tong, D.; Xiang, X.; Hu, C. *Catal. Commun.* **2009**, *10* (11), 1558–1563.
- (115) Feng, Y.; Zuo, M.; Wang, T.; Jia, W.; Zhao, X.; Zeng, X.; Sun, Y.; Tang, X.; Lei, T.; Lin, L. *J. Taiwan Inst. Chem. Eng.* **2019**, *96*, 431–438.
- (116) Zhang, W.; Zhu, Y.; Xu, H.; Gaborieau, M.; Huang, J.; Jiang, Y. *Catalysis Today*. Elsevier 2018, pp 0–1.
- (117) Osatiastiani, A.; Lee, A. F.; Brown, D. R.; Melero, J. A.; Morales, G.; Wilson, K. *Catal. Sci. Technol.* **2014**, *4* (2), 333–342.
- (118) Osatiastiani, A.; Lee, A. F.; Granollers, M.; Brown, D. R.; Olivi, L.; Morales, G.; Melero, J. A.; Wilson, K. *ACS Catal.* **2015**, *5* (7), 4345–4352.
- (119) Lopes, M.; Dussan, K.; Leahy, J. J.; da Silva, V. T. *Catal. Today* **2017**, *279*, 233–243.

- (120) Jain, A.; Shore, A. M.; Jonnalagadda, S. C.; Ramanujachary, K. V.; Mugweru, A. *Appl. Catal. A Gen.* **2015**, *489*, 72–76.
- (121) Ordonsky, V. V.; Sushkevich, V. L.; Schouten, J. C.; Van Der Schaaf, J.; Nijhuis, T. A. *J. Catal.* **2013**, *300*, 37–46.
- (122) Huang, F.; Su, Y.; Long, Z.; Chen, G.; Yao, Y. *Ind. Eng. Chem. Res.* **2018**, *57* (31), 10198–10205.
- (123) Zhang, L.; Xi, G.; Chen, Z.; Qi, Z.; Wang, X. *Chem. Eng. J.* **2017**, *307*, 877–883.
- (124) Atanda, L.; Mukundan, S.; Shrotri, A.; Ma, Q.; Beltramini, J. *ChemCatChem* **2015**, *7* (5), 781–790.
- (125) Wang, L.; Yuan, F.; Niu, X.; Kang, C.; Li, P.; Li, Z.; Zhu, Y. *RSC Adv.* **2016**, *6* (46), 40175–40184.
- (126) Liu, B.; Ba, C.; Jin, M.; Zhang, Z. *Ind. Crops Prod.* **2015**, *76*, 781–786.
- (127) Hou, Q.; Zhen, M.; Liu, L.; Chen, Y.; Huang, F.; Zhang, S.; Li, W.; Ju, M. *Appl. Catal. B Environ.* **2018**, *224* (July 2017), 183–193.
- (128) Asghari, F. S.; Yoshida, H. *Carbohydr. Res.* **2006**, *341* (14), 2379–2387.
- (129) Daorattanachai, P.; Khemthong, P.; Viriya-empikul, N.; Laosiripojana, N.; Faungnawakij, K. *Carbohydr. Res.* **2012**, *363*, 58–61.
- (130) Su, Y.; Chang, G.; Zhang, Z.; Xing, H.; Su, B.; Yang, Q.; Ren, Q.; Yang, Y.; Bao, Z. *AIChE J.* **2016**, *62* (12), 4403–4417.
- (131) Herbst, A.; Janiak, C. *New J. Chem.* **2016**, *40*, 7958–7967.
- (132) Gong, J.; Katz, M. J.; Kerton, F. M. *RSC Adv.* **2018**, *8* (55), 31618–31627.
- (133) Fringuelli, F.; Pizzo, F.; Vaccaro, L. *J. Org. Chem.* **2001**, *66* (13), 4719–4722.
- (134) Xia, H.; Hu, H.; Xu, S.; Xiao, K.; Zuo, S. *Biomass and Bioenergy* **2018**, *108* (June 2017), 426–432.
- (135) Xu, S.; Pan, D.; Hu, F.; Wu, Y.; Wang, H.; Chen, Y.; Yuan, H.; Gao, L.; Xiao, G. *Fuel Process. Technol.* **2019**, *190* (March), 38–46.
- (136) Xu, S.; Pan, D.; Li, W.; Shen, P.; Wu, Y.; Song, X.; Zhu, Y.; Xu, N.; Gao, L.; Xiao, G. *Fuel Process. Technol.* **2018**, *181* (April), 199–206.
- (137) Yang, L.; Yan, X.; Xu, S.; Chen, H.; Xia, H.; Zuo, S. *RSC Adv.* **2015**, *5* (26), 19900–19906.
- (138) Nahavandi, M.; Kasanneni, T.; Yuan, Z. S.; Xu, C. C.; Rohani, S. *ACS Sustain. Chem. Eng.* **2019**, *7* (14), 11970–11984.
- (139) Chen, D.; Liang, F.; Feng, D.; Xian, M.; Zhang, H.; Liu, H.; Du, F. *Chem. Eng. J.* **2016**, *300*, 177–184.
- (140) Gascon, J.; Corma, A.; Kapteijn, F.; Llabrés i Xamena, F. X. *ACS Catal.*

2014, 4 (2), 361–378.

- (141) Farrusseng, D.; Aguado, S.; Pinel, C. *Angew. Chemie - Int. Ed.* **2009**, *48* (41), 7502–7513.
- (142) Dhakshinamoorthy, A.; Alvaro, M.; Corma, A.; Garcia, H. *Dalt. Trans.* **2011**, *40* (24), 6344–6360.
- (143) Corma, A.; García, H.; Llabrés i Xamena, F. X. *Chem. Rev.* **2010**, *110*, 4606–4655.
- (144) Lee, J.; Farha, O. K.; Roberts, J.; Scheidt, K. A.; Nguyen, S. T.; Hupp, J. T. *Chem. Soc. Rev.* **2009**, *38* (5), 1450–1459.
- (145) Yang, X.; Wu, L.; Wang, Z.; Bian, J.; Lu, T.; Zhou, L.; Chen, C.; Xu, J. *Catal. Sci. Technol.* **2016**, *6* (6), 1757–1763.
- (146) Ragon, F.; Campo, B.; Yang, Q.; Martineau, C.; Wiersum, A. D.; Lago, A.; Guillerm, V.; Hemsley, C.; Eubank, J. F.; Vishnuvarthan, M.; Taulelle, F.; Horcajada, P.; Vimont, A.; Llewellyn, P. L.; Daturi, M.; Devautour-Vinot, S.; Maurin, G.; Serre, C.; Devic, T.; Clet, G. *J. Mater. Chem. A* **2015**, *3* (7), 3294–3309.
- (147) Taddei, M.; Dümbgen, K. C.; van Bokhoven, J. A.; Ranocchiari, M. *Chem. Commun.* **2016**, *52* (38), 6411–6414.
- (148) Mowat, J. P. S.; Miller, S. R.; Slawin, A. M. Z.; Seymour, V. R.; Ashbrook, S. E.; Wright, P. A. *Microporous Mesoporous Mater.* **2011**, *142* (1), 322–333.
- (149) Zhu, T.-T. T.; Zhang, Z.-M. M.; Chen, W.-L. L.; Liu, Z.-J. J.; Wang, E.-B. B. *RSC Adv.* **2016**, *6* (85), 81622–81630.
- (150) Breeze, M. I.; Chamberlain, T. W.; Clarkson, G. J.; De Camargo, R. P.; Wu, Y.; De Lima, J. F.; Millange, F.; Serra, O. A.; O’Hare, D.; Walton, R. I. *CrystEngComm* **2017**, *19* (17), 2424–2433.
- (151) Corma, A. *J. Catal.* **2003**, *215* (2), 294–304.
- (152) Hammond, C.; Padovan, D.; Al-Nayili, A.; Wells, P. P.; Gibson, E. K.; Dimitratos, N. *ChemCatChem* **2015**, *7* (20), 3322–3331.
- (153) Li, P.; Liu, G.; Wu, H.; Liu, Y.; Jiang, J.; Wu, P. *J. Phys. Chem. C* **2011**, *115* (9), 3663–3670.
- (154) Dijkmans, J.; Gabriëls, D.; Dusselier, M.; de Clippel, F.; Vanelderren, P.; Houthoofd, K.; Malfliet, A.; Pontikes, Y.; Sels, B. F. *Green Chem.* **2013**, *15* (10), 2777.
- (155) Van Der Graaff, W. N. P.; Li, G.; Mezari, B.; Pidko, E. A.; Hensen, E. J. M. *ChemCatChem* **2015**, *7* (7), 1152–1160.
- (156) Dzwigaj, S.; Millot, Y.; Krafft, J.-M.; Popovych, N.; Kyriienko, P. *J. Phys. Chem. C* **2013**, *117* (24), 12552–12559.
- (157) Enumula, S. S.; Gurram, V. R. B.; Kondeboina, M.; Burri, D. R.; Kamaraju, S. R. R. *RSC Adv.* **2016**, *6* (24), 20230–20239.

- (158) Ramanathan, A.; Carmen Castro Villalobos, M.; Kwakernaak, C.; Telalovic, S.; Hanefeld, U. *Chem. - A Eur. J.* **2008**, *14* (3), 961–972.
- (159) Morey, M. S.; Stucky, G. D.; Schwarz, S.; Fröba, M. *J. Phys. Chem. B.* **1999**, *103*, 2037–2041.
- (160) Koike, N.; Chaikittisilp, W.; Iyoki, K.; Yanaba, Y.; Yoshikawa, T.; Elangovan, S. P.; Itabashi, K.; Okubo, T. *Dalt. Trans.* **2017**, *46* (33), 10837–10846.
- (161) Omojola, T.; Cherkasov, N.; McNab, A. I.; Lukyanov, D. B.; Anderson, J. A.; Rebrov, E. V.; van Veen, A. C. *Catal. Letters* **2018**, *148* (1), 474–488.
- (162) Fan, Y.; Bao, X.; Lin, X.; Shi, G.; Liu, H. *J. Phys. Chem. B* **2006**, *110* (31), 15411–15416.
- (163) Shafaghat, H.; Rezaei, P. S.; Daud, W. M. A. W. *J. Ind. Eng. Chem.* **2016**, *35*, 268–276.
- (164) Lee, S. U.; Lee, Y. J.; Kim, J. R.; Jeong, S. Y. *J. Ind. Eng. Chem.* **2018**, *66*, 279–287.
- (165) Suárez, N.; Pérez-Pariente, J.; Márquez-Álvarez, C.; Grande Casas, M.; Mayoral, A.; Moreno, A. *Microporous Mesoporous Mater.* **2019**, *284* (February), 296–303.
- (166) Gołabek, K.; Palomares, A. E.; Martínez-Triguero, J.; Tarach, K. A.; Kruczała, K.; Girman, V.; Góra-Marek, K. *Appl. Catal. B Environ.* **2019**, *259* (March).
- (167) Josephson, T. R.; Jenness, G. R.; Vlachos, D. G.; Caratzoulas, S. *Microporous Mesoporous Mater.* **2017**, *245*, 45–50.
- (168) Boronat, M.; Corma, A. *Catal. Letters* **2015**, *145* (1), 162–172.
- (169) ZHU, Y.; CHUAH, G.; JAENICKE, S. *J. Catal.* **2004**, *227* (1), 1–10.
- (170) Wang, J.; Jaenicke, S.; Chuah, G.-K. *RSC Adv.* **2014**, *4* (26), 13481–13489.
- (171) Dong, W.; Shen, Z.; Peng, B.; Gu, M.; Zhou, X.; Xiang, B.; Zhang, Y. *Sci. Rep.* **2016**, *6* (1), 26713.
- (172) Vermeiren, W.; Gilson, J.-P. *Top. Catal.* **2009**, *52* (9), 1131–1161.
- (173) Choudary, N. V.; Newalkar, B. L. *J. Porous Mater.* **2011**, *18* (6), 685–692.
- (174) Vogt, E. T. C.; Weckhuysen, B. M. *Chem. Soc. Rev.* **2015**, *44* (20), 7342–7370.
- (175) *Zeolites and Catalysis: Synthesis, Reactions and Applications*; Čejka, J., Corma, A., Zones, S., Eds.; Wiley-VCH Verlag GmbH & Co. KGaA: Weinheim, Germany, 2010.
- (176) Kim, C. W.; Kang, H.-C.; Heo, N. H.; Seff, K. *J. Phys. Chem. C* **2014**, *118* (20), 11014–11025.

- (177) Kerr, G. T. *J. Phys. Chem.* **1967**, *71* (12), 4155–4156.
- (178) Graça, I.; Bacariza, M. C. C.; Chadwick, D. *Microporous Mesoporous Mater.* **2018**, *255*, 130–139.
- (179) Dapsens, P. Y.; Kusema, B. T.; Mondelli, C.; Pérez-Ramírez, J. *J. Mol. Catal. A Chem.* **2014**, *388–389*, 141–147.
- (180) Dapsens, P. Y.; Mondelli, C.; Kusema, B. T.; Verel, R.; Pérez-Ramírez, J. *Green Chem.* **2014**, *16* (3), 1176–1186.
- (181) Kerr, G. T. *J. Phys. Chem.* **1968**, *72* (7), 2594–2596.
- (182) Zhang, R.; Xu, S.; Raja, D.; Khusni, N. B.; Liu, J.; Zhang, J.; Abdulridha, S.; Xiang, H.; Jiang, S.; Guan, Y.; Jiao, Y.; Fan, X. *Microporous Mesoporous Mater.* **2019**, *278* (December 2018), 297–306.
- (183) Pan, Y.; Zhuang, H.; Hong, J.; Fang, Z.; Liu, H.; Liu, B.; Huang, Y.; Xu, R. *ChemSusChem* **2014**, *7* (9), 2537–2544.
- (184) Sakata, Y.; Nakagawa, T.; Nagamatsu, Y.; Matsuda, Y.; Yasunaga, R.; Nakao, E.; Imamura, H. *J. Catal.* **2014**, *310*, 45–50.
- (185) Hajimirzaee, S.; Leeke, G. A.; Wood, J. *Chem. Eng. J.* **2012**, *207–208*, 329–341.
- (186) Tsilomelekis, G.; Orella, M. J.; Lin, Z.; Cheng, Z.; Zheng, W.; Nikolakis, V.; Vlachos, D. G. *Green Chem.* **2016**, *18* (7), 1983–1993.
- (187) Amarasekara, A. S.; Williams, L. D.; Ebede, C. C. *Carbohydr. Res.* **2008**, *343* (18), 3021–3024.
- (188) Hulme, H.; Baxter, F.; Babu, R. P.; Denecke, M. A.; Gass, M.; Steuwer, A.; Norén, K.; Carlson, S.; Preuss, M. *Corros. Sci.* **2015**, *105*, 202–208.
- (189) Takahashi, Y.; Sakakibara, N.; Nomura, M. **2004**, *76* (15), 4307–4314.
- (190) Akatsuka, T.; Ushiro, M.; Nagamatsu, S.; Takahashi, Y.; Fujikawa, T. *Polyhedron* **2008**, *27* (14), 3146–3150.
- (191) Park, K. S.; Ni, Z.; Cote, A. P.; Choi, J. Y.; Huang, R.; Uribe-Romo, F. J.; Chae, H. K.; O’Keeffe, M.; Yaghi, O. M. *Proc. Natl. Acad. Sci.* **2006**, *103* (27), 10186–10191.
- (192) Yang, D.; Gates, B. C. *ACS Catal.* **2019**, *9* (3), 1779–1798.
- (193) Xu, C.; Fang, R.; Luque, R.; Chen, L.; Li, Y. *Coord. Chem. Rev.* **2019**, *388*, 268–292.
- (194) Kang, Y. S.; Lu, Y.; Chen, K.; Zhao, Y.; Wang, P.; Sun, W. Y. *Coord. Chem. Rev.* **2019**, *378*, 262–280.
- (195) Jiao, L.; Wang, Y.; Jiang, H. L.; Xu, Q. *Adv. Mater.* **2018**, *30* (37), 1–23.
- (196) Zhang, Y.; Degirmenci, V.; Li, C.; Hensen, E. J. M. *ChemSusChem* **2011**, *4* (1), 59–64.
- (197) Chen, J.; Li, K.; Chen, L.; Liu, R.; Huang, X.; Ye, D. *Green Chem.* **2014**,

16 (5), 2490–2499.

- (198) G. Férey, C. Mellot-Draznieks, C. Serre, F. Millange, J. Dutour, S. S. and I. M. *Science* (80-.). **2005**, 309 (5743), 2040–2042.
- (199) Bhattacharjee, S.; Chen, C.; Ahn, W.-S. *RSC Adv.* **2014**, 4 (94), 52500–52525.
- (200) Serre, C.; Mellot-Draznieks, C.; Surblé, S.; Audebrand, N.; Filinchuk, Y.; Férey, G. *Science* (80-.). **2007**, 315 (5820), 1828–1831.
- (201) Cai, X.; Lin, J.; Pang, M. *Cryst. Growth Des.* **2016**, 16 (7), 3565–3568.
- (202) Tanasaro, T.; Adpakpang, K.; Ittisanronnachai, S.; Faungnawakij, K.; Butburee, T.; Wannapaiboon, S.; Ogawa, M.; Bureekaew, S. *Cryst. Growth Des.* **2018**, 18 (1), 16–21.
- (203) Carson, F.; Su, J.; Platero-Prats, A. E.; Wan, W.; Yun, Y.; Samain, L.; Zou, X. *Cryst. Growth Des.* **2013**, 13 (11), 5036–5044.
- (204) Yu, D.; Wu, M.; Hu, Q.; Wang, L.; Lv, C.; Zhang, L. *J. Hazard. Mater.* **2019**, 367 (August 2018), 456–464.
- (205) Dhakshinamoorthy, A.; Alvaro, M.; Chevreau, H.; Horcajada, P.; Devic, T.; Serre, C.; Garcia, H. *Catal. Sci. Technol.* **2012**, 2 (2), 324–330.
- (206) Vasudevan, V.; Mushrif, S. H. *RSC Adv.* **2015**, 5 (27), 20756–20763.
- (207) Ma, M.; Bétard, A.; Weber, I.; Al-Hokbany, N. S.; Fischer, R. A.; Metzler-Nolte, N. *Cryst. Growth Des.* **2013**, 13 (6), 2286–2291.
- (208) Téllez S, C. A.; Hollauer, E.; Mondragon, M. .; Castaño, V. M. *Spectrochim. Acta Part A Mol. Biomol. Spectrosc.* **2001**, 57 (5), 993–1007.
- (209) Sun, Z. J.; Jiang, J. Z.; Li, Y. F. *Analyst* **2015**, 140 (24), 8201–8208.
- (210) Jia, S.; Xu, Z.; Zhang, Z. C. *Chem. Eng. J.* **2014**, 254, 333–339.
- (211) Ishida, H.; Seri, K. *J. Mol. Catal. A Chem.* **1996**, 112 (2), L163–L165.
- (212) Ståhlberg, T.; Sørensen, M. G.; Riisager, A. *Green Chem.* **2010**, 12 (2), 321–325.
- (213) Utami, S. P.; Amin, N. S. *Ind. Crops Prod.* **2013**, 41 (1), 64–70.
- (214) Wang, T.; Pagán-Torres, Y. J.; Combs, E. J.; Dumesic, J. A.; Shanks, B. H. *Top. Catal.* **2012**, 55 (7–10), 657–662.
- (215) Wang, T.; Glasper, J. A.; Shanks, B. H. *Appl. Catal. A Gen.* **2015**, 498, 214–221.
- (216) Weng, D.; Zheng, X.; Jin, L. *Eur. J. Inorg. Chem.* **2006**, 2006 (20), 4184–4190.
- (217) Phan, A.; Doonan, C. J.; Uribe-Romo, F. J.; Knobler, C. B.; O’Keeffe, M.; Yaghi, O. M. *Acc. Chem. Res.* **2010**, 43 (1), 58–67.
- (218) Kolmykov, O.; Chebbat, N.; Commenge, J.-M.; Medjahdi, G.; Schneider,

R. Tetrahedron Lett. **2016**, 57 (52), 5885–5888.

- (219) Sun, C.-Y.; Qin, C.; Wang, X.-L.; Yang, G.-S.; Shao, K.-Z.; Lan, Y.-Q.; Su, Z.-M.; Huang, P.; Wang, C.-G.; Wang, E.-B. *Dalt. Trans.* **2012**, 41 (23), 6906.
- (220) Gong, X.; Wang, Y.; Kuang, T. *ACS Sustain. Chem. Eng.* **2017**, 5 (12), 11204–11214.
- (221) Xu, X.; Wang, H.; Liu, J.; Yan, H. *J. Mater. Sci. Mater. Electron.* **2017**, 28 (11), 7532–7543.
- (222) Li, J.; Wu, Y.; Li, Z.; Zhang, B.; Zhu, M.; Hu, X.; Zhang, Y.; Li, F. *J. Phys. Chem. C* **2014**, 118 (47), 27382–27387.
- (223) Tanaka, S.; Kida, K.; Nagaoka, T.; Ota, T.; Miyake, Y. *Chem. Commun.* **2013**, 49 (72), 7884.
- (224) Pan, Y.; Liu, Y.; Zeng, G.; Zhao, L.; Lai, Z. *Chem. Commun.* **2011**, 47 (7), 2071.
- (225) Tanaka, S.; Kida, K.; Okita, M.; Ito, Y.; Miyake, Y. *Chem. Lett.* **2012**, 41 (10), 1337–1339.
- (226) Pan, Y.; Heryadi, D.; Zhou, F.; Zhao, L.; Lestari, G.; Su, H.; Lai, Z. *CrystEngComm* **2011**, 13 (23), 6937.
- (227) Gross, A. F.; Sherman, E.; Vajo, J. J. *Dalt. Trans.* **2012**, 41 (18), 5458–5460.
- (228) Butova, V. V.; Budnyk, A. P.; Bulanova, E. A.; Lamberti, C.; Soldatov, A. V. *Solid State Sci.* **2017**, 69, 13–21.
- (229) Munn, A. S.; Dunne, P. W.; Tang, S. V. Y.; Lester, E. H. *Chem. Commun.* **2015**, 51 (64), 12811–12814.
- (230) Tanaka, S.; Nagaoka, T.; Yasuyoshi, A.; Hasegawa, Y.; Denayer, J. F. M. *Cryst. Growth Des.* **2018**, 18 (1), 274–279.
- (231) Lewis, D. W.; Ruiz-Salvador, A. R.; Gómez, A.; Rodriguez-Albelo, L. M.; Coudert, F. X.; Slater, B.; Cheetham, A. K.; Mellot-Draznieks, C. *CrystEngComm* **2009**, 11 (11), 2272–2276.
- (232) Lee, Y.-R.; Jang, M.-S.; Cho, H.-Y.; Kwon, H.-J.; Kim, S.; Ahn, W.-S. *Chem. Eng. J.* **2015**, 271, 276–280.
- (233) Huo, J.-B.; Xu, L.; Yang, J.-C. E.; Cui, H.-J.; Yuan, B.; Fu, M.-L. *Colloids Surfaces A Physicochem. Eng. Asp.* **2018**, 539 (February 2018), 59–68.
- (234) Kaur, H.; Mohanta, G. C.; Gupta, V.; Kukkar, D.; Tyagi, S. *J. Drug Deliv. Sci. Technol.* **2017**, 41, 106–112.
- (235) Zhu, M.; Srinivas, D.; Bhogeswararao, S.; Ratnasamy, P.; Carreon, M. A. *Catal. Commun.* **2013**, 32 (3), 36–40.
- (236) Wang, H.; Zhao, L.; Xu, W.; Wang, S.; Ding, Q.; Lu, X.; Guo, W. *Theor. Chem. Acc.* **2015**, 134 (3), 1–9.

- (237) Chizallet, C.; Bats, N. *J. Phys. Chem. Lett.* **2010**, *1* (1), 349–353.
- (238) Zhang, K.; Lively, R. P.; Zhang, C.; Koros, W. J.; Chance, R. R. *J. Phys. Chem. C* **2013**, *117* (14), 7214–7225.
- (239) Notman, N. MOFs find a use
<https://www.chemistryworld.com/features/mofs-find-a-use/2500508.article> (accessed Apr 17, 2019).
- (240) Burtch, N. C.; Jasuja, H.; Walton, K. S. *Chem. Rev.* **2014**, *114* (20), 10575–10612.
- (241) Wang, C.; Liu, X.; Keser Demir, N.; Chen, J. P.; Li, K. *Chem. Soc. Rev.* **2016**, *45* (18), 5107–5134.
- (242) Cavka, J. H.; Jakobsen, S.; Olsbye, U.; Guillou, N.; Lamberti, C.; Bordiga, S.; Lillerud, K. P. *J. Am. Chem. Soc.* **2008**, *130* (42), 13850–13851.
- (243) Dhakshinamoorthy, A.; Santiago-Portillo, A.; Asiri, A. M.; Garcia, H. *ChemCatChem* **2019**, *11* (3), 899–923.
- (244) Vermoortele, F.; Bueken, B.; Le Bars, G.; Van De Voorde, B.; Vandichel, M.; Houthoofd, K.; Vimont, A.; Daturi, M.; Waroquier, M.; Van Speybroeck, V.; Kirschhock, C.; De Vos, D. E. *J. Am. Chem. Soc.* **2013**, *135* (31), 11465–11468.
- (245) Zhou, F.; Lu, N.; Fan, B.; Wang, H.; Li, R. *J. Energy Chem.* **2016**, *25* (5), 874–879.
- (246) Vermoortele, F.; Vandichel, M.; Van De Voorde, B.; Ameloot, R.; Waroquier, M.; Van Speybroeck, V.; De Vos, D. E. *Angew. Chemie - Int. Ed.* **2012**, *51* (20), 4887–4890.
- (247) Lin Foo, M.; Horike, S.; Fukushima, T.; Hijikata, Y.; Kubota, Y.; Takata, M.; Kitagawa, S. *Dalt. Trans.* **2012**, *41* (45), 13791.
- (248) Phang, W. J.; Jo, H.; Lee, W. R.; Song, J. H.; Yoo, K.; Kim, B.; Hong, C. S. *Angew. Chemie - Int. Ed.* **2015**, *54* (17), 5142–5146.
- (249) Juan-Alcañiz, J.; Gielisse, R.; Lago, A. B.; Ramos-Fernandez, E. V.; Serra-Crespo, P.; Devic, T.; Guillou, N.; Serre, C.; Kapteijn, F.; Gascon, J. *Catal. Sci. Technol.* **2013**, *3* (9), 2311–2318.
- (250) Online, V. A.; Siu, P. W.; Scheidt, K. A.; Katz, M. J.; Brown, Z. J.; Colo, Y. J.; Snurr, R. Q.; Hupp, J. T.; Farha, O. K. *ChemComm* **2013**, *49*, 9449–9451.
- (251) Yang, P.; Liu, Q.; Liu, J.; Zhang, H.; Li, Z.; Li, R.; Liu, L.; Wang, J. *J. Mater. Chem. A* **2017**, *5* (34), 17933–17942.
- (252) Hu, Z.; Peng, Y.; Gao, Y.; Qian, Y.; Ying, S.; Yuan, D.; Horike, S.; Ogiwara, N.; Babarao, R.; Wang, Y.; Yan, N.; Zhao, D. *Chem. Mater.* **2016**, *28* (8), 2659–2667.
- (253) Rubio-Martinez, M.; Batten, M. P.; Polyzos, A.; Carey, K.-C.; Mardel, J. I.; Lim, K.-S.; Hill, M. R. *Sci. Rep.* **2015**, *4* (1), 5443.

- (254) Pang, J.; Zheng, M.; Sun, R.; Wang, A.; Wang, X.; Zhang, T. *Green Chem.* **2016**, *18* (2), 342–359.
- (255) Oozeerally, R.; Burnett, D. L.; Chamberlain, T. W.; Walton, R. I.; Degirmenci, V. *ChemCatChem* **2018**, *10* (4), 706–709.
- (256) Øien, S.; Wragg, D.; Reinsch, H.; Svelle, S.; Bordiga, S.; Lamberti, C.; Lillerud, K. P. *Cryst. Growth Des.* **2014**, *14* (11), 5370–5372.
- (257) Saravanan, K.; Tyagi, B.; Bajaj, H. C. *Catal. Sci. Technol.* **2012**, *2* (12), 2512–2520.
- (258) Rada, Z. H.; Abid, H. R.; Sun, H.; Shang, J.; Li, J.; He, Y.; Liu, S.; Wang, S. *Prog. Nat. Sci. Mater. Int.* **2018**, *28* (2), 160–167.
- (259) Kandiah, M.; Nilsen, M. H.; Usseglio, S.; Jakobsen, S.; Olsbye, U.; Tilset, M.; Larabi, C.; Quadrelli, E. A.; Bonino, F.; Lillerud, K. P. *Chem. Mater.* **2010**, *22* (24), 6632–6640.
- (260) Molavi, H.; Eskandari, A.; Shojaei, A.; Mousavi, S. A. *Microporous Mesoporous Mater.* **2018**, *257*, 193–201.
- (261) Saleem, H.; Rafique, U.; Davies, R. P. *Microporous Mesoporous Mater.* **2016**, *221*, 238–244.
- (262) Molavi, H.; Joukani, F. A.; Shojaei, A. *Ind. Eng. Chem. Res.* **2018**, *57* (20), 7030–7039.
- (263) Neeli, C. K. P.; Puthiaraj, P.; Lee, Y. R.; Chung, Y. M.; Baeck, S. H.; Ahn, W. S. *Catal. Today* **2018**, *303* (May 2017), 227–234.
- (264) Song, J. Y.; Ahmed, I.; Seo, P. W.; Jhung, S. H. *ACS Appl. Mater. Interfaces* **2016**, *8* (40), 27394–27402.
- (265) Ragon, F.; Campo, B.; Yang, Q.; Martineau, C.; Wiersum, A. D.; Lago, A.; Guillerm, V.; Hemsley, C.; Eubank, J. F.; Vishnuvarthan, M.; Taulelle, F.; Horcajada, P.; Vimont, A.; Llewellyn, P. L.; Daturi, M.; Devautour-Vinot, S.; Maurin, G.; Serre, C.; Devic, T.; Clet, G. *J. Mater. Chem. A* **2015**, *3* (7), 3294–3309.
- (266) Luan, Y.; Qi, Y.; Jin, Z.; Peng, X.; Gao, H.; Wang, G. *RSC Adv.* **2015**, *5* (25), 19273–19278.
- (267) Moghaddam, Z. S.; Kaykhali, M.; Khajeh, M.; Oveisi, A. R. *Spectrochim. Acta - Part A Mol. Biomol. Spectrosc.* **2018**, *194*, 76–82.
- (268) Rada, Z. H.; Abid, H. R.; Shang, J.; Sun, H.; He, Y.; Webley, P.; Liu, S.; Wang, S. *Industrial and Engineering Chemistry Research*. 2016, pp 7924–7932.
- (269) Yang, Q.; Vaesen, S.; Ragon, F.; Wiersum, A. D.; Wu, D.; Lago, A.; Devic, T.; Martineau, C.; Taulelle, F.; Llewellyn, P. L.; Jovic, H.; Zhong, C.; Serre, C.; De Weireld, G.; Maurin, G. *Angew. Chemie Int. Ed.* **2013**, *52* (39), 10316–10320.
- (270) Rada, Z. H.; Abid, H. R.; Shang, J.; Sun, H.; He, Y.; Webley, P.; Liu, S.; Wang, S. *Ind. Eng. Chem. Res.* **2016**, *55* (29), 7924–7932.

- (271) Caratelli, C.; Hajek, J.; Cirujano, F. G.; Waroquier, M.; Llabrés i Xamena, F. X.; Van Speybroeck, V. *J. Catal.* **2017**, *352*, 401–414.
- (272) Canivet, J.; Vandichel, M.; Farrusseng, D. *Dalt. Trans.* **2016**, *45* (10), 4090–4099.
- (273) Rajabbeigi, N.; Torres, A. I.; Lew, C. M.; Elyassi, B.; Ren, L.; Wang, Z.; Je Cho, H.; Fan, W.; Daoutidis, P.; Tsapatsis, M. *Chem. Eng. Sci.* **2014**, *116*, 235–242.

Appendix A

Flow Reactor Design

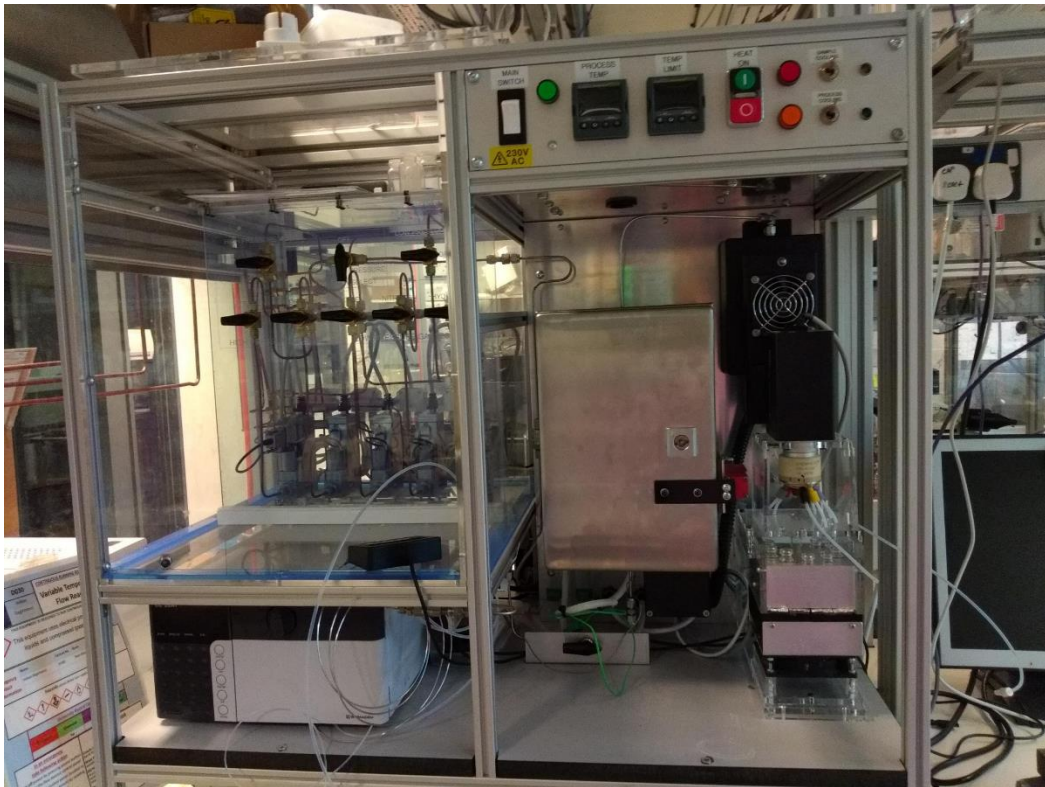


Figure A1. Flow Reactor.



Figure A2. Brass heating block and reactor tubing.

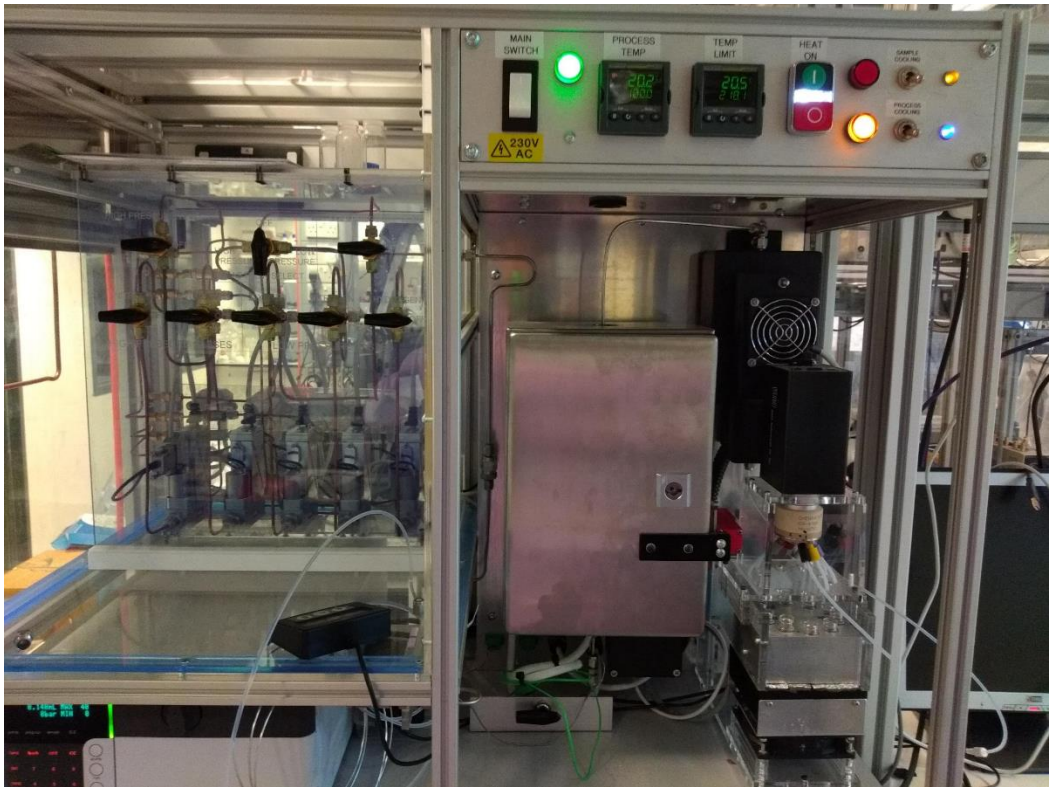


Figure A3. Flow reactor power on.

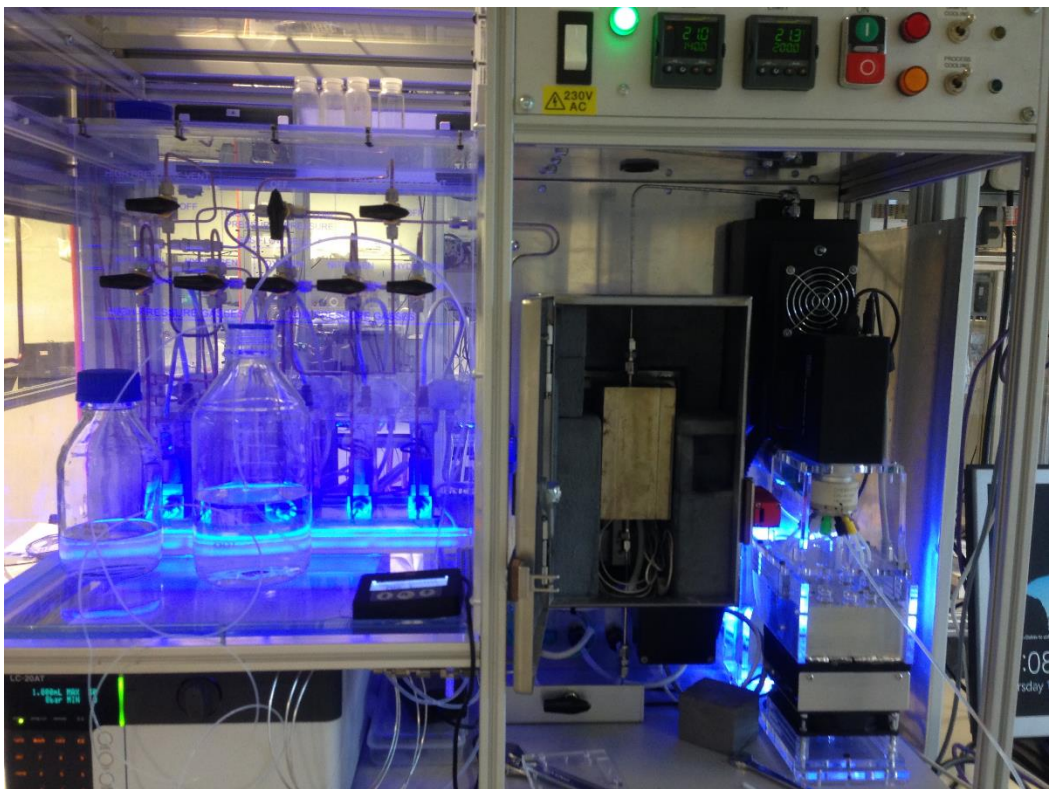


Figure A4. Flow reactor LED lighting.

Appendix B

Supporting Information for Chapter 5

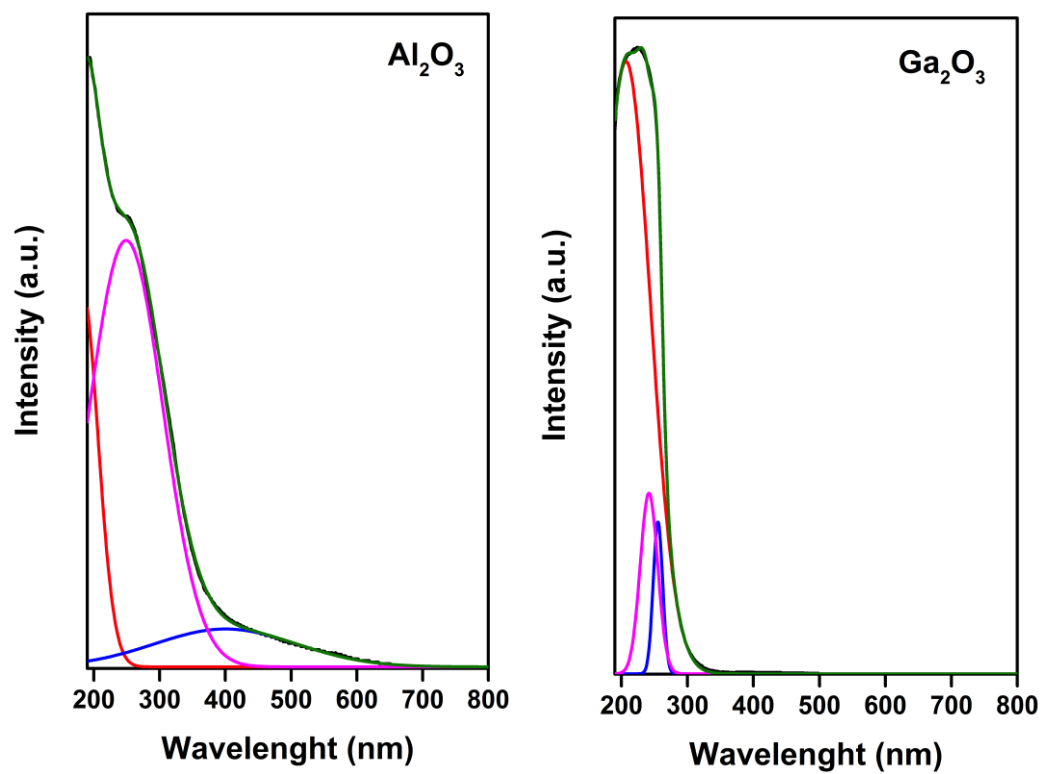


Figure B1. Deconvoluted UV-Vis spectra of aluminium oxide and gallium oxide.

Appendix C

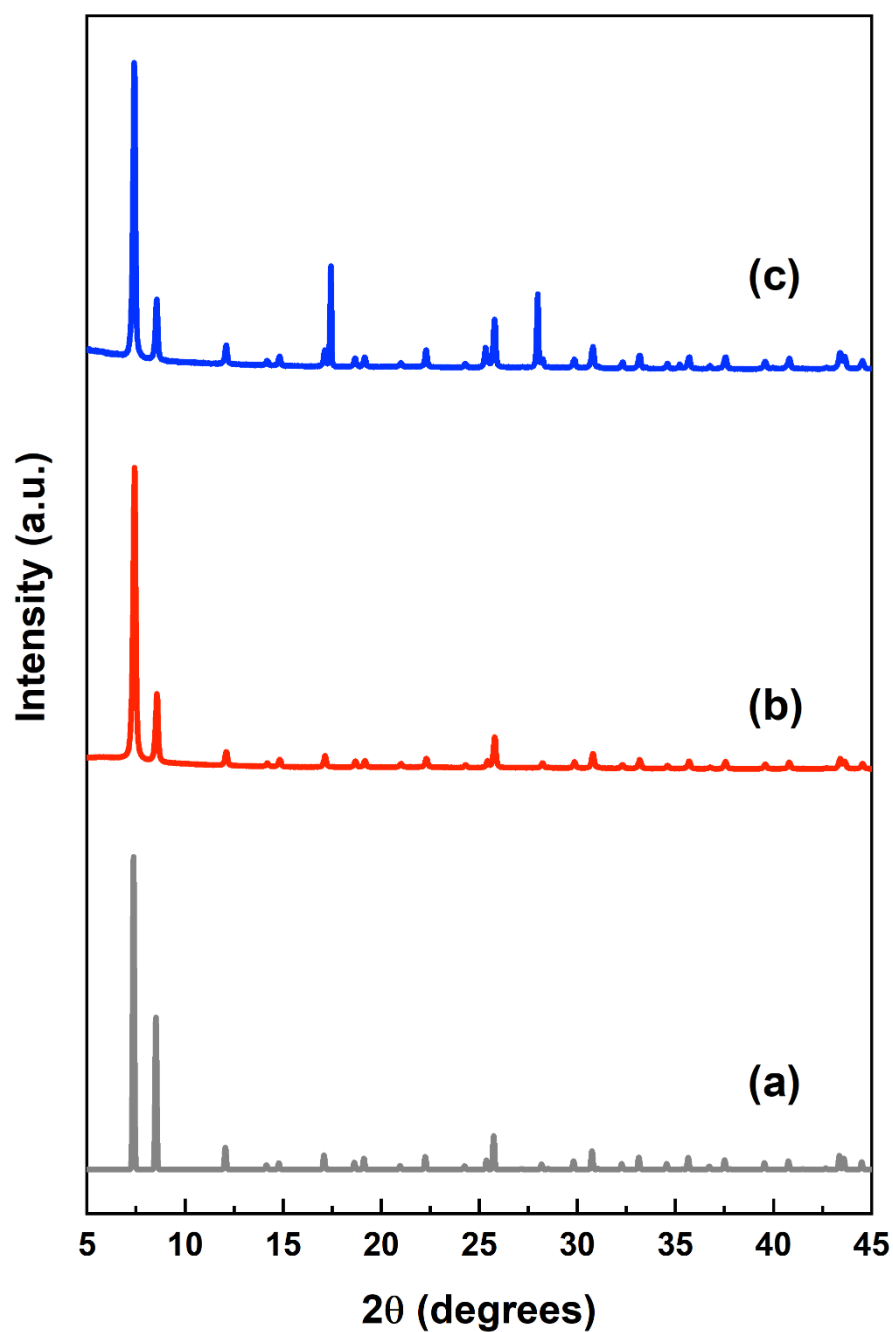


Figure C1. XRD powder analysis of UiO-66 materials (a) Simulated UiO-66 (b) UiO-66 (c) UiO-66 with additional peaks.

Appendix D

Supporting Information for Chapter 7

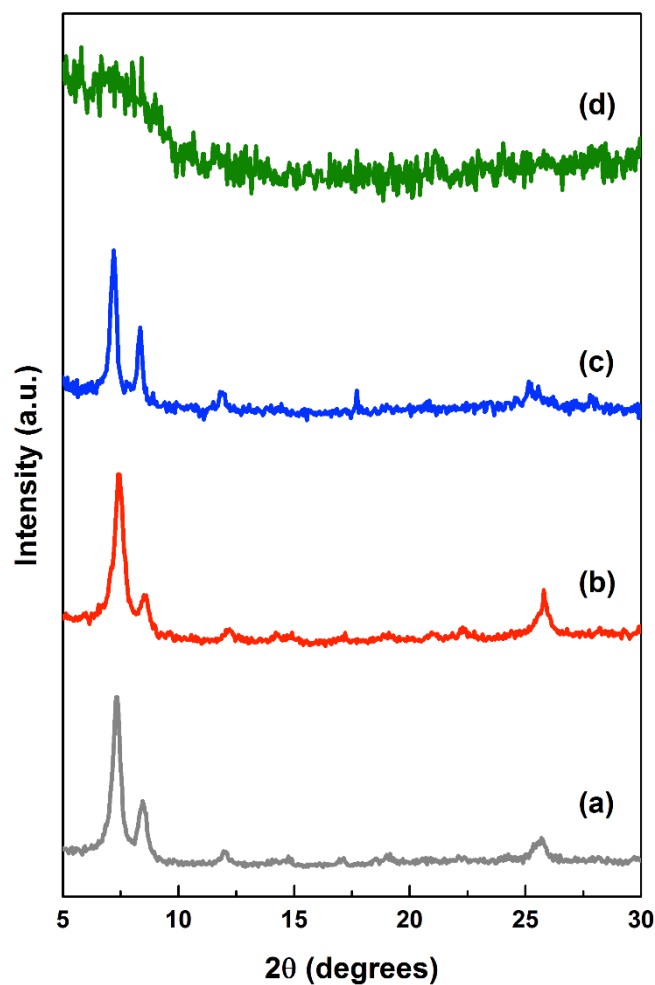


Figure D1. XRD powder analysis pre and post hydrothermal treatment at 140 °C for 24 h (a) (50)MSBDC-UiO-66 (b) (50)MSBDC-UiO-66 post hydrothermal treatment (c) (100)MSBDC-UiO-66 (d) (100)MSBDC-UiO-66 post hydrothermal treatment.

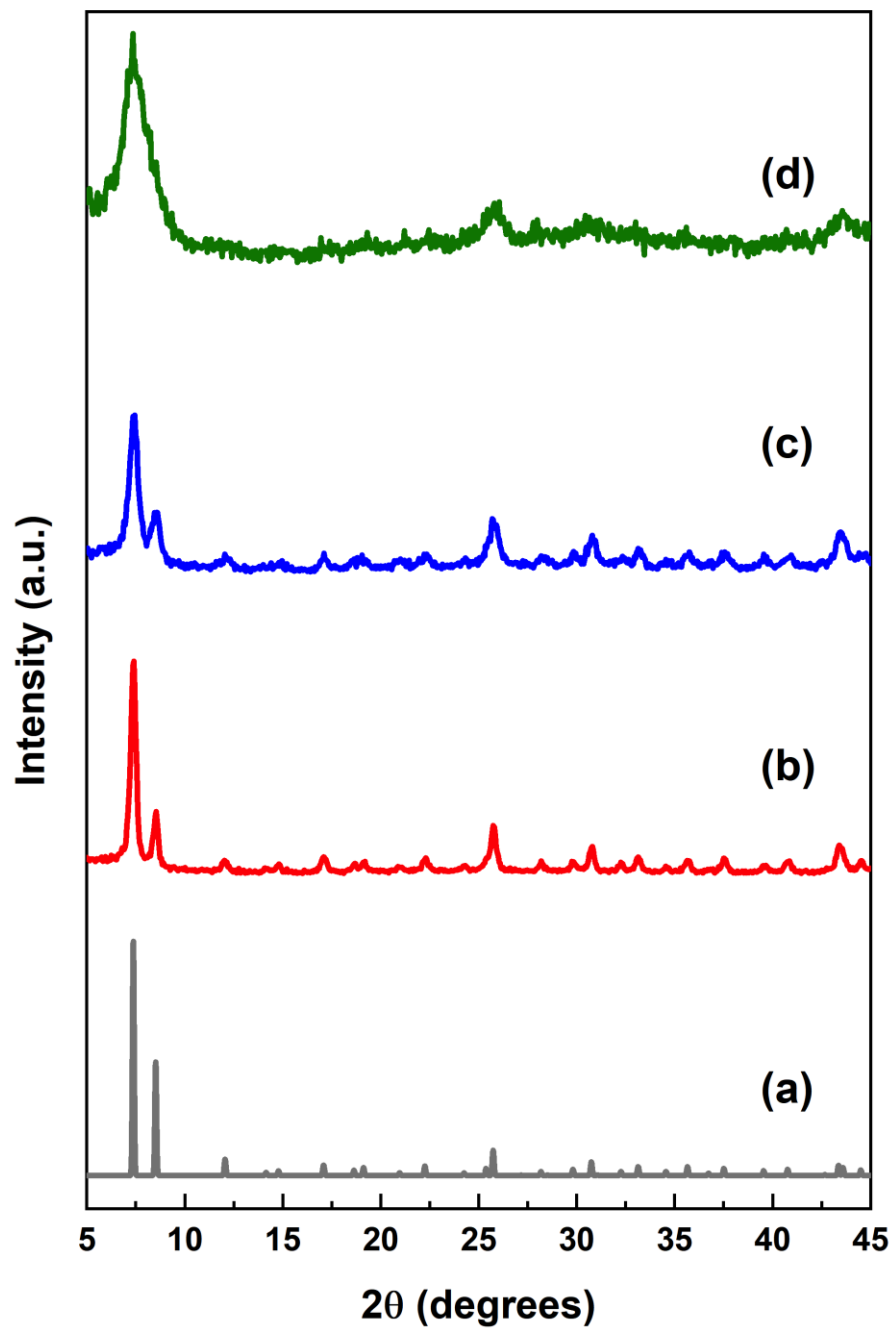


Figure D2. XRD powder analysis of UiO-66 materials (a) Simulated UiO-66 (b) Nano-UiO-66 (c) Ultra-Nano-UiO-66 (d) Poorly Crystalline UiO-66.

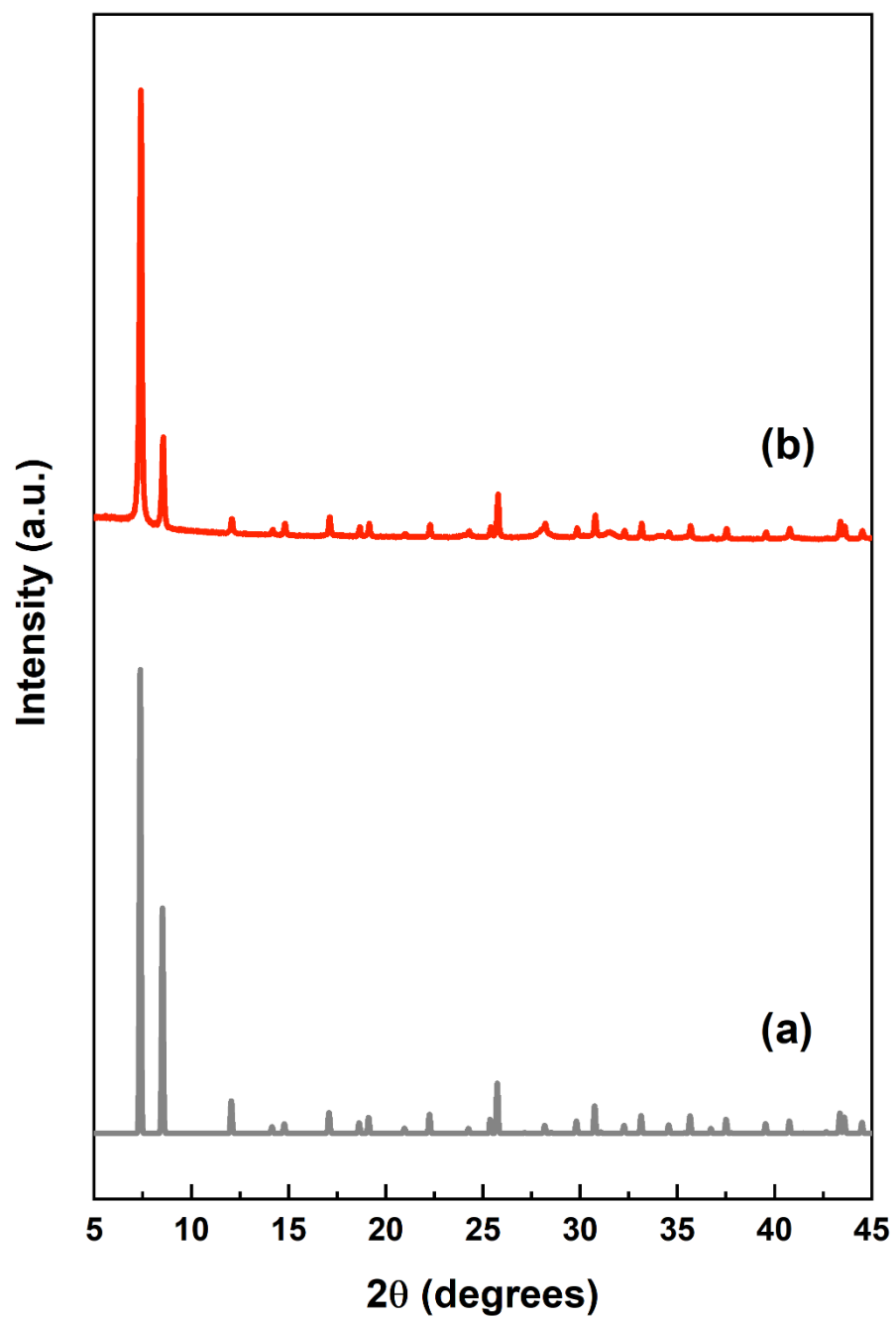


Figure D3. XRD powder analysis of UiO-66 materials (a) Simulated UiO-66 (b) Deffective-UiO-66.

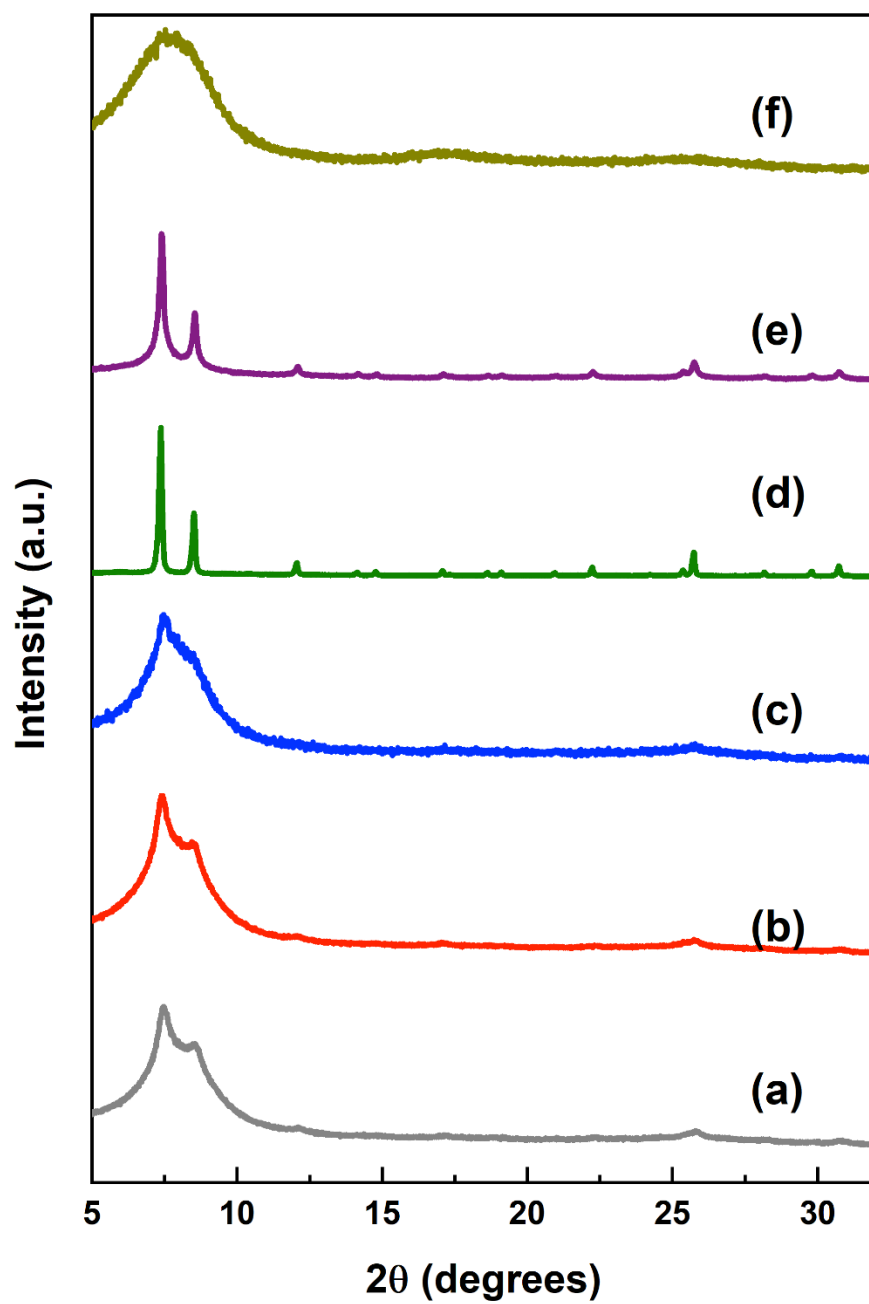


Figure D4. XRD powder analysis of UiO-66 materials (a) (20)NO₂-UiO-66 (b) (50)NO₂-UiO-66 (c) (100)NO₂-UiO-66 (d) (20)NH₂-UiO-66 (e) (50)NH₂-UiO-66 (f) (100)NH₂-UiO-66.

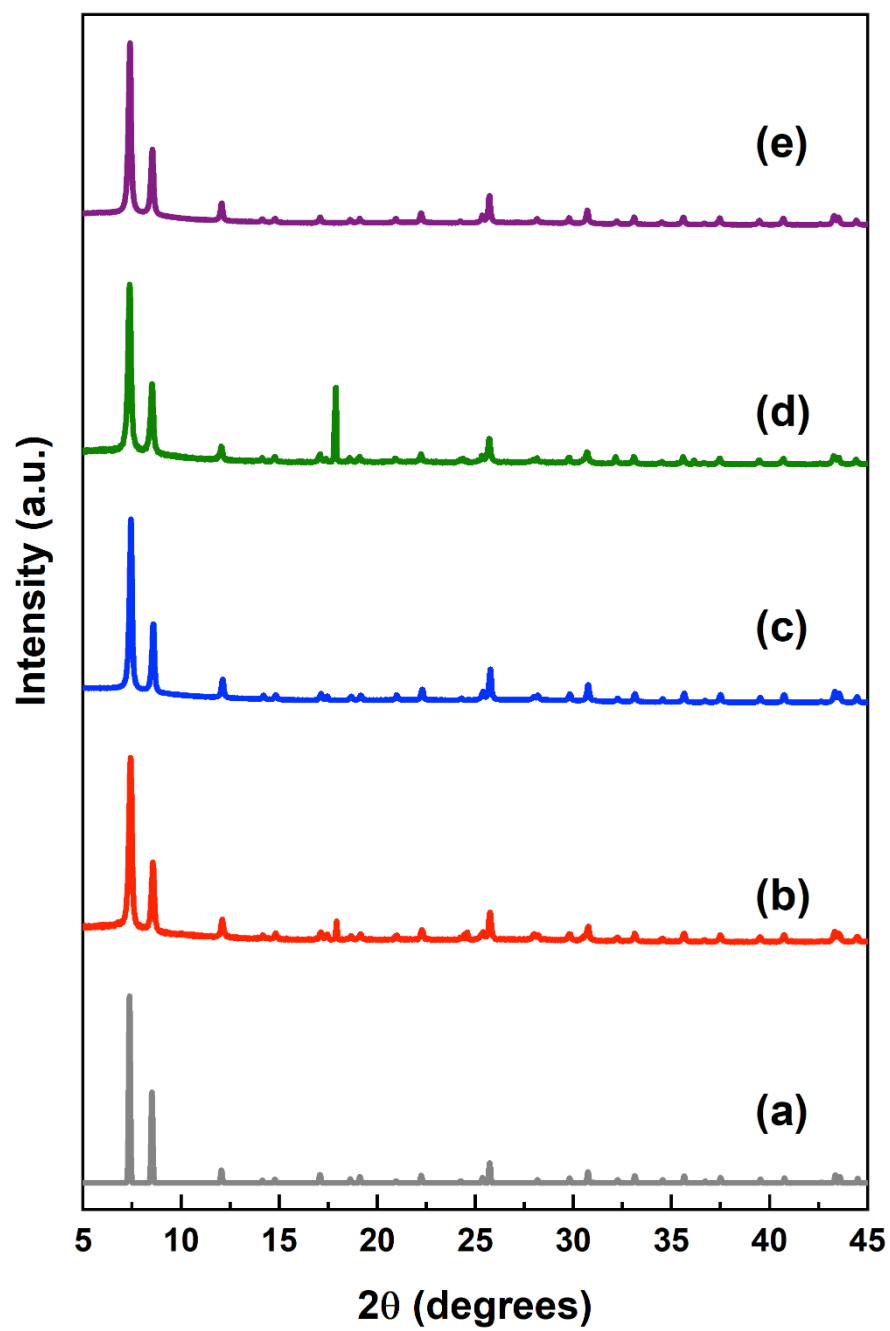


Figure D5. XRD powder analysis of UiO-66 materials (a) Simulated UiO-66 (b) (10)IPA-UiO-66 (c) (20)IPA-UiO-66 (d) (30)IPA-UiO-66 (e) (40)IPA-UiO-66.

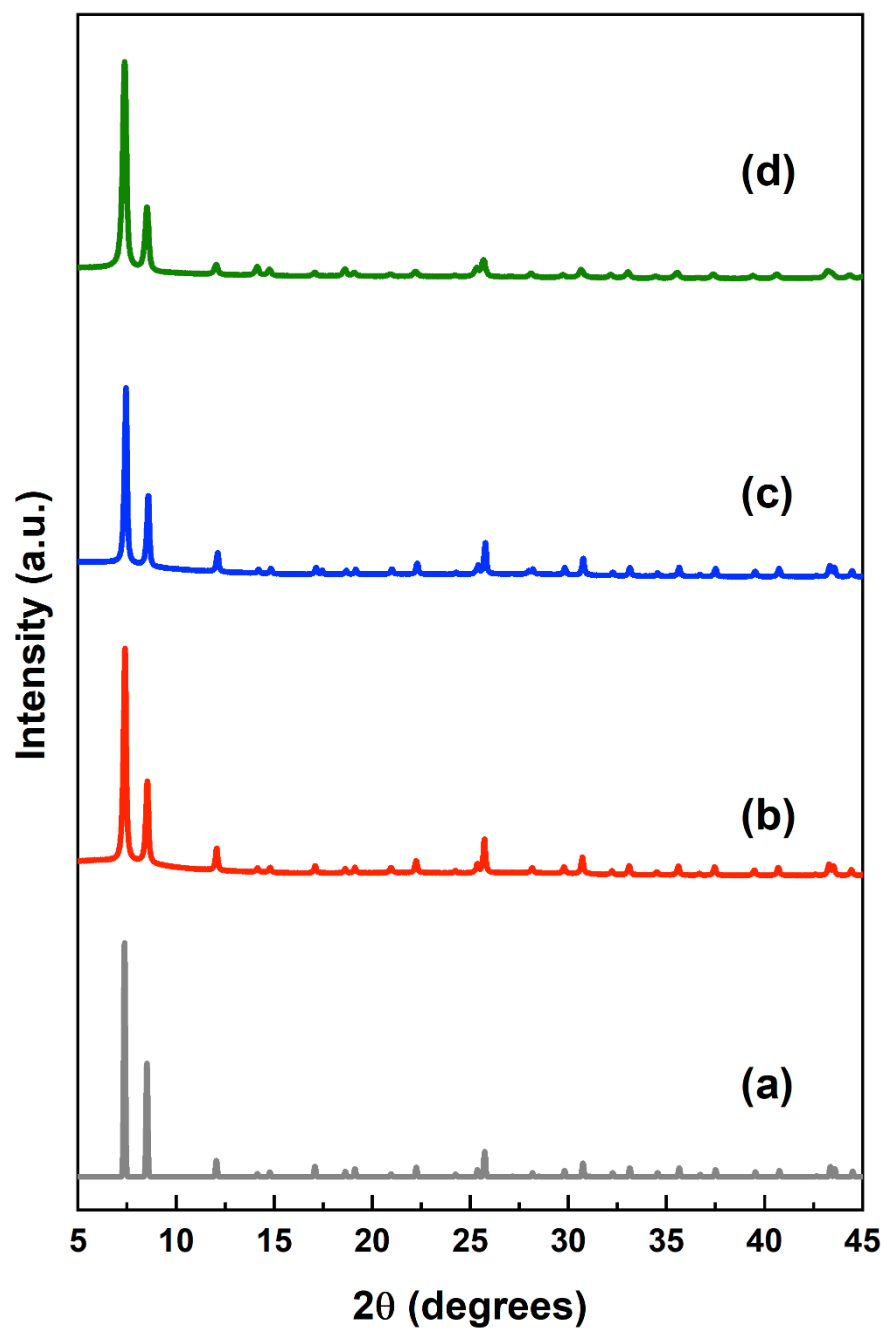


Figure D6. XRD powder analysis of UiO-66 materials (a) Simulated UiO-66 (b) (20)Naphth-UiO-66 (c) (50)Naphth-UiO-66 (d) (100)Naphth-UiO-66.

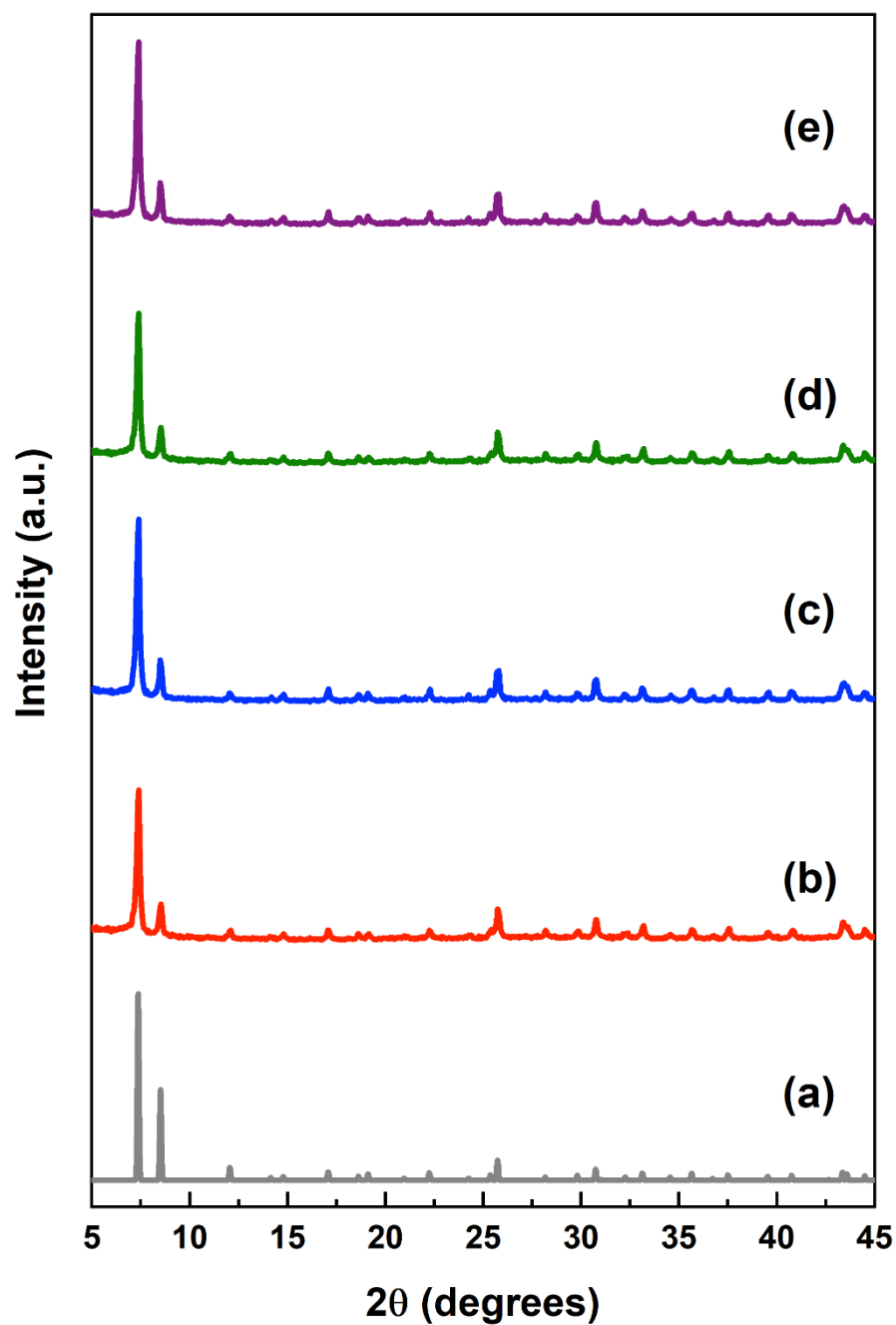


Figure D7. XRD powder analysis of UiO-66 materials (a) Simulated UiO-66 (b) (20)4-Sulfoben-UiO-66 (c) (40)4-Sulfoben-UiO-66 (d) (20)3-Sulfoben-UiO-66 (e) (40)3-Sulfoben-UiO-66.

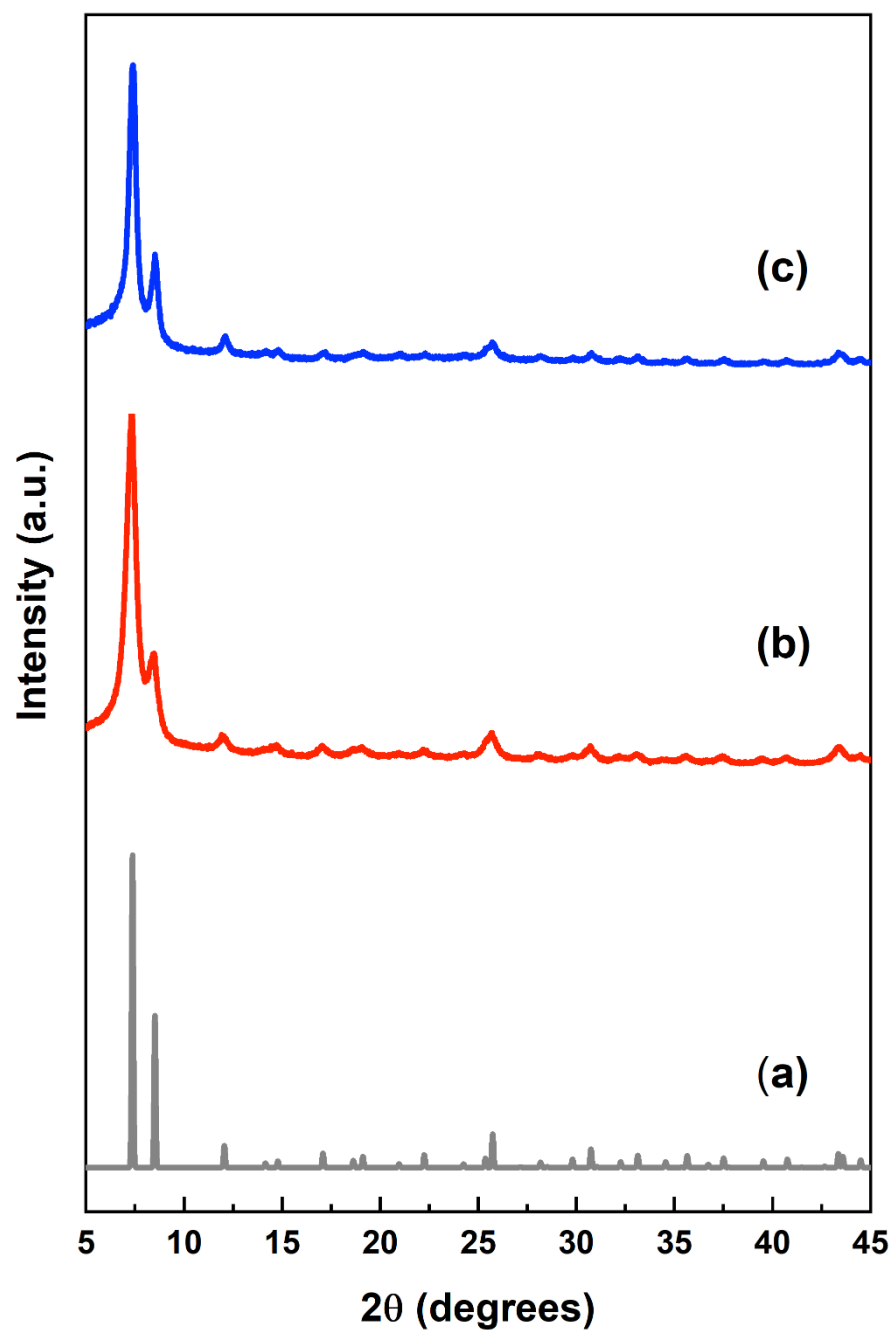


Figure D8. XRD powder analysis of UiO-66 materials (a) Simulated UiO-66 (b) (20)MSBDC-UiO-66-Nano (c) (50)MSBDC-UiO-66-Nano.

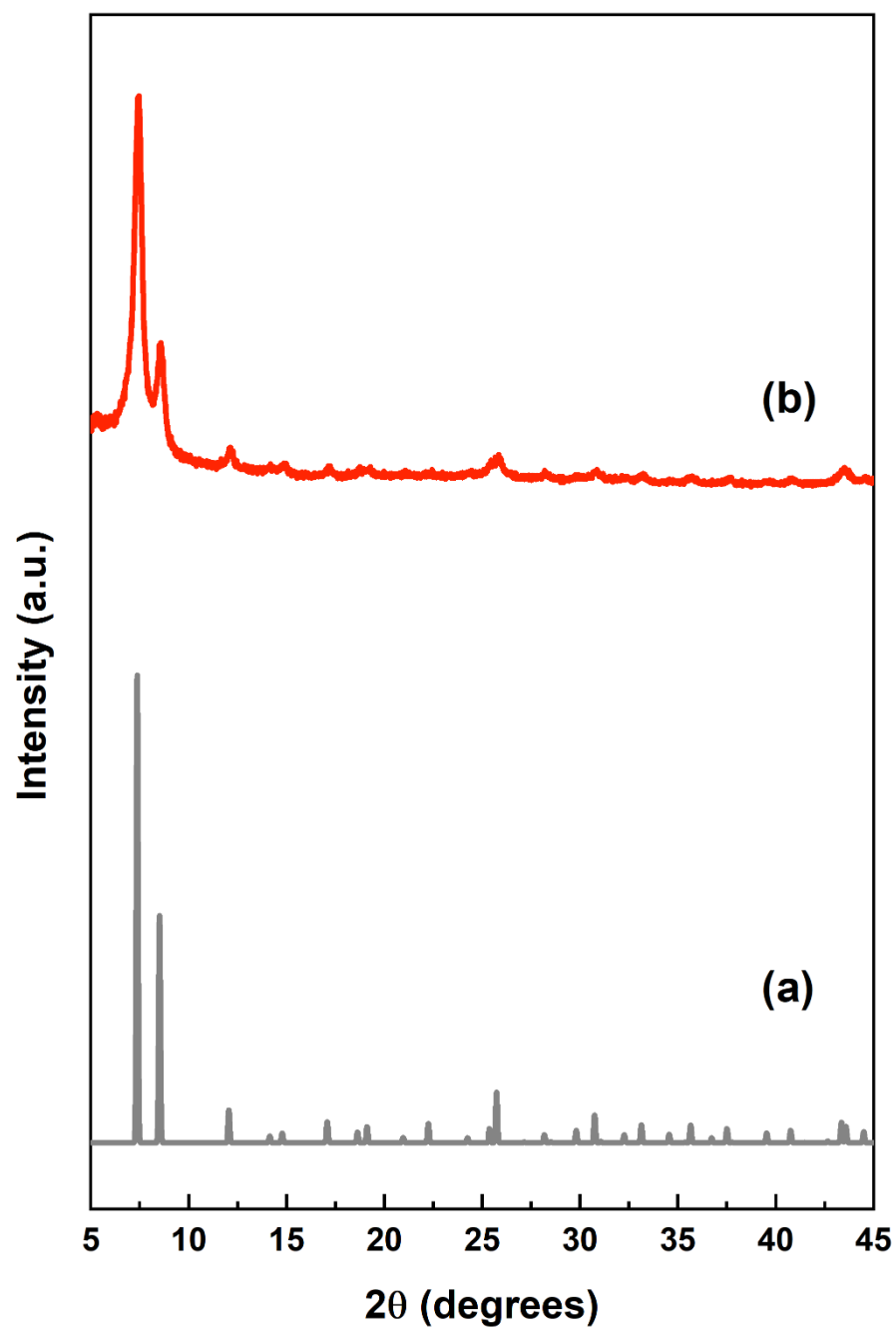


Figure D9. XRD powder analysis of UiO-66 materials (a) Simulated UiO-66 (b) (50)MSBDC-UiO-66.

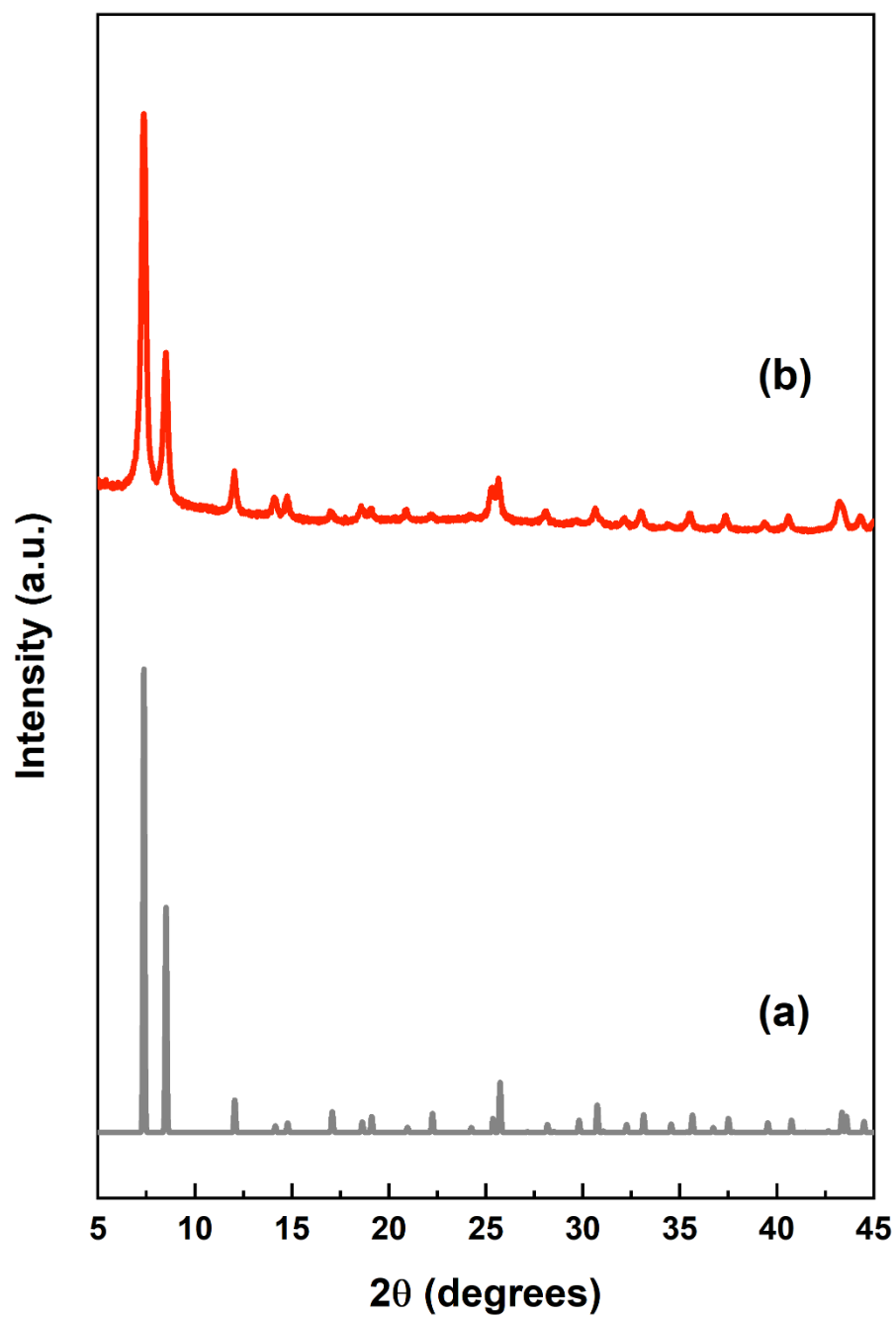


Figure D10. XRD powder analysis of UiO-66 materials (a) Simulated UiO-66 (b) (50/50)MSBDC/Naptha-UiO-66.

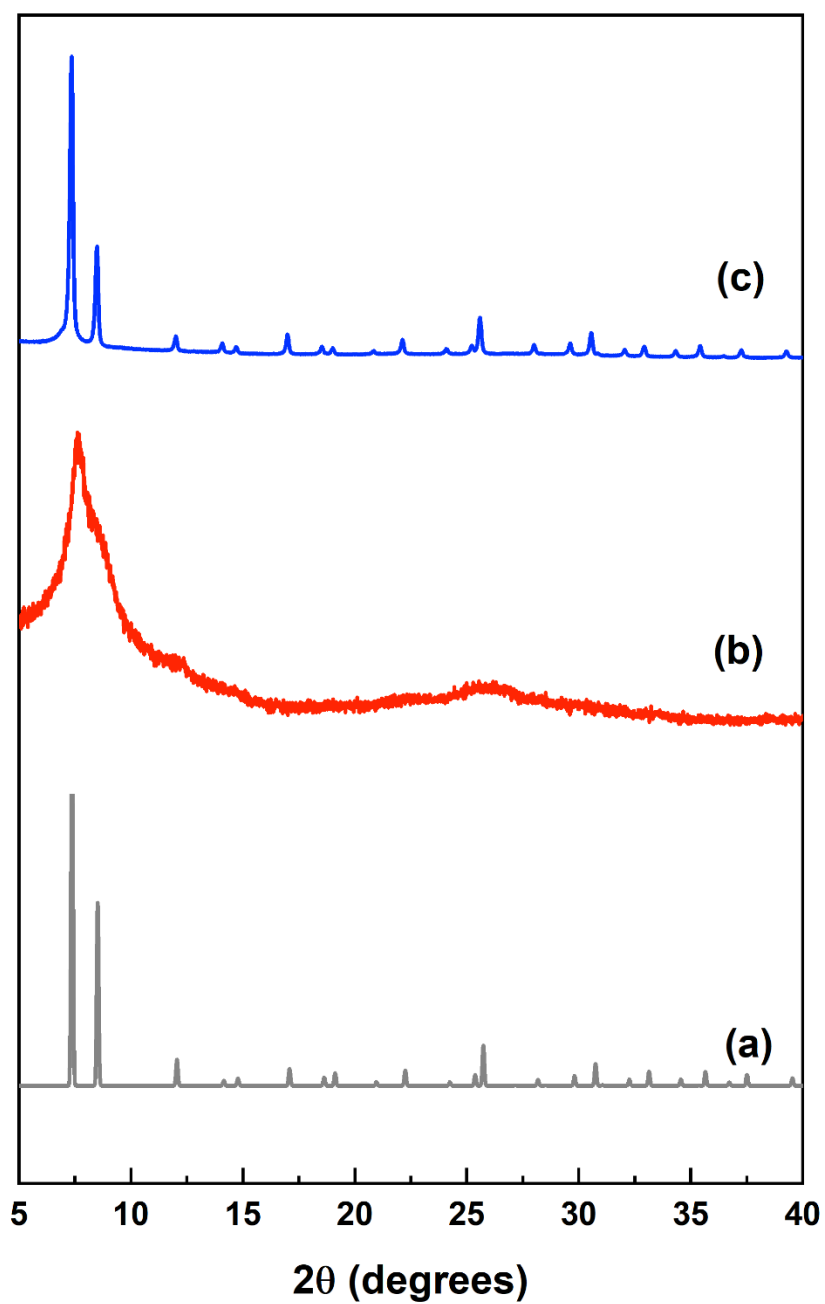


Figure D11. XRD powder analysis of UiO-66 materials (a) Simulated UiO-66 (b) BTeC-UiO-66 (c) Hydroxyl-UiO-66.

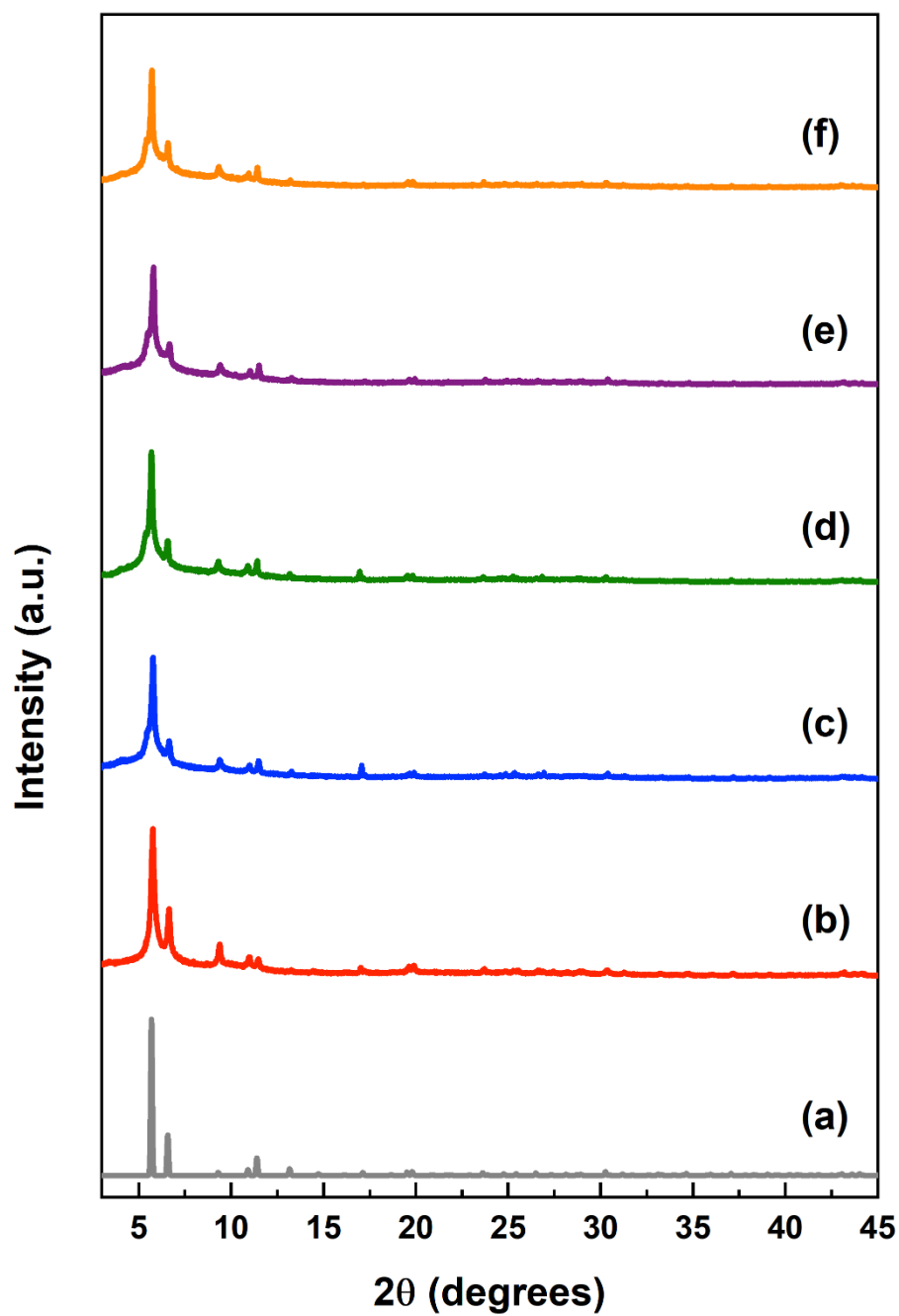


Figure D12. XRD powder analysis (a) Simulated UiO-67 (b) UiO-67 (c) (20)3-Sulfobenz-1eq (d) (20)3-Sulfobenz-2eq (e) (40)3-Sulfobenz-1eq (f) (40)3-Sulfobenz-2eq.

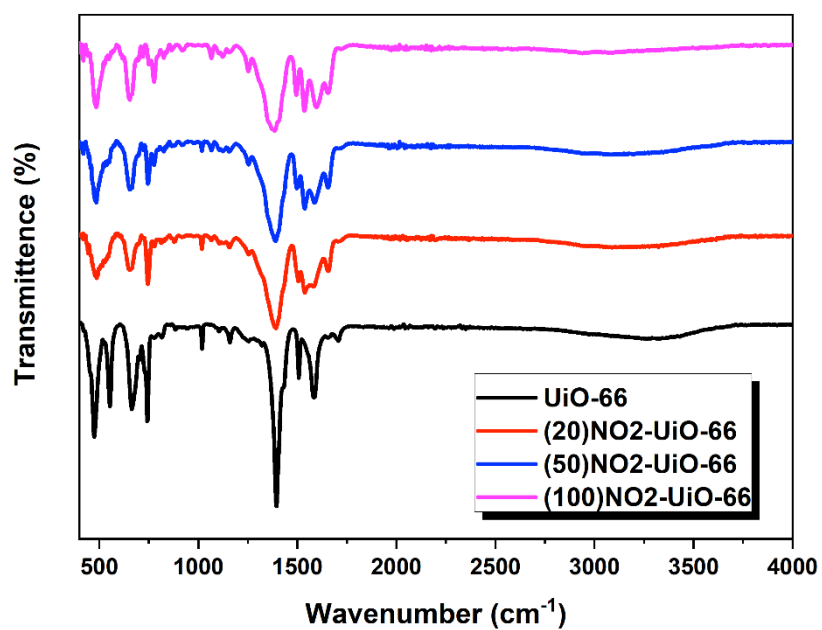


Figure D13. FTIR analysis of nitro functionalised UiO-66.

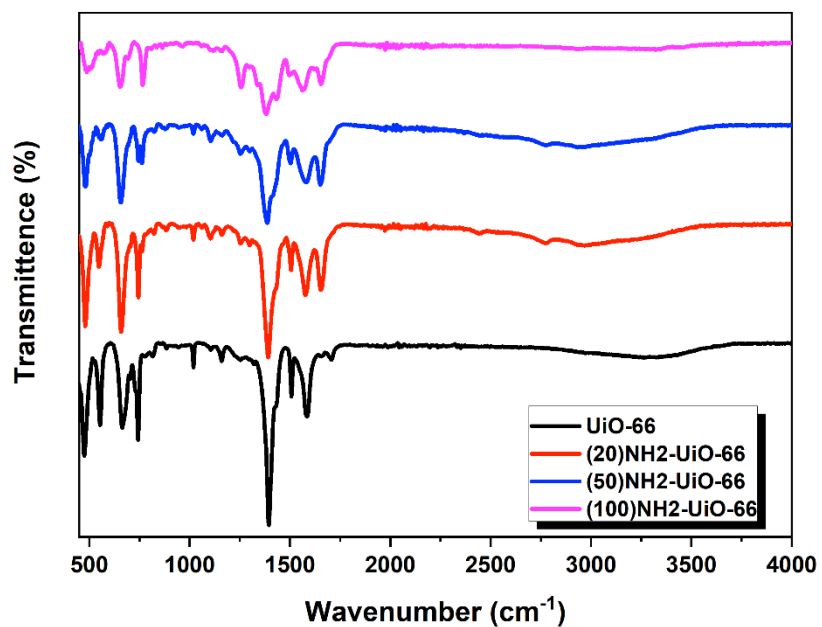


Figure D14. FTIR analysis of amine functionalised UiO-66.

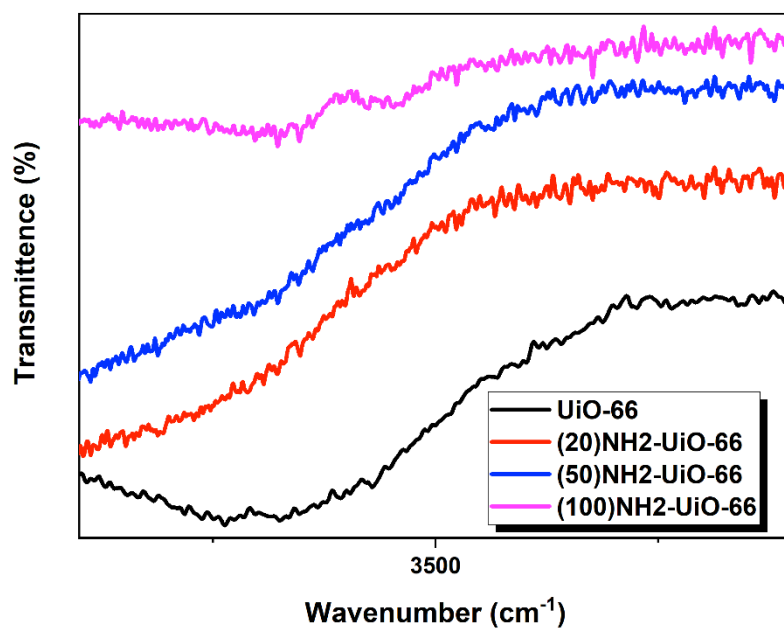


Figure D14a. FTIR analysis of amine functionalised UiO-66 around 3500 cm^{-1} .

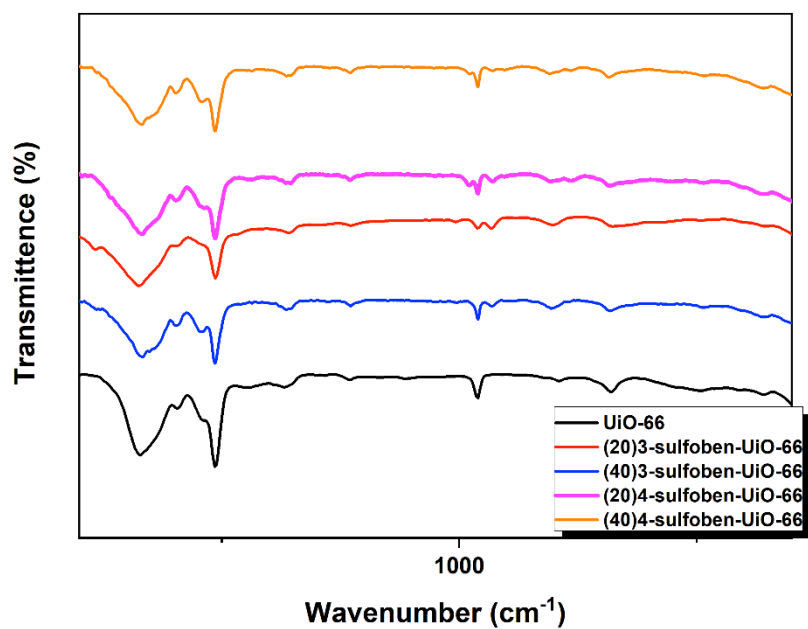


Figure D15. FTIR analysis of sulfobenzoic acid functionalised UiO-66.

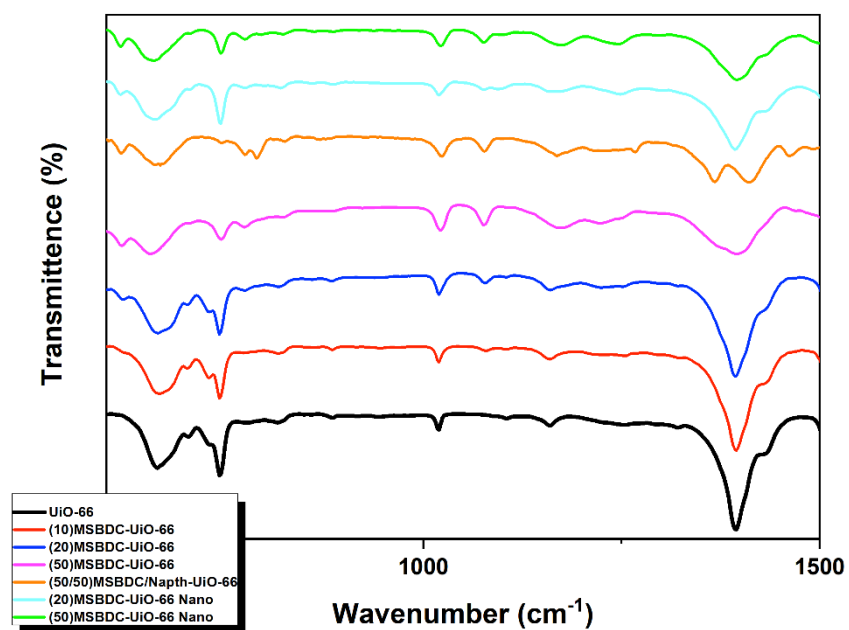


Figure D16. FTIR analysis of MSBDC functionalised UiO-66.

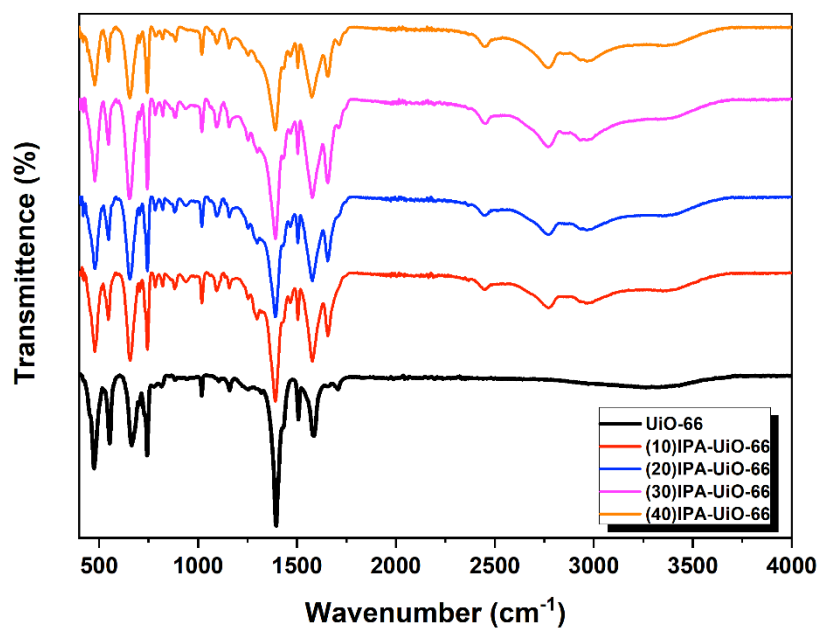


Figure D17. FTIR analysis of IPA functionalised UiO-66.

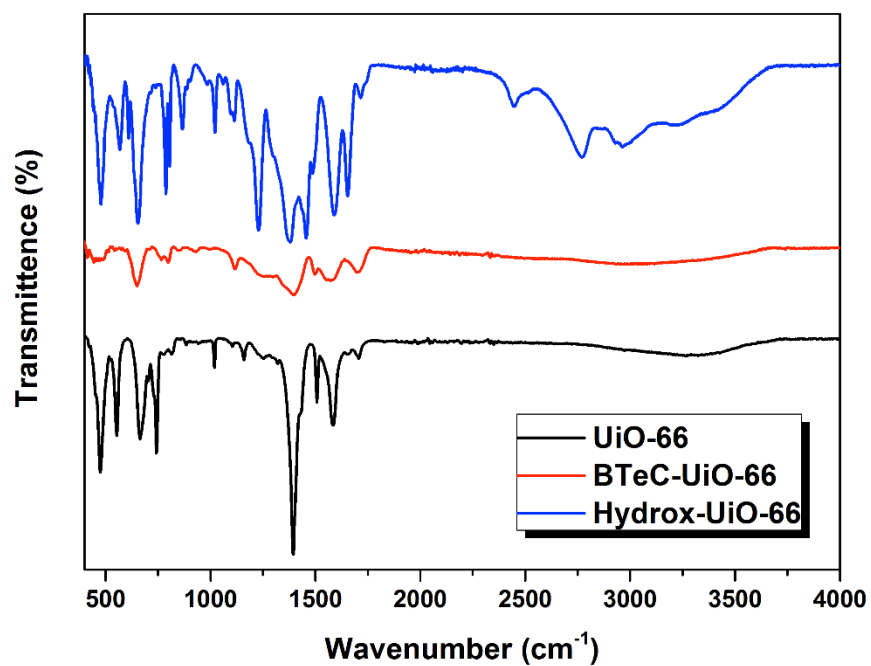


Figure D18. FTIR analysis of BTeC and Hydrox functionalised UiO-66.

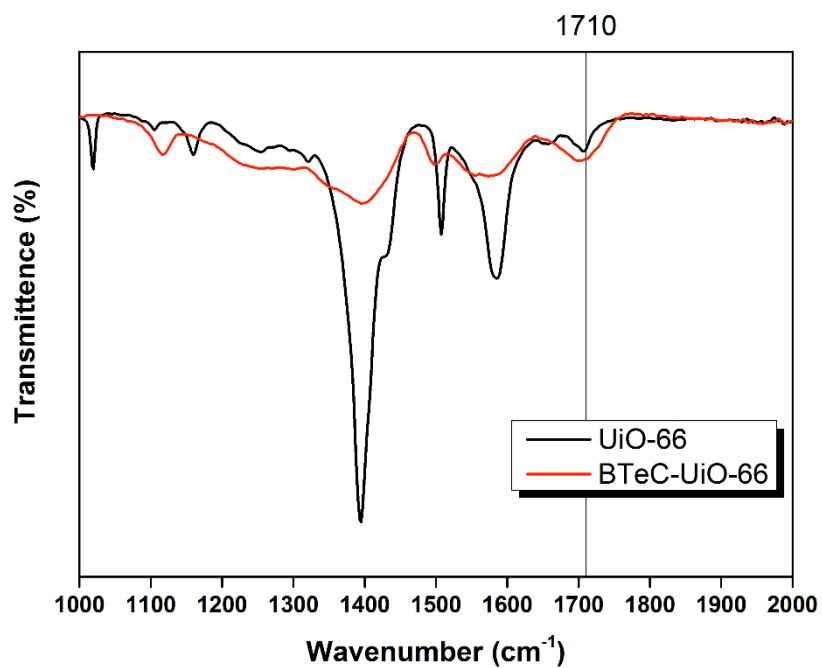


Figure D18a. FTIR analysis of BTeC peak at around 1710 cm⁻¹.

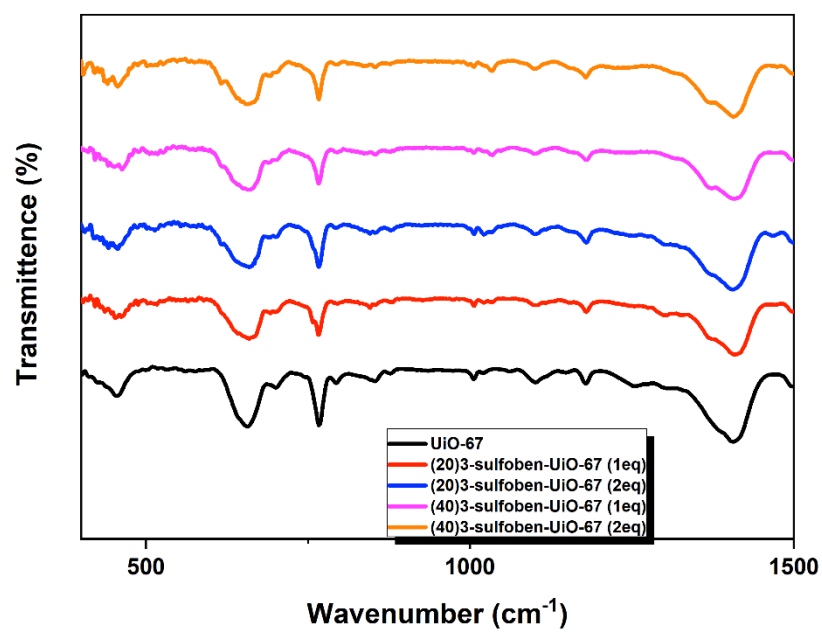


Figure D19. FT-IR analysis of functionalised UiO-67.

Table D1. Zr Coordination Numbers of UiO-66 and UiO-67 materials calculated from TGA data.

Entry	Material	Zr Coordination Number (n)	Entry	Material	Zr Coordination Number (n)
1	UiO-66	5.51	18	(20)NH ₂ -UiO-66	5.74
2	(10)MSBDC-UiO-66	5.11	19	(50)NH ₂ -UiO-66	5.71
3	(20)MSBDC-UiO-66	5.63	20	(100)NH ₂ -UiO-66	5.89
4	(50)MSBDC-UiO-66	5.87	21	(10)IPA-UiO-66	5.99
5	Deffective-UiO-66	4.12	22	(20)IPA-UiO-66	5.97
6	Nano-UiO-66	4.44	23	(30)IPA-UiO-66	6.04
7	Poorly Crystalline Nano UiO-66	5.5	24	(40)IPA-UiO-66	5.76
8	Ultra Nano UiO-66	2.13	25	(20)Naphtha-UiO-66	5.22
9	(20)MSBDC-UiO-66 Nano	4.08	26	(50)Naphtha-UiO-66	5.25
10	(50)MSBDC-UiO-66 Nano	4.87	27	(100)Naphtha-UiO-66	4.49
11	(20)3-Sulfoben-UiO-66	2.96	28	(50/50)MSDBC/Naphtha-UiO-66	4.14
12	(40)3-Sulfoben-UiO-66	3.80	29	BTeC-UiO-66	4.92
13	(20)4-Sulfoben-UiO-66	4.01	30	UiO-67	5.21
14	(40)4-Sulfoben-UiO-66	3.93	31	(20)3-Sulfoben-UiO-67(1eq)	3.42
15	(20)NO ₂ -UiO-66	5.05	32	(20)3-Sulfoben-UiO-67(2eq)	3.67
16	(50)NO ₂ -UiO-66	5.28	33	(40)3-Sulfoben-UiO-67(1eq)	2.69
17	(100)NO ₂ -UiO-66	6.01	34	(40)3-Sulfoben-UiO-67(2eq)	3.00

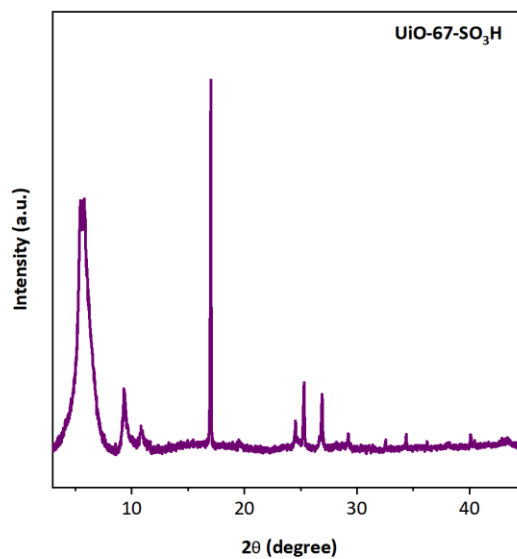
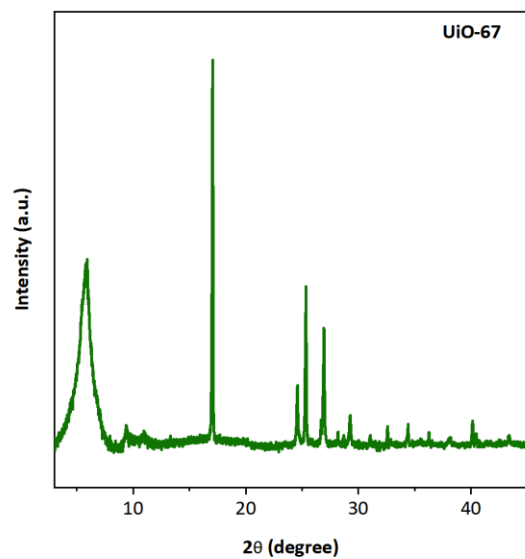
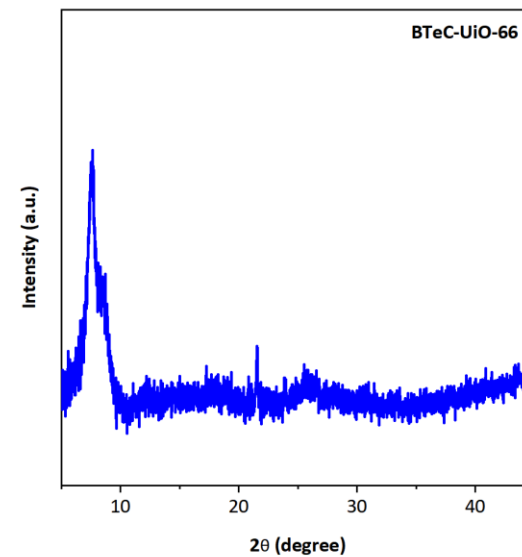
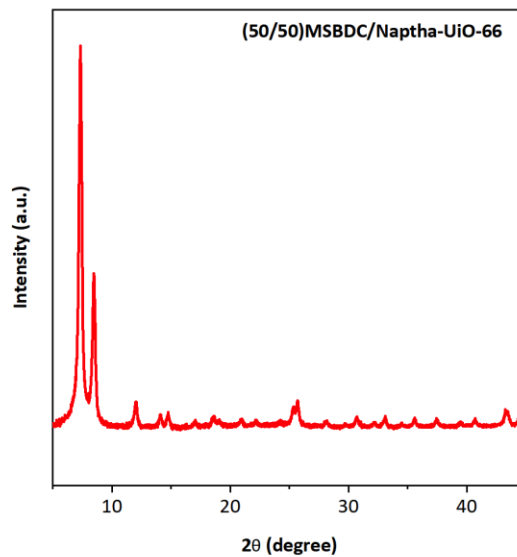
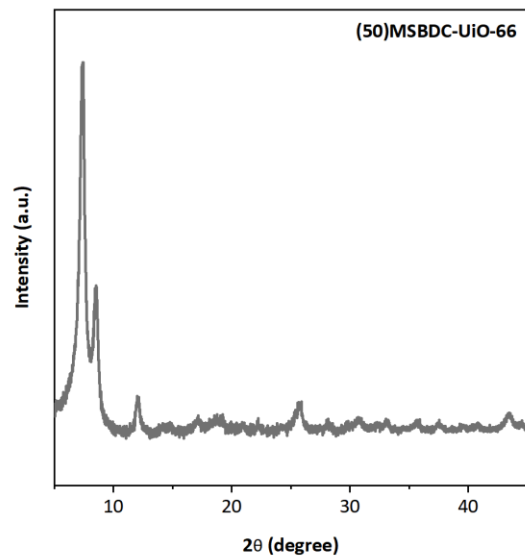


Figure D20. XRD powder analysis of UiO-66 and UiO-67 catalysts after 4 consecutive recycle reactions in water.

Final Page